# On the Nature of Propagating MHD Waves in the Solar Atmosphere

A Thesis

submitted for the award of degree of

**Doctor of Philosophy**

in

The Faculty of Science

by

**Girjesh R. Gupta**

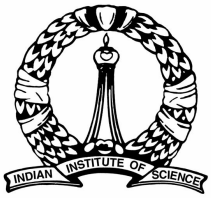


Joint Astronomy Programme

Indian Institute of Science

Bangalore – 560 012

December 2010

# Declaration

I hereby declare that the matter contained in this thesis is the result of research work carried out by me, under the supervision of Prof. Dipankar Banerjee at Indian Institute of Astrophysics, Bangalore and Dr. Tarun Deep Saini at the Department of Physics, Indian Institute of Science, Bangalore. I further declare that this thesis has not been submitted for the award of any degree, diploma, associateship, fellowship etc. of any university or institute.

Girjesh R. Gupta
S. R. No. 7610–110–051–04354

Indian Institute of Science
Bangalore - 560 012, India
December, 2010

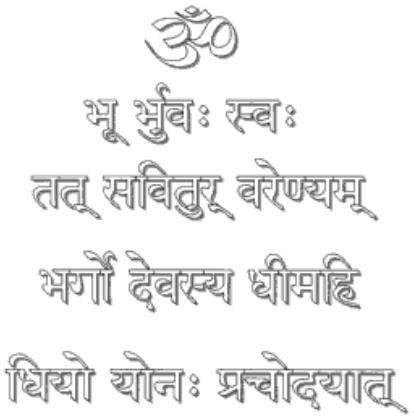


---

Dedicated to

My Parents

and

Family Members

---

# Acknowledgements

It is a pleasure to thank all those who helped me to reach at this stage of writing the acknowledgement of my Ph.D. thesis.

I am heartily thankful to my supervisor, Prof. Dipankar Banerjee for his esteem guidance and constant support throughout my Ph.D. years, without his co-operation it would not have been possible to complete this thesis. I am grateful for his encouragement to interact and collaborate with experts and at the same time allowing me to explore my own ideas. I am deeply grateful to Dr. Luca Teriaca and Dr. Eoghan O'Shea, for being our collaborators and acting more likely as my co-supervisors during this thesis work, for their extensive and fruitful discussions, comments, suggestions, and support, without which this thesis would not be possible.

I am thankful to Prof. Jagdev Singh for giving me an opportunity to analyse the data acquired during the total solar eclipses for part of my thesis related work. I am also thankful to Prof. Sami Solanki and Prof. Gerry Doyle for collaborating with us on externally funded projects, and for useful discussions and help. I am very much thankful to Dr. David Pérez-Suárez and Dr. Srividya Subramanian for teaching me to use various SolarSoft routines for processing the data during the early stages of this work. I would also like to thank Dr. M. Popescu, Dr. M. Madjarska, and Dr. S. Imada for their kind help during this research work. I am also thankful to Dr. Vigeesh for making the proof-reading of the first part of this thesis. Many thanks to Dr. M. Aschwanden for providing me the recent version of his textbook 'Physics of the Solar Corona'. I am very much thankful to UCAR for selecting me for Heliophysics summer school 2009 and for providing the different volumes of Heliophysics textbook.

I acknowledge SUMER and Hinode Team for making such an excellent telescope. A huge portion of my thesis is based on the datasets obtained from the SUMER spectrometer on-board SOHO, and EIS spectrometer on-board Hinode. The SUMER project is financially supported by DLR, CNES, NASA, and the ESA PRODEX program (Swiss contribution). Hinode is a Japanese mission developed and launched by ISAS/JAXA, with NAOJ as domestic partner and NASA and STFC (UK) as international partners. It is operated by these agencies in co-operation with ESA and NSC (Norway). I also acknowledge joint support from Department of Science

and Technology, Govt. of India and German Academic Exchange Service, which gave me an opportunity to collaborate with researchers in Max Planck Institute, Lindau, Germany under DST-DAAD joint project D/07/03045.

I humbly would take this opportunity to thank current and former JAP coordinators Prof. C. Jog and Prof. A. R. Choudhuri and Dr. T. D. Saini, IIA Director Prof. S. S. Hasan, current and former IIA Academic Deans Prof. H. C. Bhatt and Prof. V. Krishan, for providing me all the necessary facilities during my Ph.D. course-work at IISc and to carry out my thesis work at IIA. I am thankful to library and support staff for providing most of the scientific journals required for my research and for providing all the computer related help whenever required and would like to specially thank Dr. B. Varghese for all his IDL related help.

I must thank all the teachers, professors and friends from my school to college days, for their contribution and cooperation, and for developing the my interest in Mathematics and Physics. My sincere gratitude to all the friends in IIA, IISc, RRI and ISRO; without them the life here in Bangalore could not have been so enjoyable. An attempt here to record the names of all of them would inevitably lead to unintended omissions. I would like to thank all my batch-mates, class-mates, office-mates, seniors and juniors, and other present and past students, post-docs and research trainees, for giving me company during studies, discussions and many sports activities. I am thankful to them for their friendship, company, parties and fun. I am grateful to my room-mate for his presence, patience, and not to make me feel lonely throughout the our stay at IIA. I am very thankful to him and our other friends for all the shopping, movies, and Bangalore visits done together, which will always remain in memory.

I also acknowledge all the other friends, known and unknown well-wishers, for their direct and indirect support throughout my academic life.

I am indebted to my parents and all the family members for their encouragement, blessings and everlasting heartily support, which is beyond the words. I am also grateful to my elders for their blessings, and youngers for their love and affection, which cannot be expressed here.

# List of Publications

## Refereed Publications:

1. *On the statistical detection of propagating waves in polar coronal holes*
   **Gupta, G. R.**, O'Shea, E., Banerjee, D., Popescu, M., Doyle, J. G., 2009, **A&A**, 493, 251-257

2. *Propagating waves in polar coronal holes as seen by SUMER & EIS*
   Banerjee, D., Teriaca, L., **Gupta, G. R.**, Imada, S., Stenborg, G., Solanki, S., 2009, **A&A**, 499, L29-L32

3. *Intensity oscillation in the corona as observed during the total Solar eclipse of March 29, 2006*
   Singh, Jagdev, Hasan, S. S., **Gupta, G. R.**, Banerjee, D., Muneer, S., Raju, K. P., Bagare, S. P., Srinivasan, R., 2009, **Solar Physics**, 260, 125-134

4. *Accelerating waves in polar coronal holes as seen by EIS & SUMER*
   **Gupta, G. R.**, Banerjee, D., Teriaca, L., Imada, S., Solanki, S., 2010, **APJ**, 718, 11-22

5. *Propagating MHD waves in coronal holes*
   Banerjee, D., **Gupta, G. R.**, Teriaca, L., 2010, **SSRv**, Online First

6. *Spectroscopic observation of oscillations in the corona during the total Solar eclipse of July 22, 2009*
   Singh, J., Hasan, S. S., **Gupta, G. R.**, Nagaraju, K., Banerjee, D., Accepted, **Solar Physics**

7. *Nature of quiet Sun oscillations using data from Hinode, SoHO and TRACE spacecrafts*
   **Gupta, G. R.**, Subramanian, S., Banerjee, D., Madjarska, M. S., Doyle, J. G., **Submitted**

## Conference proceedings:

1. *Statistical detection of propagating waves in a polar coronal hole*

   **Gupta, G. R.**, O'Shea, E., Banerjee, D., Popescu, M., Doyle, J. G., 'Magnetic Coupling between the Interior and Atmosphere of the Sun', Astrophysics and Space Science Proceedings, 2010, 433-436

# Abstract

One of the most persistent problem in solar physics is the identification of the mechanism that heats the solar corona and accelerates the fast solar wind. Magneto-hydrodynamic (MHD) waves play a crucial role in heating of the solar corona and acceleration of the solar wind. Different types of oscillations have been now observed by various instruments. These are interpreted as due to ubiquitous presence of MHD waves. The magnetic field plays a fundamental role in the propagation and properties of these MHD waves. The topology (structure) of the magnetic fields are different in different regions of the solar atmosphere viz., active regions (high-lying closed magnetic fields), quiet Sun (low-lying closed magnetic fields) and coronal holes (open magnetic fields). The purpose of this dissertation is to study the nature of these propagating MHD waves in different regions of the solar atmosphere.

It is believed that polar coronal holes which connects the inner corona and the solar wind, are the source regions of the fast solar wind. The on-disk part of a polar coronal hole can be divided into network and internetwork regions. Long time series (*sit-and-stare*) data have been obtained from the SUMER/SoHO spectrometer in N IV 765 Å and Ne VIII 770 Å spectral lines to search for the presence of waves in these two different regions from a statistical approach. The network bright regions indicate the presence of compressional waves with a dominant period of $\approx$ 25 min in both the lines. Moreover, we found that there is a difference in the nature of the wave propagation in the bright ('network'), as opposed to the dark ('internetwork') regions, with the latter sometimes showing evidence of downwardly propagating waves that are not seen in the former. This is consistent with the magnetic topology, as open field lines are rooted in network regions whereas internetwork region has low lying closed field lines. From a measurement of propagation speeds, we found all waves are subsonic, indicating that the majority of them are slow magneto-acoustic in nature.

The off-limb part of coronal holes can be divided into plume and inter-plume regions. The simultaneous observations were performed with EIS/Hinode and SUMER/SoHO spectrometer in Fe XII 195 Å and Ne VIII 770 Å spectral lines respectively. We detected the presence of accelerating waves in a polar inter-plume region with a period of 15 min to 20 min in both the spectral lines and a propagation speed increasing from 130 $\pm$ 14 km $s^{-1}$ just above the limb, to 330 $\pm$ 140 km $s^{-1}$ around 160$''$ above the limb. These waves can be traced to originate from a bright region of the on-disk part of the coronal hole which can be visualized as the base of the

coronal funnels. The adjacent plume region also shows the presence of propagating disturbance with the same range of periodicity but with propagation speeds in the range of 135 ± 18 km $s^{-1}$ to 165 ± 43 km $s^{-1}$ only. We found that the waves within the plumes are not observable (may be getting dissipated) far off-limb whereas this is not the case in the inter-plume region. We suggested that the waves are likely either Alfvénic or fast magneto-acoustic in the inter-plume regions and slow magneto-acoustic in the plume regions. These results support the view that the inter-plume regions are a preferred channel for the acceleration of the fast solar wind.

The quiet Sun can be further divided into bright magnetic (network), bright non-magnetic and dark non-magnetic (internetwork) regions. Simultaneous observations were performed in Ca II filtergram from SOT/Hinode, TRACE 1550 Å passband and with SUMER/SoHO spectrometer in N IV 765 Å and Ne VIII 770 Å spectral lines to study the oscillations in these different regions. We detected the presence of long period oscillations with periods between 15 min to 30 min in bright magnetic regions. The oscillations were detected from chromospheric height to low coronal heights. Power maps showed that low period powers are mainly concentrated in dark regions whereas long period powers are concentrated in bright magnetic regions. We proposed that these 15 min and above periods can propagate up to the coronal heights through 'magneto-acoustic portals'. However in this case only with the spectral imaging data, it was not possible to identify the mode of wave propagation.

To detect the presence of waves in active regions, we have analysed the imaging and spectroscopic data acquired during the total solar eclipse of 2006 and 2009 respectively. We found the oscillations of periods 27 s and 20 s in imaging data obtained in green (Fe XIV 5303 Å) and red (Fe x 6374 Å) coronal emission lines respectively. Significant oscillations with high probability estimates were detected at boundary of active region and in the neighbourhood, rather than within the loops itself. We also reported the detection of oscillations in intensity, velocity and line width having periods in the range of 25 s to 50 s with spectroscopic data again obtained in green and red coronal emission lines. These high frequency oscillations were interpreted in terms of presence of fast magneto-acoustic waves or torsional Alfvén waves.

These detected propagating MHD waves may carry sufficient energy to heat the corona and provide enough momenta to accelerate the fast solar wind. In addition, these waves may also provide input for the measurement of coronal magnetic field using the technique of 'coronal seismology'.

# Contents

# List of Tables

# List of Figures

# Chapter 1

# Introduction

In all ancient cultures, the Sun has occupied a central position. *Hinduism* is the oldest Indian religion and worshipping nature is one of the distinctive characteristic that differentiate it from other cultures. In Hindu mythology, *Surya* represents the Sun god. *Surya* is considered as the only visible form of God that can be seen every day. *Surya* is the lord of excellence and wisdom and is also called the God of Light. Day in India starts with *Surya Namaskar*, by offering water to the Sun God and chanting mantras and prayers in praise of him. Rising Sun is the symbol of hope and beginning. It is the symbol of both birth and death. Konark Sun Temple, located in the eastern State of Orissa near the sacred city of Puri, is dedicated to the Sun God or *Surya*. It is a monumental representation of the Sun God *Surya's* chariot; its 24 wheels are decorated with symbolic designs and it is led by a team of six horses.

## 1.1 Why We Study the Sun

As seen, the importance of Sun was realised long back in time and that is why it got the status of 'First God'. There are various scientific reasons to study the Sun in detail. Here we will point out some of them in brief[1].

[1] `http://solarscience.msfc.nasa.gov/whysolar.shtml`

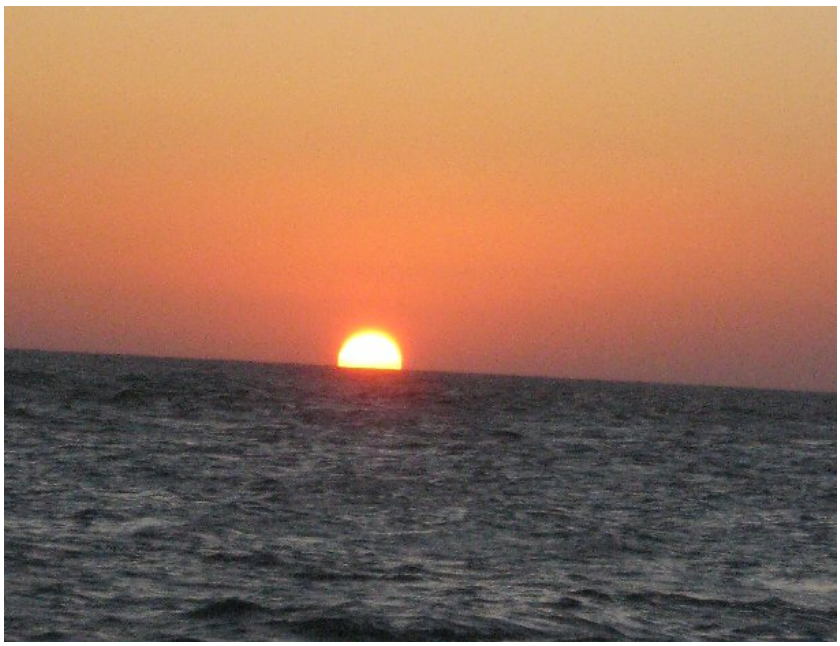

Figure 1.1: Sunset at Kanyakumari, India

### 1.1.1 The Climate Connection

The Sun is a source of light and heat for life on Earth. Our ancestors realized that their lives depend upon the Sun and they put it in the category of deity. We still recognize the importance of the Sun and find it enough motivating and inspiring to spend time and money to understand it. In addition we seek to understand how it works, why it changes, and how these changes influence us here on planet Earth. From the theory of stellar evolution, we speculate that Sun was about 30 % less luminous when life developed on Earth, and yet geological and biological evidence points to a warm young Earth which leads to the 'Faint young Sun paradox'. The quantity and quality of light from the Sun varies on time scales from milli-seconds to billions of years. During recent sunspot cycles the total solar irradiance has changed by about 0.1 % with the Sun being brighter at sunspot maximum. Some of these variations most certainly affect our climate (e.g. Bond et al., 2001) but suggested mechanisms are, however, too complex to evaluate meaningful results at present (Foukal et al., 2006).

Although the changes in solar irradiance in recent sunspot cycles have been very small, there is also evidence that the 'Maunder minimum' of sunspot activity in the seventeenth century was accompanied by a little ice-age in the northern hemisphere of the Earth. This indicates the possibility of solar influence on Earth's climate. As a change of 1–2 °C in the average terrestrial temperature could significantly affect agriculture, a good understanding of mechanism of sunspot cycle would be worth.

### 1.1.2 Space Weather

Sun is the source of *solar wind* which is a flow of gases from the Sun that streams off in all the directions at speeds more than 500 km $s^{-1}$. Hence, Earth is immersed in the escaping ionized outer atmosphere of the Sun. This solar wind, flowing against Earth's magnetic field, shapes the near-Earth space environment. Disturbances in the solar wind shake Earth's magnetic field and pump energy into the radiation belts. Regions on the surface of the Sun often flare and give off ultraviolet light and X-rays that heat up the Earth's upper atmosphere. The response of our space environment to the constantly changing Sun is known as 'Space Weather'. This space weather which describes the conditions in space affecting the Earth can change the orbits of satellites and shorten mission lifetimes. The excess radiation can physically damage satellites and pose a threat to astronauts. Shaking of the Earth's magnetic field can also cause current surges in power lines that may destroy equipment and knock out power over large areas. As we become more dependent upon satellites in space, we will increasingly feel the effects of space weather and need to predict it. The details of what causes various types of space weather are subjects of active investigation.

**Can Space Weather be Predicted?**

Our understanding of space weather is at a preliminary level. Much progress has been made since the 1960s due to the experiments carried out on spacecraft. Today, with realistic space environment models and enhanced observational capabilities for detecting disturbed space weather

conditions or their precursors, it has potential to predict space weather. This requires a framework whereby both expertise and facilities at a broad range of institutions are expected to come together on the task. Such an endeavour will be the ultimate test of our knowledge of the Sun-Earth connections.

### 1.1.3 Sun as a Star

Sun is our nearest star. The distance between the Earth and second nearest star is more than $2 \times 10^5$ times that between the Earth and Sun. Because of this large distances, other stars appear as a point source of light. Hence, the Sun serves an important role to understand the rest of the astronomical universe. It is the only star which helped us to reveal details about stellar surface, starspots and hot outer atmospheres. The Sun is the key to understand other stars. We know the Sun's age, radius, mass, and luminosity (brightness) and we have also learned detailed information about its interior and atmosphere. This information is crucial for our understanding of other stars and how they evolve, and hence in the development of stellar evolution theory. Many physical processes that occur elsewhere in the universe can be examined in detail on the Sun. In this way solar astronomy teaches us much about stars, planetary systems, galaxies, and hence the universe itself.

### 1.1.4 Sun as a Physical Laboratory

Sun produces its energy by nuclear fusion - four hydrogen nuclei are fused to form single helium nuclei deep within the Sun's core. Researchers have worked for decades to reproduce this process in a controlled manner on Earth. Most of these efforts involve extremely hot plasmas in strong magnetic fields. Much of solar astronomy involves observing and understanding plasmas under similar conditions. The theory developed for the extreme cases of high temperature, strong magnetic field and low particle density in the field of plasma physics which can not be tested under laboratory conditions, can be tested in the solar conditions. The theory behind the magnetic

reconnection in extreme cases can also be tested. Therefore, there continues to be much interaction between solar physicists and scientific researchers in these and many other areas. Hence, Sun can be considered as a physical laboratory for plasma physics.

## 1.2 The Solar Atmosphere

The solar atmosphere may be defined as the region of Sun extending outwards from a level known as the photosphere from where energy generated at the Sun's core begins to escape into space as radiation. In short, the layer from where the photon escapes into space without any collision. The photosphere can be regarded as the Sun's surface, which has the thickness of about 200 km. It is a region where optical depth $\tau$, is unity for radiation of wavelength 5000 Å, and written as $\tau_{5000} = 1$. The temperature at this level is about 6400 K.

Energy is generated in the Sun's core by nuclear reactions. This energy is transferred to the rest of the solar interior by radiation up to 0.67 $R_\odot$, and by convection from 0.67 $R_\odot$ to the photosphere. From the Second Law of Thermodynamics, we expect the temperature to fall with distance from the energy generating source at the Sun's core. This fall-off of temperature would be expected to continue in the solar atmosphere, starting from the base of the photosphere where $\tau_{5000} = 1$. In fact the temperature rises, eventually reaching extremely large values, giving rise to an atmosphere which emits radiation at extreme ultraviolet and X-ray wavelengths. The parameters and hence physics derived from these emissions are the subject matter of this thesis.

### 1.2.1 Chromosphere, Transition Region and Corona

The solar atmosphere is generally characterized by spherical shells in the lowest order. In the atmosphere density decreases as a function of radial distance or height from the surface which results due the gravitational stratification. Model solar atmosphere are guide which gives density

and temperature variation with height and help to provide definitions of atmospheric regions. Figure 1.2 shows (solid curve) the variation of temperature in the lower part of the solar atmosphere (heights up to 30,000 km above the $\tau_{5000} = 1$ level), together with variations in the number densities ($cm^{-3}$) of neutral hydrogen ($N_H$) and free electrons ($N_e$), plotted together according to three quiet-Sun models (Vernazza et al., 1981; Fontenla et al., 1990; Gabriel, 1976) over an appropriate height ranges. According to VAL average solar atmospheric models (Vernazza et al., 1981), there is a fall-off of temperature from $\tau_{5000} = 1$ level, reaching $\approx$ 4400 K at a height of about 500 km which is known as temperature minimum level. Above the temperature minimum, the temperature rises to form a broad plateau at $\approx$ 6000 K, over a height range of approximately 1000 km to 2000 km, then rises sharply. To account for large radiation losses due to hydrogen Ly-$\alpha$ emission, the VAL models require a small plateau at $\approx 20,000$ K on the sharp temperature rise. According to the model by Gabriel (1976), this rise continues on to temperatures of $1.4 \times 10^6$ K or more. The physical understanding of this high temperature in the solar corona is still a fundamental problem in astrophysics.

The solar *chromosphere* is defined as the region between the temperature minimum and the region where temperature is $\approx 20,000$ K. The region where temperature reaches $\approx 10^6$ K and densities are very low compared with the chromosphere is known as the solar *corona*. Furthermore, a thin layer where temperature changes sharply from $\approx 20,000$ K to $\approx 10^6$ K and separates cool chromosphere and hot corona is known as *transition region*. The characteristic radiation emitted by material with temperatures between $10^5$ K and a few MK has photon energies between 10 eV and a few 100 eV, corresponding to wavelengths between $\approx$ 1000 Å and less than $\approx$ 100 Å. Therefore, solar chromosphere and corona are strong emitters of ultraviolet and soft X-ray radiations.

To heat the corona to such a high temperature, a heating mechanism due to non-radiant energy source is required. This energy source as well as structures in the chromosphere and corona are strongly correlated with the Sun's magnetic field. Regions of the solar atmosphere, hotter than their surroundings are highly correlated with strong magnetic field regions in the photosphere

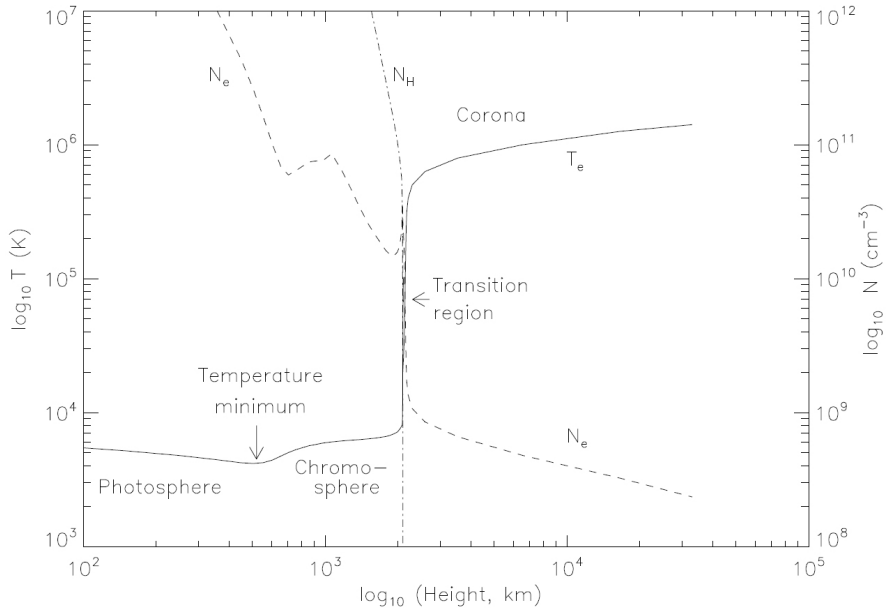


Figure 1.2: The variation of temperature with height in the solar atmosphere (solid curve), based on one-dimensional model calculations of Vernazza et al. (1981); Fontenla et al. (1990); Gabriel (1976). The chromospheric and transition region part of this model atmosphere is for the average quiet Sun. Based on these idealized representations of the solar atmosphere, the transition region is a thin layer with $T = 10^5$ K separating the chromosphere and corona. Variations in the number densities ($cm^{-3}$) of neutral hydrogen atoms ($N_H$) and electrons ($N_e$) (dot-dash and dash curves respectively) are also shown. *Credit:* Phillips et al. (2008).

as deduced from ultraviolet and X-ray observations (Vaiana et al., 1973; Vaiana, 1976). Hence, magnetic fields play an important role in the solar atmospheric dynamics.

### 1.2.2 Ultraviolet and Extreme-Ultraviolet Spectrum of the Solar Atmosphere

Beyond the temperature minimum region, the solar atmosphere has high temperatures and low densities, which results in the spectrum having the wavelength range in ultraviolet and X-ray. Below $\approx$ 1400 Å, the spectra is made up of emission lines and continuum.

Figure 1.3 shows the ultraviolet and extreme ultraviolet disk spectrum of the quiet Sun. Upper panel shows the spectra in the range 675–1600 Å obtained from the Solar Ultraviolet Mea-

surements of the Emitted Radiation (SUMER) instrument on-board the Solar and Heliospheric Observatory (SOHO). The most notable feature in this spectra is the presence of recombination edges in the continuum spectrum. Some of these are at 912 Å (the Lyman continuum edge, due to the recombination of hydrogen), at 1100 Å (recombination to neutral carbon, C I), and at 1197 Å (due to S I). The most intense line of the entire solar ultraviolet spectrum, is the Ly-$\alpha$ line at 1215.67 Å which is emitted in the chromosphere. The total width (FWHM) of this line is 0.7 Å whereas wings of the line extends out to $\approx$ 15 Å either side of the line core. In this quiet Sun spectrum, thousands of other emission lines are present in the range 675–1600 Å. These lines are emitted in the chromosphere, transition region, and corona by several ions of various elements present in the solar atmosphere.

The lower panel of Figure 1.3 shows the spectra in the range 175–210 Å obtained from the Extreme-ultraviolet Imaging Spectrometer (EIS) on the Hinode spacecraft. The spectrum includes resonance lines of a range of Fe ions, from Fe VIII to Fe XIV and hence covers the temperature range of little less than 1 MK to about 2 MK.

### 1.2.3 Structure of the Solar Atmosphere

Due to the structuring of the magnetic field, the solar atmosphere is highly inhomogeneous. The magnetic field $B$ exerts a Lorentz force on the charged particles of the atmospheric plasma which consists of mainly electrons and ions. This suggests that dynamics of solar atmosphere is not only governed by thermal gas pressure but also by the magnetic pressure and tension. Hence, dynamics of the solar atmosphere can be characterized to be controlled by the decisive parameter called as plasma-$\beta$ parameter which is defined as the ratio of the thermal pressure $p_{th}$ to the magnetic pressure $p_{mag}$,

$$\beta = \frac{p_{th}}{p_{mag}} = \frac{2\xi n_e k_B T_e}{B^2/2\pi} \tag{1.1}$$

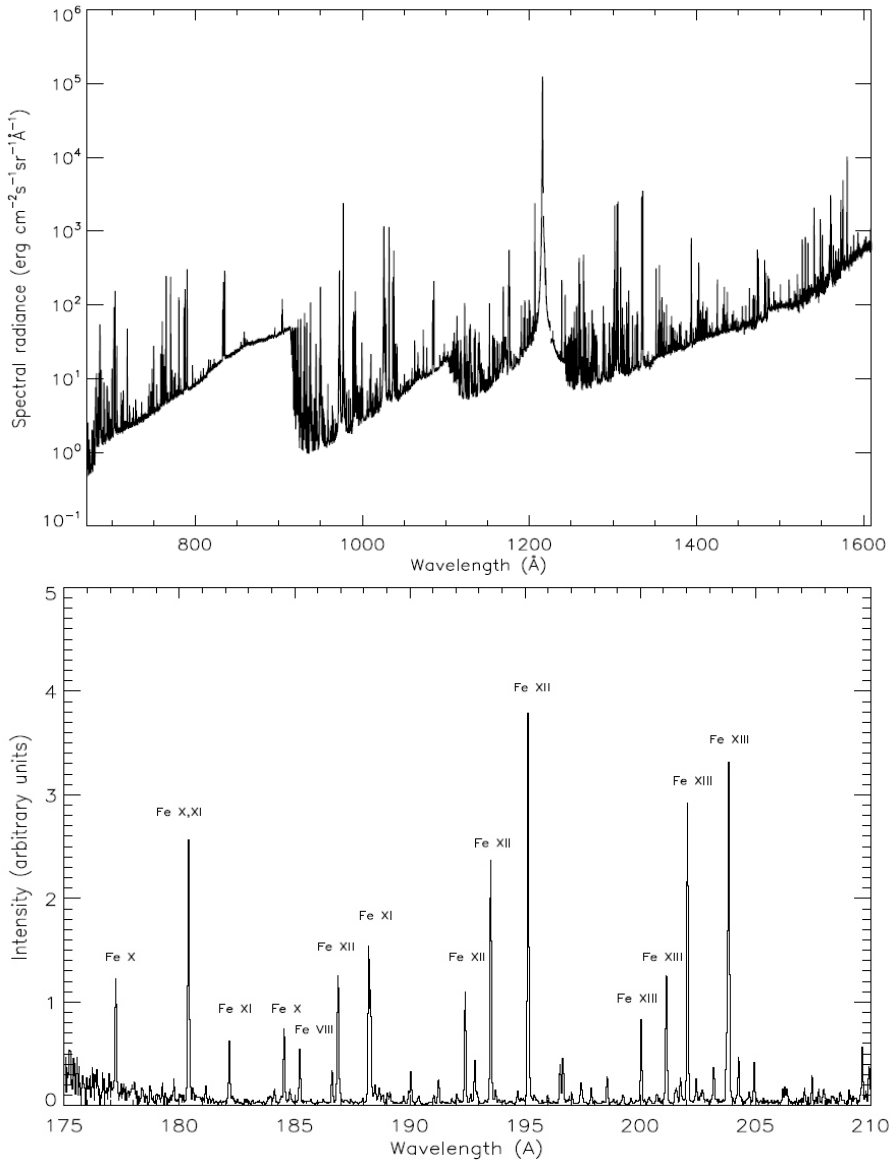


Figure 1.3: Examples of ultraviolet and extreme ultraviolet solar spectra. (Upper:) SUMER/SOHO quiet Sun disk spectrum in the range 675–1600 Å, showing the Lyman lines (particularly Ly-$\alpha$ line at 1215.67 Å), the Lyman recombination edge at 911.8 Å and the C I recombination edge at 1101.2 Å. *Courtesy:* SUMER/SOHO. (Lower:) Quiet Sun disk spectrum from the Extreme-ultraviolet Imaging Spectrometer (EIS) on the Hinode spacecraft, showing the diagnostically important lines of Fe ions between 175 Å and 210 Å, formed at coronal temperatures. *Courtesy:* EIS/Hinode. Extracted from Phillips et al. (2008).

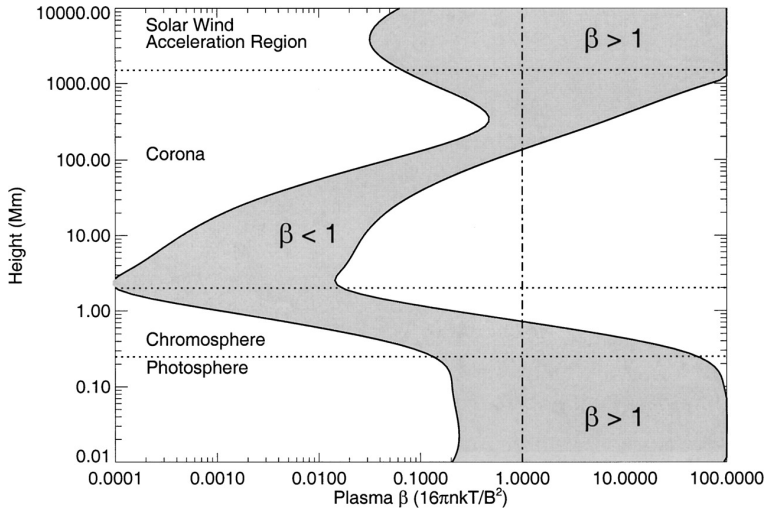


Figure 1.4: Plasma-$\beta$ in the solar atmosphere for two assumed field strengths, 100 G and 2500 G. In the inner corona ($R \lesssim 0.2\ R_\odot$), magnetic pressure generally dominates static gas pressure. As with all plots of physical quantities against height, a broad spatial and temporal average is implied (Gary, 2001). *Credit:* Aschwanden (2005)

Where $n_e$ is electron density, $k_B$ is Boltzmann constant, $T_e$ is electron temperature and $\xi = 1$ is the ionization fraction for the corona (and $\xi = 0.5$ in the photosphere).

A comprehensive model of the plasma-$\beta$ parameter has been built by Gary (2001), using a large number of physical parameters quoted in the literature. The model gives a well-constrained range of $\beta$-values for any given height, $\beta(h)$, and is shown as a grey zone in Figure 1.4. We see that most parts of the chromosphere and corona have a plasma-$\beta$ parameter of $\beta < 1$, whereas in the photosphere and outer corona plasma-$\beta$ parameter has values $\beta > 1$. Therefore, most parts of the corona are magnetically confined and can be considered as magnetosphere.

The evolution of our perception of the topological structure of the solar corona from the different space mission observations is depicted in Figure 1.5. So, we can conceive the topology of the solar atmosphere by structures that are aligned with the magnetic field. There are two types of magnetic field lines: closed field lines that start and end at the solar surface, and open field lines which start at the solar surface and reaches up to the interplanetary space. Hence, the inhomogeneous nature of the solar atmosphere can be attributed to its magnetic field.

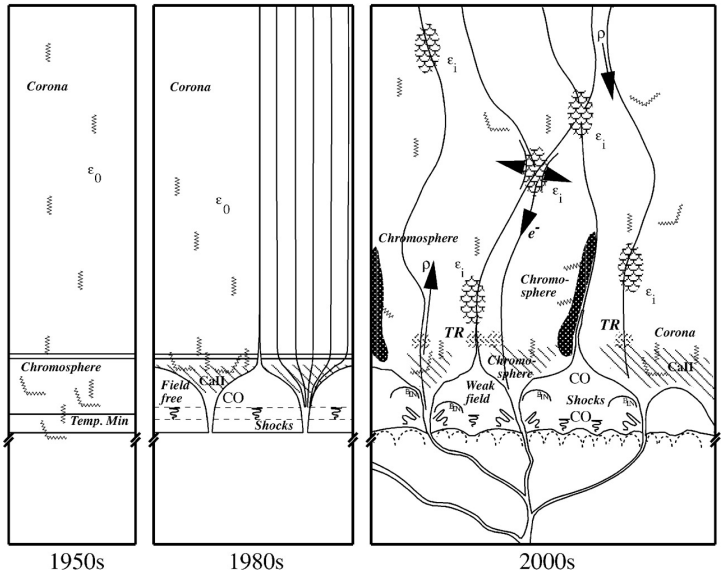


Figure 1.5: Evolution of the corona cartoon: gravitationally stratified layers in the 1950s (left), vertical flux tubes with chromospheric canopies in the 1980s (middle), and a fully inhomogeneous mixing of photospheric, chromospheric, transition region (TR), and coronal zones by such dynamic processes as heated up-flows, cooling down-flows, intermittent heating, reconnections, emission from hot plasma, acoustic waves, and shocks (right) (From Schrijver, 2001).

Due to the convection in solar interior, a small scale convection pattern consisting of cell structures or *granules* occurs near the solar surface. The structures have typical size of $\approx$ 100 – 1100 km and lifetimes of the order of several minutes. Granules are visible in white light images of photosphere as brighter areas with polygonal shapes which are due to the convective motion (see Figure 1.6). These features are the top parts of convection cells where hot fluid rises up from the interior in the bright areas, spreads out across the surface, cools and then sinks inward along the dark lanes. For our purpose, the more important features are the *supergranules*, which are much larger versions of granules (about 35,000 km across and lifetimes of one to several days). These features are best seen in measurements of the Doppler shift where radiation from fluid moving toward us is blue-shifted while that moving away from us is red-shifted. These features also cover the entire Sun and are continually evolving (see Figure 1.7). The observed fluid flows in supergranules carry magnetic field bundles to the edges of the cells and produces the structure which is termed as *chromospheric magnetic network* whereas the region within the cells is termed as *internetwork*.

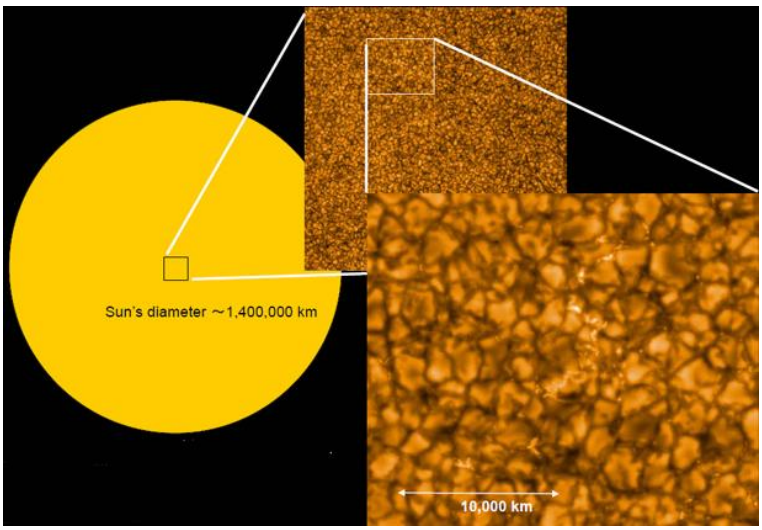


Figure 1.6: Left: The Sun in the white light. Right top and bottom: From SOT showing in detail solar granulation (convection cells), and bright points between granules that are locations of concentrations of magnetic field. *Credit:* JAXA/Hinode

## 1.3 Regions in Solar Atmosphere

It is customary to divide the solar atmosphere into three regions:

- Active regions
- Quiet Sun regions
- Coronal holes

### 1.3.1 Active Regions

*Active Regions* are regions of strong magnetic field concentrations, visible as sunspot groups in optical wavelengths or magnetograms[2] on photosphere. Sunspot groups typically exhibit a strongly concentrated leading magnetic polarity which is followed by a more fragmented trailing

[2]Magnetograms are synthetic images constructed by measuring the magnetic field along the line-of-sight at a given location on the solar surface, and assigning a colour according to the field strength.

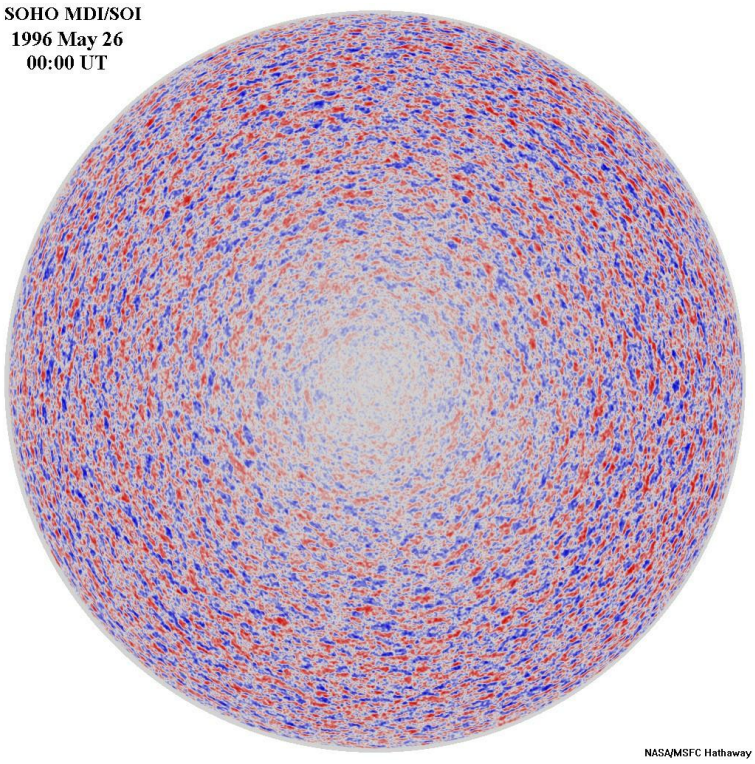


Figure 1.7: Full Sun dopplergram from data obtained with the MDI/SOI on SOHO on 26 May 1996. Blue areas indicate material moving towards us while red ones moving away from us. The observed pattern is known as supergranules. *Credit:* NASA/MSFC

group of opposite polarity. Due to this bipolar nature active regions are mainly made up of closed magnetic field lines. A number of dynamic processes such as plasma heating, flares, and CMEs occur in active regions. Due to plasma heating in the chromosphere, up-flows into coronal loops occur, which give active regions the familiar appearance of numerous filled loops, which are hotter and denser than the background corona, producing bright emission in soft X-rays and extreme ultraviolet wavelengths. In the composite EUV image shown in Figure 1.8, active regions appear in white.

### 1.3.2 Quiet Sun Regions

The remaining areas outside of active regions are called as *quiet Sun regions*. However, many dynamic processes have been discovered all over the solar surface, so that the term quiet Sun is

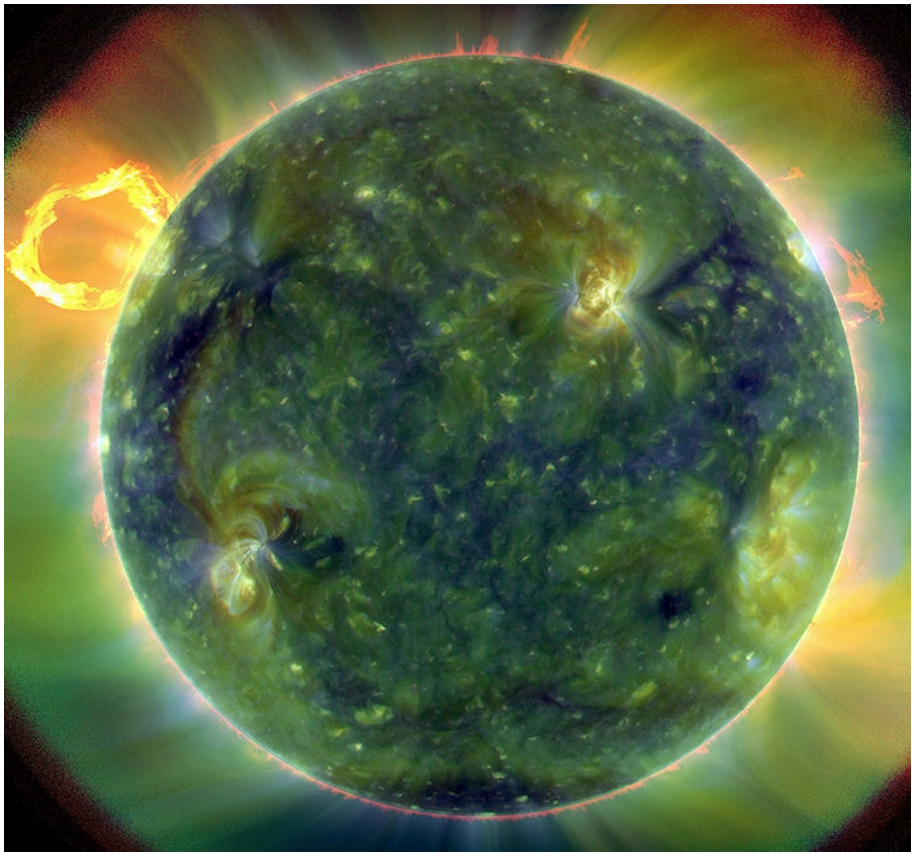

Figure 1.8: A full-disk multi-wavelength extreme ultraviolet image of the Sun taken by SDO on March 30, 2010. False colours trace different gas temperatures. Reds are relatively cool (≈ 60,000 K); blues and greens are hotter (> 1 MK). The composite image shows active regions in white colour, because they contain many loops with different temperatures. Between the active regions, quiet Sun appears in light blue. A clear presence of coronal holes can be seen in polar regions. *Credit:* NASA AIA/SDO

considered as a misnomer and is justified only in relative terms. The distinction between active regions and quiet Sun regions becomes more and more blurred because most of the large-scale structures rooted in active regions, overarch quiet Sun regions. Thus a good definition of quiet Sun would be a regions encompassing all closed magnetic field regions excluding active regions. This definition distinguishes the quiet Sun territory from coronal holes which encompasses open magnetic field regions. Figure 1.8 shows the presence of quiet Sun region between the active regions in light blue colour. Quiet Sun regions are further divided into network and internetwork regions as seen in Figure 1.7.

### 1.3.3 Coronal Holes

During solar eclipse observations in 1950s, Max Waldmeier found northern and southern polar regions to be darker than equatorial regions in green line. Thus, coronal holes are regions of cool and low density plasma that are 'dark' at coronal temperatures (Munro and Withbroe, 1972). These regions are dominated by open magnetic field lines through which heated plasma escape into the solar wind. Because of this, coronal holes have comparatively low density of plasma most of the time, and thus appear much darker than the quiet Sun, where plasma is trapped in closed field lines. A coronal hole is visible in Figure 1.8 at the south pole, where the field structures point radially away from the Sun and show a cooler temperature ($T \leq 1$ MK) than the surrounding quiet Sun regions.

### 1.3.4 Magnetic Field Strengths in Different Regions

The magnetic field on the solar surface is very inhomogeneous. The strongest magnetic field regions are in sunspots, where field strengths are of the order of $B \approx 2000$–$3000$ G. In the atmosphere, active regions and their plages comprise a larger area around sunspots, with average photospheric fields of $B \approx 100$–$300$ G, containing small-scale pores with typical fields of $\approx 1100$ G. The background magnetic field in the quiet Sun and in coronal holes has a net field of $B \approx 0.1$–$0.5$ G, whereas in the resolved elements, the absolute field strengths amount to $B \approx 10$–$50$ G. Recently, using the spectropolarimeter (SP/SOT) on-board Hinode, Orozco Suárez et al. (2007) and Lites et al. (2008) found that internetwork fields tend to be horizontal and have field strengths below 0.5 kG. Whereas Tsuneta et al. (2008a) indicated the presence of many vertically oriented magnetic flux tubes with field strengths as strong as 1 kG scattered in polar region consistent with the global polarity of the polar region.

## 1.4 Coronal Heating

### 1.4.1 Introduction

In 1942, Bengt Edlén and Walter Grotrian identified Fe IX and Ca XIV lines in the solar spectrum (Edlén, 1943). From the formation temperature of these highly ionized atoms, a coronal temperature of $T \approx 1$ MK was inferred for the first time. Comparing this coronal temperature with the photospheric temperature of 6000 K (4800 K in sunspots), we are confronted with the puzzle of how the 200 times hotter coronal temperature can be maintained, the so-called *coronal heating problem*. According to Second Law of Thermodynamics, the temperature in the corona should steadily drop down from the chromospheric value with increasing distance due to thermal conduction. Moreover, due to radiative losses by EUV emissions, corona would just cool off within the duration of hours to days. Hence, to maintain the coronal plasma temperature to $\approx 1$ MK, a continuous source of heating is required. Table 1.1 lists the coronal energy losses due to several mechanisms in different coronal regions. From the table, we can summarize that the minimum heating requirement at any place on the solar surface is $\gtrsim 3 \times 10^5$ erg cm$^{-2}$ s$^{-1}$. The total energy budget of corona is just a $10^{-4}$ fraction of the Sun's total energy output. Today, the question is not from where does the non-thermal energy comes, but how does this energy is carried to the corona and how does it dissipate efficiently there.

Reviews on the coronal heating problem can be found in Withbroe and Noyes (1977); Ulmschneider et al. (1991); Zirker (1993); Aschwanden et al. (2001); Aschwanden (2005); Klimchuk (2006) and Erdélyi and Ballai (2007).

### 1.4.2 Heating Mechanisms

In general, any heating process is usually split into three phases: (i) the generation of energy (may be magneto-convection and flux emergence); (ii) the transport of energy from the location

Table 1.1: Coronal energy losses, extracted from Withbroe and Noyes (1977).

| Parameter | Coronal hole | Quiet Sun | Active region |
|---|---|---|---|
| Coronal temperature [K], at $r \approx 1.1R_\odot$ | $10^6$ | $1.5 \times 10^6$ | $2.5 \times 10^6$ |
| Coronal energy losses [erg cm$^{-2}$ s$^{-1}$] | | | |
| – Conductive flux $F_C$ | $6 \times 10^4$ | $2 \times 10^5$ | $10^5 - 10^7$ |
| – Radiative flux $F_R$ | $10^4$ | $10^5$ | $5 \times 10^6$ |
| – Solar wind flux $F_W$ | $7 \times 10^5$ | $\lesssim 5 \times 10^4$ | $(< 10^5)$ |
| – Total corona loss $F_C + F_R + F_W$ | $8 \times 10^5$ | $3 \times 10^5$ | $10^7$ |
| Solar wind mass loss [g cm$^{-2}$ s$^{-1}$] | $2 \times 10^{-10}$ | $\lesssim 2 \times 10^{-11}$ | $(< 4 \times 10^{-11})$ |

of generation to the solar atmospheres (may be wave propagation); (iii) and mechanism for dissipation of energy in the atmosphere (may be phase mixing, resonant absorption, etc). However, there is a real difficulty in how the transported energy is dissipated efficiently on a time-scale so that the corona is not relaxed thermally. A brief and schematic summary of the most commonly accepted heating mechanisms is given in Figure 1.9.

In most part of the solar atmosphere, plasma is embedded in magnetic fields. To describe these kind of system, a single unified framework, called *Magneto-HydroDynamics* (MHD) approach is more appropriate. As solar corona is highly dynamic and contains many different structures. Intuitively, it becomes obvious to visualize presence of waves in the solar atmosphere. While propagating, waves carry energy with themselves and can be dissipated in the medium in which they travel. These are the qualities which make MHD waves worthy for study in order to solve the coronal heating problem.

## 1.5 AC Mechanisms: MHD Wave Heating

With increased spatial and time resolution and sensitivity of modern observational instruments, it became possible to directly observe the wave and oscillatory processes in the solar atmosphere. In recent years, oscillations in the solar corona have been detected and are summarized in Walsh and Ireland (2003); Roberts (2004); Nakariakov and Verwichte (2005); Banerjee et al. (2007)

| Energy carrier | Dissipation mechanism |
|---|---|
| **Hydrodynamic heating mechanisms** | |
| Acoustic waves<br>Pulsational waves | Shock dissipation |
| **Magnetic heating mechanisms** | |
| 1. Alternating current (AC) or wave mechanisms | |
| Slow waves | Shock damping,<br>resonant absorption |
| Fast MHD waves | Landau damping |
| Alfvén waves | Mode coupling,<br>resonant heating,<br>phase mixing,<br>viscous heating,<br>turbulent heating,<br>Landau damping,<br>resonant absorption |
| 2. Direct current (AC) mechanisms | |
| Current sheets | Reconnection |

Figure 1.9: Summary of the various popular heating mechanisms. *Credit:* Erdélyi (2007)

and Taroyan and Erdélyi (2009).

In order to understand the various oscillations and waves in the solar atmosphere, a description of MHD equations and waves are necessary.

### 1.5.1 Ideal MHD Equations

Not only solar plasma but also many astrophysical plasmas such as astrophysical disks and jets are characterized by a set of equations called as *ideal MHD equations*. These equations include the continuity Equation 1.2, the momentum Equation 1.3, equation of state for energy conservation (e.g., incompressible, isothermal, or adiabatic) by Equation 1.4, Maxwell's Equations 1.5, 1.6 and 1.7, and Ohm's law by Equation 1.8. Thus, a full set of ideal MHD equations (for an

adiabatic equation of state) is represented as:

$$\frac{D}{Dt}\rho = -\rho\ \nabla \cdot \mathbf{v}\ , \tag{1.2}$$

$$\rho\frac{D\mathbf{v}}{Dt} = -\nabla p - \rho\mathbf{g} + (\mathbf{j} \times \mathbf{B})\ , \tag{1.3}$$

$$\frac{D}{Dt}(p\rho^{-\gamma}) = 0\ , \tag{1.4}$$

$$\nabla \times \mathbf{B} = 4\pi\mathbf{j}\ , \tag{1.5}$$

$$\nabla \times \mathbf{E} = -\frac{1}{c}\frac{\partial \mathbf{B}}{\partial t}\ , \tag{1.6}$$

$$\nabla \cdot \mathbf{B} = 0\ , \tag{1.7}$$

$$\mathbf{E} = -\frac{1}{c}(\mathbf{v} \times \mathbf{B})\ . \tag{1.8}$$

Here $\rho$ is plasma density, $\mathbf{v}$ is plasma fluid velocity, $p$ is kinetic pressure, $\mathbf{g}$ is acceleration due to gravity, $\gamma$ is ratio of specific heat, $\mathbf{B}$ is magnetic field, $\mathbf{j}$ is current density, $\mathbf{E}$ is electric field and,

$$\frac{D}{Dt} = \left(\frac{\partial}{\partial t} + \mathbf{v} \cdot \nabla\right) = \left(\frac{\partial}{\partial t} + v \cdot \frac{\partial}{\partial s}\right)\ , \tag{1.9}$$

signifies the total derivative where v($s$) is the velocity and $s$ the length coordinate along a 1-D loop.

While deriving these equations, several approximations were assumed which are listed here as mentioned in Aschwanden (2005),

1. Plasma is charge-neutral, $\rho_E = 0$ which implies $\nabla \cdot \mathbf{E} = 0$ and $\nabla \cdot \mathbf{j} = 0$,
2. Plasma has very large *magnetic Reynolds number*,
3. The non-relativistic approximation, $v \ll c$,
4. MHD time scales are much longer than collisional time scales,

5. isotropic pressure,

6. the total pressure is sum of the partial pressures $p = \sum_\alpha p_\alpha$ which are mainly due to electron and ion,

7. adiabatic gas with energy equation of state $p\rho^{-\gamma} = const.$

### 1.5.2 MHD Waves

Depending upon the way plasma is structured in terms of density and magnetic field, different modes of MHD oscillations are supported. In the simplest case, we can consider the perturbation as a local phenomenon and neglect the large-scale gradients of macroscopic parameters. The MHD equations then yield the dispersion relation for incompressible case,

$$V_A^2 = \frac{\omega^2}{k^2} \tag{1.10}$$

Where **k** is wave propagation vector, $\omega$ is angular frequency and $V_A$ is associated Alfvén speed given by,

$$V_A = \frac{B_0}{\sqrt{4\pi\rho_0}} \tag{1.11}$$

Due to incompressible nature, no density or pressure changes are associated with it. This incompressible wave is called a *shear Alfvén wave* and falls into the category of *transverse waves*. Alfvén waves are driven by magnetic tension force alone and propagates along the magnetic field. These waves were first predicted by Hannes Alfvén (Alfvén, 1942), for which he received the Nobel Prize in 1970.

For compressible case, above described plasma will lead to the dispersion relation (Aschwanden, 2005),

$$\omega^4 - k^2(C_S^2 + V_A^2)\omega^2 + k_z^2 k^2 C_S^2 V_A^2 = 0 \tag{1.12}$$

Where wave propagation vector $\mathbf{k} = (k_x, k_y, k_z)$ has an absolute value of $k = |\mathbf{k}| = (k_x^2 + k_y^2 + k_z^2)^{1/2}$. The cosine of the wave vector in the direction to the magnetic field is $k_z$, so the *propagation angle* $\theta$ is

$$\cos\theta = \frac{k_z}{k} , \tag{1.13}$$

and $C_S$ is the sound speed in the medium and is given by,

$$C_S = \left(\frac{\gamma p}{\rho}\right)^{1/2} \tag{1.14}$$

Introduction of compressibility do not change the Alfvén wave mode, but leads to the additional two wave modes called as *fast* and *slow magneto-acoustic waves*. Dividing the dispersion relation (Equation 1.12) by $k^4$, it can be expressed as a function of the phase speed $V_{ph}$ and propagation angle $\theta$,

$$V_{ph}^4 - v_{ph}^2(C_S^2 + V_A^2) + C_S^2 V_A^2 \cos^2(\theta) = 0 \tag{1.15}$$

Using this equation, phase speed diagram $V_{ph}(\theta)$ is shown as polar plot in Figure 1.10 for a specific ratio of $C_S/V_A$. It can be seen that the *slow mode* has a phase speed in the range of $0 \leq V_{ph} \leq min(C_S, V_A)$, having a maximum for propagation along the magnetic field and cannot propagate perpendicularly to the magnetic field. Whereas the *fast mode* has a phase speed in the range of $max(C_S, V_A) \leq V_{ph} \leq (C_S^2 + V_A^2)^{1/2}$, with the fastest mode propagating perpendicularly to the magnetic field.

## 1.6 Observational Evidence of Propagating MHD Waves

Detection of these waves in the outer solar atmosphere is made possible by analysing the effects these waves have on the plasma. The presence or signature of compressional waves may be seen in the form of variations or oscillations in radiance, due to change in plasma density, and also in the line-of-sight (LOS) velocities, due to plasma motions (when they have a significant

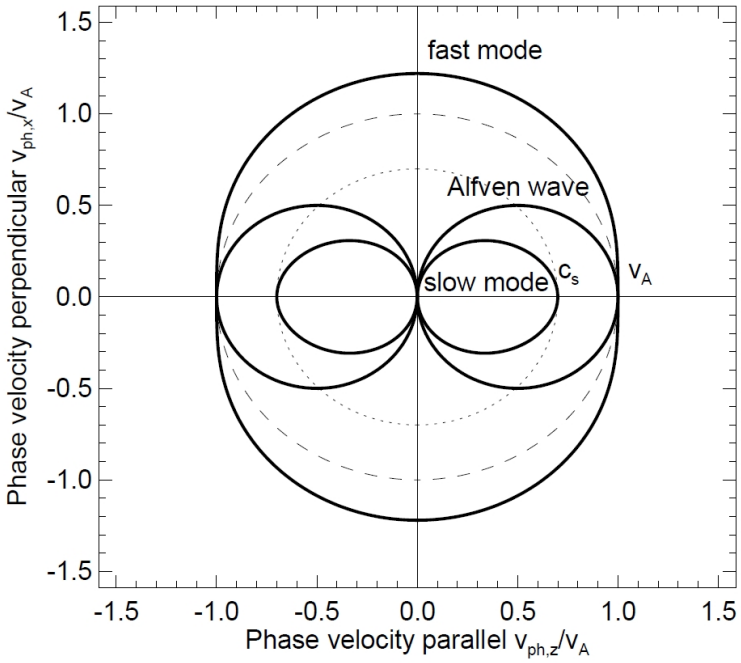


Figure 1.10: Polar diagram of phase speeds $V_{ph}$ of magneto-acoustic waves, shown for a ratio of $C_S/V_A = 0.7$. The sound speed $C_S$ is marked with a dotted circle, and the Alfvén speed with a dashed line. The slow and fast magneto-acoustic modes, and the Alfvén wave are shown with thick curves. *Credit:* Aschwanden (2005).

component directed towards the observer). On the other hand, transverse waves give rise to only LOS effects when they propagate substantially perpendicular to the observer. Moreover the latter give no radiance signature in the theoretical limit of incompressible Alfvén waves. Temporally and spatially resolved motions result in shifts of the observed profiles while unresolved motions result in broadening of the spectral lines. These effects can be measured from the spectroscopic studies of spectral lines.

As described in Banerjee et al. (2007), the first observations of MHD waves in the corona were reported by Chapman et al. (1972). Using the extreme-ultraviolet spectroheliograph on OSO-7, intensity oscillation of 262 s in emission lines of He II 304 Å, Mg VIII 315 Å and Mg IX 368 Å were detected. Similar kind of 300 s velocity oscillations were already detected in the photospheric and low chromospheric lines by Leighton et al. (1962) and Evans and Michard (1962). It was speculated that the photospheric and chromospheric evanescent waves become vertically

propagating, gravity-modified acoustic waves at that height in the chromosphere where temperature rise admits propagation, by reducing the critical frequency above which propagation is possible. Whereas the first observational indication of the presence of compressional perturbations in polar plumes was reported by Withbroe (1983) from Skylab observations. Statistically significant short period variations of Mg x 625 Å line radiance were detected, with propagating speed in the range of 100 to 200 km $s^{-1}$ and amplitudes of about 10 %.

Using Harvard College Observatory EUV spectroheliometer on Skylab, Antonucci et al. (1984) detected oscillations of 117 s and 141 s in the ultraviolet lines of C II 1335 Å, O IV 554 Å and Mg x 625 Å during a loop brightening on August 7, 1973. They suggested that the intensity fluctuation of the EUV lines are caused by small-amplitude waves, propagating in the plasma confined in the magnetic loop and that size of the loop might be important in determining its preferential heating in the active region. Using data from the Hard X-ray Imaging Spectrometer on-board Solar Maximum Mission (SMM), soft X-ray (3.5–5.5 keV) pulsations of period 24 min were detected for six hours by Harrison (1987). Pulsations were also recorded in coronal loops from radio observations (Aschwanden, 1987). These pulsations were thought to be produced by a standing wave or a travelling wave packet which existed within the observed loop. It was concluded that the candidates for the wave were either fast or Alfvén MHD modes of Alfvénic surface waves.

After the launch of Solar and Heliospheric Observatory (SOHO, Domingo et al., 1995), Transition Region And Coronal Explorer (TRACE, Handy et al., 1999) and Hinode (Kosugi et al., 2007) new data shed lights onto the dynamical events such as short time scale variability or oscillations in the solar atmosphere observed at Vacuum Ultraviolet (VUV: 100 to 1600 Å) wavelengths. These periodic oscillations generally carry information from the emitting regions which allows us to diagnose the frozen-in magnetic fields as well as the plasma contained in the different magnetic structures (e.g., plumes, magnetic networks, loops). The wavelengths of these waves are often comparable to the characteristic sizes of these coronal structures and measured time scales are in the range of seconds to few minutes. A summary on the main features of the

Table 1.2: Overview of the periodicities and propagation speeds of propagating MHD waves detected in coronal structures by remote sensing.

| Authors | Regions | Periods (s) | Speed (km $s^{-1}$) | Instrument |
|---|---|---|---|---|
| Ofman et al. (1997) | off-limb CH | 360 | – | UVCS |
| DeForest and Gurman (1998) | plumes | 600-900 | 75-150 | EIT |
| Berghmans and Clette (1999) | active region | $\approx$ 600 | 75-200 | EIT |
| Schrijver et al. (1999) | coronal loop | 300 | 70-100 | TRACE |
| Ofman et al. (2000) | off-limb CH | 400-625 | 160-260 | UVCS |
| Banerjee et al. (2000a) | plume | 600-1200 | – | CDS |
| De Moortel et al. (2000) | active region | 180-420 | 70-165 | TRACE |
| Banerjee et al. (2001a) | inter-plume | 1200-1800 | – | CDS |
| Banerjee et al. (2001b) | equatorial CH | 600-1200 | – | CDS |
| De Moortel et al. (2002) | coronal loop | 282± 93 | 122± 43 | TRACE |
| Sakurai et al. (2002) | coronal loop | 180-600 | 100-200 | Norikura |
| Williams et al. (2002) | coronal loop | 6 | 2100 | SECIS |
| King et al. (2003) | active region | 120-180 & 300-480 | 25-40 | TRACE |
| Marsh et al. (2003) | coronal loop | 300 | 50-195 | CDS-TRACE |
| Katsiyannis et al. (2003) | coronal loop | 7-4 | – | SECIS |
| Popescu et al. (2005) | off-limb CH | 600-5400 and 10200 | – | SUMER |
| O'Shea et al. (2006) | off-limb CH | 300-1000 | 150-170 | CDS |
| O'Shea et al. (2007) | equatorial CH | 300-1000 | 50-70 | CDS |
| Tomczyk et al. (2007) | off-limb corona | 300 | 1000-4000 | CoMP |
| Bemporad et al. (2008) | Off-limb CH | 10000-350000 | – | UVCS |
| Tian and Xia (2008) | equatorial CH | 300-600 | 30-60 | TRACE |
| Erdélyi and Taroyan (2008) | active region | 300-830 | – | EIS |
| Jess et al. (2009) | bright-point group | 126-700 | – | SST |
| Wang et al. (2009a) | coronal loop | 300 | – | EIS |
| Wang et al. (2009b) | coronal loop | 720 & 1500 | 128± 25 | EIS |

observed oscillations along these structures is provided in Table 1.2.

### 1.6.1 Waves in Closed Structures

Using EIT/SOHO, Berghmans and Clette (1999) were the first to report on slow modes in closed loop structures. Following the success of SOHO, observers using TRACE also searched successfully for quasi-periodic disturbances in coronal loops as mentioned in Table 1.2. King et al.

(2003) detected quasi-periodic EUV disturbances simultaneously observed in 171 Å and 195 Å TRACE passbands which were propagating outwardly in a fan-like magnetic structure of a coronal active region. They interpreted these disturbances in terms of parallel-propagating slow magneto-acoustic waves. Periodic patterns of two distinct periods: 2 min to 3 min and 5 min to 8 min were detected in both passbands, existing simultaneously and at the same distance along the loop (see Figure 1.11) and measured propagation speeds were in between 25 km $s^{-1}$ to 40 km $s^{-1}$. This confirms that the diverging fan structures consist of multiple loop threads with different temperatures. A detailed overview of some of the observed properties of propagating intensity perturbations along coronal loop is given in De Moortel et al. (2002). Typical speeds of $v \approx (122 \pm 43)$ km $s^{-1}$ were measured from TRACE 171 Å data, where the mean sound speed is expected to be $C_S \approx 147$ km $s^{-1}$ at $T \approx 1.0$ MK. These waves can be interpreted in terms of slow magneto-acoustic waves based on: (1) the observed propagation speed roughly corresponds to the expected sound speed in the used temperature band, and (2) slow-mode (acoustic) waves being compressional waves, producing a modulation of the density and EUV flux, and thus observed as EUV intensity modulation (which is not the case for Alfvén waves). The energy flux associated with these propagating waves were $(342 \pm 126)$ erg $cm^2$ $s^1$ which is supposed to be far below the requirement for coronal heating.

From a ground-based coronagraphic observation at the Norikura Solar Observatory, Sakurai et al. (2002) have reported on the detection of coronal waves from Doppler velocity data. The propagation speed of the waves was estimated by correlation analysis. The line intensity and line width did not show clear oscillations, but their phase relationship with the Doppler velocity indicated propagating waves rather than standing waves. These waves possibly could also be slow magneto-acoustic in nature.

Williams et al. (2002) and Katsiyannis et al. (2003) reported on the presence of high-frequency MHD waves in coronal loops observed during a total solar eclipse of 11 August 1999 with the Solar Eclipse Coronal Imaging System (SECIS) instrument. The detections lie in the frequency range 0.15 Hz to 0.25 Hz (4 s to 7 s), last for at least three periods at a confidence level of more

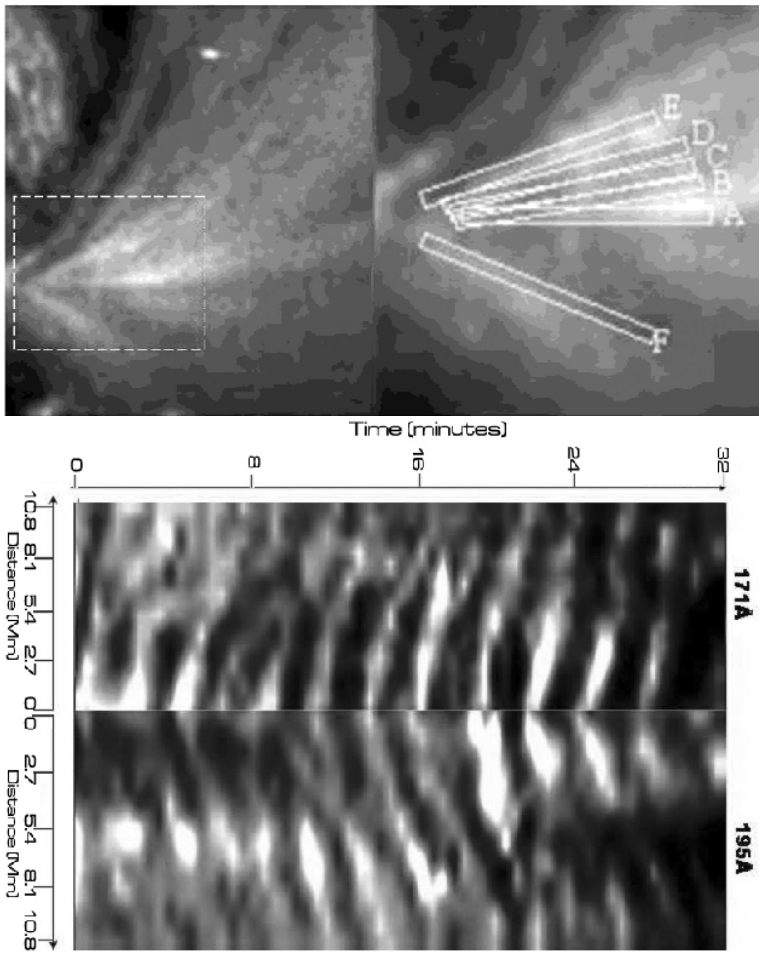


Figure 1.11: Top left panel: active region AR8253 observed by TRACE on July 2 1998 at 06:00 UT in the 195 Å passband. Top right panel: positioning of the slits on an enlarged image of the region indicated by dashes in the left panel. Bottom: simultaneous time-distance plots of propagating EUV disturbances observed by the TRACE in 171 Å and 195 Å passbands along slit A. The distance along the slit is shown in opposite directions to demonstrate that the disturbances observed in different passbands form a 'fishbone' structure. From King et al. (2003).

than 99 %, and arise just outside known coronal loops. This led them to suggest that they occur in low emission measure or different temperature loops associated with active regions.

Similar searches for waves with CDS/SOHO data, which has substantially less spatial resolution than TRACE and EIT data, have only revealed marginal signals of oscillatory wave activity (Marsh et al., 2003; O'Shea et al., 2006, 2007), due to the overwhelming confusion with other spatially unresolved and time-varying coronal structures.

Tomczyk et al. (2007) have conclusively shown that low amplitude (1 km $s^{-1}$) waves are ubiquitously present in the solar corona using the Fe XIII 10747 Å coronal emission line with the Coronal Multi-Channel Polarimeter (CoMP) instrument at the National Solar Observatory, New Mexico. Ubiquitous upward propagating waves were seen, with phase speeds of 1000 to 4000 km $s^{-1}$ with periods near 5 min and trajectories were consistent with the direction of the magnetic field. An estimate of the energy carried by the waves indicates that they are too weak to heat the solar corona; however, unresolved Alfvén waves may carry sufficient energy.

### 1.6.2 Waves in Open Structures

The first undoubted detection of propagating slow MHD waves was made by the Ultraviolet Coronagraph Spectrometer (UVCS/SOHO). Detection of slow waves in an open magnetic structure high above the limb of coronal holes but within a heliocentric distance of $r = 1.9 - 2.45\ R_\odot$ was reported by Ofman et al. (1997, 2000). Fourier power spectra of *polarized brightness* time series revealed significant power at a period of $P \approx 6$ min. Whereas DeForest and Gurman (1998) analysed Extreme-ultraviolet Imaging Telescope (EIT/SOHO) data of polar plumes, detected similar compressive disturbances with linear amplitudes of the order of 10 % to 20 % and periods of 10 min to 15 min. They plotted the EUV brightness of polar plumes (Figure 1.12, top) as a function of time (Figure 1.12, bottom), using the EIT 171 Å passband, propagating features were noticed which had an outward speed of $\approx$ 75 km $s^{-1}$ to 150 km $s^{-1}$. Based on the speed, which is close to the sound speed ($T \approx 1.0$ MK, $C_S = 147$ km $s^{-1}$), and the density modulation inferred from the EUV brightness variation, Ofman et al. (1999) interpreted that these wave trains in plumes to be propagating slow-mode magneto-acoustic waves as it is compressible in nature.

A number of studies using the CDS and SUMER spectrographs on SOHO have reported oscillations in plumes, inter-plumes, and coronal holes in the polar regions of the Sun (Banerjee et al., 2000a, 2001a,b; Popescu et al., 2005; O'Shea et al., 2006, 2007). These oscillations were

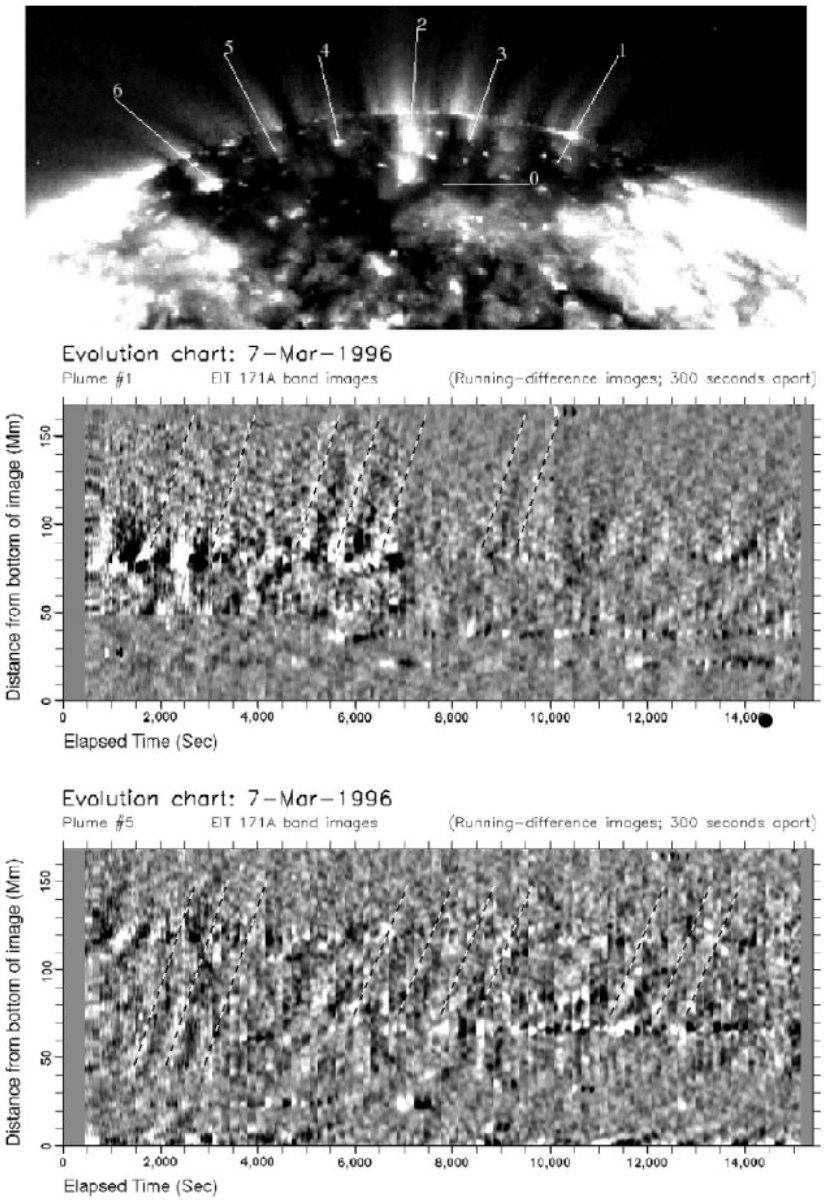


Figure 1.12: Top: polar plumes observed over the South Pole of the Sun with SOHO/EIT on March 7, 1996 at a wavelength of 171 Å after subtraction of the radial background model. Bottom: running time difference images of plume #5, with strips averaged over 360 s. Diagonal features have velocities of $\approx 100$ km s$^{-1}$. Extracted from DeForest and Gurman (1998).

also interpreted as slow magneto-acoustic waves. Up to now evidences for the fast magneto-acoustic wave modes in these same regions are absent, even though recent results by Verwichte et al. (2005) have shown that propagating fast magneto-acoustic waves can be present in open magnetic field structures. For the observation of fast-mode MHD waves, probably the high time

cadence and high-density contrast is needed.

### 1.6.3 Spectral Observations of Alfvén Waves in Open Structures

So far, it has been mentioned that waves may be detected by using the oscillatory signatures they impose on the plasma (density changes and plasma motions). Another method of detecting waves is to examine the variation they produce in line widths measured from spectral lines. The measured broadening of the optically thin spectral lines of ions is due to two effects, thermal broadening and non-thermal broadening associated with Doppler shifts as a result of unresolved line-of-sight motions (e.g., caused by Alfvén waves, see details in section 3.5).

Doschek and Feldman (1977) measured the non-thermal velocities of about $\approx$20 km s$^{-1}$ above the limb ($\approx$ 30$''$) in coronal hole region in Si VIII 1446 Å spectral line recorded by the NRL slit spectrograph on Skylab. Measurements with SUMER/SOHO revealed that the non-thermal velocity increases systematically with the altitude above the limb (Doyle et al., 1998a), which corresponds to a velocity increase that is consistent with the theoretical prediction of undamped radially propagating Alfvén waves. Banerjee et al. (1998) confirmed this result over a larger height range, finding an increase of the non-thermal velocity of the Si VIII line pair (1446 Å and 1440 Å) from $\Delta v(h_1) = 27$ km s$^{-1}$ at $h_1 = 20$ Mm to $\Delta v(h_2) = 46$ km s$^{-1}$ at $h_2 = 180$ Mm, over which range the density decreased from $n_e(h_1) = 1.1 \times 10^8$ cm$^{-3}$ to $n_e(h_2) = 1.6 \times 10^7$ cm$^{-3}$; so the observed velocity increase $\Delta v(h_2)/\Delta v(h_1) = 46/27 = 1.70$, agrees well with the theoretical prediction $[n_e(h_2)/n_e(h_1)]^{-1/4} = (0.16/1.1)^{-1/4} = 1.62$.

Banerjee et al. (2009a) plotted Figure 1.13 and 1.14 to search Alfvén waves in inter-plume using EIS/Hinode data. The solid lines are the theoretically predicted functional forms of the variation of number density with non-thermal velocity and the diamonds are the observed data. The proportionality constant have been chosen to match the calculated energy flux. For the inter-plume data they have used $B \approx 8$ G at certain height. Once again the agreement is very good,

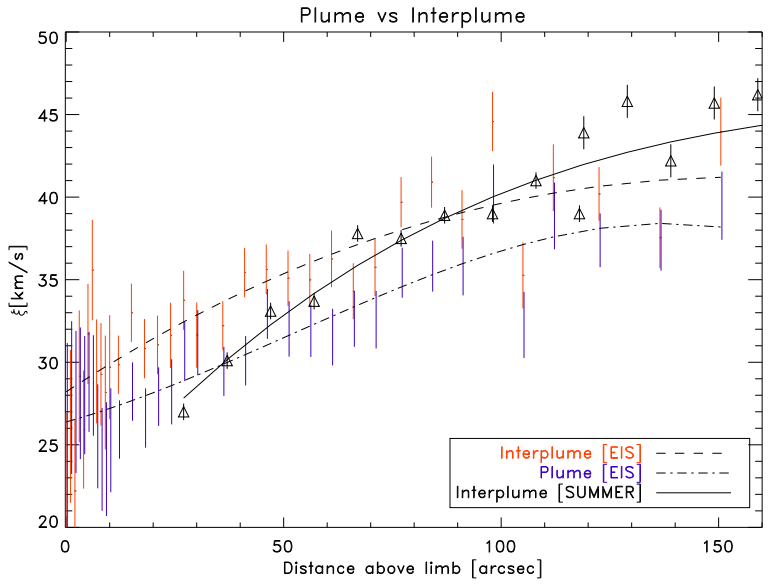


Figure 1.13: Variation in non-thermal velocity with height as recorded by Fe XII 195 Å along a polar plume and inter-plume. The solid line corresponds to the non-thermal velocity as derived from Si VIII 1446 Å (Banerjee et al., 1998). The dashed line is a third-order polynomial fit. From Banerjee et al. (2009a).

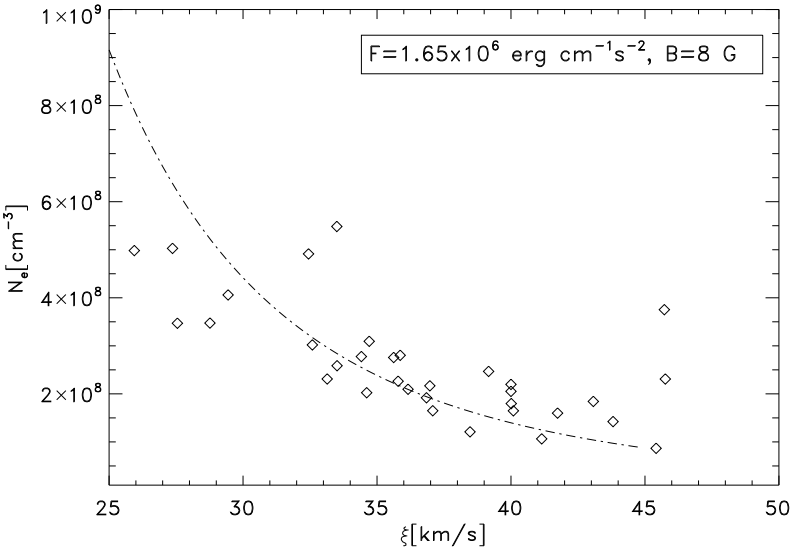


Figure 1.14: Variation in electron density with non-thermal velocity for the polar coronal hole. The squared boxes represent the observed values and the solid line represents the theoretical relation for fixed magnetic field strength as indicated. From Banerjee et al. (2009a).

especially when we are away from the limb. Thus it becomes possible to detect Alfvén waves from the study of the variation of line widths. Jess et al. (2009) have reported the detection of oscillatory phenomena of line width (FWHM) associated with a large bright point group located near the solar disk centre which indicates the presence of Alfvén waves in that region. Dolla and Solomon (2008) have also reported the detection of Alfvén waves from the study of variation of line widths in solar off-limb region, where they do not find evidence for damping of the Alfvén waves.

Taking all these spectroscopic measurements together, there seems to be strong support for the presence of fast-mode or shear (Alfvén) MHD waves in the open field structures of the solar corona. To find the propagating evidence of these MHD waves in these regions is one of the aim of this thesis.

### 1.6.4 The Source of the Propagating Waves

De Pontieu et al. (2004) and De Pontieu and Erdélyi (2006) developed the general framework of how photospheric oscillations can leak into the atmosphere along inclined magnetic flux tubes, to answer the origin of propagating coronal waves. In a non-magnetic atmosphere $p$ modes are evanescent and can not propagate upwards through the temperature minimum barrier since their period $P$ ($\approx$ 200 s to 450 s) is above the local acoustic cut-off period $P_c \approx 200$ s. However, in a magnetically structured atmosphere, where the field lines have some natural inclination ($\theta$), the acoustic cut-off period takes the form $P_c \sim \sqrt{T}/\cos\theta$ with the temperature $T$, where $\theta$ is measured between the magnetic guide channelling the oscillations and the vertical. This inclination will allow some non-propagating evanescent wave energy to tunnel through the temperature minimum into the hot chromosphere of the wave-guide, where propagation is once again possible because of higher temperatures ($P_c > 300$ s). There has been recent attempts to numerically model the direct propagation of acoustic waves, driven harmonically at the solar photosphere, into the three-dimensional solar atmosphere in the framework of ideal magneto-hydrodynamics

(Erdélyi et al., 2007; Malins and Erdélyi, 2007; Fedun et al., 2009, 2011). They have studied the leakage of 5 min global solar acoustic oscillations into the upper, gravitationally stratified and magnetised atmosphere, where the modelled solar atmosphere possesses realistic temperature and density stratification. They have shown that high frequency waves can propagate from the lower atmosphere across the transition region, experiencing relatively low reflection, and transmitting most of their energy into the corona. The thin transition region acts as a wave guide for horizontally propagating surface waves for a wide range of driver periods. One must point out that these modelling has been restricted to either for simple extended flux tubes or non-magnetic atmosphere. More realistic models are needed to verify some of these calculations.

## 1.7 The Solar Wind

### 1.7.1 Introduction

*Solar wind* is a stream of energized, charged particles flowing outward from the upper atmosphere of the Sun into the space. The wind contains roughly equal number of electrons and protons, along with a few heavier ions, and blows continuously from the atmosphere of the Sun into interplanetary space with an average velocity of about 400 km $s^{-1}$. This wind also blows the tails of comets back away from the bodies of comets as they go through the solar system.

Solar wind was first predicted theoretically by Parker (1958) which suggested that the open corona can not be in hydrostatic equilibrium and it is continuously expanding in an outward direction as the outward pressure exceeds the inward gravitational force at larger distances. It was first detected in space by the Soviet Luna 1 probe in 1959, and the first extensive measurements of the solar wind were made by the Mariner 2 spacecraft in 1962 en route to Venus (Neugebauer and Snyder, 1962).

During solar minimum, Ulysses observations clearly show that the solar wind exhibits two

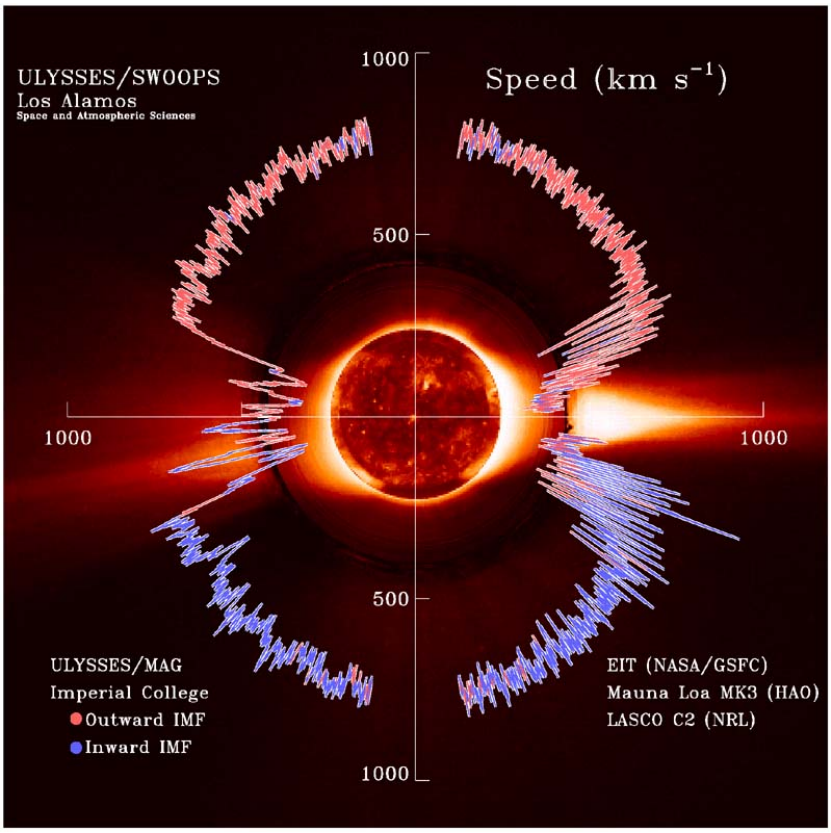


Figure 1.15: Ulysses observations of the solar wind as a function of latitude. The red and blue lines in the polar plot show the solar wind speed for outward and inward (respectively) magnetic field direction. Extracted from McComas et al. (2003).

modes of outflow: the fast wind, associated with polar coronal holes, with outflow speeds of $\approx$ 800 km s$^{-1}$ and the slow wind with outflow speeds of $\approx$ 400 km s$^{-1}$ associated with equatorial regions (Woch et al., 1997; McComas et al., 2000). Observations show that the fast solar wind is relatively steady and uniform, while the slow wind is highly variable and dense as compared to fast wind (McComas et al., 2000, 2003). The bi-modal structure of the solar wind is most evident during the first Ulysses orbit near solar minimum activity period as seen in Figure 1.15.

The acceleration of the slow solar wind can be understood in terms of thermal expansion of hot coronal plasma into the interplanetary space, where the solar gravity acts as a nozzle. Whereas the fast solar wind can not be explained by Parker's thermal expansion model alone, and an additional source of momentum is required to reach the fast solar wind speed. It is

estimated that the required input energy flux is $5 \times 10^5$ ergs cm$^{-2}$s$^{-1}$ with about 80 % deposition below the sonic point $r < 3\ R_\odot$ and about 20 % deposition between the sonic point and a height of several solar radii to accelerate the high-speed streams.

### 1.7.2 MHD Wave Acceleration of Solar Wind

Low frequency MHD waves can carry the energy and momentum to large distances, and have been proposed as the mechanism that accelerates the fast solar wind in coronal holes (Alazraki and Couturier, 1971; Belcher and Davis, 1971; Belcher, 1971). There are several theoretical models which describe the role of MHD waves in the acceleration of the fast solar wind in coronal holes. Some of these models were investigated using 1.5D MHD equations (Boynton and Torkelsson, 1996; Lau and Siregar, 1996; Stark, 1996; Nakariakov et al., 2000; Saito et al., 2001; Lou, 2002; Suzuki, 2004; Cranmer and van Ballegooijen, 2005), 2.5D MHD equations (Ofman and Davila, 1995, 1997), 2.5D multi-fluid MHD equations (Ofman and Davila, 2001; Ofman, 2004). The common thread in the above models of the fast solar wind acceleration is the required presence of non-linear MHD waves, or shock wave trains. Some of these wave driven wind models have been reviewed by Ofman (2005).

Evidence for Alfvénic fluctuations, and MHD waves are obtained by *in situ* and remote sensing observations throughout the heliosphere. With the Ultra-Violet Coronagraph Spectrometer (UVCS/SOHO, Kohl et al., 1995), measurements of the visible polarization brightness (pB) were used to infer the presence of density oscillations (Ofman et al., 1997) at larger heights in solar atmosphere. Interplanetary scintillation (IPS) observations of radio signals passing through the corona allow some properties of plasma irregularities to be determined. One way of detecting random fluctuations in the bulk solar wind is by measuring departures from a frozen-in diffraction pattern measured by different sets of radio receivers. Armstrong and Woo (1981) made an early attempt to separate the bulk solar wind flow speed from the random wave-like velocity component within the 30 $R_\odot$. Radio IPS measurements are sensitive to density fluctuations over a wide range of spatial scales. Spangler (2002) presented integrated values of $\delta\rho/\rho_o$ from VLBI

measurements, and compared them to predictions based on specific MHD modes. The Helios 1 and 2 probes uniquely measured the *in situ* plasma properties between Mercury and the Earth, and they measured MHD fluctuations spanning a wide range of time scales (e.g., Tu and Marsch, 1995; Goldstein et al., 1995b). The *in situ* density fluctuation spectra between 0.3 and 1 AU show a large intrinsic variability, with no clear radial trend discernible (Tu and Marsch, 1994). Ulysses spacecraft has detected a spectrum of outward propagating and inward propagating waves in the milli-Hertz frequency range with power laws of $f^{-1}$, at low frequency ($< 10^{-4}$ Hz) and $f^{-5/3}$ for higher frequencies beyond 1 AU (Goldstein et al., 1995a), as well as large amplitude ultra low frequency Alfvén waves (Tsurutani et al., 1995).

## 1.8 Outline of the Thesis

As discussed in previous sections, waves are potentially important for the heating of the solar corona and in the acceleration of the fast solar wind. The goal of the present thesis work consists of detection of propagating MHD waves in the solar atmosphere from high spectral, spatial and temporal resolution observations carried out simultaneously with multiple instruments such as EIS/Hinode, SOT/Hinode, SUMER/SOHO and TRACE. Apart from these, several ground based observations were taken during the total solar eclipses in search of the waves in corona. A short description of various instruments on-board SOHO and Hinode spacecraft along with TRACE spacecraft are given in Chapter 2. The data reduction and calibration procedures are also outlined for all the above mentioned instruments.

In order to extract the physical parameters from these observations and their interpretations, we require knowledge about the formation of emission lines with atomic processes responsible for them. Chapter 3 gives the brief description about the mechanism of emission line formation and also the various means which will affect these line profiles and their correction procedures.

We have seen that solar atmosphere can be divided into three regions which has different magnetic topologies. The nature of propagating waves would be different in these different mag-

netic regions. Hence we are looking for the signature of propagating waves in these regions separately and the results are presented in different chapters.

Coronal holes which connects the inner corona and the solar wind, are the source region of the fast solar wind which has predominantly unipolar magnetic field (e.g., Krieger et al., 1973). The network pattern is also visible in these regions where open field lines are expected and internetwork regions could include closed field magnetic regions. We look for nature of waves in these network and internetwork regions in detail in Chapter 4. A method is developed to identify propagating waves using statistical technique which gives the time delay between the oscillations at two different heights in the solar atmosphere. In Chapter 5, we analysed the off-limb part of coronal hole in detail and looked for propagating waves in the plume and inter-plume regions. From the observed characteristics of these waves, we interpreted the different modes of waves in these regions which suggests the preferred channel for the acceleration of fast solar wind.

Chapter 6 deals with the nature of propagating waves in network (magnetic in nature) and internetwork (non-magnetic in nature) region of quiet Sun using the multi-spacecraft observations to probe the different layers of solar atmosphere simultaneously.

In Chapter 7, the ground based observation taken during the solar eclipses are described. During the solar eclipses, off-limb active regions loops were clearly visible and were observed using the imaging and spectroscopic instruments. Ground based experimental set-up and optical region CCDs allows to record high frequency images and spectra. This has allowed us to detect high frequency waves, which are normally difficult to detect from space based EUV instruments so far. The nature of waves inferred from these observations in these regions are detailed in this chapter.

The conclusions drawn from these observations and analyses are given in Chapter 8. The results from the different regions of the solar atmosphere are summarized in this chapter. The related future prospects of these studies are also described in this chapter.

# Chapter 2

# Instrumentation and Data Reduction

## 2.1 Introduction

Studying astronomy from the Earth's surface is limited by the filtering and distortion of electromagnetic radiation due to the Earth's atmosphere. However, this can be reduced with the use of adaptive optics. A telescope orbiting the Earth outside the atmosphere will not be affected by twinkling and light pollution from artificial light sources on the Earth.

Space based astronomy is even more important for frequency ranges which are outside the optical and radio window, the only two wavelength ranges of the electromagnetic spectrum that are not severely attenuated by the atmosphere (see Figure 2.1). For example, X-ray astronomy is nearly impossible when done from the Earth, and has reached its current importance in astronomy only due to orbiting X-ray telescopes such as the Chandra observatory and the XMM-Newton observatory. Infrared and ultraviolet part of the electromagnetic spectrum are also greatly blocked. Today there are many telescopes on the Earth, and in orbit around Earth, which observes the Universe in different part of electromagnetic spectrum (see Figure 2.2).

The Sun's atmosphere which plays an important role in Space Weather, is extremely hot, more than a million degree. Such high temperature gas emits high energy radiation known as

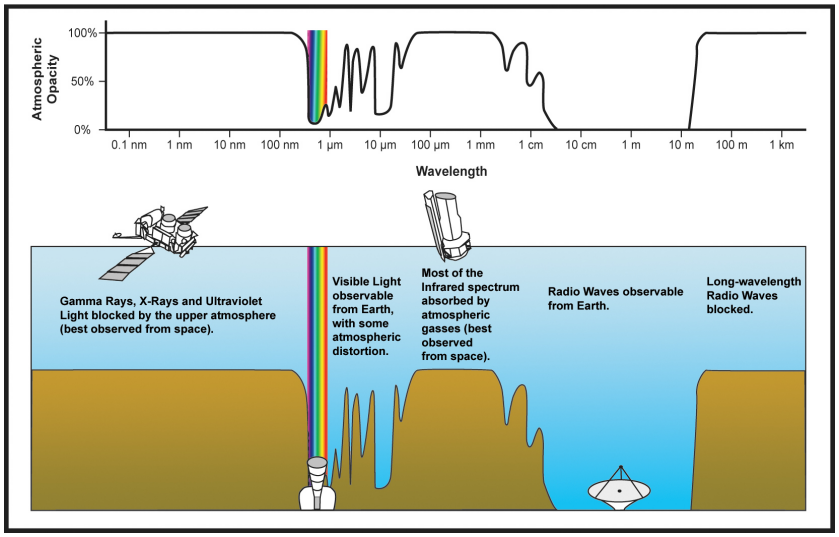


Figure 2.1: Earth's atmospheric opacity to electromagnetic spectrum. *Credit:* JPL/NASA

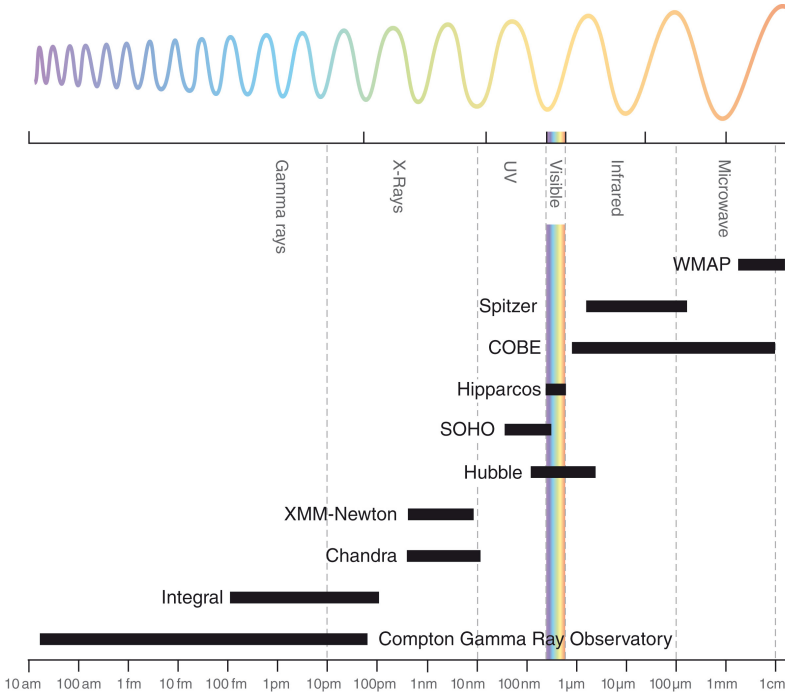


Figure 2.2: Space observatories and their working wavelength range.

Extreme Ultraviolet (EUV) and X-ray radiation. EUV and X-rays are used to view the Sun's corona since they allow us to differentiate the hot and cold parts of the Sun. By imaging the Sun from space at these wavelengths, heating mechanisms of these gases can be understood along with its effect on the Earth and its space environment. Using the spectroscopic data, different parameters obtained from line profiles can provide important clues about the dynamical structure of the solar atmosphere. To study and understand these solar phenomena, data obtained from recent space based observatories SOHO, TRACE and Hinode are described in this chapter together with the summary of data reduction procedures employed.

### 2.1.1 SOHO

Solar and Heliospheric Observatory[1] (SOHO, Domingo et al., 1995), is a project of international collaboration between European Space Agency (ESA) and the US National Aeronautics and Space Administration (NASA) to study the Sun from its deep core to the outer corona and the solar wind.

The SOHO spacecraft was built in Europe by industrial companies in 14 European countries, led by prime contractor Matra Marconi Space (now EADS Astrium) under overall management by ESA. SOHO was launched by an Atlas II-AS (AC-121) from Cape Canaveral Air Station (Florida, United States) on December 2, 1995, at 08:08 UT. SOHO moves around the Sun in step with the Earth, by slowly orbiting around the First Lagrangian Point (L1), where the combined gravity of the Earth and Sun keep SOHO in an orbit locked to the Earth-Sun line. The L1 point is approximately 1.5 million kilometers away from Earth (about four times the distance of the Moon), in the direction of the Sun. There, SOHO enjoys an uninterrupted view of our daylight star.

The scientific payload of SOHO comprises 12 complementary instruments, developed and furnished by 12 international consortia involving 29 institutes from 15 countries. Nine consortia are led by European scientists, the remaining three by US scientists. In this chapter, the experi-

[1] http://sohowww.nascom.nasa.gov/about/about.html

ments forming the SOHO's payload are described shortly with particular attention to the SUMER spectrograph.

### 2.1.2 Hinode

The Hinode[2] (Solar-B) (Kosugi et al., 2007) is a highly sophisticated observational satellite equipped with three advanced solar telescopes. It was launched on September 22, 2006, at 21:36 UT (September 23, 2006, at 6:36 am in Japan time). The spacecraft is in polar, Sun-synchronous orbit at 600 km with an inclination of -98°, allowing 9 months of continuous observations and a three months eclipse period. Its solar optical telescope (SOT) has an unprecedented $0.2''$ resolution for the observation of solar magnetic fields. It would resolve a feature with the size of 50 cm, if it observe towards the Earth. The X-ray telescope (XRT) has a resolution of three times as high as Yohkoh, and the EUV imaging spectrometer (EIS) has sensitivity ten times as high as the SOHO/ESA instrument. These X-ray and EUV telescopes would reveal the heating mechanisms and dynamics of the active solar corona. The advantage of Hinode over previous satellites is its ability to measure the vector magnetic fields. All together, they are studying the generation, transport, and dissipation of magnetic energy from the photosphere to the corona.

With this suite of telescopes, we can address the following key questions in solar physics : Why does a hot corona exist above the cool atmosphere? What drives explosive events such as solar flares? What creates the Sun's magnetic fields? In this chapter, the experiments forming the Hinode's payload are described in brief.

## 2.2 The Instruments on-board SOHO

The SOHO spacecraft has a payload consisting of 12 experiments (see Figure 2.3) that can be divided into three main groups, according to their area of research: helioseismology instruments, solar transition region and corona instruments, and solar wind *in situ* instruments. The list of the

[2] `http://solar-b.nao.ac.jp/index_e.shtml`

twelve instruments on-board SOHO is reported below[3].

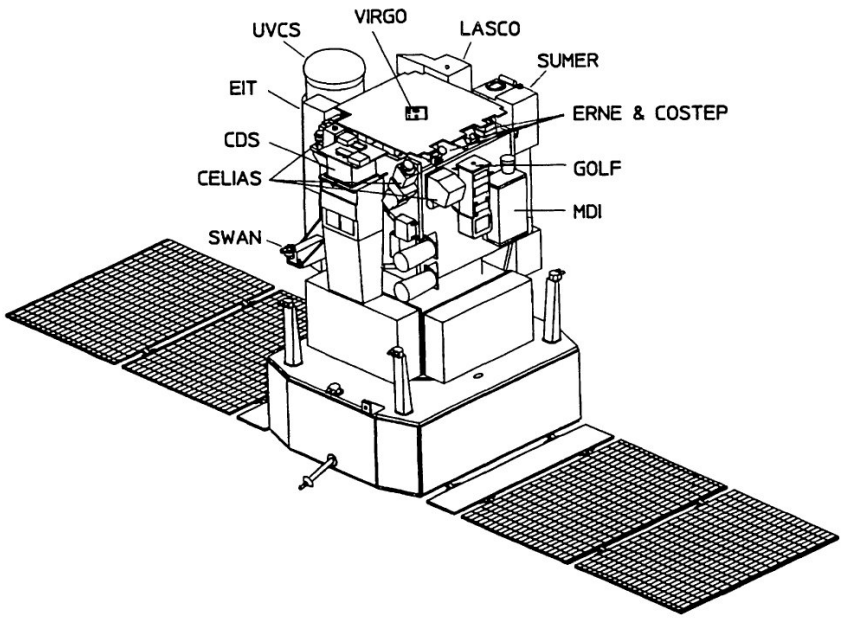


Figure 2.3: Schematic representation of the SOHO spacecraft with the 12 experiments forming its payloads. From Domingo et al. (1995).

### 2.2.1 Helioseismological Experiments

*Global Oscillations at Low Frequencies* (GOLF, Gabriel et al., 1995)
GOLF studies the internal structure of the Sun by measuring velocity oscillations over the entire solar disk.
*Principal Investigator*: Alan Gabriel, Institute dÓrsay, France.

*Michelson Doppler Imager/Solar Oscillations Investigation* (MDI/SOI, Scherrer et al., 1995)
MDI records the vertical motion ('tides') of the Sun's surface at a million different points for each minute. By measuring the acoustic waves inside the Sun as they perturb the photosphere, the structure and dynamics of the Sun's interior can be studied. MDI also measures the longitudinal component of the Sun's magnetic field.

[3] `http://sohowww.nascom.nasa.gov/about/docs/SOHO_Fact_Sheet.pdf`

*Principal Investigator*: Philip H. Scherrer, Stanford University, California, USA.

*Variability of Solar Irradiance and Gravity Oscillations* (VIRGO, Fröhlich et al., 1995)
VIRGO characterises solar intensity oscillations and measures the total solar irradiance (known as the 'solar constant') to quantify its variability over periods of days to the duration of the mission.
*Principal Investigator*: C. Fröhlich, Physikalisch-Meteorologisches Observatorium Davos, Switzerland.

### 2.2.2 Solar Transition Region and Corona Remote Sensing

*Coronal Diagnostic Spectrometer* (CDS, Harrison et al., 1995)
CDS detects emission lines from ions and atoms in the solar corona and transition region, providing diagnostic information on the solar atmosphere, especially of the plasma in the temperature range from 10 000 °C to more than 1 000 000 °C.
*Principal Investigator*: R. Harrison, Rutherford Appleton Laboratory, Chilton, Didcot, Oxfordshire, UK.

*Extreme ultraviolet Imaging Telescope* (EIT, Delaboudinière et al., 1995)
EIT provides full disc images of the Sun at four selected colours in the extreme ultraviolet, mapping the plasma in the low corona and transition region at temperatures between 80 000 °C and 2 500 000 °C.
*Principal Investigator*: J.P. Delaboudiniére, Institut d'Astrophysique Spatiale; Orsay, France.

*Large Angle and Spectrometric Coronograph* (LASCO, Brueckner et al., 1995)
LASCO observes the outer solar atmosphere (corona) from near the solar limb to a distance of 21 million kilometres, that is, about one seventh of the distance between the Sun and the Earth. LASCO blocks direct light from the surface of the Sun with an occulter, creating an artificial eclipse, 24 hours a day, 7 days a week. LASCO has also become SOHO's principal comet finder.
*Principal Investigator*: R. Howard, Naval Research Laboratory, Washington DC, USA.

*Solar Ultraviolet Measurements of Emitted Radiation* (SUMER, Wilhelm et al., 1995)
The SUMER instrument is used to perform detailed spectroscopic plasma diagnostics (flows, temperature, density, and dynamics) of the solar atmosphere, from the chromosphere through the transition region to the inner corona, over a temperature range from 10 000 °C to 2 000 000 °C and above.
*Principal Investigator*: W. Curdt, Max-Planck-Institut für Sonnensystemforschung (MPS), 37191, Katlenburg-Lindau, Germany.

*Solar Wind Anisotropies* (SWAN, Bertaux et al., 1995)
SWAN is the only remote sensing instrument on SOHO that does not look at the Sun. It watches the rest of the sky, measuring hydrogen that is 'blowing' into the Solar System from interstellar space. By studying the interaction between the solar wind and this hydrogen gas, SWAN determines how the solar wind is distributed. As such, it can be qualified as SOHO's solar wind 'mapper'.
*Principal Investigator*: J. L. Bertaux, Service dÁéronomie du CNRS, Verriéres-Le-Buisson, France.

*UltraViolet Coronograph Spectrometer* (UVCS, Kohl et al., 1995)
UVCS makes measurements in ultraviolet light of the solar corona (between about 1.3 $R_\odot$ and 12 $R_\odot$ from the centre) by creating an artificial solar eclipse. It blocks the bright light from the solar disc and allows observation of the less intense emission from the extended corona. UVCS provides valuable information about the microscopic and macroscopic behaviour of the highly ionised coronal plasma.
*Principal Investigator*: John L. Kohl, Smithsonian Astrophysical Observatory, Cambridge, Massachusetts, USA.

### 2.2.3 Solar Wind *in situ* Measurements

*Charge, Element, and Isotope Analysis System* (CELIAS, Hovestadt et al., 1995)
CELIAS continuously samples the solar wind and energetic ions of solar, interplanetary and interstellar origin, as they sweep past SOHO. It analyses the density and composition of particles present in this solar wind. It warns of incoming solar storms that could damage satellites in Earth orbit.
*Principal Investigator*: P. Bochsler, University of Bern, Switzerland.

*Comprehensive Suprathermal and Energetic Particle Analyser* (COSTEP, Müller-Mellin et al., 1995)
The COSTEP instrument detects and classifies very energetic particle populations of solar, interplanetary, and galactic origin. It is a complementary instrument to ERNE (for more information, see below).
*Principal Investigator*: H. Kunow, University of Kiel, Germany.

*Energetic and Relativistic Nuclei and Electron experiment* (ERNE, Torsti et al., 1995)
ERNE measures high-energy particles originating from the Sun and the Milky Way. It is a complementary instrument to COSTEP. COSTEP and ERNE together form CEPAC (COSTEP-ERNE Particles Analyser Collaboration).
*Principal Investigator*: J. Torsti, University of Turku, Finland.

### 2.2.4 The SUMER Spectrograph

SUMER[4] on-board SOHO is a powerful UV instrument capable of making reliable measurements of bulk motions in the chromosphere, transition region and low corona with an accuracy better than 2 km $s^{-1}$ (Wilhelm et al., 1997), with a spatial resolution of $1''$ ($1''$ at L1 corresponds to 715 km on the Sun) across the slit and $2''$ along the slit (Lemaire et al., 1997). The basic char-

[4] `http://www.mps.mpg.de/projects/soho/sumer/`

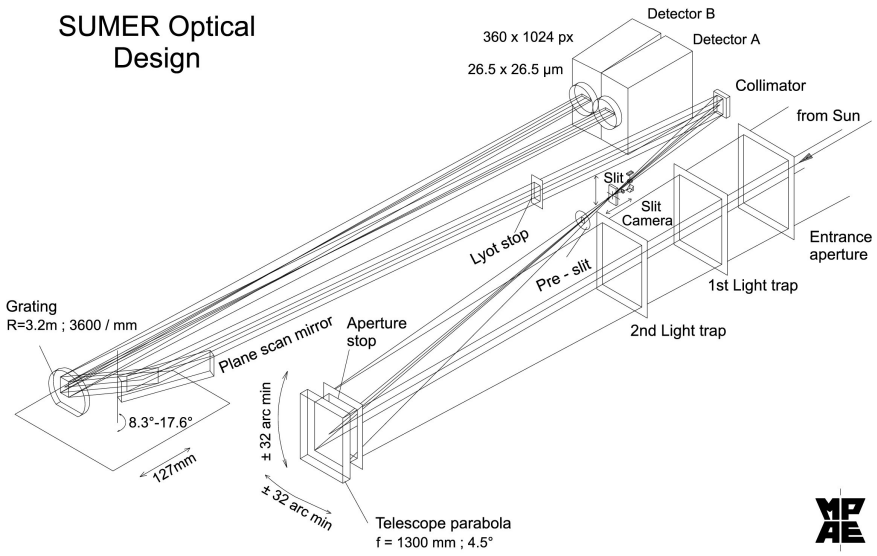


Figure 2.4: Optical layout of the SUMER instrument showing the light-path through the system. The ranges of movements of various mechanisms provided to control the position of the optical components are indicated by arrows. The entrance door and its mechanism are not shown. The spectrometer compartment is completely encapsulated in order to achieve good stray light performance and will only be illuminated through the slit engaged. Adapted from Wilhelm et al. (1995).

acteristics, capabilities and operations of SUMER are well described by Wilhelm et al. (1995, 1997) and Lemaire et al. (1997). The optical design (see Figure 2.4) is based upon two parabolic mirrors, a plane mirror and a spherical concave grating, all made of silicon carbide (SiC). The first off-axis telescope parabola, which has pointing and scan capabilities, images the Sun on the spectrometer entrance slit. The second off-axis parabola collimates the beam leaving the slit. This beam is then deflected by the plane mirror onto the grating. Two detectors (called A and B), located in the focal plane of the concave grating, collect the monochromatic images of the spectrometer entrance slit. The centre of detector A is located on the grating normal, while the centre of the other detector is off by a quantity $\Delta = 70.4$ mm. Coverage of the full spectral range of the instrument requires a wavelength scan performed by rotating the plane mirror. A baffle system, consisting of an entrance aperture, light traps, an aperture stop, a pre-slit and a Lyot stop, completes the design.

SUMER allows the study of small scale plasma structures at the spatial resolution of $1''$ from

the high chromosphere to the low corona, as well as its dynamics at a temporal resolution of few seconds. The instrument is able to investigate EUV and FUV line profile changes with a very good spectral resolution (40 mÅ in first order), in a temperature range of $10^4$ °C to $2 \times 10^6$ °C. The two photon counting detectors has wavelength range as: for detector A, 390 Å to 805 Å ($2^{nd}$ order) and 780 Å to 1610 Å ($1^{st}$ order); for detector B, 330 Å to 750 Å ($2^{nd}$ order) and 660 Å to 1500 Å ($1^{st}$ order), but in the range below 500 Å the sensitivity is very low. Each detector has 1024 spectral and 360 spatial pixels. When the exposure is taken, either the full (1024 pixels) spectrum or selected spectral windows (25, 50, 256 or 512 pixels wide) are transmitted to the ground. The spectrograph has recorded more than 1,000 emission lines, many for the first time. A SUMER spectral atlas for disk features was compiled by Curdt et al. (2001) and for coronal features by Curdt et al. (2004). The list of SUMER spectral lines identified in the wavelength range from 668 Å to 1611 Å of the average quiet Sun (QS), a coronal hole (CH) and a on-disk sunspot (SS) is given on SUMER homepage[5].

## 2.3 The Instruments on-board Hinode

The Hinode spacecraft has a payload consisting of three experiments (see Figure 2.5) which are solar optical telescope (SOT), EUV imaging spectrometer (EIS) and X-ray telescope (XRT).

### 2.3.1 Solar Optical Telescope (SOT)

The Solar Optical Telescope[6] (SOT, Tsuneta et al., 2008b) consists of the main 50 cm aperture telescope (Optical Telescope Assembly, OTA) and focal plane package (FPP). The combined SOT system is optimized for accurate measurement of the vector magnetic field in the photosphere and dynamics of both the photosphere and chromosphere associated with the magnetic fields.

[5] http://www.mps.mpg.de/projects/soho/sumer/FILE/Atlas.html
[6] http://solar-b.nao.ac.jp/sot_e/

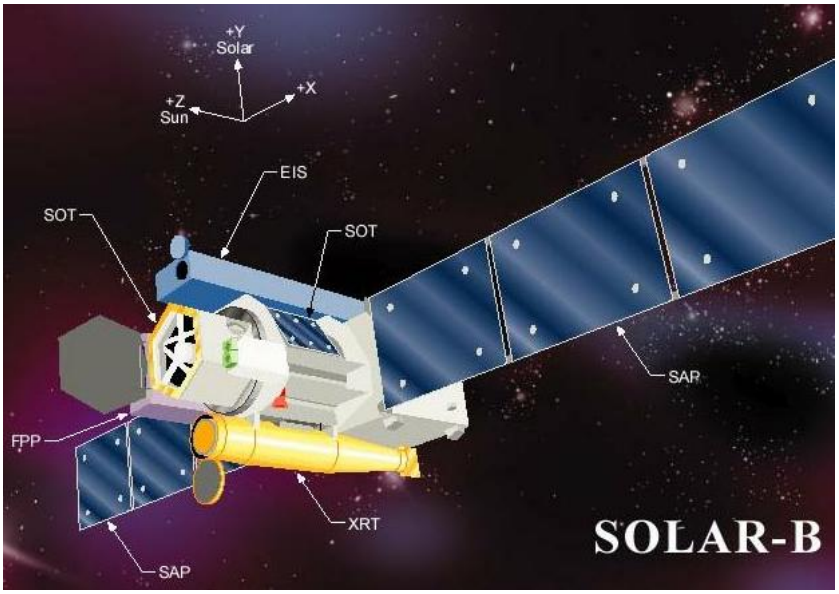


Figure 2.5: Artist's impression of Hinode spacecraft. *Credit:* MSFC/NASA

A wide range of scientific advances have been achieved from the SOT instrument, as a result of the major advances it represents in observational capability. The 50 cm diameter SOT obtains a continuous, seeing-free series of diffraction-limited images ($0.2''$ to $0.3''$) in 3880 Å to 6680 Å range. The images are acquired under very stable conditions (stability requirement $< 0.09''$ in 3 sigma) archived by a combination of structural design and active image stabilization. The image stabilization system consists of a piezo-driven tip-tilt mirror (CTM) in OTA in a closed-loop servo using a displacement error estimated from correlation tracking of solar granulation (correlation tracker, CT). This system minimizes jitter in solar images on the focal plane CCDs. The Sun-synchronous orbit of the Hinode (formerly Solar-B) and the contact with Svalbard ground station in Norway (ESA) allows downlink of data nearly every orbit, hence observations are possible 24 hours a day for about 8 months of the year.

Figure 2.6 shows the optical layout of the SOT. The OTA is an aplanatic Gregorian-type telescope with 50 cm aperture primary mirror. The distance between the primary and secondary mirrors is 1.5 m. A heat dump mirror at the primary focus removes the unused solar light (heat) outside of the $328'' \times 164''$ field-of-view (FOV). The collimator lens (CLU) feeds a collimated light to the FPP.

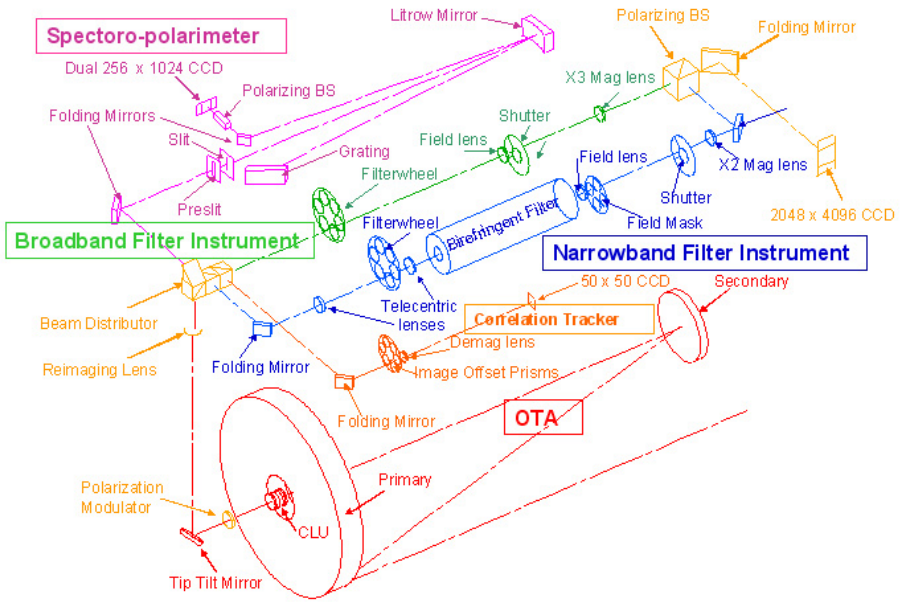


Figure 2.6: Optical layout of SOT/Hinode instrument.

The FPP instrument performs both imaging and spectral observations at high polarimetric precision. It has the broad-band filter imager (BFI), the narrow-band filter imager (NFI) and the spectropolarimeter. BFI produces photometric images with broad spectral resolution in 6 bands (CN band, Ca II H line, G-band, and 3 continuum bands) at the highest spatial resolution (0.0541″ per pixel sampling) and at rapid cadence (< 10 s typical) over a FOV of 218″ × 109″. The Narrow-band Filter Imager (NFI) provides intensity, Doppler, and full Stokes polarimetric imaging at high spatial resolution (0.08″ per pixel) in any one of 10 spectral lines (including Fe lines having a range of sensitivity to the Zeeman effect, MgIb, NaD lines, and $H_\alpha$) over a full field of view 328″ × 164″. The spectropolarimeter records full Stokes *IQUV* profiles of the magnetic sensitive Fe I 6302 Å with a spectral resolution of about 25 mÅ. For precise measurements of polarization with diffraction limited imaging, a highly stabilized images are required. SOT has an image stabilization system, in which the displacement estimated from the correlation tracking of solar granules over a small FOV of about 11″ × 1″ is fed back to the system which minimizes

image jitter in the frequency range lower than 14 Hz.

### 2.3.2 X-ray Telescope (XRT)

The X-Ray Telescope[7] (XRT, Golub et al., 2007) is a high resolution grazing incidence telescope, consisting of an X-ray optics (2 Å to 200 Å) and visible light optics at G-band wavelength (4305 Å). It is a successor to the highly successful Yohkoh Soft X-Ray Telescope (SXT). It has a better spatial resolution by a factor of 2.5 times than SXT. One of the unique features of XRT is its wide temperature coverage ($6.1 < log\ T < 7.5$) with a spatial resolution of about $1''$ and temporal resolution of up to 2 s cadence.

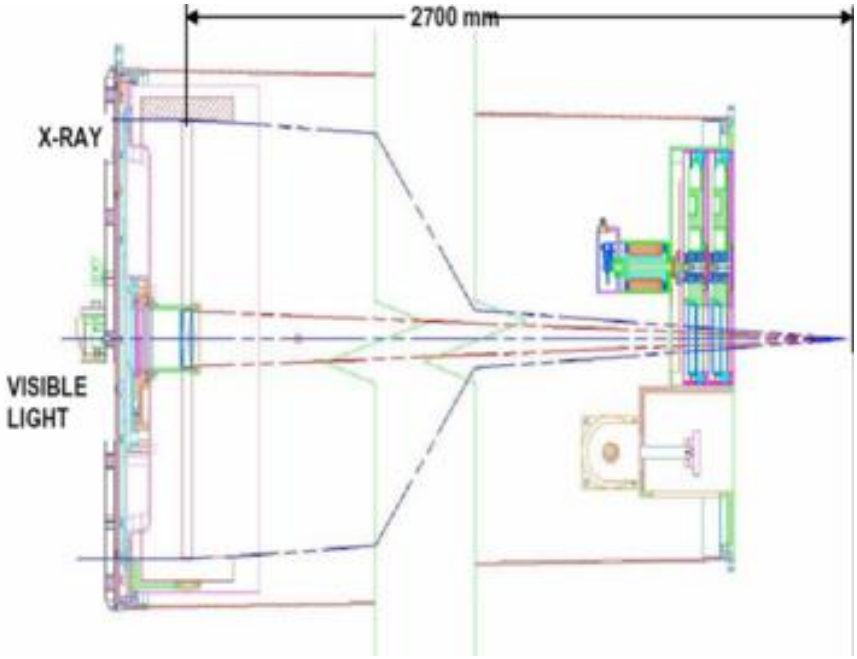


Figure 2.7: Optical layout of XRT/Hinode instrument.

The optical layout of the instrument is shown in Figure 2.7. Solar radiation enters the telescope and the entrance aperture Al pre-filters reject the visible radiation from entering the instrument and transmitting more than 70 % of the X-rays from 2 Å to 60 Å. There are nine focal plane (FP) filters which provide variable passbands at soft X-ray wavelengths for plasma diagnostics

[7] http://solar-b.nao.ac.jp/xrt_e/index_e.shtml

and to further reduce the visible light reaching the focal plane detector. They have different low temperature cut-offs which help to constrain differential emission measure (DEM) reconstructions for the observed coronal plasma. The detector is a 2k × 2k back-illuminated CCD with $1''$ pixels. The FOV is $34' \times 34'$ which can see the entire solar disk. The nine FP filters are Al mesh, Al poly, C poly, Ti poly, thin Be, medium Al, medium Be, thick Al, thick Be and white light ($SiO_2$) which can be used to observe the corona at different temperature regimes. High resolution soft X-ray images reveal the evolution of the magnetic field, and the process of building up, storage and dissipation of energy.

### 2.3.3 EUV Imaging Spectrometer (EIS)

The Extreme-ultraviolet Imaging Spectrometer[8] (EIS, Culhane et al., 2007) is one of the three major scientific instruments of the Solar-B. Figure 2.8 shows the optical layout of the EIS instrument. It utilizes an off-axis parabolic primary and a toroidal diffraction grating in a normal incidence optical layout with high-reflectance Mo/Si multi-layer coatings. The multi-layer coatings have high reflectance in two wavelength ranges, 170 Å to 210 Å and 250 Å to 290 Å, and these wavelength ranges are simultaneously observed with two large back-illuminated CCDs. Many EUV emission lines from the transition region, the corona, and flares are contained in these wavelength ranges and observers can select the number of spectral windows up to 25 in the imaging area of two CCDs. There is a slit/slot exchanger that contains two narrow slits ($1''$ and $2''$ width) and two wide slots ($40''$ and $266''$ width) at the prime focus of the primary mirror, and two dimensional EUV images are obtained with one of the narrow slits in a raster observation by a pivot rotation of the primary mirror in the east-west direction or by one of the wide slot observation without primary-mirror motion, though the velocity information is convolved in the latter case. The centre of the field-of-view can be changed by $\pm 890''$ in the east-west direction by a translational motion of the primary mirror and it enables to see a high-altitude region of the corona at the limb or to see the region near the limb when the nominal observing region of the Solar-B is located near the centre of the Sun.

[8] http://solar-b.nao.ac.jp/eis_e/index_e.shtml

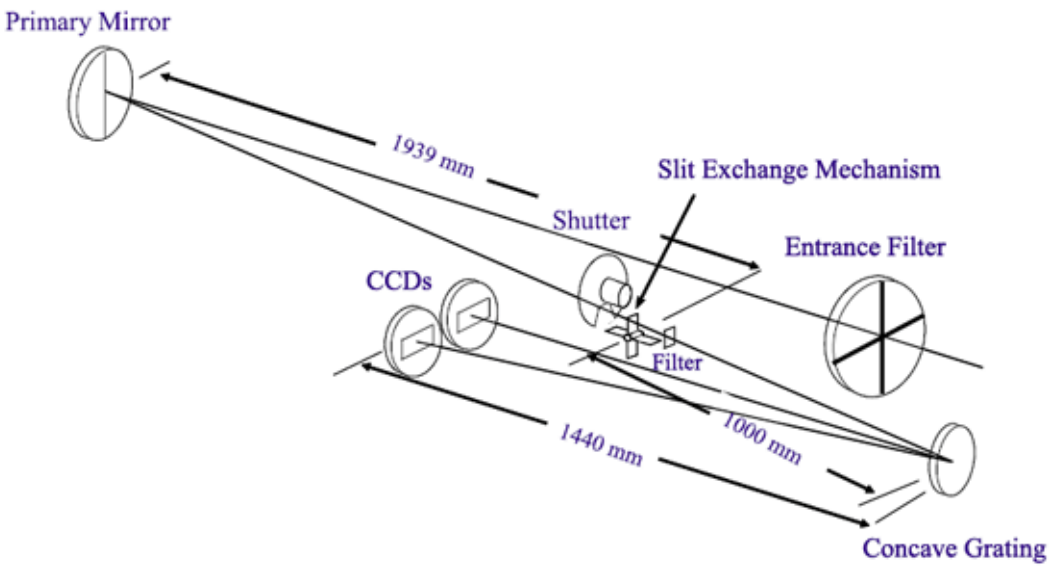


Figure 2.8: Optical layout of EIS/Hinode instrument.

EIS has a spectral resolution of about 22 mÅ per pixel with an instrumental FWHM of $\approx$ 44 mÅ. Though EIS can observe with slots, quantitative plasma properties like density, temperature, etc., can be obtained mainly from the slit observations with high spectral resolution. EIS can measure the intensity and the shape of the line profiles, if the lines are adequately resolved. Bulk motions of the plasma relative to the line-of-sight, lead to red and blue wavelength shifts. Any increase in line widths over the thermal Doppler width allow the measurement of non-thermal or turbulent motion of the plasma. EIS can observe plasma flows of 3 km $s^{-1}$ and 25 km $s^{-1}$ for line widths. Finally, the observation of multiple lines simultaneously allows the plasma differential emission measure to be constructed.

## 2.4 TRACE

The Transition Region And Coronal Explorer[9] (TRACE, Handy et al., 1999) is a NASA Small Explorer (SMEX) mission to image the solar atmosphere from the photosphere to the corona at high spatial and temporal resolution. TRACE was launched in April, 1998. A cut-away view of TRACE is shown in the Figure 2.9. The spacecraft is in a polar orbit which allows continuous

[9] http://trace.lmsal.com/

uninterrupted observations for approximately 9 months each year, the remaining 3 months is the eclipse season where the view from part of the orbit is occulted by the Earth's atmosphere. The objectives of TRACE mission are to (i) follow the evolution of magnetic field structures from the photosphere to the corona and plasma confinement; (ii) investigate the mechanisms of coronal heating; (iii) investigate the triggering mechanisms of solar flares and coronal mass ejections (CMEs).

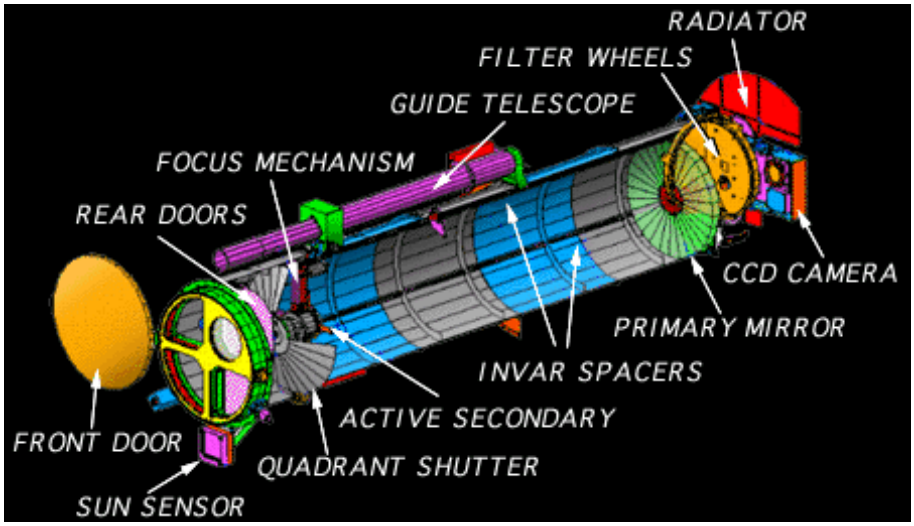


Figure 2.9: TRACE cut-away view.

It consists of a 30 cm aperture Cassegrain telescope which observes the Sun in white light, UV continuum, Lyman $\alpha$, C IV 1550 Å, Fe IX 171 Å, Fe XII 195 Å, Fe XV 284 Å with a FOV of $8.5' \times 8.5'$ and a spatial resolution of $0.5''$. The telescope is divided into four quadrants optimised for specific wavelengths: 171 Å, 195 Å, 284 Å and 1200 Å to 1700 Å. Filters are mounted at the entrance of the telescope to reduce visible and stray light entering the telescope. The pointing of the telescope is internally stabilized to $0.1''$ against satellite jitter.

Coordination with all Hinode, TRACE and SOHO provides an unprecedented opportunity to follow the emergence of magnetic flux from the base of the convection zone deep inside the Sun, through the photosphere, chromosphere and transition region, to the outer corona with high spatial and temporal resolution.

## 2.5 Data Reduction

In this section, we will discuss different methods employed on the obtained data from different instruments, before start analysing it for the scientific purposes.

### 2.5.1 SUMER Data Reduction

A 'Data correction cookbook' which gives a step-by-step description of the routines used for the reduction of SUMER data, together with other useful information about the instrument, are available at the SUMER homepage[10].

SUMER data from the original telemetry are available in two different forms: FITS file (stored in the SOHO archive at GSFC) and IDL-restore files (produced at MPAe). Reduction of SUMER raw images follows several stages, *i.e.* decompression and reversion (for IDL-restore files), dead-time correction, local gain correction, flat-field correction, a correction for geometrical distortion and radiometric calibration (in order to pass from count $px^{-1}$ $s^{-1}$ to erg $cm^{-2}s^{-1}Sr^{-1}Å^{-1}$ and to correct for the differences in sensitivity between the KBr and the bare micro-channel plate). Unless specified, all the mentioned corrections have been applied to the data presented in this thesis. Some other corrections can also be important in particular cases.

- **Dead time and local gain correction:** For a total counting rate greater than $5 \times 10^4$ event $s^{-1}$, a correction for the electronic dead-time effect needs to be applied (Wilhelm et al., 1995; Hollandt et al., 1996). For certain bright lines (i.e. C III 977 Å or O VI 1032 Å), when levels around 10 counts $pix^{-1}$ $s^{-1}$ or higher is reached, a loss of dynamic range will be present for such strong lines due to a local reduction in the micro-channel plate (MCP) gain (Wilhelm et al., 1997). In these cases a correction for the local gain depression needs to be applied at the initial stage. Local gain correction requires dead-time correction to be applied first.

[10] `http://www.mps.mpg.de/projects/soho/sumer/text/webluca/ch_inst.html`

- **Flat-field correction:** In order to correct for non-uniformities in the sensitivity of the detector on scales of about 20 pixels or less, flat-field correction is necessary. These are mostly due to a non-linearity of the A/D-converters and the hexagonal pattern of microfibre bundles of the MCPs. Flat-field images are taken approximatively every month with a $\approx 3$ hour exposure in the Lyman continuum between 860 Å and 900 Å while the spectrometer grating is de-focused (Wilhelm et al., 1997).

- **Geometrical distortion:** The electronic design of the detector induces a geometrical distortion of the images produced by SUMER (Wilhelm et al., 1997) in an 'inverse cushion' fashion that is most evident at the extremities of the image. This effect can be corrected using different routines all based on *destr_bilin.pro* that uses rectangular grid tables obtained through spatially averaged spectra of narrow O I lines by Moran (2002).

- **Radiometric calibration:** Radiometric calibration consists in linking pixels intensities to a physical parameter. The radiometric calibration of the SUMER spectrograph was performed in the laboratory using a secondary source standard, traceable to the Berlin Electron Storage ring for SYnchrotron radiation BESSY I (Hollandt et al., 1996). The radiometric calibration is performed through the provided software (*radiometry.pro*, written by K. Wilhelm).

- **Wavelength calibration:** There is no calibration source available on-board, so the wavelength calibration is done using some chromospheric lines of neutral atoms. These lines are formed in the chromosphere at temperatures around 6500 K (e.g. S II and S I, Chae et al., 1998) and are supposed to be at rest. These lines should therefore allow the determination of an absolute wavelength scale. Figure 2.10 shows an example of a quiet Sun SUMER spectrum recorded around 1400 Å. It is possible to see some second order lines overlapping the first order ones as well as chromospheric lines that can be used for wavelength calibration.

After applying all the above corrections, the spectra are ready to be analysed. However, in particular cases, some other corrections are important to apply.

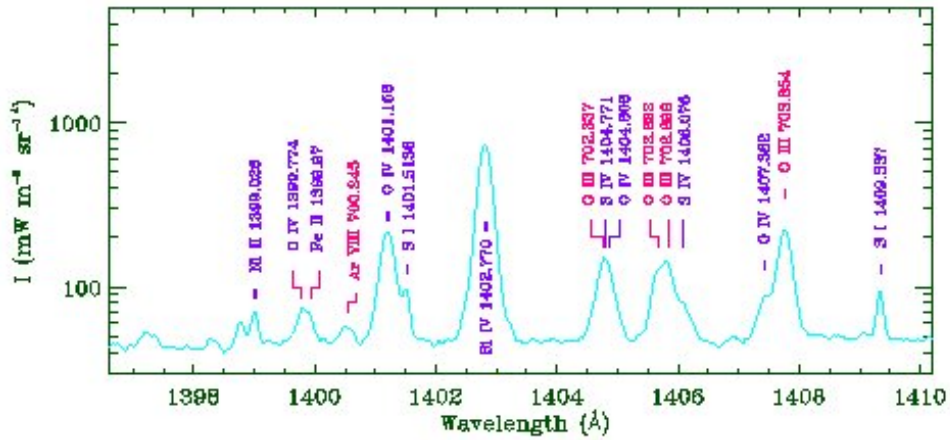


Figure 2.10: SUMER spectrum of the quiet Sun around 1400 Å. The spectrum has been obtained averaging along the slit a full detector exposure obtained on 10 July 1996. Note the lines from both first and second order present in this spectral range and, particularly, the ones belonging to the O IV 1400 Å multiplet and, superposed, a group of second order O III lines.

- **Instrumental broadening:** This is a problem common to any spectroscopic analysis and concerns the fact that recorded line profiles are the result of the convolution of the instrumental profile with the true flux spectrum. Emission lines arising from optically thin transition region and coronal plasma can be considered as Gaussian in shape to a very good approximation (Mariska, 1992). This is not strictly true for the instrumental profile. This implies that, in theory, the recorded spectral profiles should be not Gaussian in shape leading to the necessity of deconvolution processes of the data in order to extract the 'true' spectrum. In order to perform the reconstruction process we should have the instrumental profiles for all the possible detector-grating angle-slit combinations. These profiles can be obtained in laboratory before the launch, but not during the flight (there are no calibration lamps on-board). However, in the large majority of cases (outside dynamic events and for lines formed in an optically thin plasma), SUMER line profiles can be fitted reasonably well by a single Gaussian.

- **Slit magnification and displacement:** The existence of a discrepancy between the orientation of the grating and the detector, causes the spectrum to be inclined with respect to the detector horizontal lines. This leads to a change in the vertical position of the slit

image on the detector plane as a function of wavelength. Moreover, the position of the slit image on the detector is also shifted due to the non-linearity of the grating focus mechanism which is moved simultaneously with the wavelength scan. The vertical displacement and spatial scale of the slit image as a function of wavelength can be determined using the provided software (*delta_pixel.pro* and *magnification.pro*, respectively). The above correction needs to be applied only when comparing images obtained at different wavelengths.

- **Long and short time instrumental periodicities:** Despite the very high thermal and mechanical stability characterizing the instrument (the temperature inside the spectrometer compartment being controlled to within ± 0.15 K, Wilhelm et al., 1997), a drift of the whole spectral image with an amplitude up to 1 pixel and a periodicity of 1 to 2 hour has been detected due to *thermoelastic oscillations* (Curdt et al., 1997). These oscillations are interpreted as the effect of mechanical deformations of the spectrometer structure due to small temperature changes induced by the spectrometer heaters.

### 2.5.2 EIS Data Reduction

Before start analysing the EIS data, there are several instrumental corrections needed to be applied on the data. Each step of these corrections are explained in the EIS Data Analysis Guide[11].

- **Calibration:** EIS spectra and images are recorded on CCD. Before analysing those, it needs to be calibrated. The calibration consists of correcting the raw images to values which gives the physical parameter of the intensity of light that fell on the CCD during the exposure. The calibration involves many steps such as removing the bias, subtracting the dark current, and dividing the image by the flat-field. The EIS data is calibrated using the SolarSoft routine *eis_prep.pro* which by default does the following things:
  - Flag any saturated data as missing (saturated data have a DN value of 16383)

[11] http://solar.bnsc.rl.ac.uk/~young/solarb_eis/paris_tutorial/

  - Remove the CCD pedestal and dark current
  - Flag hot pixels as missing
  - Flag warm pixels as missing (not implemented at present)
  - Flag cosmic rays as missing
  - Calibrate data, and create error arrays

- **Fitting Gaussian to the data:** Generally the EIS emission lines have a Gaussian shape and, by fitting a Gaussian function to the spectrum, one can derive line intensity, line width and velocity maps. The high sensitivity of EIS means that for many lines it is possible to perform good quality fits at each pixel in the image. The routine *eis_auto_fit.pro* in SolarSoft fits a single Gaussian to each pixel in the image.

- **Correcting for slit tilt and orbit variation:** There are four EIS slits ($1''$, $2''$, $40''$ and $266''$) and they are designed to be perpendicular to the dispersion axes of the EIS CCDs. Due to the difficulties in aligning optical elements of spectrometers, none of the four EIS slits are perfectly perpendicular to the CCD axes, and the small tilts that are present can affect data analysis. Due to these EIS velocity maps are affected by motion of the line centroids on the EIS detectors during the 100 min Hinode orbit. A more subtle effect is the tilt of the EIS slits relative to the detector orientation which leads to line profiles at the bottom of the EIS slit being blue shifted relative to profiles at the top of the slit. Software exists to correct both of these effects in the *eis_auto_fit.pro* structure.

- **Spatial offsets between the two CCDs in the *X* direction:** There is a spatial offset of about $2''$ in the $X$ direction between images formed from long wavelength (LW) band emission lines, and those formed from short wavelength (SW) band emission lines. The reason for this offset lies in the fact that the two CCD images arise from different halves of the primary mirror. The focal points of the two mirror halves could thus be different. A key consequence of this offset is that images from the different CCDs taken with sit-and-stare observations can not be directly compared since they show different parts of the Sun.

  In order to reduce the $X$-offset between the detectors, tests were performed to see if moving the slit position would improve the situation. The EIS slit assembly has a 'paddle-wheel'

design, with four paddles that contain the slits. Normally the paddle-wheel is rotated through 90° to bring the different slits into the beam. The paddle wheel can also be moved by small amounts (a fraction of a degree). After inspecting various data-sets, an optimum position for the slit assembly was found and a permanent change was made on 24 August 2008. Preliminary checks on the data suggest that the spatial offset between the two CCDs is now around $0.5''$.

- **Spatial offsets between the two CCDs in the *Y* direction:** There is an offset of $\approx 16''$ between the short and long wavelength CCDs in the y-direction. Due to this effect, solar features imaged in the short wavelength band will occur at higher Y-pixel numbers than those imaged in the long wavelength band. The offset between the two bands seems to vary with wavelength. A routine has been written to give the offset relative to the EIS reference line (He II 256 Å) for any wavelength, and it is called as *eis_ccd_offset.pro*.

### 2.5.3 TRACE Data Reduction:

The routine *trace_prep.pro* is intended to guide the processing of TRACE data from raw to level 0 according to the order and algorithms defined by the TRACE Team. By default, *trace_prep.pro* performs the following steps:

- Read in image(s) from a datacube and index structure
- Fill pixels of value = 0 with mean pixel value of entire image
- Replace near saturated pixels with value > 4095
- Subtract the dark pedestal (ADC offset) and current from each image
- Output the corrected image(s) in an updated structure and data cube

Optionally, the following corrections are applied if the appropriate keywords are used:

- Remove radiation belt spikes and streaks from each image (/unspike, /destreak)
- Remove background diffraction pattern (and readout herringbone) (/deripple)
- Normalize each image for exposure (/normalize)
- Correct pointing in the index structure for each channel (/wave2point)
- Extract a sub-image from each image (keywords sllex, slley, subimgx, subimgy)

Spikes caused by high energy particles in the images can be removed by *tracedespike.pro* or *trace_unspike.pro*. The routines *trace_unspike.pro* and *trace_destreak.pro* (together with *trace_cleanjpg.pro*) can be used to remove spikes and streaks, and repair some of the damage caused when the spikes are compressed by the JPEG algorithm. In a series of images, the routine *trace_unspike$_t$ime.pro* will remove spike-like features that only occur in one frame. The herringbone patterning on the CCD pedestal can be removed with *trace_knoise.pro*.

### 2.5.4 SOT Data Reduction:

To process an SOT FG dataset: BFI or NFI filtergram, magnetogram, dopplergram or Stokes set, SolarSoft routine *fg_prep.pro* is used. The following steps are performed in this process:

- Identify type of data: BFI or NFI image or NFI image set (e.g. Stokes IV [m,n,2] array).
- Correct camera readout defects (e.g. missing rows at center).
- Subtract ADC offset and dark current from the frame.
- Multiply by gain image (1/flat-field image).
- Optional: remove radiation-belt/cosmic-ray spikes and streaks.
- Optional: remove BFI 6684 red spot. NYI.
- Optional NFI: Correct for NFI tunable filter I-ripple. NYI.
- Optional NFI: Calibrate velocities for dopplergram modes. NYI.

- Optional NFI: Apply polarization calibration to magnetogram modes. NYI.
- Optional: shift/scale to reference frame coordinates.
- Optional: extract a sub-image from each image.
- Output the corrected image(s) in an updated structure and data cube, and optionally output a FITS file with 1 or more images plus a binary extension or as 2D flat FITS files (1 per image).

# Chapter 3

# Emission Line Spectroscopy

## 3.1 Introduction

Thermal radiation from the Sun is emitted from temperature as low as T $\approx$ 4400 K in sunspot umbra during solar minimum to as high as T $\approx$ 40 MK in the superhot flares. The transition region and corona are hot and has temperature range between few $10^4$ K to few $10^6$ K with very low density plasma. Thus, the radiation coming from these regions falls mainly in the EUV and soft X-rays range of wavelength domain. If the temperature, density and velocity of the plasma is known at each location then at least to first order, the thermodynamic state of the gas can be obtained. This information can be extracted through an understanding of the processes that excite and ionize the atoms in the plasma.

Till now whatever known about the transition region and corona is based on analyses of UV and EUV spectra, detailed understanding of the line formation process is needed. This chapter presents an overview of optically thin emission line formation. In this chapter, we summarize the relevant atomic physics and explain the basic assumptions inherent in the analysis of UV and EUV emission lines.

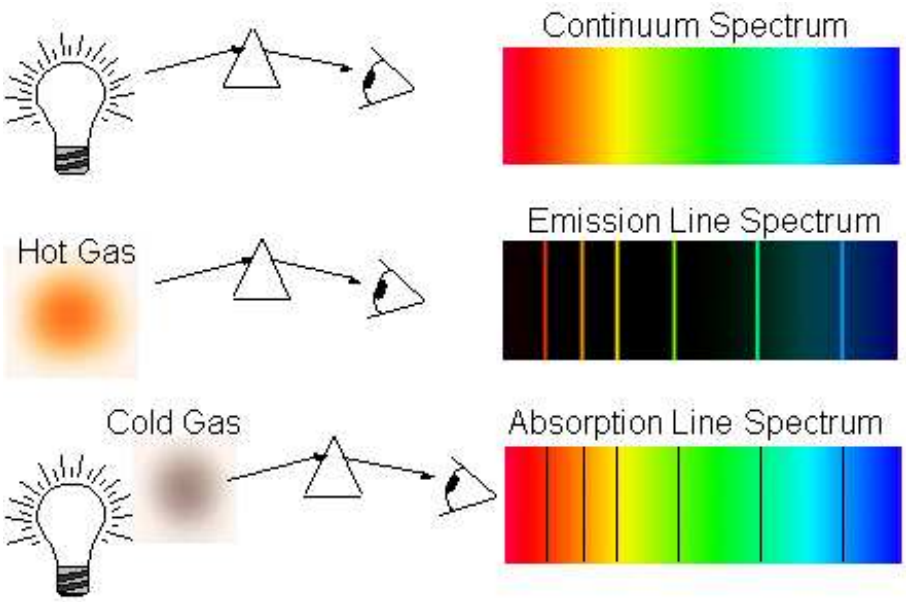


Figure 3.1: Three types of spectra. *Courtesy:* Cornell University

## 3.2 What is Spectroscopy?

Spectroscopy[1] is the study of what kinds of light is emitted from an object. It is a measure of the quantity of each wavelength of light. It is one of the most important tools in astronomy. In fact, most of what we know in astronomy is a result of spectroscopy. It can reveal the temperature, velocity and composition of an object as well as can be used to infer mass, distance and many other pieces of information. Spectroscopy is done at all wavelengths of the electromagnetic spectrum, from radio waves to gamma rays.

Spectroscopy began in 1859 when Gustav Robert Kirchoff (1824–1887) and Robert Wilhelm Bunsen (1811–1899) built an improved spectroscope. They found that there are three types of spectra: continuous spectra, emission (or bright) line spectra, and absorption (or dark) line spectra, as illustrated in Figure 3.1.

[1] `http://www.ph.surrey.ac.uk/astrophysics/files/spectroscopy.html`

To understand the formation of different types of spectra, the Bohr model of the atom can be used. Emission or absorption of light only takes place when a photon has an energy equal to the difference in quantized energy states that an electron can occupy in its orbit around the nucleus.

### 3.2.1 Continuous Spectra

In a very hot gas, the atoms have high kinetic energies and collisions between them are very frequent. Their electrons are raised to excited states and produces emission lines while de-excitation. However, if the gas is at very high pressure and density, then an electron in its excited state may not have enough time to de-excite to its ground state before it undergoes another collision from a neighbouring atom. This has the effect of blurring the sharpness of each emission line into a broad band of wavelengths. The same thing happens to neighbouring lines so that by the time the light emerges from the gas it has smeared out into a continuous spectrum at all wavelengths (see top panel of Figure 3.2).

### 3.2.2 Emission Spectra

In the low temperature, a gas containing only one kind of atoms, the electrons will all be in their ground state. As the gas is heated, kinetic energy of the atoms increases and they start colliding with their neighbours, causing their electrons to be raised to excited states. As the electrons de-excite, photons are emitted with many different energies and wavelengths, corresponding to the particular electron energy level of the gas. The emission of these lines will result in brightness of the gas at wavelengths corresponding to the electron energy transitions. For moderate temperatures, it may be possible that only the first excited state of the atom is attained, so the emission light will consist of a single bright emission line corresponding to the difference in energies between the first excited and ground states (see second panel of Figure 3.2). As the temperature increases further, more emission lines start to appear until at higher temperatures many lines become visible corresponding to all the allowed energy transitions of electrons in the gas. In this

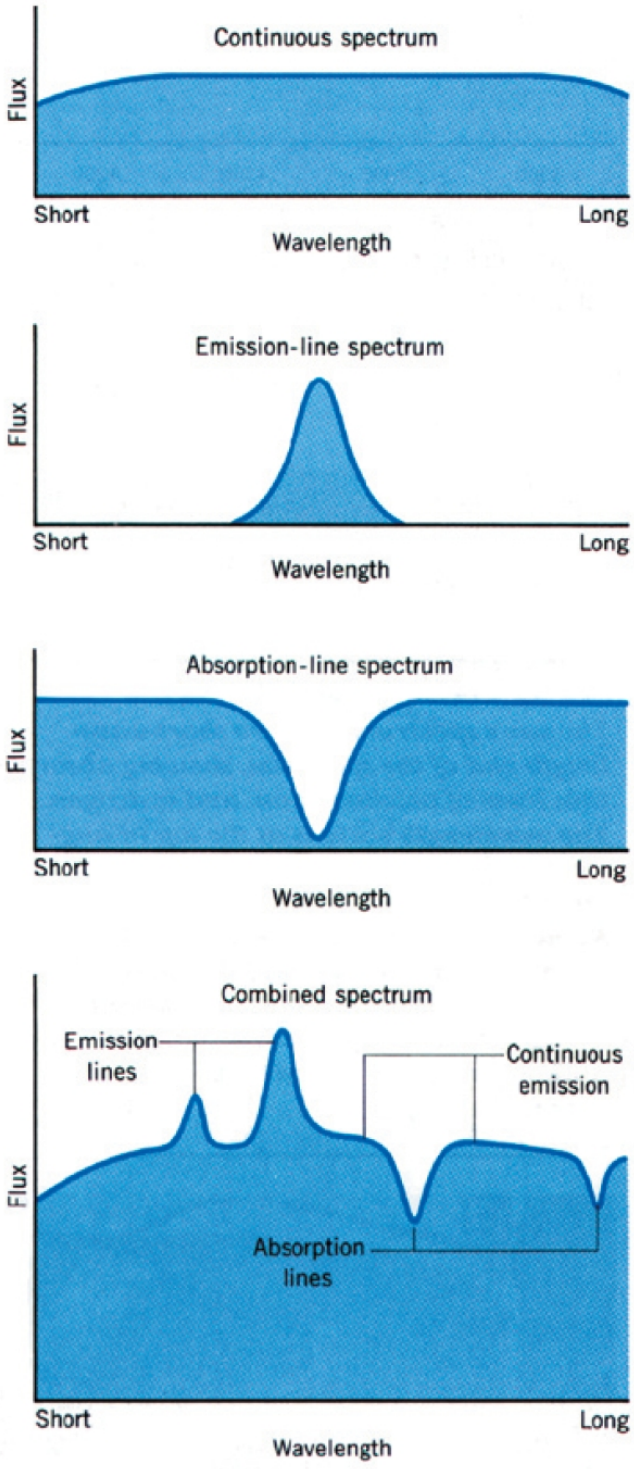


Figure 3.2: Spectra plotted as flux (the amount of light) as a function of wavelength. In the bottom panel, all are shown together as they might appear in an object's spectrum. *Credit:* NOAO

way an emission line spectrum is formed that is related to the elemental composition of the gas.

### 3.2.3 Absorption Spectra

Consider a source of light that emits a continuous spectrum containing photons of all energies and wavelengths. Suppose a gas of unknown composition is placed in front of this source. Now in this case if energy of some of these photons is exactly equal to the difference between the ground state and an excited state of an atom in the unknown gas, then that photon will be absorbed from the incident light. The excited electron will then quickly return to the ground state by emitting a photon, however, this photon is usually emitted in a different direction. Thus at the source, the re-emitted photons are not observed through a spectroscope, and the continuous spectrum appears to have dark lines at the wavelengths corresponding to excited states of the atoms in the unknown gas (see third panel of Figure 3.2). Also at these wavelengths, it can be noticed that light would be emitted in an emission spectrum if the unknown gas was heated to a high temperature.

Hence, presence of elements in a gas can be inferred from these emission and absorption spectra. From the previous section, we have seen that the solar atmosphere is hotter than its surface and has a comparatively very less density which leads to the atmosphere to give emission lines in spectra.

## 3.3 Atomic Transition Probabilities

The solar spectrum in EUV and soft X-rays is dominated by a large number of emission lines (see Figure 1.3). The line strength strongly depends upon the temperature of the plasma and number density of the emitting chemical element or ion. This also depends on the relative transition probabilities between the quantized atomic energy levels in each chemical element or ion.

An atom in an excited state $m$ of energy level $\epsilon_m$ can spontaneously decay to a lower state $n$ of energy level $\epsilon_n$ by emitting a photon of wavelength $\lambda_{ij} = (\epsilon_m - \epsilon_n)/hc$. The Boltzmann equation for the population density of excited states at temperature $T$ is

$$N_m = \frac{g_m}{g_0} N_0 exp\left(-\frac{\chi_m}{k_B T}\right) \tag{3.1}$$

where $\chi_m$ is the excitation energy (of state $m$), $N_0$ is the number of atoms in ground state, and $g_m$ is the statistical weight of the state $m$. Thus the relative population of the energy states $\epsilon_m$ and $\epsilon_n$ is,

$$\frac{N_n}{g_n} = \frac{N_m}{g_m} exp\left(-\frac{\epsilon_n - \epsilon_m}{k_B T}\right) \tag{3.2}$$

A standard method used to calculate the relative line strengths in the coronal plasma involves the assumption of ionization equilibrium. While deriving the Boltzmann equilibrium relation (Equation 3.2) for two energy states, this assumption was inherent. Same assumption can also be extended to bound-free transitions to include ionization processes. In this case, energy difference will consists of the ionization energy $\epsilon_i$ plus the kinetic energy of the free (ionized) electron (i.e., $h\nu = \epsilon_k + \frac{1}{2} m_e v_e^2$), hence the term bound-free transitions. Thus the Boltzmann equilibrium Equation 3.2 for the population ratio $N_k/N_0$ of the continuum population $N_k$ to the ground state population $N_0$ is

$$\frac{N_n}{N_0} = \frac{g_k}{g_0} exp\left(-\frac{\epsilon_k + \frac{1}{2} m_e v_e^2}{k_B T}\right) \tag{3.3}$$

where the statistical weight $g_k = g_k^{'} \cdot g_e$ is now composed of the statistical weight of the ground state $g_k^{'}$ of the ionized atom and $g_e$ of the free (ionized) electron and is given by.

$$g_e = \frac{8\pi m_e^3 v_e^3}{n_e h^3} \tag{3.4}$$

where $n_e$ is electron density.

Substituting the statistical weight $g_e$ (Equation 3.4) into Boltzmann equilibrium Equation 3.3 and integrating over velocity space, leads to the Saha equation derived by M. Saha in 1920 (Saha, 1921),

$$\frac{N_k}{N_0} = \frac{2}{n_e}\frac{(2\pi m_e k_B T)^{3/2}}{h^3}\frac{g_k^{'}}{g_0} exp\left(-\frac{\epsilon_k}{k_B T}\right) \tag{3.5}$$

The Saha equation, which gives the population ratios relative to the ground state, $N_0$, can be generalized for the relative ratio between any two different ionization states $k$ and $k+1$,

$$\frac{N_{k+1}}{N_k} = \frac{2}{n_e}\frac{(2\pi m_e k_B T)^{3/2}}{h^3}\frac{g_{k+1}}{g_k} exp\left(-\frac{\epsilon_{k+1}-\epsilon_k}{k_B T}\right) \tag{3.6}$$

The presence of electron density $n_e$ in the Saha Equation 3.6, indicates that soft X-ray line ratios of the same element are density sensitive whereas density does not occur in the Boltzmann equation which depends only on the temperature.

Although the derivation of the Boltzmann and Saha equations rests on the assumption of ionization equilibrium, and thus strictly applies only to processes with photons such as induced absorption, stimulated emission, and photo-ionization. A similar argument can be made for the equilibrium situation of collisional processes such as collisional excitation, de-excitation, and ionization. This is primarily important in the chromosphere and transition region, where the collision rates are much higher than interactions between photons and atoms or ions.

The important atomic processes in the transition region along with the expressions for their rates and estimates of their characteristic times is summarized in Table 3.1. All the calculations are done for the C IV ion at temperature of $10^5$ K and an electron density of $10^{10}$ cm$^{-3}$. Excitation processes have been calculated for the C IV resonant transition at 1548 Å. Characteristic times for auto-ionization and dielectric recombination are not included because they become important for the C IV only at a much higher temperature (Mariska, 1992).

Table 3.1: Important atomic processes and their characteristic times in the transition region. From Mariska (1992).

| Process | Rate ($cm^{-3}s^{-1}$) | Characteristic time (s) |
|---|---|---|
| Collisional excitation | $N_n n_e C_{nm}$ | $2 \times 10^{-3}$ |
| Collisional de-excitation | $N_m n_e C_{mn}$ | $2 \times 10^{-3}$ |
| Spontaneous radiative decay | $N_m A_{mn}$ | $4 \times 10^{-9}$ |
| Collisional ionization | $n_e n_{ion} q_{coll}$ | 107 |
| Radiative recombination | $n_e n_{ion} \alpha_{rad}$ | 88 |

## 3.4 Line Emissivity

If plasma density is low enough such that probability of emitted photon interacting with other atoms before escaping from the plasma becomes negligible (condition of plasma *optically thin*), it is not necessary then to solve the radiative transfer equation. In that case emissivity of spectral line of wavelength $\lambda_{ij}$ (or frequency $\nu_{ij}$), produced by transition of electrons from higher energy level $\epsilon_j$ to a lower level $\epsilon_i$ is defined as,

$$P(\lambda_{ij}) = \frac{hc}{\lambda_{ij}} N_j A_{ji} \psi(\lambda) \qquad [erg\ cm^{-3} s^{-1} \text{Å}^{-1}] \tag{3.7}$$

where $A_{ji}$ ($s^{-1}$) is the Einstein coefficient of the spontaneous transition probability (i.e., $N_j$ the number density of the upper level $j$ of the emitting ion), and $\psi(\lambda)$ is the emission profile (normalized to unity when integrated over all wavelengths). Practically we can consider that total power emitted in the transition will be distributed over a certain wavelength range according to the emission profile. We can, hence now consider the total emissivity and consider later the mechanisms responsible for the line broadening. We have,

$$P_{ij} = \frac{hc}{\lambda_{ij}} N_j A_{ji} \qquad [erg\ cm^{-3} s^{-1}] \tag{3.8}$$

which can be rewritten as,

$$P_{ij} = \frac{hc}{\lambda_{ij}} \frac{N_j}{N_{ion}} \frac{N_{ion}}{N_{el}} \frac{N_{el}}{N_H} \frac{N_H}{n_e} n_e A_{ji} \tag{3.9}$$

where $N_j/N_{ion}$ is the fraction of ions in the upper emitting level $j$ (it is weakly dependent on temperature, but can be strongly dependent on the electron density), $N_{ion}/N_{el}$ is the relative abundance of the ionic specie with respect to the number density of the element to which the ion belongs (containing a strong temperature dependence), $N_{el}/N_H$ is the element abundance with respect to the hydrogen and $N_H/n_e$ is the hydrogen number density relative to the electron number density ($\approx 0.83$ for a totally ionized solar plasma). All these density and temperature dependent terms can be grouped together in the *Contribution function* $G(n_e, T)_{ij}$ and written as,

$$G(n_e, T)_{ij} = \frac{\epsilon(\lambda_{ij})}{n_e} \frac{N_{ion}}{N_{el}} \frac{N_{el}}{N_H} \frac{N_H}{n_e} \qquad [erg\ cm^3 s^{-1}] \tag{3.10}$$

where $\epsilon(\lambda_{ij})$ is the emissivity of the spectral line normalized to the number density of the emitting ion $N_{ion}$.

$$\epsilon(\lambda_{ij}) = \frac{P_{ij}}{N_{ion}} = \frac{hc}{\lambda_{ij}} \frac{N_j}{N_{ion}} A_{ji} \qquad [erg\ s^{-1}] \tag{3.11}$$

Hence, Equation 3.8 can be written as,

$$P_{ij} = G(n_e, T)_{ij} n_e^2 \tag{3.12}$$

Integrating the line emissivity over the emitting column of plasma, having unitary surface A and height $h$ along the line-of-sight ($V = Ah$), we obtain the total line intensity (erg $cm^{-2}s^{-1}ster^{-1}$) as,

$$I_{ij} = \frac{1}{4\pi} \int_h G(n_e, T_e)_{ij} n_e^2 dh \tag{3.13}$$

If a unique relationship exists between $n_e$ and $T_e$, then the *differential emission measure (DEM)* function can be defined as,

$$DEM(T) = n_e^2 \frac{dh}{dT} \qquad [cm^{-5}\ K^{-1}] \tag{3.14}$$

which allows us to express the line intensity (Equation 3.13) in the simple form of an integral over the temperature range,

$$I_{ij} = \frac{1}{4\pi} \int_T G(n_e, T_e)_{ij} DEM(T) dT \qquad [erg\ cm^{-2} s^{-1} ster^{-1}] \tag{3.15}$$

The DEM(T) gives an indication of the amount of plasma along the line-of-sight, that is able to emit the observed radiation in the interval between $T$ and $T + dT$. It is a primary characteristic that any model of the solar transition region and corona should be able to produce.

In order to evaluate the line intensity from either Equation 3.13, or 3.15, we need to know the contribution functions as expressed in Equation 3.10. This means to evaluate the population of the excited level, the ionization fraction and the element abundance with respect to hydrogen.

## 3.5 Emission Line Profiles

High spectral resolution observations reveal the details of emission line profiles. These line profiles carries information about the physical conditions in the line forming region. The emissivity of an optically thin emission line is given by Equation 3.7, in which many processes can contribute to the emission profile $\psi(\lambda)$. In the solar transition region and corona, Doppler broadening is the most important process for the formation of the optically thin EUV emission lines. As each atom is in thermal motion, the observed wavelength of any photon it emits at a fixed wavelength (in a stationary frame) will be different. Each atom has its own velocity, and hence Doppler shift, which in result spread the line emission in wavelength but keeps the total line strength same.

Assuming the Maxwellian distribution of atomic velocities, the probability $df$ that velocity of an atom lies between $v$ and $v + dv$ is,

$$df = (\beta/\pi)^{1/2}\ exp(\beta v^2) dv \tag{3.16}$$

where $\beta = m/2kT$ and $m$ is mass of the atom. The Doppler shift $\Delta\lambda$ caused by the velocity component $u$ in the line-of-sight is given by,

$$\frac{\Delta\lambda}{\lambda} = \frac{vcos\theta}{c} = \frac{u}{c} \tag{3.17}$$

where $\theta$ is the angle between $v$ and the line-of-sight. Substituting Equation 3.17 in Equation 3.16, the distribution of relative intensity (the line profile) as a function of wavelength shift $\Delta\lambda$ from the line centre $\lambda_0$ is given by,

$$\psi(\lambda) = constant \times \ exp\left(-\beta\frac{c^2}{\lambda^2}\Delta\lambda^2\right) \tag{3.18}$$

The most frequently used measure of line width is the full-width at half maximum intensity (FWHM), found by setting the exponential in Equation 3.18 equal to 1/2. Hence,

$$FWHM = 2\Delta\lambda_{1/2} = 1.67\frac{\lambda}{c}\left(\frac{2kT}{m}\right)^{1/2} \tag{3.19}$$

where $\Delta\lambda_{1/2}$ is called as the half-width at half-maximum intensity.

Alternatively, Equation 3.18 can also be solved for the thermal Doppler half-width where the intensity falls to $1/e$ of its central intensity, and hence,

$$\Delta\lambda_D = \frac{\lambda}{c}\left(\frac{2kT}{m}\right)^{1/2} \tag{3.20}$$

In these expressions the temperature is an ion temperature, since it is the ions that are in thermal motion. At the temperatures and densities of the transition region, the electrons and ions rapidly equilibrate, on the time-scale of 0.04 s (Mariska, 1992). Hence assuming a single temperature for the quiet transition region plasma is therefore reasonable.

### 3.5.1 Non-thermal Line Broadening

Along with thermal motions, when additional motion associated with unresolved small and large scale velocity fields and/or wave propagation are present, a further term is added to Equation 3.19 or 3.20. Assuming that this additional velocity field is also Maxwellian with the most probable non-thermal velocity $\xi$, we get

$$FWHM = 2\Delta\lambda_{1/2} = 1.67\frac{\lambda}{c}\left(\frac{2kT}{m} + \xi^2\right)^{1/2} \tag{3.21}$$

Sometimes, the non-thermal velocity is expressed in terms of a root mean square velocity $v_{rms}$,

$$v_{rms} = (3/2)^{1/2}\xi \tag{3.22}$$

There are also other mechanisms present which may broaden the spectral lines, such as natural broadening and collisional broadening. When natural broadening, which produces a Lorentz profile, is combined with Doppler broadening, the resultant line profile is then described by a Voigt function.

### 3.5.2 Instrumental Broadening

In addition to these, the line profile is also broadened by the finite spectral resolution of the spectrometer. If the true profile of the line is $\psi(\lambda)$ and the spectrometer's instrumental profile is $G(\lambda)$, the observed profile $O(\lambda)$ is then given by the convolution integral,

$$O(\lambda_0) = \int_{-\infty}^{\infty} \psi(\lambda - \lambda_0)G(\lambda)d\lambda \tag{3.23}$$

The instrumental profile $G(\lambda)$ represents the smoothing by the spectrometer of an infinitely narrow spectral line. If $\psi(\lambda)$ is a Gaussian of half width $\Delta\lambda_{1/2}$ and the instrumental profile is ap-

proximated by a Gaussian of half width $\Delta\lambda'_{1/2}$, then the observed profile will also be a Gaussian of half width

$$\Delta\lambda^2_{1/2}(obs) = (\Delta\lambda_{1/2})^2 + \left(\Delta\lambda'_{1/2}\right)^2 \tag{3.24}$$

Hence, the true half width $\Delta\lambda_{1/2}$ can be evaluated, provided $\Delta\lambda'_{1/2}$ is known.

## 3.6 Plasma Diagnostics

Plasma diagnostic techniques allow the measurement of the physical properties of optically thin plasmas. These techniques can be used to measure the electron and ion temperatures, electron density etc.

### 3.6.1 Electron Density Diagnostics

The electron density enters in the emission line intensity equation through the number density of ions in the excited level and through the density dependence of the collision states. Electron densities can be measured by using the intensity ratio of two spectral lines. For a non-isothermal plasma, the intensity ratio of two lines emitted by the same ion is given by Equation 3.15:

$$\frac{I_{ij}}{I_{kl}} = \frac{\int_T G(n_e, T_e)_{ij} DEM(T) dT}{\int_T G(n_e, T_e)_{kl} DEM(T) dT} \tag{3.25}$$

Since the ion and elemental abundances are same for both the lines, integrals only depend on the populations of upper levels $i$ and $k$ of the lines and respective Einstein coefficients of both the transitions. The density sensitivity of the population ratio can be due to the population of lower level from which the upper level is populated.

### 3.6.2 Electron Temperature Diagnostics

The temperature sensitivity of intensity ratios of lines from different ions is mostly due to the different temperature dependence of the abundances of the ions emitting the line pair. This sensitivity is usually very strong, independent of the excitation energy of the two lines. Such ratios are taken for the lines emitted by ions of the same element to avoid uncertainties in element abundances. These ratios have stronger temperature sensitivity than ratios of lines of the same ion, but they are subject to the uncertainties in the ion fraction calculations. In these calculations, any departures from equilibrium will lead to misleading results. The line ratios should not have any dependence on $n_e$.

# Chapter 4

# Propagating Waves in On-disk Coronal Holes

## 4.1 Context

Coronal holes are regions of cool and low density plasma that are 'dark' at coronal temperatures (Munro and Withbroe, 1972). During the years of solar minimum, coronal holes are confined to the Sun's polar regions, while at solar maximum they can also be found at lower latitudes, usually associated with remnant active regions, as so-called 'equatorial' coronal holes (Timothy et al., 1975). The predominantly unipolar magnetic field from coronal hole regions is thought to give rise to the fast solar wind (Krieger et al., 1973).

The prominent feature of the coronal holes and quiet Sun in the chromosphere and transition region is the magnetic network (see Figure 4.1), which is believed to be the upward extension of the supergranular boundaries above the photosphere (Reeves, 1976). The network is identified as bright lanes in radiance images, the darker areas within the network cells are termed as internetwork. It is suggested that part of the network fans out in the corona into a funnel shape. Recently, it has been further suggested that the fast solar wind originates from coronal hole funnels, which have their foot points located at the edges of the magnetic network (Tu et al., 2005). As below the surface of the Sun there are large convection cells present, which has magnetic fields associated

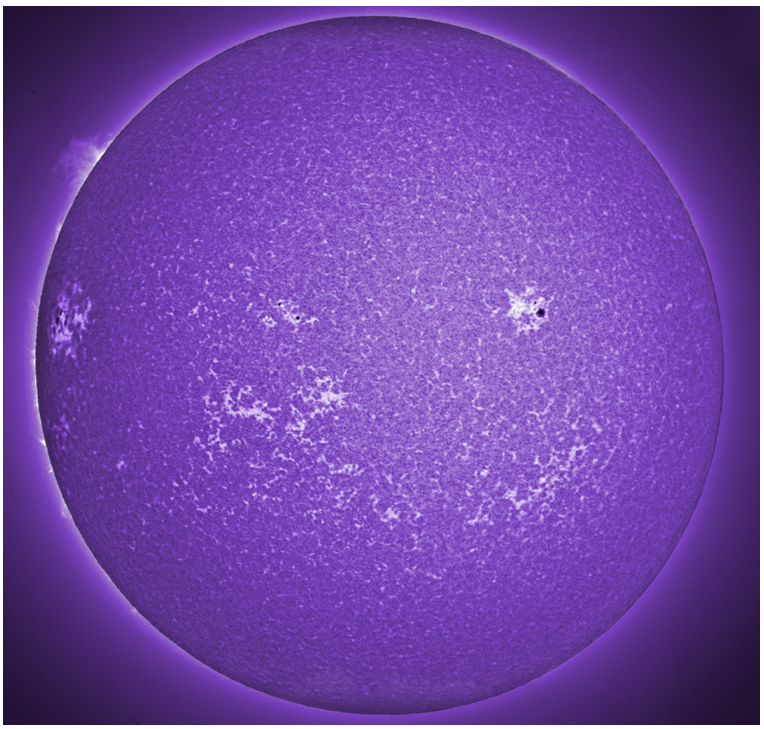

Figure 4.1: Glowing white magnetic network structure of solar disk taken on July 29, 2005, using a violet calcium-K solar filter. *Credit:* Science@NASA.

with it. These fields are concentrated in the network lanes by magneto-convection, where the funnel necks are anchored. The plasma, which are confined in small loops, are brought by convection to the funnels and then released there. The fast solar wind seems to originate from these coronal funnels with a speed of about 10 km $s^{-1}$ at a height of 20 000 km above the photosphere as seen from the Ne VIII 770 Å spectral line of SUMER (Tu et al., 2005). Figure 4.2 shows the origin regions of the solar wind and illustrates the location and geometry of three-dimensional magnetic field structures in the solar atmosphere. Some other studies have also found evidence for outflows (blue shifts) of typically 10 km $s^{-1}$ in both polar (Wilhelm et al., 2000; Popescu et al., 2004) and equatorial (Xia et al., 2004) coronal holes at transition region temperatures.

As described in Section 1.4.2 and 1.7.2, waves are important for coronal heating and acceleration of solar wind. A number of studies have measured oscillations in coronal holes in the polar off-limb regions of the Sun (Ofman et al., 1997, 2000; Banerjee et al., 2001b; Popescu et al.,

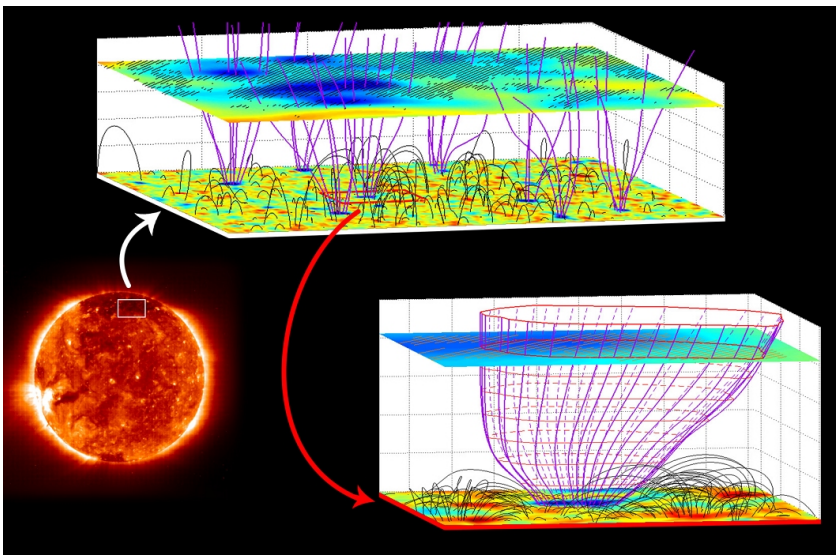

Figure 4.2: Source regions of the fast solar wind. The figure illustrates the location and geometry of three-dimensional magnetic field structures in the solar atmosphere. The magenta coloured curves illustrate open field lines, and the dark grey solid arches show closed ones. In the upper plane, inserted at 20 600 km, the Ne VIII 770 Å Doppler shift is compared with the model field. The hatched area indicates where the outflow speed of highly charged $Ne^{+7}$ ion is larger than 7 km $s^{-1}$. Note the funnel constriction by pushing and crowding of neighbouring loops (Tu et al., 2005). *Credit:* SOHO/ESA.

2005). All of these studies point to the presence of compressional waves, thought to be slow magneto-acoustic waves as found by DeForest and Gurman (1998); O'Shea et al. (2006, 2007).

In this chapter, we describe the additional evidence of waves in the disk part of polar coronal hole regions which are detected by carrying out a statistical study of oscillations and their phase properties, both in the intensity and velocity domain. We will focus on the behaviour of oscillations detected in the bright network regions which are suppose to be the site of origin of fast solar wind and in the darker internetwork regions[1].

For this study, observations were carried out with the SUMER spectrometer on-board SOHO spacecraft (Wilhelm et al., 1995).

[1]Results discussed in this chapter are published in Gupta et al. (2009, 2010b).

## 4.2 Observations and Data Analysis

The data selected for this study were obtained as time series in two polar coronal holes (hereafter pCHs, cf. Table 4.1 ) by SUMER. The two lines used in this study are the transition region line, N IV 765 Å at a temperature of log T=5.0 K (T = 100 000 K) and the coronal line of Ne VIII 770 Å at a temperature of log T=5.8 K (T = 630 000 K). During the observation, the SUMER slit was kept fixed at the north pole ($x = 0''$, $y = 909.75''$) for pCH 1 and at the south pole ($x = 0''$, $y = -950.25''$) for pCH 2 with part of the slit off-limb and part in the disk part of the coronal hole (sit-and-stare observations). The two pCHs observed are shown in Figure 4.3. Figure shows the initial position of the SUMER slit over-plotted on an EIT (the Extreme ultraviolet Imaging Telescope on the SOHO spacecraft) image taken in the 195 Å filter. The two pCH can be clearly identified in the image as very dark regions of reduced coronal emission at the poles.

The slit width ($1''$) gives the spatial resolution along the $x$-direction, whereas the resolution along the slit in the $y$-direction (north-south; positive towards north) is given by the pixel size of the detector, and is also approximately $1''$. For sit-and-stare observations one needs to consider the effect of the solar rotation on the detectable minimum frequency. We used the program, *rot_xy.pro* within SolarSoft[2], which incorporates $diff\_rot.pro$[3], to calculate the rotation rate. The $diff\_rot.pro$ procedure uses standard equations for calculating solar rotation, while *rot_xy.pro* converts the results of this from degrees/day to arcsec/day (second). At the lowest pixel location, $Y \approx 760''$, the rotation rate is $\approx 3.7''$/hour. Thus the highest frequency that can possibly be affected by rotation is $\approx 1.03$ mHz (Doyle et al., 1998b). Whereas at high latitudes ($Y \approx 950''$ and higher) the solar rotation is very slow ($\leq\approx 0.255''$/hour) and thus the spreading of the frequencies is negligible ($\leq\approx 0.071$ mHz). In general, most frequencies are measured from pixels above $Y \approx 760''$ and, thus, the effects of rotation will be at values much less than $\approx 1.03$ mHz.

[2] http://www.astro.washington.edu/deutsch-bin/getpro/library32.html?ROT_XY()
[3] http://www.astro.washington.edu/deutsch-bin/getpro/library32.html?DIFF_ROT()

Table 4.1: Temporal series observations from the SUMER in polar coronal holes.

| | pCH 1 | pCH 2 |
|---|---|---|
| Date | 20/10/1996 | 25/02/1997 |
| Time (UT) | 19:57 – 23:57 | 00:03 – 13:58 |
| Solar co-ordinate (x,y) | 0″, 909.75″ | 0″, -950.25″ |
| Wavelength used (Å) | N IV 765, Ne VIII 770 | N IV 765, Ne VIII 770 |
| Detector and slit | B2 (1″ × 300″) | B2 (1″ × 300″) |
| Exposure time (s) | 30 | 60 |

We applied the standard procedures for correcting and calibrating the SUMER raw data, namely decompression, reversal as well as flat field, dead-time, local-gain, and geometrical corrections as described in Section 2.5.1. The method used to deduce the line parameters (radiance, central position of the spectral line and width) is described as follows. We calculated the central position for every pixel, by integrating the line radiance across a certain spectral window and determining subsequently the location of the 50 % level with sub-pixel accuracy. This procedure is frequently used to obtain SUMER Dopplergrams (see details in Dammasch et al., 1999) and dramatically reduces the computing time for a large number of data. The results deduced by this method are statistically consistent with those obtained by using the standard Gaussian fitting programme (Xia et al., 2003). In addition, a line-position correction was applied, to remove spurious spectral line shifts caused by thermal deformations of the instrument, and to eliminate residual errors (systematic variation along the slit) after the geometric correction, using the standard software (Dammasch et al., 1999; Xia et al., 2003). The uncertainty in velocity from this calculation is ±1.2 km $s^{-1}$ (Dammasch et al., 1999). The line-of-sight (LOS) velocity values presented here are measured relative to the limb velocity, i.e., the velocity at the limb is assumed to be effectively zero. We binned over two time frames to increase the signal to noise, which yields an effective cadence of 60 s for the first dataset. We also binned over two spatial pixels for both the datasets. The Nyquist frequency, therefore, is ≈ 8.33 mHz (Jenkins and Watts, 1968). The total observation time for the first dataset is 240 min = $1.44 \times 10^4$ s and, hence, the frequency resolution is ≈ $6.94 \times 10^{-2}$ mHz. The observation time for the second dataset is 835 min = $5.01 \times 10^4$ s, which gives a frequency resolution of ≈ $2 \times 10^{-2}$ mHz. In the following Fourier

analysis, phase delays for each dataset will be measured at all the frequencies up to the Nyquist frequency, at steps dictated by the frequency resolution.

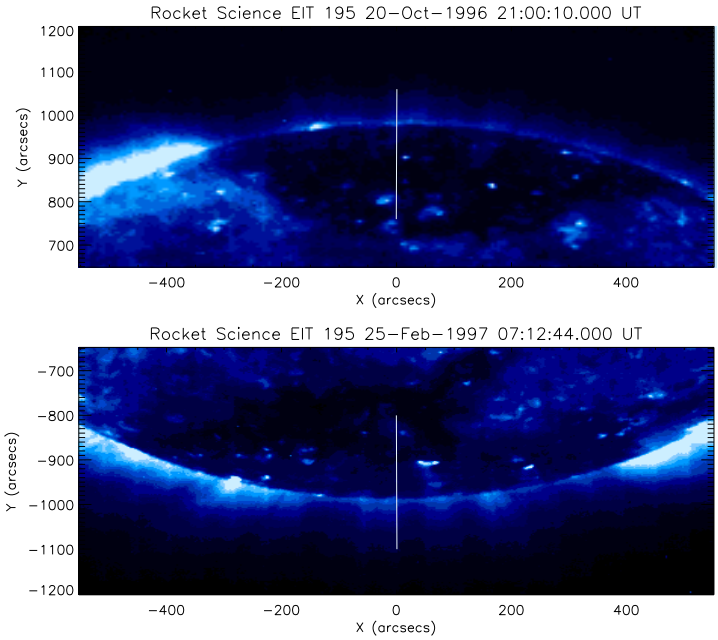


Figure 4.3: Solar polar coronal holes imaged by EIT/SOHO in the 195 Å band. The vertical white lines show the fixed position of the SUMER slit during the two observations.

The quiet Sun (QS) chromosphere and transition region show a network pattern all over the disk, with intensity enhancements in the network boundaries, as seen in Figure 4.1. Within coronal holes such patterns also exist (Tu et al., 2005). Presumably, the magnetic field is predominantly concentrated on such network boundaries and, within coronal holes, the foot-points of coronal funnels emanate from these network regions. Recent studies from SOT/Hinode also indicate that these funnels originate from small magnetic patches with very strong kG magnetic fields (Tsuneta et al., 2008a). Tsuneta et al. (2008a) further claims that all the open field lines forming the polar coronal hole essentially originate from such scattered small but intense magnetic patches, and the fast solar winds emanate from these vertical flux tubes seen in the photosphere. We assume that our intensity enhanced regions could correspond to these magnetic patches. Thus, to identify such locations and distinguish between network and internetwork pixels, the subsets of data to be used in our study were selected on the basis of bright ('network') and

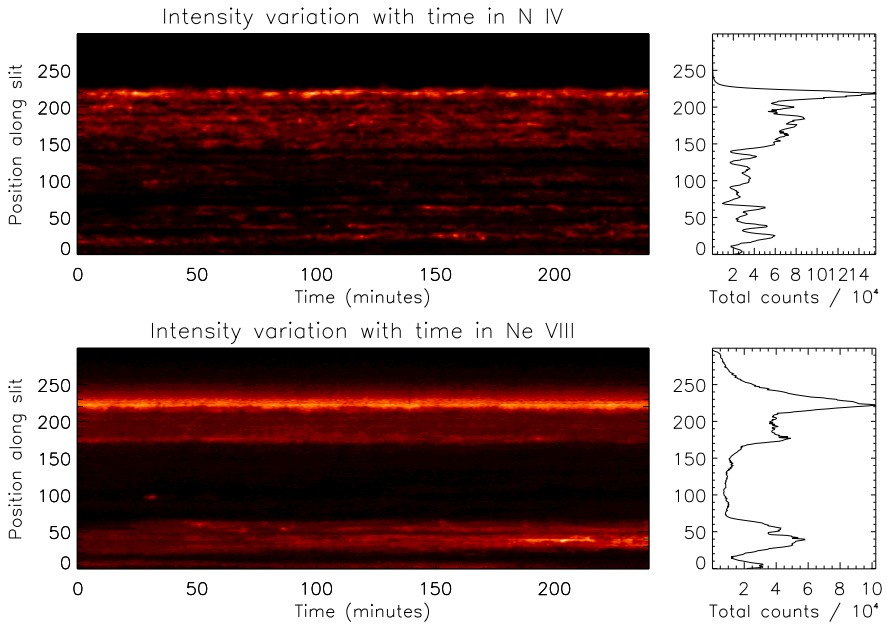


Figure 4.4: Top (bottom) left panel shows the variation of the N IV 765 Å (Ne VIII 770 Å) intensity along the slit (in pixel units) with time. Right panel shows the variation of the total summed counts over time along the slit.

dark ('internetwork') locations. The left panels of Figure 4.4 show the variation of the N IV 765 Å (top panel) and the Ne VIII 770 Å (lower panel) intensity along the slit with time for pCH 1. The right panels show the variation of the total summed counts over time at each pixel position along the slit. The intensity enhanced locations marks the location of network boundary. For choosing the bright ('network') locations, we have used the arbitrary criterion that pixels having an intensity higher than 1.35 times the average intensity ($\approx$ 42 000 counts) are network pixels (excluding those very close to the limb and off-limb pixels, beyond $\approx$210 pixels). This corresponds to the intensity enhancements in the right top panel of Figure 4.4 and their nearest neighbours. The pixels numbered 23–26 and $\approx$149–200 are identified as bright (network) pixels and other pixels as dark (internetwork) for the low temperature N IV 765 Å line (note that in this particular case the network boundary spans a large spatial domain along the slit, maybe it is a bigger patch as seen by recent Hinode studies).

For pCH 2, we used a slightly different criterion for choosing the bright pixels. As this dataset has very long duration of observation, the location of bright and dark pixels along the slit will change with time. For this reason, we have analysed the whole dataset pixel by pixel and time-frame by time frame. For example, for one time instance we first found the average intensity along the slit. All pixels having an intensity higher than 1.25 times this average intensity were chosen as bright pixels. If, for example, this pixel was bright for at least 60 min (or 60 time frames), then that pixel was considered to be a bright ('network') location over that time interval. We would then use that 60 min or longer sequence for doing our analysis. In pCH 2 the number of locations chosen for analysis was smaller than in pCH 1. This is because in pCH 1 the average variation in intensity along the slit is smooth, whereas in pCH 2 it changes rapidly which causes many pixels which would otherwise be considered bright to be lost to our analysis. The network pixels obtained from N IV 765 Å line are assumed to be the same in the higher temperature Ne VIII 770 Å line.

## 4.3 Results and Discussions

### 4.3.1 Analysis of Oscillations

In Figures 4.5 and 4.6, we show a representative example of the type of the oscillations we measured in a bright region of the pCH 1 at the pixel location 180–181 which corresponds to the solar-$Y$ location of $\approx 940''$. At this location the rotation rate is $\approx 0.87''$/hour. Thus the highest frequency that can possibly be affected by rotation is $\approx$ 0.24 mHz. Whereas Figure 4.7 shows a representative example of the oscillations measured in a bright region of the pCH 2 at pixel location 115–116 which corresponds to the solar-$Y$ location of $\approx -915''$. Details on the wavelet analysis, which provides information on the temporal variation of a signal, are described in Torrence and Compo (1998). For the convolution with the time series in the wavelet transform, we chose the Morlet function, as defined in Torrence and Compo (1998). The oscillations shown in the upper panels had their background trend removed by subtracting from the original time series a 30–point running average (i.e., a ≈30 min interval) (hereafter we will use the term intensity for

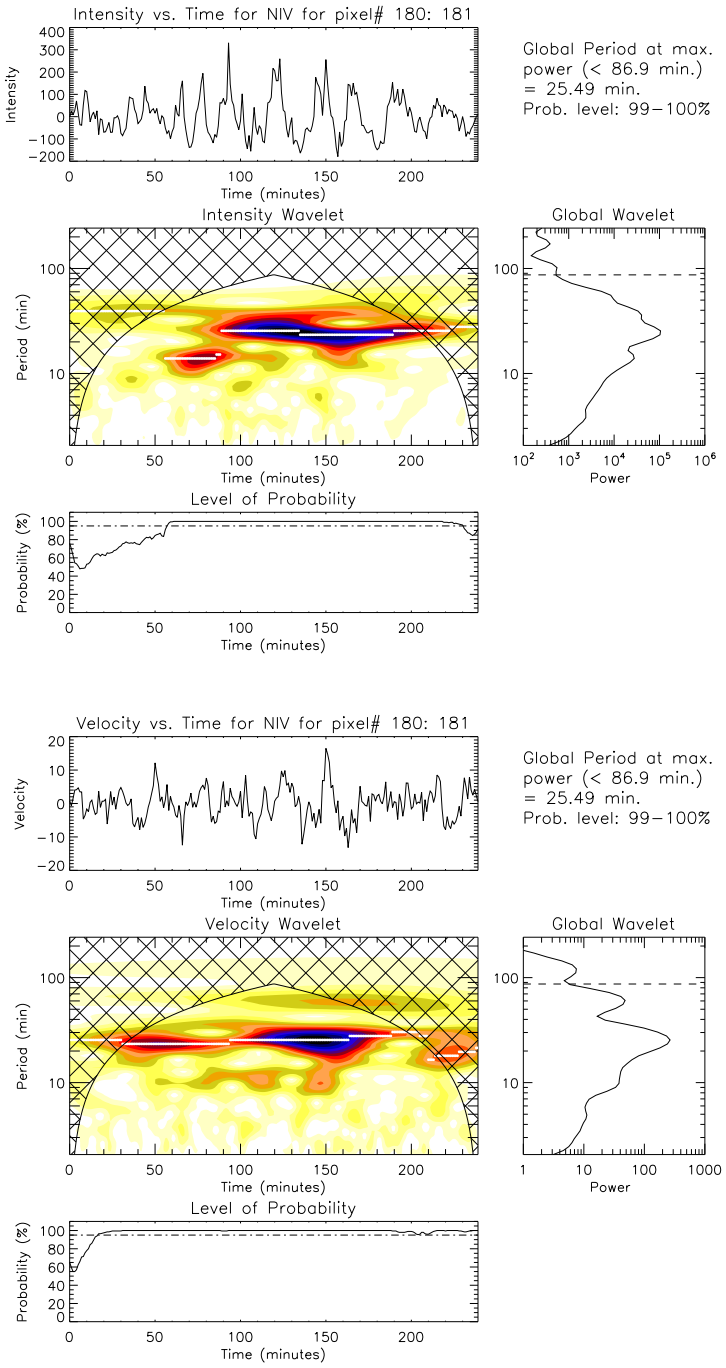


Figure 4.5: Wavelet result for a bright location (pixel no. = 180–181 which corresponds to $Y \approx 940''$) in the N IV 765 Å intensity and velocity in pCH 1. In each set the top panels show the relative (background trend removed) radiant flux/velocity as marked, the central panels show the colour inverted wavelet power spectrum, the bottom panels show the variation of the probability estimate associated with the maximum power in the wavelet power spectrum (marked with white lines), and the right middle panels show the global (averaged over time) wavelet power spectrum. Above the global wavelet the period, measured from the maximum power from the global wavelet, together with probability estimate, is printed.

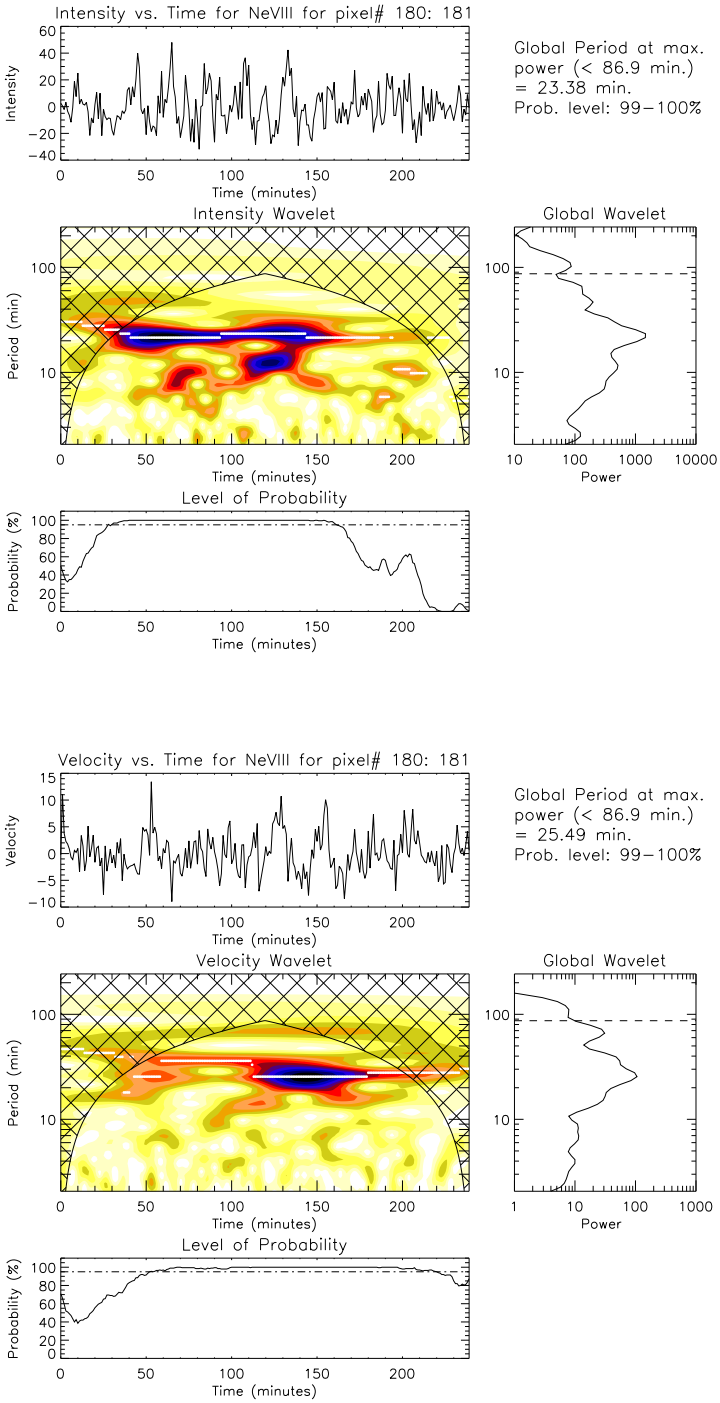


Figure 4.6: Wavelet analysis results for a bright location (pixel no. = 180–181 which corresponds to $Y \approx 940''$) in the intensity (top side) and in velocity (bottom side) data for the Ne VIII 770 Å line in pCH 1. Descriptions about the different panels are the same as in Figure 4.5.

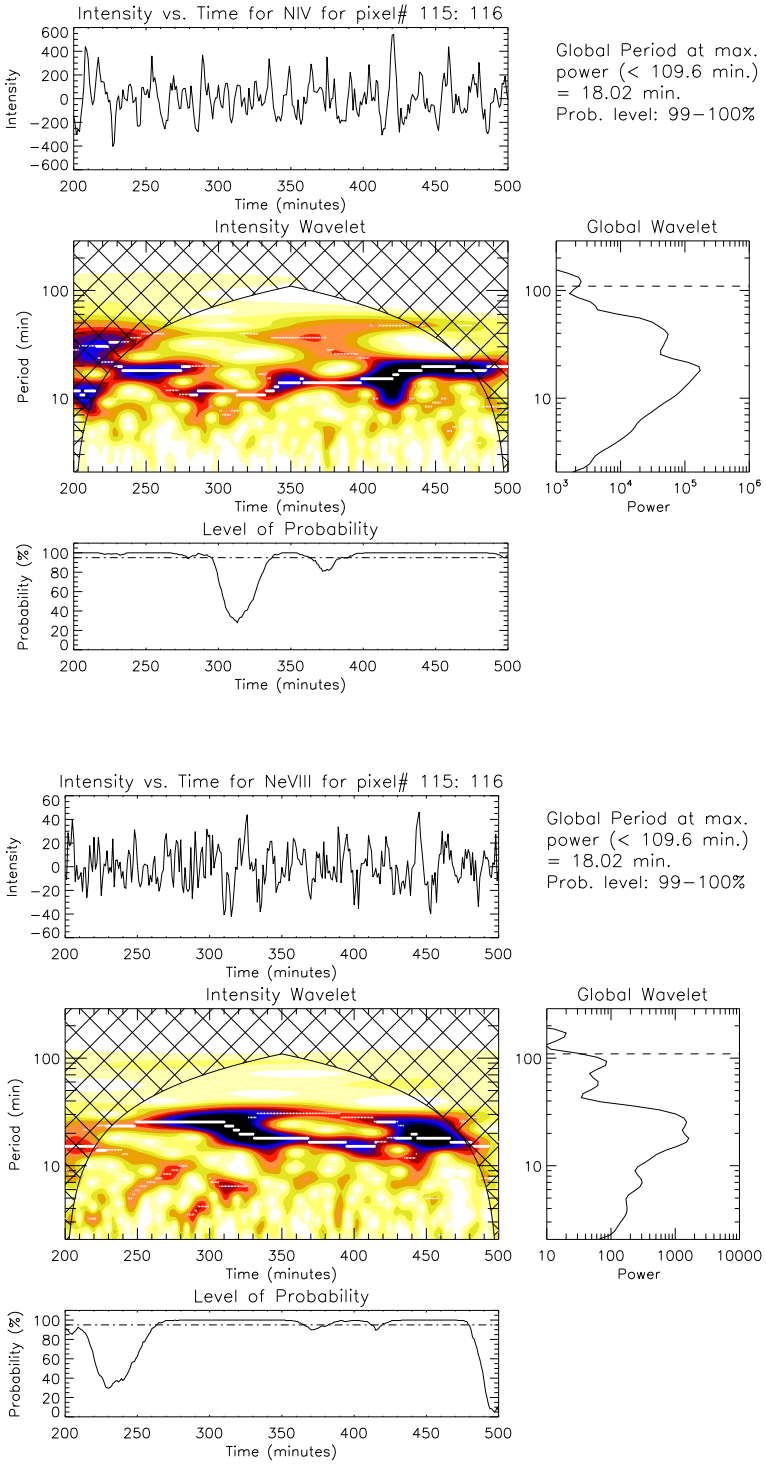


Figure 4.7: Wavelet analysis results for a bright location (pixel no. = 115–116 which corresponds to $Y \approx -915''$) in the N IV 765 Å and Ne VIII 770 Å intensities in pCH 2. Descriptions about the different panels are the same as in Figure 4.5.

trend subtracted radiant flux). In the wavelet spectrum, the cross-hatched regions are locations where estimates of oscillation period become unreliable. This is the so-called cone-of-influence (COI), see Torrence and Compo (1998). As a result of the COI, the maximum measurable period is shown by a dotted line in the global spectrum plots. Above the global wavelet spectrum of Figure 4.5 is shown the period, measured at the location of the maximum in the global wavelet spectrum, together with an estimate of the probability that this oscillation is not due to noise. The probability estimate was calculated using the randomisation method with 200 permutations as outlined in detail in O'Shea et al. (2001). A randomisation test is based on the assumption that, if there is no periodic signal in the time series data, then the measured values (intensity, velocity, etc.) are independent of their observation times. For example, the intensities $I_1$**,** $I_2$**,...** $I_n$, observed at times $t_1$**,** $t_2$**,...** $t_n$, are just as likely to have occurred in any other order $I_{r(1)}$**,** $I_{r(2)}$**,...** $I_{r(n)}$, where n is the total number of observations and r(1), r(2),... r(n) is a random permutation of the subscripts 1, 2,... n. Only those oscillations with a probability >95 % are considered to be significant. Below the wavelet power spectrum, in the lower panels, we show the variation of the probability estimate, calculated using the randomisation technique, associated with the maximum power at each time in the wavelet power spectrum. The location of the maximum power is indicated by the over-plotted white lines. We should also point out that there are 240 points in the intensity time series, with a separation of 60 s, which result in a range of (non-linear) period scales, or values, given by the wavelet. These scales (or period values) from the wavelet are at fixed values of period and so small variations of period between one oscillation period and another can be lost. In our case, in Figures 4.5 and 4.6, we see periods at a reduced range of values of 25.49 min and 23.38 min. It is most probable that the oscillations have a range of values between 23 min to 26 min. However, their precise values must remain unknown due to the relative crudity of the temporal resolution given by the wavelet scales. Thus we can see oscillations of $\approx$ 25 min period in both the intensity and the velocity. So, we may say that these oscillations are likely to be present due to the propagation characteristics of a compressional wave. These oscillations can be seen in both lines (N IV 765 Å and Ne VIII 770 Å), cf. Figures 4.5–4.7 and summarized in Table 4.2. We note that the fact we see a similar periodicity in the intensity and velocity wavelets is a sign of 'correlation' at the strongest period of oscillation. As the oscillations are seen in both

the lower and the higher temperature lines, it is likely that the waves producing these oscillations are propagating between the different temperature regions where these lines form.

Table 4.2: Periodicities observed in different spectral lines in pCH 1.

| Spectral line (Å) | Period (min) | |
|---|---|---|
| | Intensity | Velocity |
| N IV 765 | 25.49 | 25.49 |
| Ne VIII 770 | 23.38 | 25.49 |

### 4.3.2 Phase Difference Analysis

To investigate whether waves are propagating between the different temperature regions, we measure the phase delays in intensity and also in the LOS relative velocity between both lines for each of the measurable pixels along the slit. For all separate frequencies the 'correlation' is determined by the squared coherency spectral estimate, which is a function of frequency, with values between 0 and 1 that indicates how well a time series $x$ corresponds to a time series $y$ at each frequency. The phases are calculated from cross power spectral estimates, following the techniques outlined in Doyle et al. (1999), and is also described in Appendix B. Only phases (corresponding to each spatial pixel) where the squared coherencies are greater than a significance of 95.4 % ($2\sigma$) are used in the analysis (see O'Shea et al., 2006, and references therein). The errors in the phase is calculated based on the equation (A23) of Doyle et al. (1999). In this work we follow the treatment used by Athay and White (1979) and O'Shea et al. (2006), in which the calculated phase delays are plotted over the full $-180^\circ$ to $+180^\circ$ ($360^\circ$) range and as a function of the measured oscillation frequency. Since the expected phase delay or difference is given by the equation:

$$\Delta\phi = 2\pi f T \tag{4.1}$$

where $f$ is the frequency and $T$ the time delay in seconds, the phase difference will vary linearly with $f$, and will change by $360^\circ$ over frequency intervals of $\Delta f = 1/T$. This will give rise to parallel lines in $\Delta\phi$ vs. $f$ plots at fixed frequency intervals ($\Delta f = 1/T$), corresponding to a fixed time delay $T$.

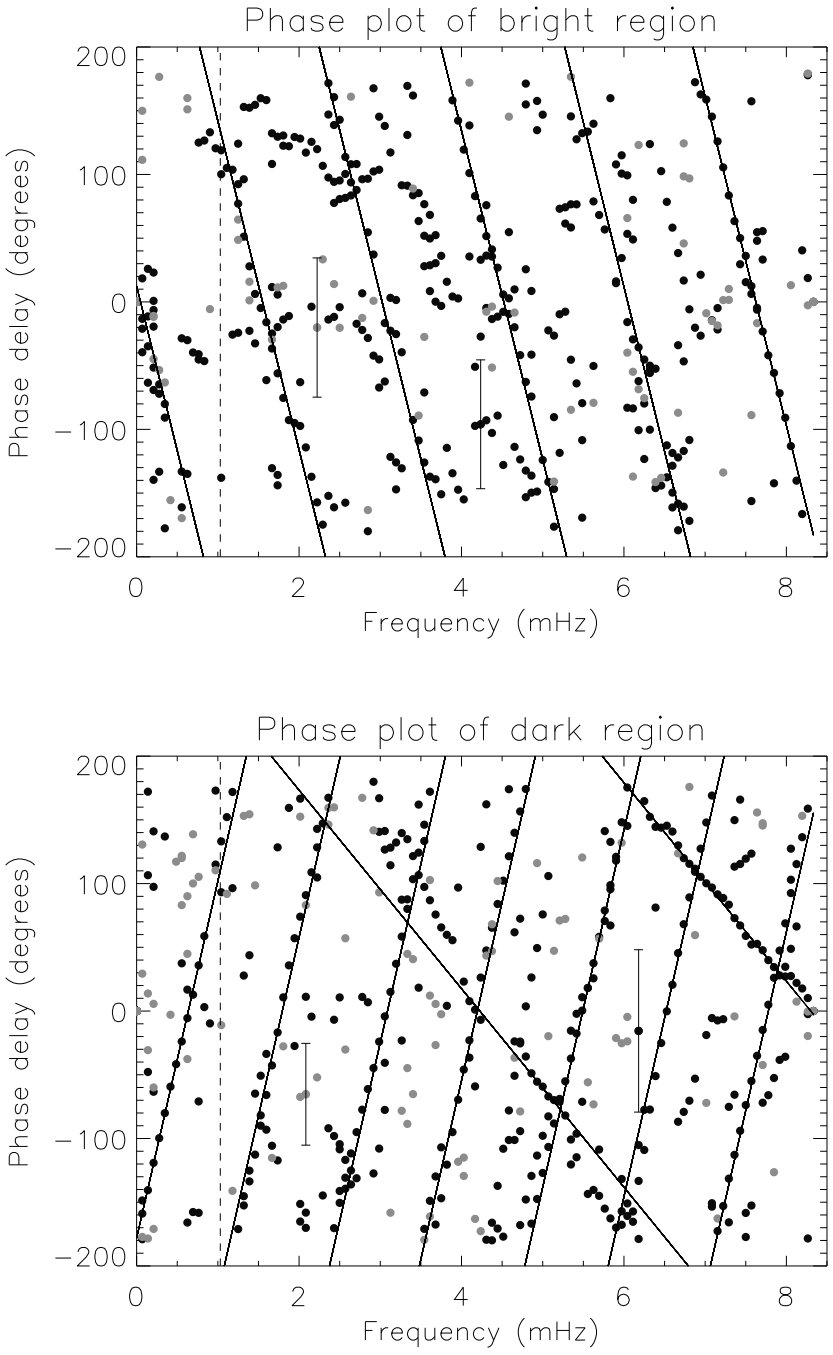


Figure 4.8: Phase delays measured between the oscillations in the spectroscopic line pair for the bright (top panel) and dark (bottom panel) locations for pCH 1. The phases in radiant flux oscillations are shown in the grey circle symbols while that in LOS velocities are shown as the black circle symbols. Overplotted on each figure are black parallel lines, corresponding to fixed time delays. The vertical dashed line drawn at 1.03 mHz indicates that some phase values below this could be affected by solar rotation. Representative errors on the phase measurements are indicated by the error bars.

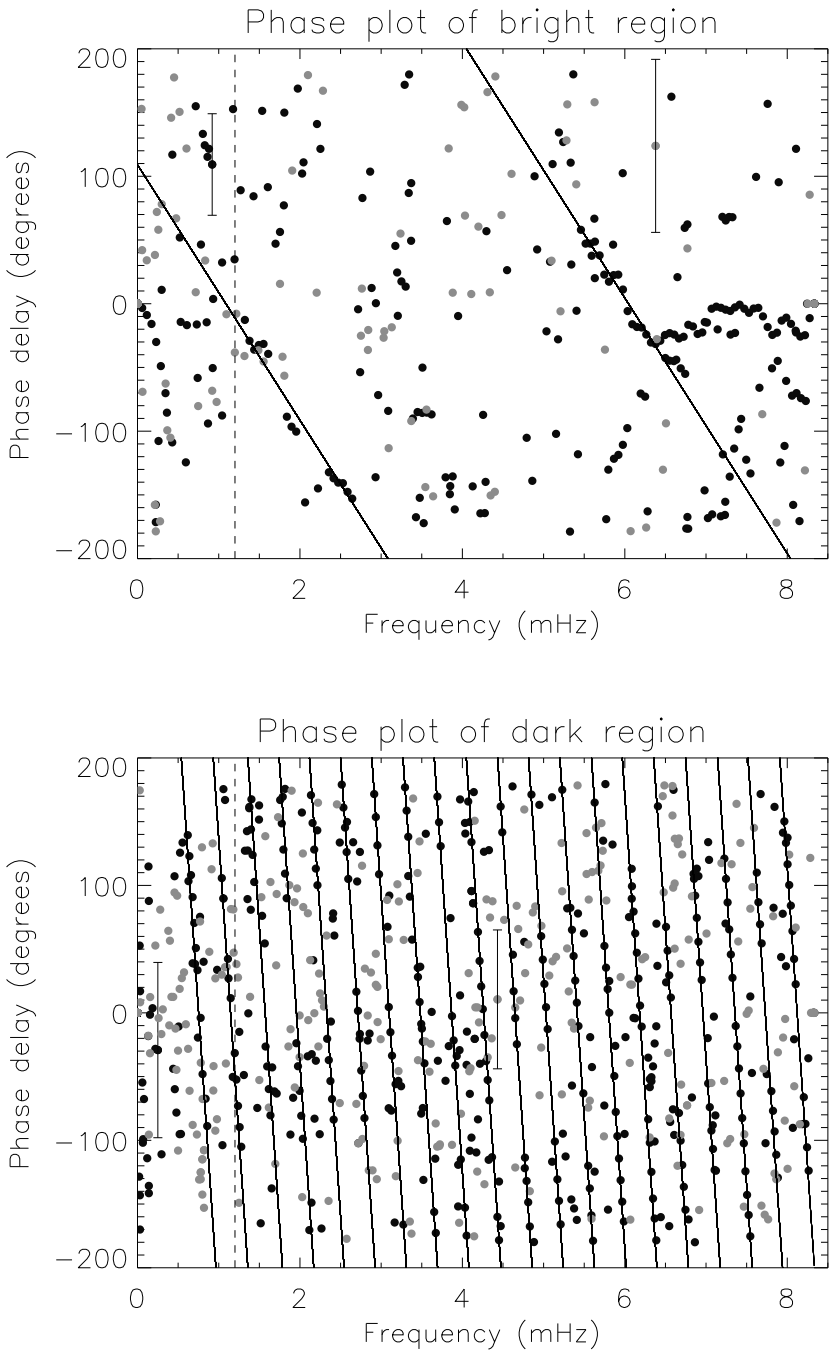


Figure 4.9: Phase delays measured between oscillations in the spectroscopic line pair for the bright (top panel) and dark (bottom panel) locations for pCH 2. Description about the different panels is same as in Figure 4.8 but the vertical dashed line is drawn at 1.2 mHz.

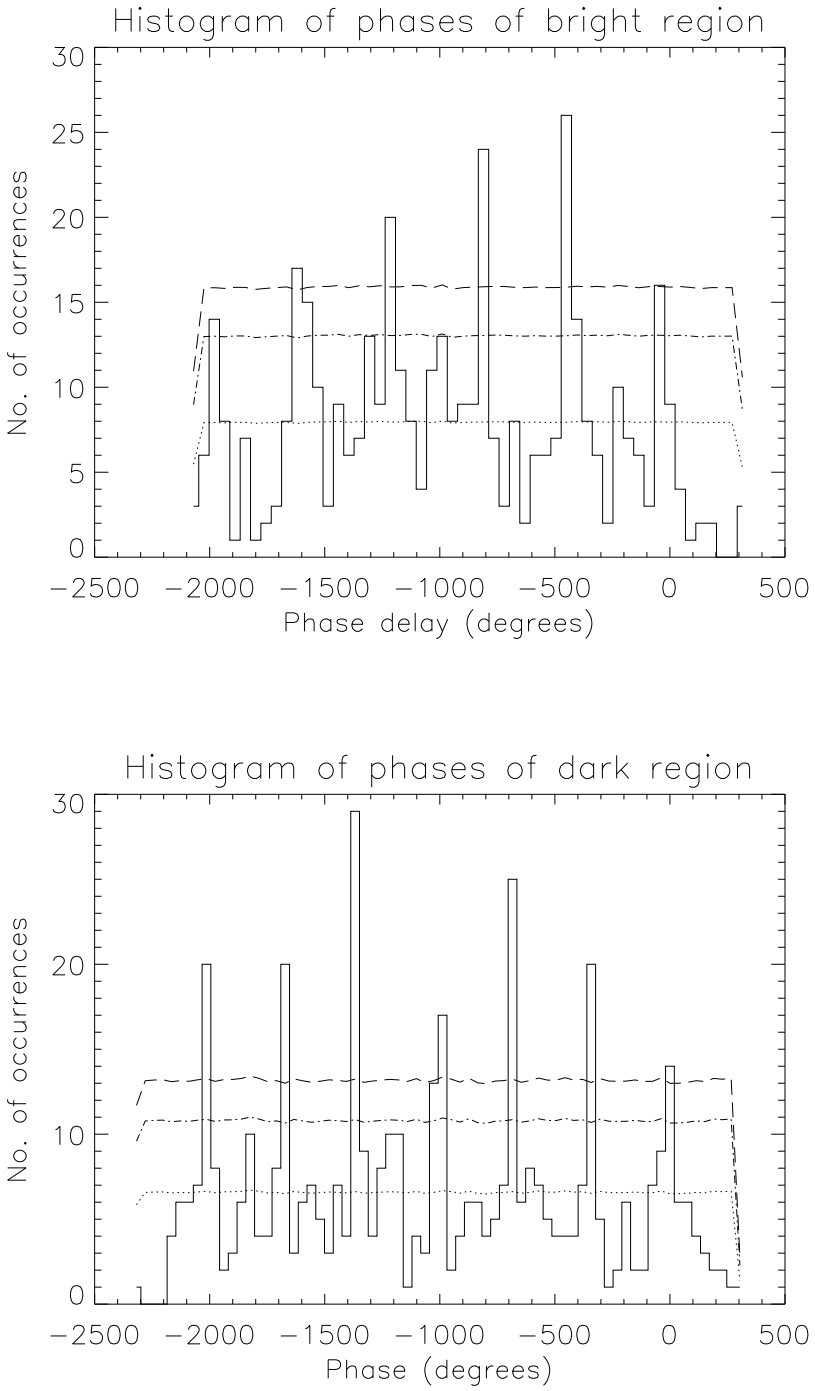


Figure 4.10: Histogram showing the distribution of phase delay measurements as a function of frequency for the bright (top panel) and dark (bottom panel) locations of pCH 1 for the downwardly propagating waves only. The horizontal dotted, dot-dashed and long dashed lines show the 68.3 % (i.e.,1$\sigma$), 90 % ($\approx$1.64$\sigma$) and 95 % ($\approx$2$\sigma$) confidence levels, respectively, calculated using Monte-Carlo simulations with 5000 permutations.

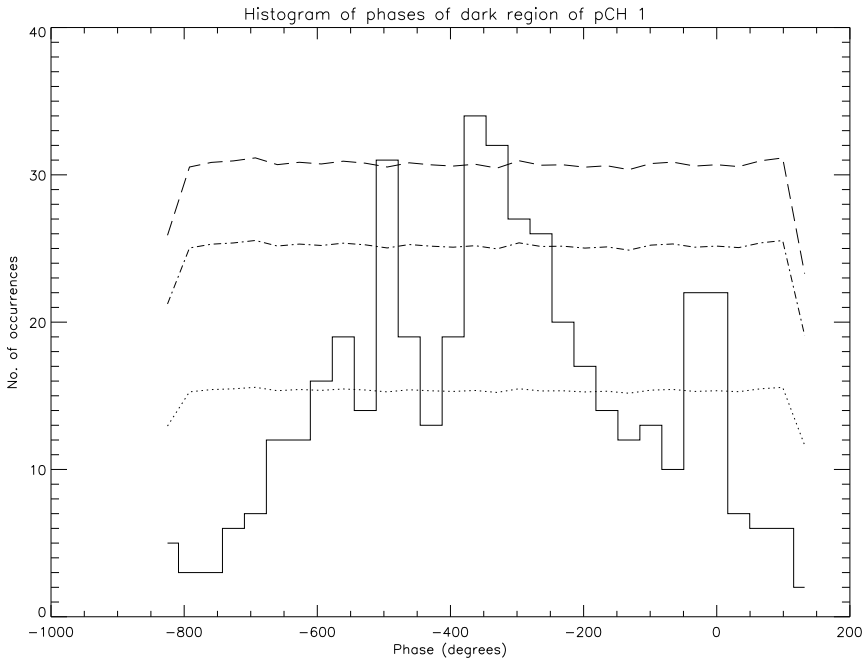


Figure 4.11: Histogram showing the distribution of phase delay measurements as a function of frequency for the dark locations of pCH 1 for the upwardly propagating waves. Description about the panel is same as in Figure 4.10.

Following the techniques outlined in O'Shea et al. (2006), we show in Figure 4.8, the combined phase delay results for bright and dark regions. The phase here is calculated for the line pair N IV 765–Ne VIII 770 in intensity and in relative velocity. If the oscillations are due to magneto-acoustic waves, it is to be expected that wave signatures will be present in both intensity and velocity. For this reason, the calculated phases for both of these quantities are plotted together, which also helps to improve the statistics. The phases from radiant flux oscillations are shown as the grey circle symbols, while those from LOS velocities are shown as the black circle symbols. We should point out here that we have approximately 50 network and 50 internetwork pixels after binning. Each panel of Figure 4.8 has about 450 phases points, including intensity and velocity phase points. On average, for each pixel position (along the slit) we have about 9 phase points, that have a significance of 95.4 % and above, with more velocity points as compared to intensity points. We can see immediately that the phases in Figure 4.8 are distributed between $-180^{\circ}$ and $180^{\circ}$. If there are fixed time delays present between the oscillations in the different lines, as in

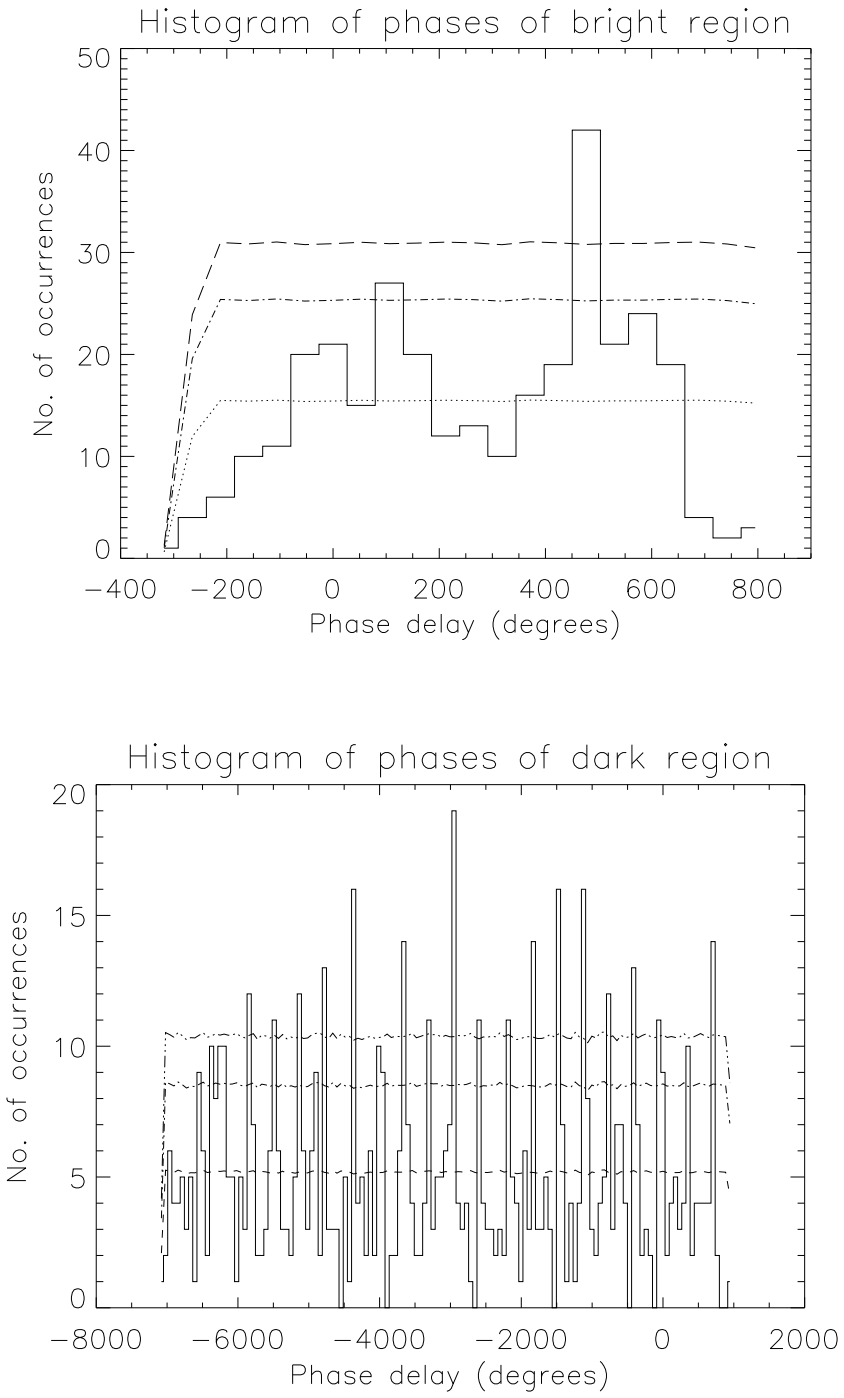


Figure 4.12: Histogram showing the distribution of phase delay measurements as a function of frequency for the bright (top panel) and dark (bottom panel) locations for pCH 2. Description about different panels is same as in Figure 4.10.

O'Shea et al. (2006), then we might expect the phases to line up along inclined parallel lines as predicted by the phase equation (Equation 4.1). We briefly summarise the method followed here. In the phase plot (Figure 4.8), we first identify the location where the strong clustering of phase points forming the straight line takes place e.g., a clear line of points between 7 and 8 mHz in the left panel of Figure 4.8. This line need not pass through the origin i.e. point where the phase equals zero for $f = 0$ as done in the previous studies (O'Shea et al., 2006, 2007). We note, however, that the first line does pass through this point, as expected. For the plot in the right-hand panel, showing mostly downward propagating waves, the first line does not pass through the $f = 0$ point. If we imagine, however, a further line to the left of the first line, with the same spacing in $f$, then this would likely pass through the zero point, assuming that the errors in the phases are ≈50°–60°. After identifying the location, a straight line (between 7–8 mHz in the left-hand plot) is fitted to these phase points. After fitting this line, all the phase points are shifted by a fixed amount which is determined from the slope of the fitted line, resulting in a transform which make the lines horizontal. Finally histograms are produced with these results (Figure 4.10). Numerous peaks are present in the histogram. Now to check if these peaks are statistically significant or just due to a random distribution, we applied the Monte-Carlo technique, where the phase data were randomised 5000 times, to give estimates of the 'noise' ($1\sigma$) level in the histogram. We have then calculated the 90 % and 95.4 % significance levels. So in the histogram, peaks above the 95.4 % level are statistically more significant. Furthermore, each of these peak indicates the presence of a straight line at that position. Hence, other parallel straight lines are drawn in the phase plot in Figure 4.8 by using these positions. Thus, by fitting lines to the phase measurements in the phase plots, we estimate the slopes and therefore the time delays between the line pair for the bright and dark regions. Looking at the top panel of Figure 4.8 first, for the bright (network) locations, it is clear that parallel lines are present in the data. These lines of phase are more obvious in the measurements made from the velocity oscillations. The implications of this result will be dealt with in the conclusion section. The slope of these lines gives a time delay of $-717 \pm 114$ s.

It is noticeable that these histogram peaks are constantly spaced at ≈400°. As the errors in

the phases shown in Figure 4.8 are of the order of $\approx \pm 55°$, it is likely that what we see here is really just the expected variation of phases over 360° for upwardly propagating waves. The consistent variation of ≈400° suggests, as in O'Shea et al. (2006, 2007), that we may also be seeing a signature of cavity resonance. The result can indeed be interpreted as:

$$\Delta\phi = 2\pi(f \pm n\Delta f)T \tag{4.2}$$

where $n$ is the order of the frequency shift, i.e., 0,1,2, etc., and $\Delta f$ is $f/9$ for the results found here. For example, for the time delay of -717 s (equivalent to a $f$ of 1.39 mHz), this shift, $\Delta f$, of $f/9$ would give an exact phase spacing of 400°.

In the dark locations ('internetwork') (bottom panel of Figure 4.8), we find two sets of parallel straight lines with opposite slope. The presence of parallel lines with opposite slope indicates the presence of both upward and downward propagating waves. This is the first time, to our knowledge, that this has been reported in the literature. The measured time delays in this location are 778 ± 133 s (downwardly propagating), with the lines sloping towards the right, and $-216 \pm 37.8$ s (upwardly propagating), with the lines sloping towards the left. In bottom panel of Figure 4.10, we plot the histograms corresponding to the downwardly propagating waves. Notice that in the bottom panel of Figure 4.10 the histogram peaks are all above the 95 % significance level, indicating that it is very unlikely that the lines of phase are due to noise. Notice also that the spacing of the histogram peaks is not constant, but varies between ≈300°–340°. We suggest that this is the expected 360° phase difference for unimpeded downwardly propagating waves, modified by the errors of $\approx \pm 55°$ in the phase measurements. In Figure 4.11, for the upwardly propagating waves, there are only two significant peaks, corresponding to the two phase lines in Figure 4.10. These peaks, however, are only separated by ≈140°, again suggesting the presence of some form of resonance. In this case, and in reference to Equation 4.2, a $\Delta f$ of $7f/18$ would give the required phase difference of ≈140°.

For the bright locations of pCH 2 (top panel of Figure 4.9), the measured time delay between

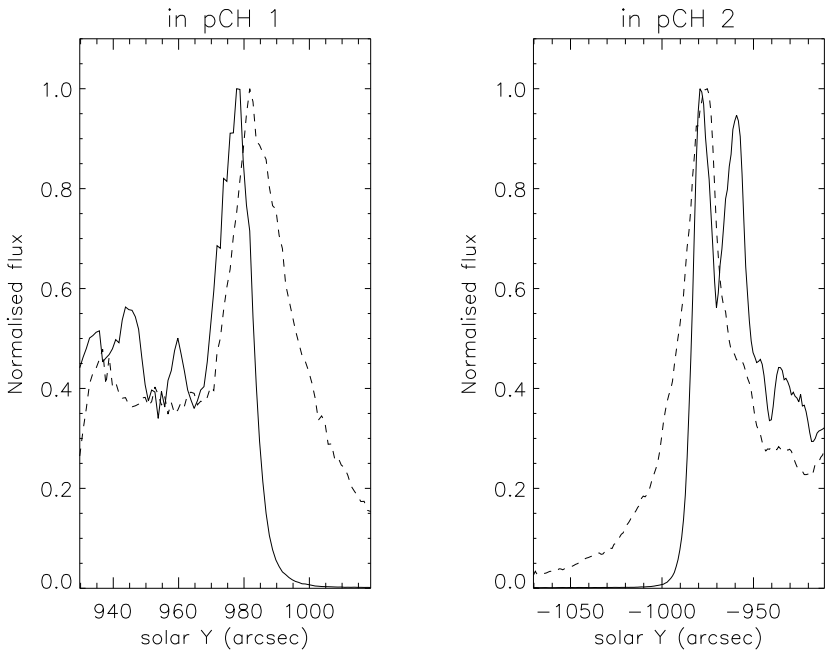


Figure 4.13: Normalised flux distribution with height for pCH 1 (left panel) and pCH 2 (right panel). The solid line shows the distribution for N IV 765 Å, while the dashed line shows the distribution for Ne VIII 770 Å. The location of maximum brightness for each line is used for determining the height difference.

the two lines is $-278 \pm 32.1$ s. Examining the histogram of these phases in Figure 4.12 (top panel), we find that there is only one peak above the significance level of 95 %, with another just above the 90 % level. The difference between these peaks is $\approx 400^\circ$ and, in reference to Figure 4.10, this may again indicate a resonance with a $\Delta f$ of $f/9$.

In the dark locations of pCH 2 (bottom panel of Figure 4.9), we measured a time delay of $-2607 \pm 491.0$ s, indicating upwardly propagating waves. Notice the many closely spaced, steeply sloped, parallel phase lines that correspond to this long time delay. In bottom panel of Figure 4.12 these many parallel phase lines correspond to many significant peaks above 95 % significance in the histogram. Here, the peaks are equally spaced at the phase difference of $360^\circ$ that would be expected for unimpeded propagating waves.

The measured time delays from the different pCHs may be used to estimate propagation

speeds for the waves assumed to be causing the oscillations. In order to calculate the propagation speeds, one needs information on the height difference in the atmosphere between the different lines in the line pair. As described in O'Shea et al. (2006), we studied for both the pCHs, the variation of the summed flux over time along the slit position near the limb (see Figure 4.13). The flux for both lines has been normalised in order to plot them together. Noting the peak intensity location we have estimated the difference in their formation heights. Note that, for the N IV line of pCH 2, we have estimated the average formation height, using a weighted average between the two peaks based on their respective values of flux. So using this height difference and the measured time delays, we show in Table 4.3 the resulting calculated propagation speeds.

Table 4.3: Propagation speeds measured in the polar coronal holes.

| pCH | Height Diff. (km) | Delay time (s) | | Wave speed (km $s^{-1}$) | |
|---|---|---|---|---|---|
| | | Bright location | Dark location | Bright location | Dark location |
| 1 | 2860 | $-717.0 \pm 114.1$ | $778.0 \pm 133.5$<br>$-216.4 \pm 37.80$ | $-3.989 \pm 0.6348$ | $3.676 \pm 0.5365$<br>$-13.22 \pm 2.309$ |
| 2 | 4095 | $-278.4 \pm 32.07$ | $-2607 \pm 491.2$ | $-14.71 \pm 1.695$ | $-1.570 \pm 0.2959$ |

The sound speed in the solar atmosphere can be expressed as function of temperature alone (Priest, 1984) by the equation:

$$C_S = 152\, T^{1/2} \quad m\, s^{-1} \tag{4.3}$$

where $T$ is the temperature in K. From this, and using the formation temperature of the lines, we can estimate the sound speeds to be 48 km $s^{-1}$ at the temperature of N IV 765 Å ($T \approx 1 \times 10^5$) and 120 km $s^{-1}$ at the temperature of Ne VIII 770 Å ($T \approx 6.3 \times 10^5$). It can be clearly seen, therefore, that the speeds we measured for different locations in the coronal holes are subsonic.

## 4.4 Conclusions

Using the spectral diagnostic capabilities of the SUMER spectrograph, and with a rigorous statistical approach, we have found evidence for propagating magneto-acoustic waves in polar coronal

hole regions. For a typical bright enhanced network location the dominant period is ≈18 min and 25 min. Phase measurements were carried out over the full range of frequencies measurable in our data, not just at the dominant period. From these phase measurements, we find evidence that the waves producing the oscillation signatures propagate both upwards and downwards. This is the first time, to our knowledge, that this has been reported in the literature. The dark ('internetwork') areas in pCH 1 show evidence of both upward and downward propagating waves, while bright ('network') areas, by comparison, show only upwardly propagating waves. This may indicate different physical processes occurring in the 'internetwork' and 'network' regions. From a study of the height variations of the sizes of chromospheric and transition-region features in a small coronal hole and the adjacent quiet Sun, Tian et al. (2008) concluded that loops are much lower in the coronal hole than in the quiet Sun region. From a study of the height variation of the Half-Width at Half-Maxima of $|B_z/B|$, they further suggested that an open magnetic structure expands through the upper transition region and lower corona more strongly in coronal holes than in the quiet Sun. We may conjecture that the internetwork regions within coronal holes are composed of low-lying coronal loops, where waves can travel both upwardly and downwardly, whereas the network regions are filled with more open, funnel like structures where only upward propagation is possible. Recently, Gömöry et al. (2006) reported detection of compressive waves that propagate downward from transition region to the chromosphere in a particular chromospheric network in a quite Sun region. They propose a coronal source of these compressive waves resulting from a nano-flare scenario. In our case clearly we see presence of downward propagation only for internetwork location. One can conjecture that the magnetic topology in quiet Sun could be slightly different than in the coronal holes, with presence of more low-lying loop systems in the internetwork regions of coronal loops.

Plotting the phases as histograms, we saw a possible cavity resonance effect on the waves, e.g., $\Delta f$s of $f/9$, inferred in reference to Equation 4.2, as well as the expected unimpeded propagation of the waves, e.g., a measured phase difference of 360° between the different parallel lines of phases. We note that the speeds we derived (cf. Table 4.3) are lower than those found by O'Shea et al. (2007) in polar coronal holes on-disk, and much lower than those found by O'Shea

et al. (2006) off-limb. However, the wave speeds measured by O'Shea et al. (2007) were for lines with high formation temperature and, hence, higher up in the atmosphere as compared to our lines. We hypothesise that at lower heights the waves have lower speeds, but the speeds will increase with height in the solar atmosphere. We found the propagation speeds to be consistent with slow magneto-acoustic waves. We should also point out that statistically we find more velocity oscillations than intensity oscillations in this study. For compressional types of waves, we should have signatures in both. So if there are only velocity oscillations present in some locations this implies the presence of transverse-type waves, like Alfvénic. Recent studies from Hinode by De Pontieu et al. (2007b) suggest that the chromosphere is permeated by Alfvén waves with strong amplitudes of the order of 10 km $s^{-1}$ to 25 km $s^{-1}$ and periods of 100 s to 500 s. Tsuneta et al. (2008a) have further conjectured that the vertical flux tubes originating from the kG patches in coronal holes will fan out in the lower atmosphere of the coronal holes and will serve as efficient chimney for the propagation of Alfvén waves. These waves may carry enough energy flux for the acceleration of the solar wind. So, it is quite possible that some of these Alfvénic waves have also been detected in our statistical analysis as we see more velocity points as compared to intensity points in the phase plots.

Hence, from this study, it can be inferred that in coronal holes, the internetwork regions are composed of low-lying coronal loops, where waves can travel both upwardly and downwardly, whereas the network regions are filled with more open, funnel like structures where only upward propagation is possible (Gupta et al., 2009). These upward propagation of waves from bright region, carries energy from lower layer to upper layers of solar atmosphere in the form of magneto-acoustic and Alfvén waves which are important for the coronal heating and the acceleration of fast solar wind. This also suggests that the on-disk bright regions may be the preferred source channel for the acceleration of solar wind which originates from the same regions as suggested by Tu et al. (2005). However, in this case, the detected waves are rather slow and may not carry enough energy flux for the acceleration of the solar wind (Gupta et al., 2010b).

# Chapter 5

# Propagating Waves in Polar Coronal Holes

## 5.1 Context

Coronal holes are regions of cool and low density plasma that, as such, are 'dark' at coronal temperatures (Munro and Withbroe, 1972). During solar minima, coronal holes are generally confined to Sun's polar regions, while at solar maxima they can also be found at lower latitudes, usually associated with remnant active regions, as so-called 'equatorial' coronal holes. The predominantly unipolar magnetic field from coronal hole regions is thought to give rise to the fast solar wind (e.g., Krieger et al., 1973). During solar minimum, Ulysses observations clearly show that the solar wind exhibits two modes of outflow: the fast wind, associated with polar coronal holes, with outflow speeds of $\approx$ 800 km s$^{-1}$ and the slow wind with outflow speeds of $\approx$ 400 km s$^{-1}$ associated with equatorial regions (Woch et al., 1997; McComas et al., 2000). However, during solar maxima, low latitude coronal holes also show faster than average solar wind speed up to $\approx$ 600 km s$^{-1}$ (Zhang et al., 2003). Extreme-ultraviolet (EUV) images of polar coronal holes reveal the presence of diffuse, spike-like, or sheet-like structures called plumes (Bohlin et al., 1975; Ahmad and Withbroe, 1977), which subtend an angle of roughly 2° relative to the Sun centre at low altitude and expand super-radially with the coronal hole (DeForest et al., 1997, see Figure 5.1). Regions between these structures are termed as inter-plumes. From

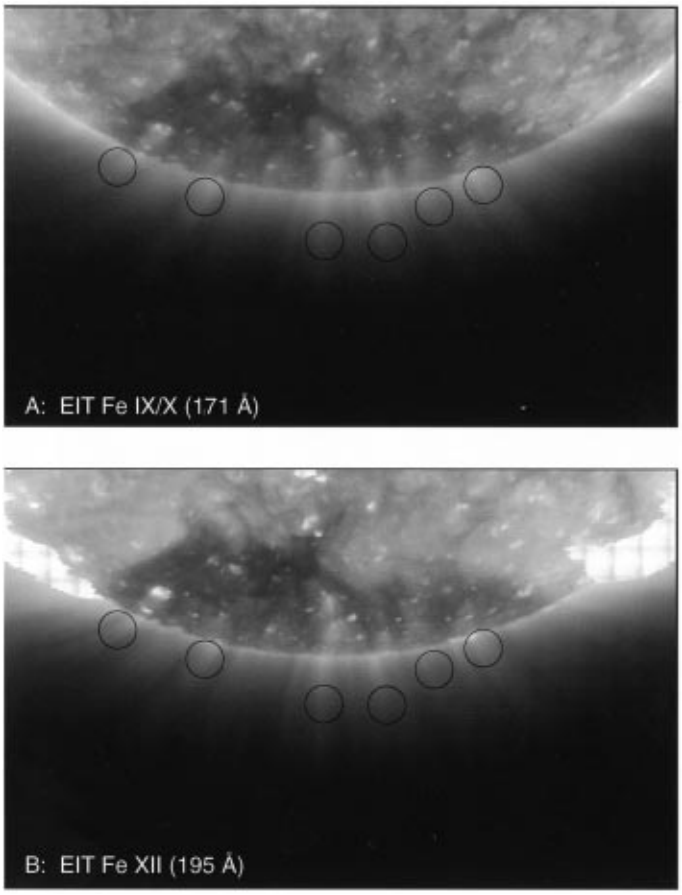


Figure 5.1: Images taken on May 8, 1996, by the Extreme-ultraviolet Imaging Telescope (EIT) on-board SOHO show ultraviolet images of polar plumes near the south solar pole at about 1 MK in the Fe IX/X 171 Å passband (top) and at about 1.6 MK in the Fe XII 195 Å passband (bottom). *Credit:* DeForest et al. (1997).

vacuum ultraviolet (VUV) spectroscopy, plumes are known to be denser and cooler than the surrounding inter-plume regions (e.g., Wilhelm, 2006), while spectral lines are observed to be broader in inter-plumes (i.e., Banerjee et al., 2000b; Giordano et al., 2000; Teriaca et al., 2003). However, differences in mass, momentum, and energy flux in plumes and inter-plumes are still not known precisely.

There are several theoretical models which describe the role of magneto-hydrodynamic (MHD) waves in the acceleration of the fast solar wind in coronal holes (see review by Ofman, 2005; Cranmer, 2009, and references therein) and inter-plumes are often believed to be the primary

site for this acceleration. It is further conjectured that these waves originate from the on-disk bright network regions (Wang et al., 1997; Patsourakos and Vial, 2000; Giordano et al., 2000; Banerjee et al., 2001b). A number of studies (Ofman et al., 1997, 2000; Banerjee et al., 2001b; Popescu et al., 2005) have reported the detection of oscillations in the off-limb regions of polar coronal holes. All these studies point to the presence of compressional waves, thought to be slow magneto-acoustic waves (DeForest and Gurman, 1998; O'Shea et al., 2006, 2007). On the other hand, possible evidence for Alfvén waves propagating into the corona had been reported by Banerjee et al. (1998, 2009a); Dolla and Solomon (2008) and Landi and Cranmer (2009) by studying the line width variations with height in polar coronal holes. Recent reports of detections of low-frequency ($< 5$ mHz), propagating transverse motions in the solar corona (Tomczyk et al., 2007, from coronagraphic observation) and chromosphere (De Pontieu et al., 2007b) and their relationship with chromospheric spicules observed at the solar limb (De Pontieu et al., 2007a) with the Solar Optical Telescope on-board Hinode (Kosugi et al., 2007) have widened interest in the subject. Recently, Jess et al. (2009) have reported the detection of torsional Alfvénic motions associated with a large on-disk bright-point group. These waves are believed to be a promising candidate for the heating of the corona and the acceleration of the solar wind (Belcher, 1971; Suzuki and Inutsuka, 2005).

Furthermore, it has been suggested that the fast solar wind streams originate from coronal hole funnels and are launched by reconnection at network boundaries (Tu et al., 2005). Measurements of the outflow speed in the extended corona have been obtained with the Ultraviolet Coronagraph Spectrometer (UVCS) on-board SOHO (e.g., Antonucci et al., 2000; Teriaca et al., 2003; Antonucci et al., 2004; Telloni et al., 2007). Some of these studies concluded that plumes have lower outflow speeds than inter-plume regions (Noci et al., 1997; Giordano et al., 2000; Wilhelm et al., 2000; Patsourakos and Vial, 2000; Teriaca et al., 2003; Raouafi et al., 2007) and, hence, may not contribute significantly to the fast solar wind, whereas some other theoretical and observational studies find higher outflow speeds in plumes than in inter-plume regions for at least some altitudes above the photosphere (Casalbuoni et al., 1999; Gabriel et al., 2003, 2005). These contradictory reports led to the debate on whether plumes or inter-plumes are the preferred

source regions for the acceleration of the fast solar wind. This topic is highly debated and still open for further confirmation.

In this chapter, we combine the capabilities of SUMER/SOHO (Wilhelm et al., 1995) and EIS/Hinode (Culhane et al., 2007) to observe the on-disk, limb, and far off-limb regions of the coronal hole to search for the origin of waves close to the Sun and study their propagating nature in plume and inter-plume regions[1].

## 5.2 Observations

### 5.2.1 Data

The data analysed here were obtained in two cycles during a Hinode/SUMER joint observing campaign as part of the Hinode Observing Program (HOP) 45/Joint Observing Program (JOP) 196. The first cycle was run during $8^{th}$ and $15^{th}$ April 2007 whereas second cycle was run during the $13^{th}$ November 2007. The data consist of time series taken by SUMER and EIS in the polar coronal holes.

- **Description of April 2007 data:**

  For SUMER, the $1'' \times 120''$ slit was centred on the limb and spectral profiles of the Ne VIII 770 Å were acquired from 19:13 to 20:47 UTC on $8^{th}$ and from 10:44 to 14:45 UTC on $15^{th}$ April 2007, with a cadence of 18.12 s. For EIS, the $40''$ wide slot was used to obtain $40'' \times 160''$ images in several spectral lines over the time interval 18:42 to 20:58 UTC on $8^{th}$ and 10:54 to 15:57 UTC on $15^{th}$ April 2007. The EIS data consist of a series of elementary rasters each formed by two slot images displaced by $20''$ in the $X$ direction to maximise the chances of overlapping with the other instruments. Each slot image was exposed for about

[1]Results discussed in this chapter are published in Banerjee et al. (2009b) and Gupta et al. (2010a).

7.5 s. As a result, for each dataset, we have two time series with a cadence of 19.3 s that we identify hereafter with $slot_0$ (East) and $slot_1$ (West). Before the start of the temporal series, raster images were obtained with SUMER and EIS to allow the co-alignment of the different instruments.

- **Description of November 2007 data:**

  For SUMER, the $1'' \times 120''$ slit was centred on the limb and spectral profiles of the Ne VIII 770 Å, O IV 790 Å, and S V 786 Å were acquired from 19:13 to 22:15 UTC with an average cadence of 18.12 s in sit–and–stare mode. The exposure time was 18 s and a total of 600 time frames were obtained during the observation. For EIS, the $40''$ wide slot was used to obtain $40'' \times 512''$ images in several spectral lines in the wavelength ranges of 170–210 Å and 250–290 Å with spatial resolution of $1''$ pixel$^{-1}$ over the time interval from 18:20 to 23:50 UT. The exposure time was 45 s with an effective cadence of $\approx$ 47 s. A total of 420 time frames were obtained during the observation. Before the start of the temporal series, raster images were obtained with SUMER and EIS in order to co-align and to provide context.

During the November observation, the EIS slot covered the quiet Sun south of the coronal hole as well as the on-disk and off-limb parts of the hole (see Figure 5.3). Table 5.1 lists the emission lines included in this study from EIS and SUMER, their formation temperature, and the location where the radiance maximum is observed. The top left panel of Figure 5.3 shows the location of the different slits on an EIT image taken in the Fe XII 195 Å passband. The rectangular box marks the location of the EIS slot while the dashed line gives the location of the SUMER slit. The radiance variation along the solar-$X$ at solar-$Y \approx 1000''$ is over-plotted as a white line in arbitrary units and allows us to identify the locations of plume and inter-plume regions within our field of view revealing that the SUMER slit is pointed within an inter-plume region while the EIS slot covers both plume and inter-plume regions. The bottom left panel shows the context raster obtained by EIS in Fe XII 195 Å line, whereas the right panels show the context rasters in O IV 790 Å (top) and Ne VIII 770 Å (bottom) spectral lines as obtained

by SUMER. Figure 5.4 corresponds to the images obtained by EUVI/STEREO (Howard et al., 2008) for the same region. The angular separation between the two spacecraft, about 40°, allows an estimate of the orientation of the plume.

Table 5.1: Emission lines observed with EIS and SUMER and position of the respective limb brightening.

| Ion | Wavelength (Å) | log $T_{max}$ (K) | Limb Brightening |
|---|---|---|---|
| He II | 256.32 | 4.9 | 985″ |
| S V | 786.47 | 5.2 | 988″ |
| O IV | 790.19 | 5.2 | 989″ |
| Mg VI | 270.39 | 5.6 | 990″ |
| Fe VIII | 185.21 | 5.6 | 990″ |
| Mg VII | 278.40 | 5.8 | 991″ |
| Si VII | 275.35 | 5.8 | 993″ |
| Ne VIII | 770.42 | 5.8 | 993″ |
| Fe X | 190.04 | 6.0 | 993″ |
| Fe XI | 188.23 | 6.1 | – |
| Fe XII | 195.12 | 6.1 | 992″ |

### 5.2.2 Data Reduction and Alignment

All data have been reduced and calibrated with the standard procedures given in the SolarSoft (SSW)[2] library. SUMER data were first decompressed, corrected for response inhomogeneities (flat field), dead-time, local-gain, and for geometrical distortion (de-stretch), using the most recent standard routines (see Wilhelm et al., 1997; Teriaca et al., 1999) as described in Section 2.5.1. After these steps, data still showed a residual pattern from the micro-channel plate structure that was removed using a correction matrix obtained by first averaging all spectral images and then applying a low–pass filter to the average. Single Gaussian fitting was used to retrieve the line amplitude, position, and line widths of the SUMER spectral lines. Before fitting, a running average over 3 pixel along the slit and over three consecutive spectra was applied to improve the signal to noise ratio of the SUMER data. Line positions from the fitting are then converted into Doppler shifts by taking as reference the average over the disk part of the

[2] http://sohowww.nascom.nasa.gov/solarsoft/

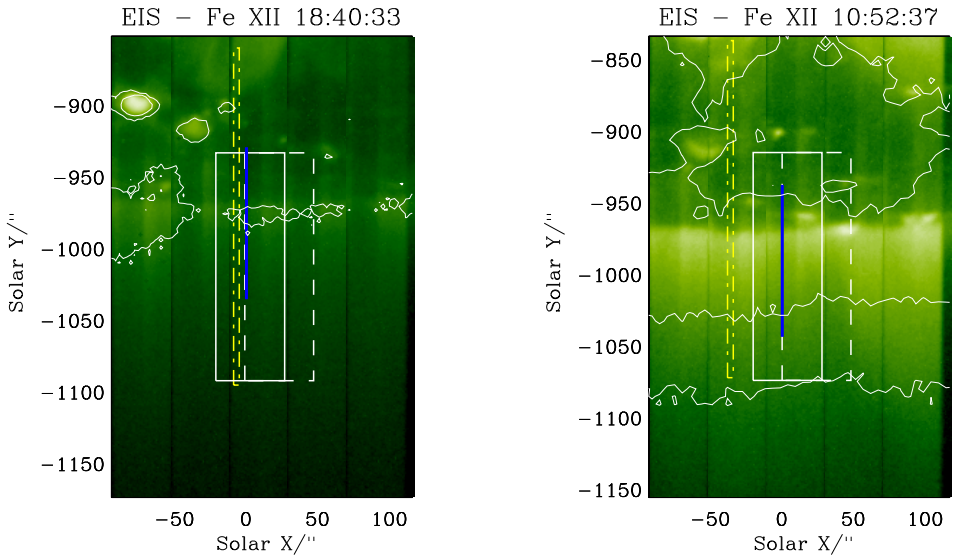


Figure 5.2: Left (right) panel shows the location of different slits and slots on the Fe XII 195 Å EIS context raster on $8^{th}$ April ($15^{th}$ April). The context rasters are made of five adjacent slot images, covering a $200'' \times 320''$ area. In both panels, radiance iso-contours (white) are from EIT Fe XII 195 Å images. The two white rectangular boxes are the location of the EIS slots (solid $\text{slot}_0$, dashed $\text{slot}_1$). The solid vertical blue line represents the location of the SUMER 1″ wide slit whereas the yellow dash-dot elongated box gives the location of the 4″ wide CDS slit.

image. The observed line widths are corrected for the instrumental profile by applying a deconvolution function taking into account the order of diffraction and the slit width used during the observations (SolarSoft routine *con_width_funct_4.pro*). The raw EIS data were processed by the standard SolarSoft programme *eis_prep.pro*, which helps in removing detector bias and dark current, hot pixels and cosmic rays and returns absolutely calibrated data. The movement of the slot image on the detector due to thermal variations along the orbit was corrected. The displacement in the dispersion (solar-$X$) direction was obtained by measuring the position of the edge of the Fe XII 195 Å slot image over time. The displacement in the $Y$ direction is taken equal to 2.5 times that in the $X$ direction. The validity of the latter assumption was verified by checking the limb $Y$ position versus time. Finally, EIS data were corrected for the spacecraft jitter by using housekeeping data. Figure 5.5 shows the variation of the radiance along a vertical

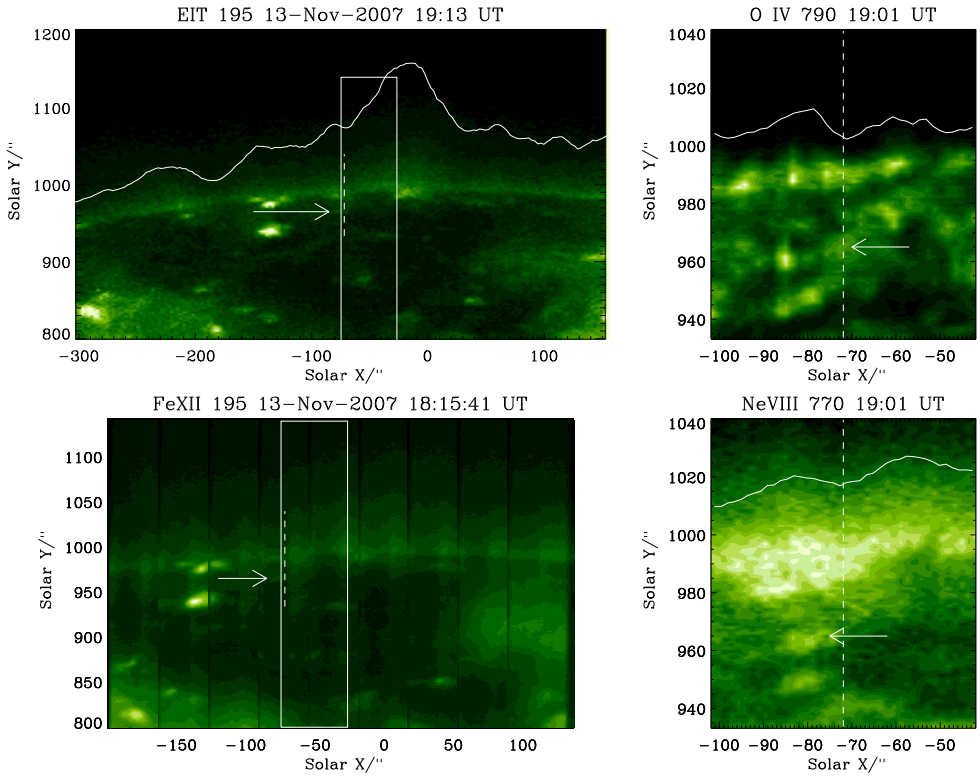


Figure 5.3: Top left: location of the different slits are over-plotted on the EIT/SOHO image taken on 13$^{th}$ November 2007 in the passband dominated by the Fe XII 195 Å line. The rectangular box marks the location of the EIS slot, while the dashed line gives the location of the SUMER slit. The EIT radiance variation along the solar-$X$ is over-plotted as a white line in arbitrary units at fixed solar-$Y \approx 1000''$. This variation along the solar-$X$ allows us to identify the location of plume and inter-plume regions. Bottom left: EIS context raster taken in the same Fe XII line shows the location of both the EIS slot (rectangular box) and the SUMER slit (dashed line) during the sit–and–stare sequence. Right: SUMER context rasters taken in the O IV (top) and Ne VIII (bottom) spectral lines. The continuous line gives the radiance variation along the solar-$X$ in an arbitrary unit. In all panels, the arrow indicates the location of the bright region from where waves are presumably originating.

strip (about 100 pixel long, centred over the limb) at the overlap position of the EIS slot with the SUMER slit as a function of time ($x$–$t$ slice). The $x$–$t$ slices are for data without any correction (top panel), with the orbital effects corrected (middle), and with correction for both orbital and jitter effects (bottom). Data are also affected by passage of the spacecraft through South Atlantic Anomaly (SAA). The regions of affected data appear around 20:35 and 22:15 UTC and, less clearly visible, around 18:55 UTC. These affected portions are replaced by linear interpolation.

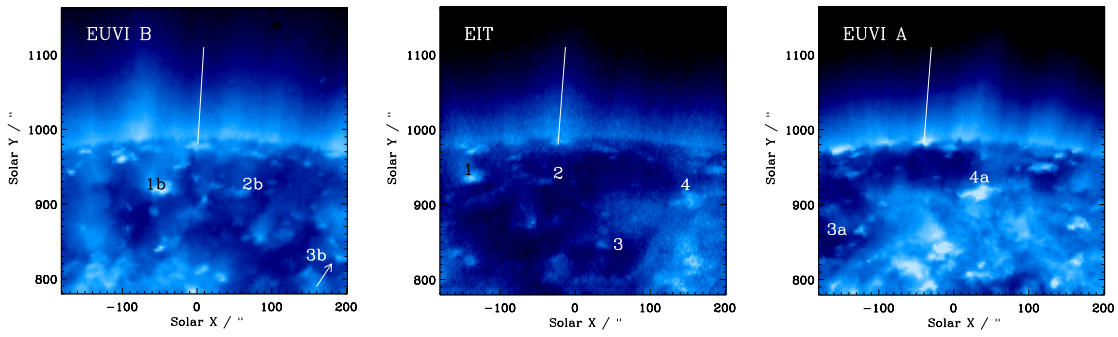


Figure 5.4: EUVI/STEREO and EIT/SOHO images in the 171 Å passband taken around 19:00 UT on $13^{th}$ November 2007. The solid line shows the plume axis as obtained by fitting the positions of the radiance maxima of horizontal cuts on the EIT image. Separation between the two STEREO spacecraft was 40° (20° with Earth/SOHO). The different angular scale (km arcsec$^{-1}$) was taken into consideration. Numbers from 1 to 4 on the EIT image identify reference elements that can be recognized on the EUVI-B image (suffix b) and/or on the EUVI-A image (suffix a).

It should be finally noticed that for wavelet analysis, EIS data have been binned over 5 and 9 pixel in the $X$ and $Y$ directions, respectively. This will further smooth out any residual jitter or orbital variation. The data from the short wavelength detector were shifted in the $Y$ direction to compensate the wavelength dependent offset between the short and long wavelength detectors (Kamio & Hara, private communication). To align the different instruments, the SUMER context raster has been chosen as reference. Hence, the EIS context raster has been cross-correlated with the SUMER raster and an offset of $9''$ in the east–west direction (solar-$X$), and $-24''$ in the north–south direction (solar-$Y$) was found and corrected for November dataset. We estimate the alignment to be accurate within $2''$. After the alignment, the pointing of the different instruments are plotted in Figure 5.2 & 5.3. We have plotted the variation of radiance along the solar-$Y$ at the overlap region of the SUMER slit and EIS slot at solar-$X \approx -72''$ (see Figure 5.6). This allows us to identify the location of the limb brightening in various spectral lines and their radiance fall-off in the off-limb region. We set the limb position at solar-$Y \approx 985''$, as identified from the limb brightening of He II in Figure 5.6. The radiance peaks of the He II line for the disk part of the coronal hole are used to identify bright locations (presumably the foot-point of the coronal

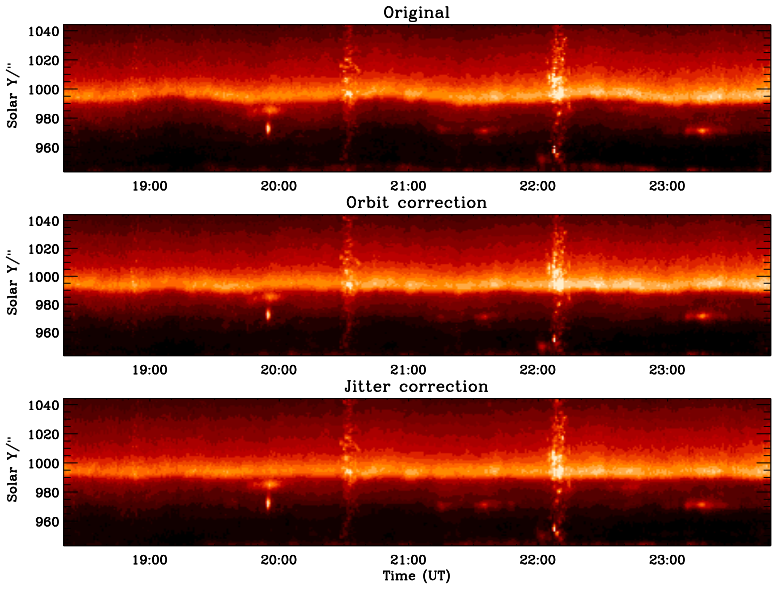


Figure 5.5: Variation of radiance over time along the slice of corona recorded by both SUMER and EIS on $13^{th}$ November 2007. The top panel shows the distance–time map of the Fe XII line as recorded by EIS. Here the limb clearly shows the effect due to orbital variation and instrumental jitter. The middle panel shows the distance–time map after orbit correction and the bottom panel shows the map after orbit and jitter correction applied, showing the limb position to be much more stable in solar-$Y$ as compared to the uncorrected data. In the panels, two visible vertical stripes around 20:35 and 22:15 UTC are damaged data, probably due to SAA transits (another, less visible stripe is present around 18:55 UTC).

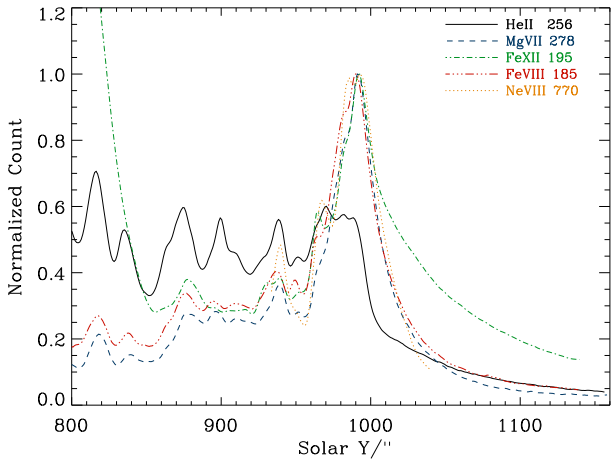


Figure 5.6: Time-averaged radiance variations along the SUMER slit and EIS slot (solar-$Y$) at solar-$X \approx -72''$ for different lines as labelled.

funnels).

## 5.3 Results from April 2007 Dataset

In this section we will present detailed analysis of the sit-and-stare observation as recorded by EIS and SUMER. From the context images, Figure 5.2 and 5.3, it is clear that the SUMER slit is pointing likely to a plume region during the April 2007 observation, whereas during the November 2007 SUMER slit is pointing to an inter-plume region and the EIS slot covers both plume and inter-plume region, overlapping with the SUMER slit.

### 5.3.1 Radiance *x–t* Slices

Maps of the radiance along the slit versus time (*x–t* slices) were first built using the SUMER Ne VIII integrated line radiances and EIS Fe XII radiances averaged over 5″ in the *X* direction at the position overlapping the SUMER slit. The resulting maps were then contrast enhanced and low-pass filtered to produce the maps shown in Figures 5.7 and 5.8 for the $8^{th}$ and $15^{th}$ April datasets, respectively. EIS radiance maps were normalised by dividing by the average along the *Y* direction (to remove the strong limb signature), the result elevated to the power of 3 (to increase the contrast between high/low radiance regions), and, finally, low-pass filtered. SUMER enhanced radiance maps were obtained as the median over 3×3 pixels of the quantity $exp(a+0.15\times b)^2$ where $b$ is the original image, and a is a highly smoothed version of the original image obtained by convolving with an isotropic kernel. The difference in the treatment of the data from the two instruments depends on the different noise level and image scale. In Figure 5.7, we note that the EIS time series starts at a later time (denoted by a dashed vertical line in the top panel of the figure). On *x–t* slices, the presence of alternate bright and dark regions indicates the presence of oscillations. Moreover, diagonal radiance enhancements (marked by dotted yellow lines and dashed blue lines in Figures 5.7 and 5.8) are a signature of propagating disturbances.

Thus, from such maps, it is possible to estimate periods and projected propagation speeds.

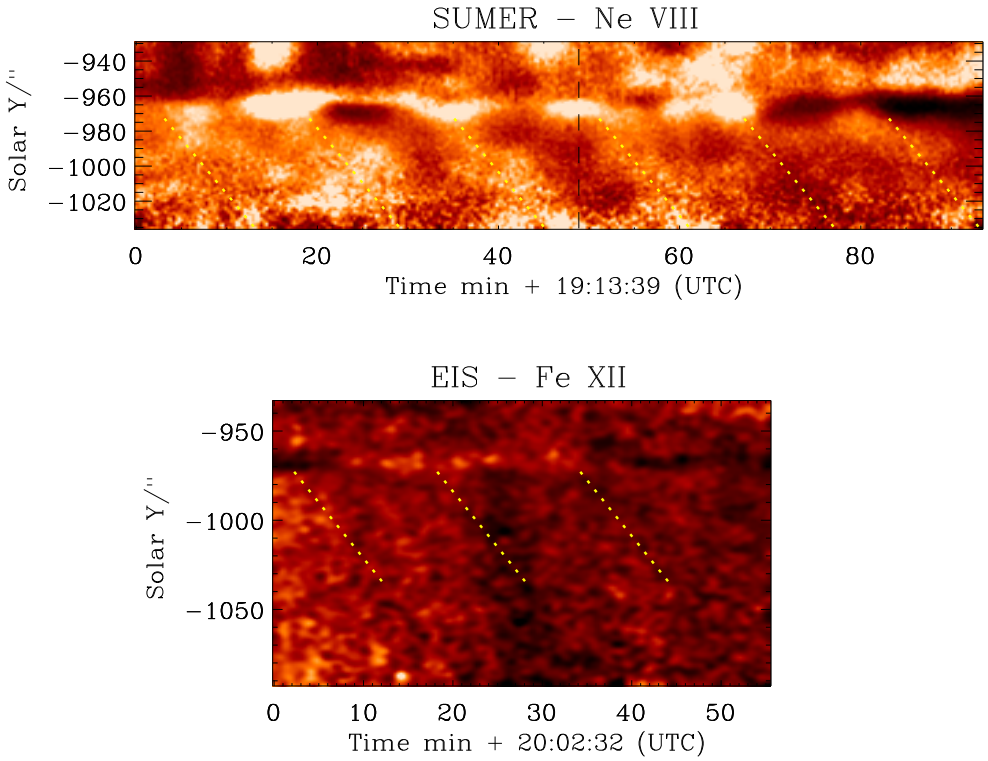


Figure 5.7: Enhanced (see text) maps of radiance variation along the slit (solar-$Y$ direction) with time for Ne VIII 770 Å as recorded by SUMER (top panel) and Fe XII 195 Å as recorded by EIS (bottom panel) on $8^{th}$ April 2007. The vertical black dashed line on the SUMER enhanced radiance map depicts the starting point of the EIS time series (shown in the bottom panel). The slanted dotted yellow lines correspond to disturbances propagating with a speed of 75 km $s^{-1}$ and a period of about 15 min, as determined from the SUMER data.

From the SUMER data on both dates we measure a propagation speed of ≈75 km $s^{-1}$ and a periodicity of about 15 min. The propagation fronts are much more visible on the $8^{th}$ April data (see top panel of Figure 5.7) but are also visible on the $15^{th}$ April data. In the case of the EIS data, no definitive conclusions can be drawn from the $8^{th}$ April data (see bottom panel of Figure 5.7), while propagating fronts are clearly visible in the $15^{th}$ April data (see bottom panel of Figure 5.8). However, both the propagation speeds and the periodicity are higher than for the SUMER data, with values of ≈125 km $s^{-1}$ and 30 min, respectively (see the dashed blue lines in the bottom panel of Figure 5.8). The observed propagation speeds are actually a lower limit as

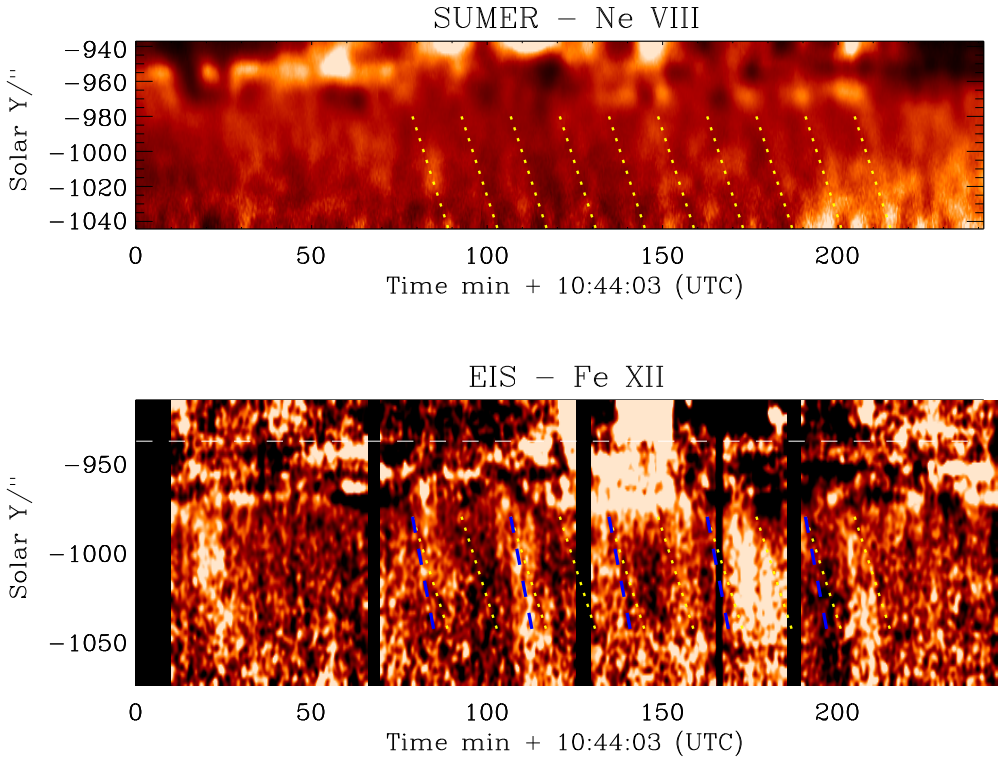


Figure 5.8: Enhanced radiance maps as in Figure 5.7, but for the $15^{th}$ April data. Black vertical stripes correspond to data gaps in the EIS time series. The horizontal white dashed line on the EIS enhanced radiance map depicts the upper edge of the SUMER FOV. The slanted dotted yellow lines correspond to disturbances propagating with a speed of 75 km $s^{-1}$ and a period of about 15 min as determined from the SUMER data. The slanted dashed blue lines on the EIS map correspond to disturbances propagating with a speed of ≈125 km $s^{-1}$ and a period of about 30 min as determined from the EIS data.

the field lines may form an angle with the plane of the sky. However, these angles are very likely small and the speeds are most probably subsonic. For the propagation speeds, we estimate the uncertainty to be around 10 %. The ratio of the Fe XII to Ne VIII propagation speeds, about 1.7, is close to the ratio of the sound speeds of about 1.5 (at the two formation temperatures of 0.6 and 1.3 MK). The observed radiance perturbations have an amplitude of a few percent. No evidence of propagating disturbances can be found in the LOS velocity *x*–*t* maps.

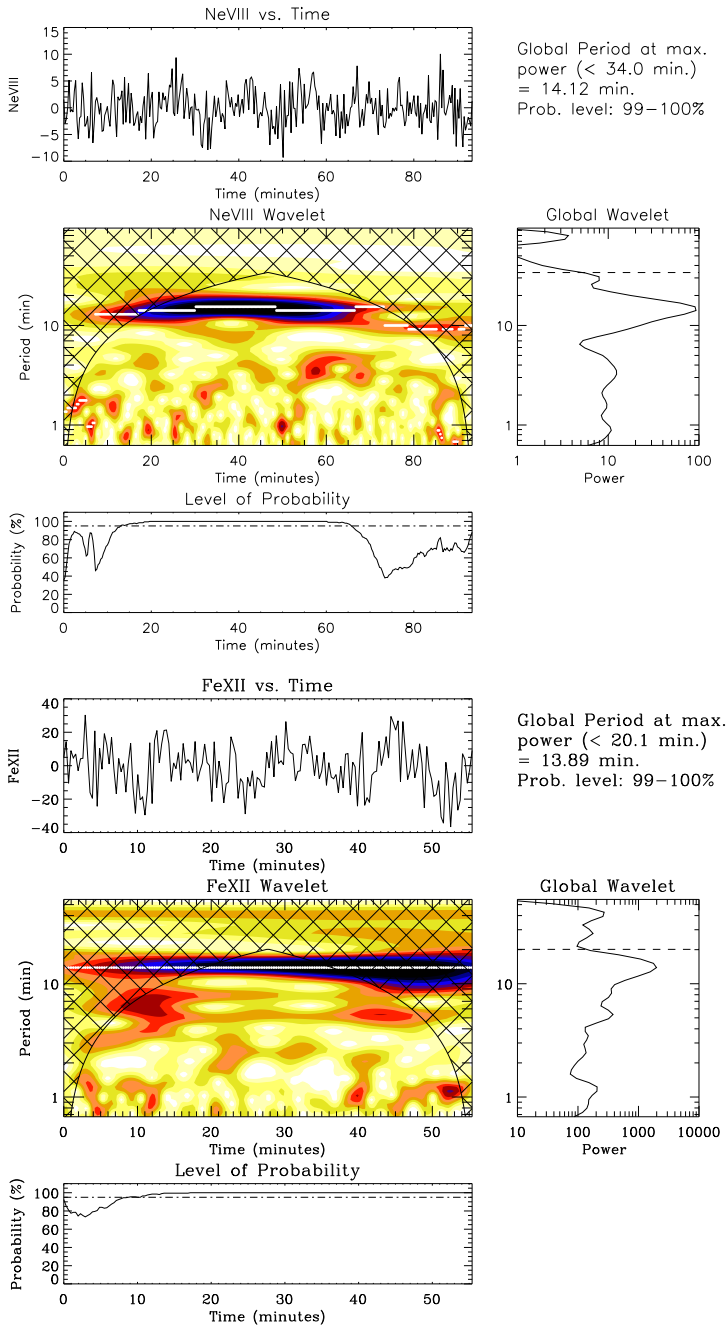


Figure 5.9: Wavelet analysis for the $8^{th}$ April data at Solar-$Y \approx -995''$ for both Ne VIII 770 Å (top) and Fe XII 195 Å (bottom). Both light curves are obtained by averaging over 9″ along the slit. In each set we show the relative (background trend-removed) radiance (top panels), the colour inverted wavelet power spectrum (central panels), the variation of the probability estimate associated with the maximum power in the wavelet power spectrum (marked with white lines) (bottom panels), and the global (averaged over time) wavelet power spectrum (right middle panels). Above the global wavelet, the period (measured from the maximum power of the global wavelet), and the probability estimate, are given.

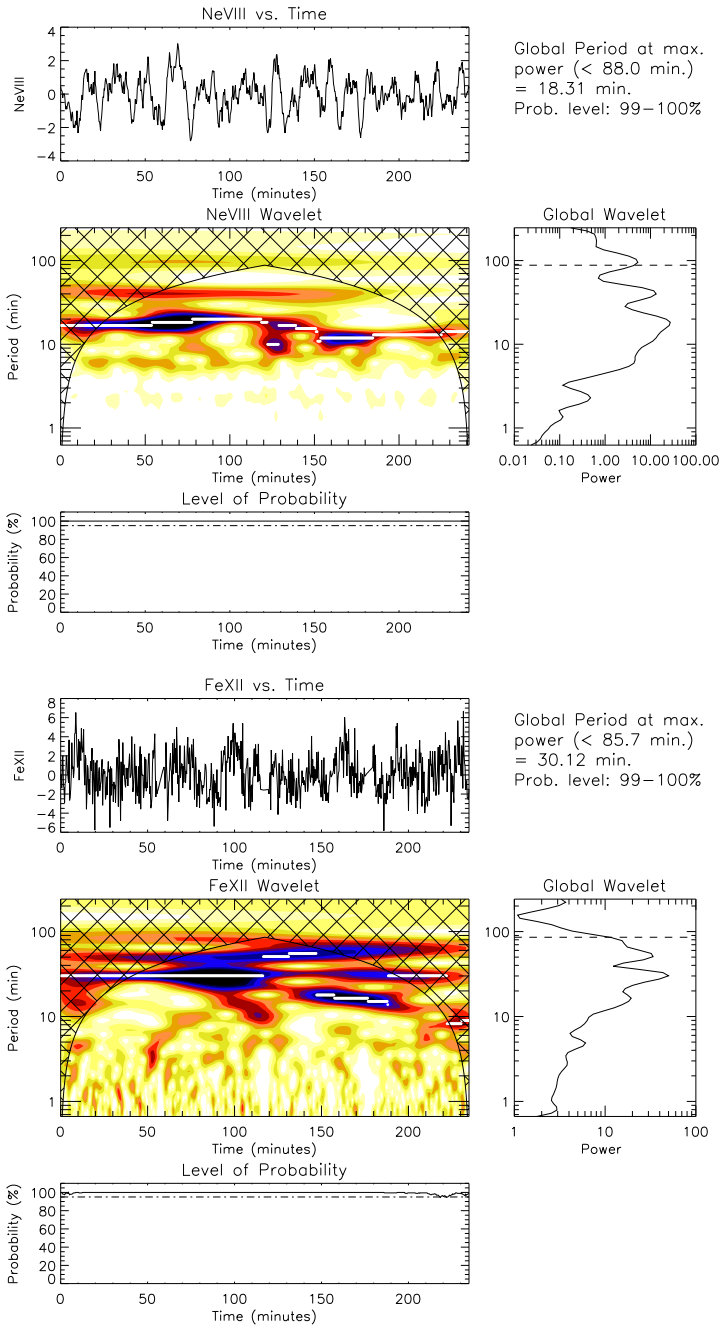


Figure 5.10: Wavelet analysis for the $15^{th}$ April data at Solar-$Y \approx -995''$ for both Ne VIII 770 Å (top) and Fe XII 195 Å (bottom). Both light curves are obtained by averaging over $9''$ along the slit. Descriptions about the different panels are the same as in Figure 5.9.

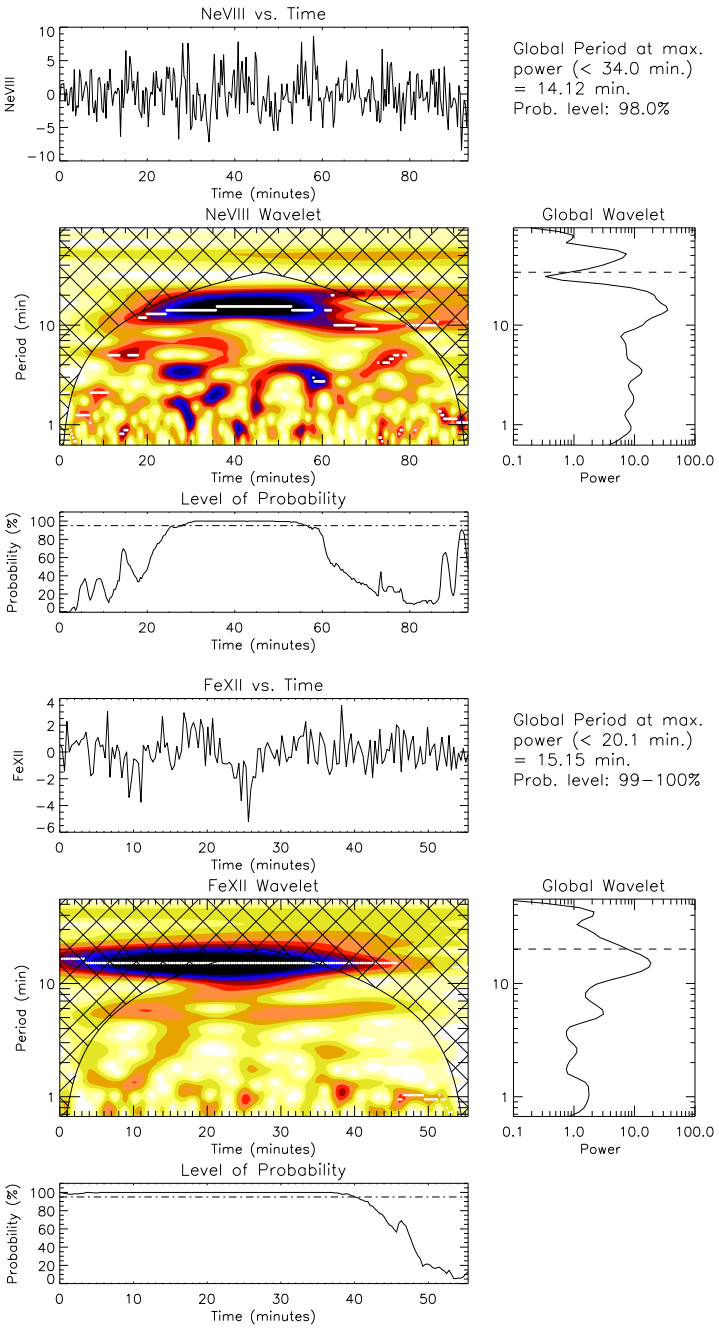


Figure 5.11: Wavelet analysis for the $8^{th}$ April data at solar-$Y \approx -1003''$ for both Ne VIII 770 Å (top) and Fe XII 195 Å (bottom). Both light curves are obtained by averaging over 9″ along the slit. Descriptions about the different panels are the same as in Figure 5.9.

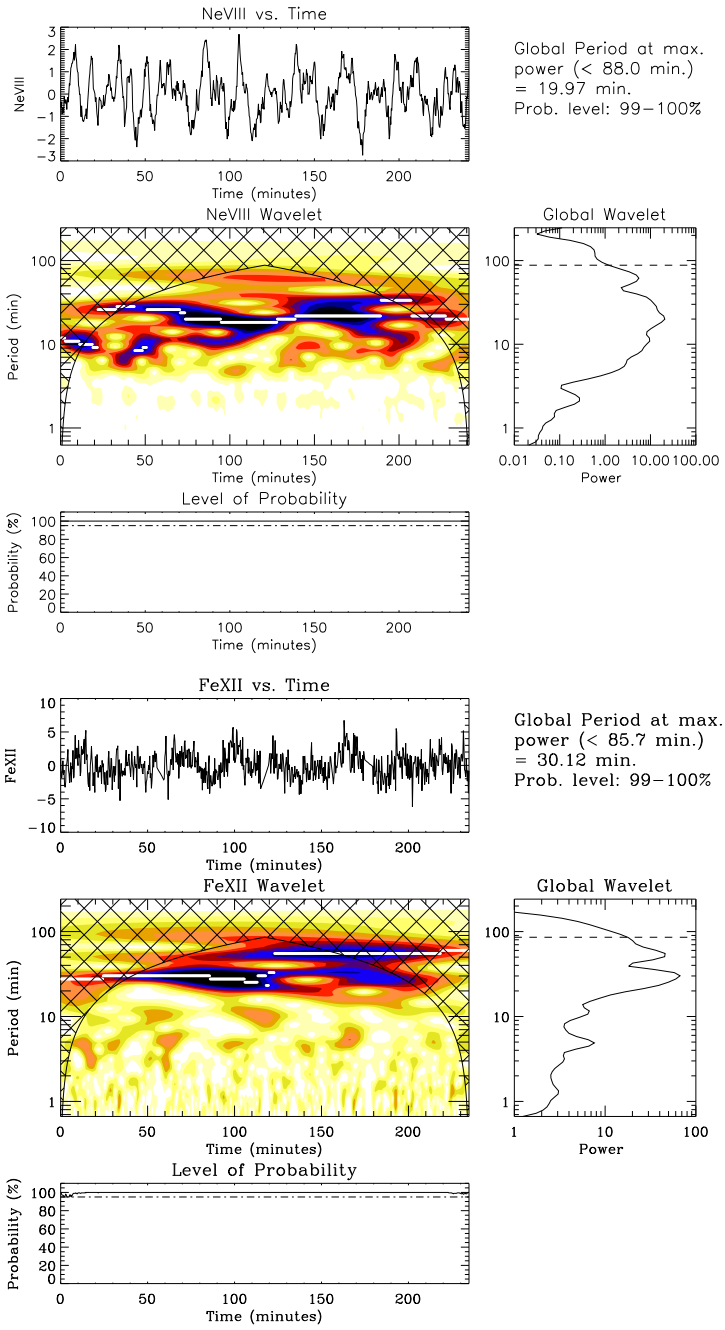


Figure 5.12: Wavelet analysis for the $15^{th}$ April data at solar-$Y \approx -1003''$ for both Ne VIII 770 Å (top) and Fe XII 195 Å (bottom). Both light curves are obtained by averaging over $9''$ along the slit. Descriptions about the different panels are the same as in Figure 5.9.

### 5.3.2 Analysis of Oscillations

To better study the properties of the propagating disturbances seen in the enhanced-radiance $x$–$t$ slices in Figures 5.7 and 5.8, we make use of wavelet analysis and focus on individual locations (heights) in the off-limb corona. For this purpose we extracted radiance versus time curves at a given height by averaging over $9''$ in the $Y$ direction for both SUMER and EIS original (without filtering or contrast enhancement) radiance maps. In Figures 5.9 and 5.10, we show representative examples of the type of oscillation measured at $Y \approx -995''$ ($\approx 28''$ above the limb) from $8^{th}$ and $15^{th}$ April 2007 datasets. The top panels of these figures show the variation of the radiance (hereafter we will use the term radiance for trend-subtracted line radiance). Details on the wavelet analysis, which provides information on the temporal variation of a signal, are described in Torrence and Compo (1998). For the convolution with the time series in the wavelet transform, we chose the Morlet function, as defined in Torrence and Compo (1998). The light curves shown in the upper panels had their background trend removed by subtracting from the original time series a 60−point ($\approx$ 18.1 min) running average for $8^{th}$ April data and a 100−point ($\approx$ 30.2 min) for SUMER and 150−point ($\approx$ 45.3 min) for the EIS running average for $15^{th}$ April data. In the wavelet spectrum (middle-left panels), the cross-hatched regions are locations where estimates of oscillation periods become unreliable. This is the so-called cone-of-influence (COI, see Torrence and Compo, 1998). As a result of the COI, the maximum measurable period is shown by a dotted line in the global spectrum plots (middle-right panels). Above the global wavelet spectrum of Figures 5.9 and 5.10, we show the prevalent period measured at the location of the maximum of the global wavelet spectrum, together with an estimate of the probability that this oscillation is not due to noise. The probability estimate was calculated using the randomisation method with 200 permutations as outlined in detail in O'Shea et al. (2001) and are briefly described in Section 4.3.1.

Below the wavelet power spectrum, in the lower panels, we show the variation of the probability estimate, calculated using the randomisation technique, associated with the maximum

power at each time in the wavelet power spectrum. The location of the maximum power is indicated by the over-plotted white lines in the middle-left panels. Figure 5.9 shows that the oscillations detected in the $8^{th}$ April data have periodicities with maximum power at ≈14.1 min in Ne VIII (SUMER) and ≈13.9 min in Fe XII (EIS). Note that the wavelet technique reveals highly significant power in Fe XII (also at other heights), although no clear oscillation could be discerned by eye in the EIS enhanced radiance map (see bottom panel of Figure 5.7). On the other hand, for $15^{th}$ April data, which have a longer time series, Ne VIII shows its maximum power around 18 min and Fe XII shows maximum power around 30 min, consistent with the results from the analysis of the *x*–*t* slices. Also note that there are multiple peaks seen in the global wavelet spectra (right panels), which implies that the signal could be composed of multiple modes of oscillation. To study the oscillation behaviour at different heights we also look at the wavelet results at Y= $-1003''$ and plot the results in Figures 5.11 and 5.12, respectively. For the $8^{th}$ April data at $Y \approx 1003''$, SUMER reveals a strong peak at 14.2 min, while EIS shows a peak at 15.15 min. For the $15^{th}$ April data at $Y \approx -1003''$ SUMER shows a strong peak at 20 min, whereas EIS shows a peak at 30 min. Finally, we also attempted to search for oscillations in the LOS velocity (by fitting the profiles obtained using the same binning as for the radiance wavelet analysis). No evidence of oscillations with an amplitude larger than 2 km $s^{-1}$ can be found in the LOS velocity data. This is the accuracy achievable with SUMER when observing the Ne VIII line in the first order of diffraction.

## 5.4 Results from November 2007 Dataset

As mentioned before, here in this dataset, SUMER slit is pointing to an inter-plume region and the EIS slot covers both plume and inter-plume regions, overlapping with the SUMER slit. Thus, in the inter-plume region EIS and SUMER both provide information, whereas in the plume region only EIS observations are available. Analysis of the radiance maps (*x*–*t* slices), wavelet analysis, and correlation analysis are performed at the two locations as described in the following three subsections.

### 5.4.1 Radiance *x*–*t* Slices

Maps of radiance along the slit versus time (distance–time map or *x*–*t* slices) were built using the SUMER Ne VIII integrated line radiance and the EIS Fe XII radiance averaged over 5″ in the *X* direction at the position overlapping with the SUMER slit (which covers the inter-plume region). The resulting maps were then smoothed over ≈ 3 min and the background trend of ≈ 20 min has been subtracted from each solar-*Y* pixel along time. In general, similar procedures are applied while doing the Fourier or wavelet analysis of a time series. In the *x*–*t* slices, the presence of alternate bright and dark regions indicate the presence of oscillations. Moreover, diagonal or slanted radiance enhancements are signature of propagating disturbances. Thus, from such maps it becomes possible to estimate periods and projected propagation speeds (see, e.g. DeForest and Gurman, 1998).

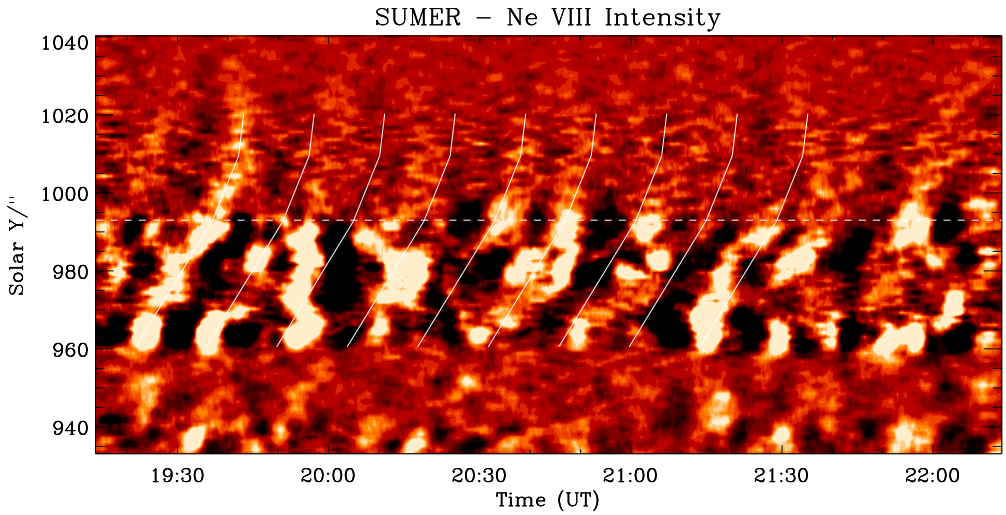


Figure 5.13: Enhanced distance–time (*x*–*t*) map of radiance (along solar-*Y*) variation at solar X≈ −72″ as recorded by SUMER in the Ne VIII 770 Å spectral line on 13$^{th}$ November 2007. Here the slit covers the on-disk, limb, and off-limb regions of the polar coronal hole and it is positioned in the inter-plume region. The slanted lines correspond to the disturbances propagating outward with increasing speed. The dashed horizontal line indicates the position of the limb brightening in Ne VIII. In the on-disk region the disturbance propagates with a speed of 25 ± 1.3 km s$^{-1}$, increasing to 38 ± 4.5 km s$^{-1}$ close to the limb, and to about 130 ± 51 km s$^{-1}$ in the off-limb region. The periodicity is in the range of ≈ 14–20 min as also obtained from the wavelet analysis (see Figures 5.16 and 5.17).

Both the SUMER slit and the EIS slot are centred on the solar limb and, hence, cover the region on-disk as well as off-limb. As the observed region is near to the pole, the effect of solar rotation is very small and amounts to less than about $3''$ per hour at $100''$ below the limb. We first concentrate our attention to the inter-plume location, around solar-$X \approx -72''$, probed by both instruments. Figure 5.13 shows the $x$–$t$ map of the radiance of the Ne VIII spectral line, where the presence of slanted bright and dark region is clearly visible. A disturbance appears from the on-disk bright region around solar-$Y \approx 967''$ (see Figures 5.3 and 5.6), and propagates toward the limb. The signature of oscillations is very strong in this bright region. No signature of propagation is visible below solar-$Y \approx 967''$ (the SUMER slit covers down to solar-$Y \approx 930''$). Hence the assumption that this bright region is the source of these propagating disturbances is justified (Figure 5.13). The speed of propagation measured from the slope of the enhanced slanted radiance stripes is $25 \pm 1.3$ km s$^{-1}$. This average speed is measured up to solar-$Y \approx 992''$ which is very close to the region of limb brightening (see also Figure 5.6). As the propagation reaches the limb, its speed increases and the enhanced features become more vertical. Up to solar-$Y \approx 1010''$, the measured speed is $38 \pm 4.5$ km s$^{-1}$. This change in speed is a clear signature of acceleration of the propagating disturbance. Furthermore, when this propagation reaches beyond the limb brightening height, i.e., in the corona, its speed further increases to $130 \pm 51$ km s$^{-1}$ and the propagation is seen up to solar-$Y \approx 1020''$. Beyond this height the signature of propagation becomes very poor, most likely due to the low signal. The periodicity of the fluctuations is $\approx$ 14 min to 20 min. In Figure 5.13, the over-plotted white lines follow the slope of the enhancements and are plotted with a periodicity of $\approx$ 14 min. It can be seen that in some places the over-plotted white line do not coincide with the enhanced lanes but it is nevertheless parallel to it. This suggests that even if the periodicity changes within a certain range the propagation speeds are fairly uniform. There is no clear evidence of propagating disturbances (in terms of velocity fluctuations) in the line-of-sight (LOS) velocity (obtained from Doppler shift) $x$–$t$ map, although periodicities are revealed by the wavelet analysis (see the following section).

Figure 5.14 shows the radiance $x$–$t$ map of the Fe XII 195 Å line at the same location (solar-$X \approx -72''$, inter-plume region). The image was processed as described above. The analysis of the

*x–t* map over the coronal hole reveals that there is no clear signature of propagating disturbances in the on-disk coronal hole region. These alternate bright and dark regions are clearly visible only around the limb and far off-limb, hence only these regions are plotted in Figure 5.14. In this map, the propagating disturbances are visible from solar-$Y \approx 1000''$ up to the upper end of the EIS slot at solar-$Y \approx 1140''$. In this inter-plume region, the disturbance propagates with an average speed of $130 \pm 14$ km s$^{-1}$ from solar-$Y \approx 1000''$ to solar-$Y \approx 1085''$ increasing to an average speed of $330 \pm 140$ km s$^{-1}$ up to solar-$Y \approx 1135''$, clearly showing signatures of acceleration. The periodicity of the fluctuations is in the range of $\approx 15$ min to 18 min. Here the over-plotted white lines give the slope of the enhancements and are plotted with a periodicity of $\approx 17$ min. It can be again seen here that in some places the over-plotted white line does not coincide with the enhanced lanes but is nevertheless parallel to it as was discussed for the results from the Ne VIII line.

Summarizing, observations in the Ne VIII spectral line reveal a propagating disturbance originating in a bright region in the on-disk coronal hole that starts propagating toward the limb region with speed $25 \pm 1.3$ km s$^{-1}$. Near the limb the speed increases to $38 \pm 4.5$ km s$^{-1}$ and reaches $130 \pm 51$ km s$^{-1}$ in the off-limb region. A similar speed is measured at the same height in the Fe XII spectral line by EIS. Hence, both instruments see approximately the same speed in the same region, which is different from the result reported in Section 5.3 for a likely plume region, where different propagation speeds are found in different lines. Further off-limb, the speed of the propagating disturbance reaches $330 \pm 140$ km s$^{-1}$ as seen by EIS in the Fe XII spectral line. Overall, the acceleration of propagating disturbances is observed from on-disk to far off-limb in an inter-plume region simultaneously by two different instruments on different satellites.

The EIS slot also covers part of a plume, and the position around solar-$X \approx -39''$ is selected to represent this region. The processed *x–t* radiance map is plotted in Figure 5.15. Also in this case, there is no clear signature of propagating disturbances in the on-disk coronal hole region. These alternate bright and dark regions are clearly visible only at the limb and off-limb, hence again only these regions are plotted in Figure 5.15. In this map, the propagating disturbances

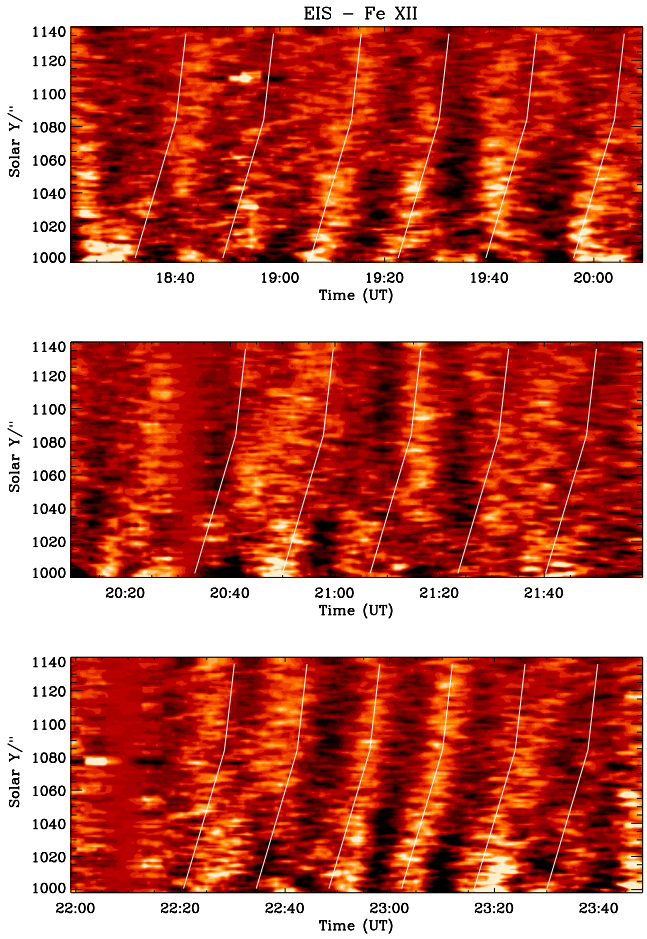


Figure 5.14: Enhanced *x–t* map of radiance variation along solar-$Y$ at solar-$X \approx -72''$ as recorded by EIS in Fe XII 195 Å on $13^{th}$ November 2007. The height range shown here covers the near off-limb and far off-limb regions of the polar coronal hole and corresponds to the inter-plume region. The slanted lines correspond to the disturbances propagating outward with increasing speed. In the near off-limb region, the disturbance propagates with a speed of $130 \pm 14$ km s$^{-1}$, and accelerates to $330 \pm 140$ km s$^{-1}$ in the far off-limb region. The periodicity is in the range of $\approx$ 15–18 min as obtained from the wavelet analysis (see Figure 5.19).

are visible from solar-$Y \approx 1000''$ up to solar-$Y \approx 1120''$. In this plume region, the disturbance propagates with a speed of $135 \pm 18$ km s$^{-1}$ from solar-$Y \approx 1000''$ to solar-$Y \approx 1075''$ and with $165 \pm 43$ km s$^{-1}$ up to solar-$Y \approx 1120''$. Beyond this height the map becomes diffuse and there is no clear signature of propagation. Although this may be interpreted in terms of wave dissipation, this lack of signature at greater heights may be simply due to merging with the background signal.

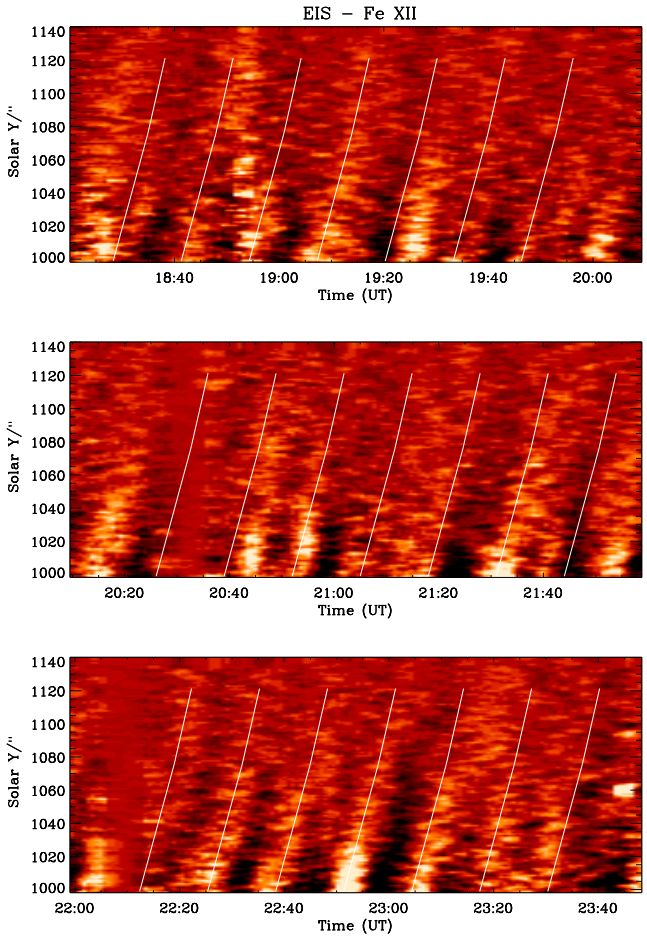


Figure 5.15: Enhanced $x$–$t$ map of radiance variation along solar-$Y$ at solar-$X \approx -39''$ as recorded by EIS in Fe XII 195 Å on $13^{th}$ November 2007. The height range shown here covers the near off-limb and far off-limb regions of the polar coronal hole and falls in the plume region. The slanted lines correspond to the disturbances propagating outward with nearly a constant speed. In the near off-limb region, the disturbance propagates with a speed of 135 $\pm$ 18 km s$^{-1}$, and accelerates to 165 $\pm$ 43 km s$^{-1}$ in the far off-limb region. The periodicity is in the range of $\approx$ 15–20 min as obtained from the wavelet analysis (see Figure 5.20).

### 5.4.2 Analysis of Oscillations

In this subsection, in order to study the detailed properties of the propagating disturbances as seen in the enhanced radiance $x$–$t$ maps (Figures 5.13–5.15), we make use of wavelet analysis and focus on individual locations in the on-disk and off-limb corona. The full SUMER time series is used to detect oscillations in the radiance, Doppler shift as well as in the Doppler width

of the Ne VIII spectral line at several locations. The bright location is identified on-disk using the maximum radiance seen in He II 256 Å by EIS. At several off-limb locations, there is sufficient signal to noise ratio to detect oscillations with a high confidence level. Figures 5.16–5.19 show examples of oscillations measured in the polar region at fixed solar-$X \approx -72''$ (which corresponds to the inter-plume region) and at several solar-$Y$ locations: $\approx 967''$ (on-disk), $\approx 1020''$ (off-limb, but close to the limb), and $\approx 1120''$ (far off-limb), as mentioned in the figure caption. On the other hand, Figure 5.20 shows oscillation measured at solar-$X \approx -39''$ (which corresponds to the plume region) and solar-$Y \approx 1030''$ (off-limb). In these figures, the top panel shows the variation of the radiance (hereafter the term radiance will be used for trend-subtracted integrated line radiance) with time. The oscillations shown in the upper panel had their background trend removed by subtracting from the original time series a 100−point ($\approx$ 30 min) and 35−point ($\approx$ 30 min) running average for SUMER and EIS data, respectively. In the wavelet spectrum, the cross-hatched regions are locations where estimates of oscillation period become unreliable which is called as the cone-of-influence (COI). As a result of the COI, the maximum measurable period is shown by a horizontal dashed line in the global wavelet plots, which are obtained by taking the mean over the wavelet time domain. This global wavelet is very similar to the Fourier transform as both are giving the distribution of power with respect to period or frequency. Whenever the Fourier spectrum is smoothed, it approaches the global wavelet spectrum. The period at the location of the maximum in the global wavelet spectrum is printed above the global wavelet spectrum.

From the *x*–*t* map analysis (Figure 5.13), it was seen that outward propagating disturbances at the inter-plume location (solar-$X \approx -72''$) originate from a bright on-disk region at solar-$Y \approx 967''$. As this region has been covered by the SUMER slit, we have information about the radiance, Doppler shift, as well as the Doppler width of the Ne VIII spectral line. Time series have been obtained at this bright location by taking a $5''$ average over solar-$Y$ and then wavelet power spectra have been plotted for both radiance and LOS velocity in Figure 5.16. There is a clear presence of $\approx 15 - 20$ min periodicity in both radiance and velocity. Going to the off-limb inter-plume at solar-$Y \approx 1020''$, time series in both radiance and Doppler velocity were obtained by averaging

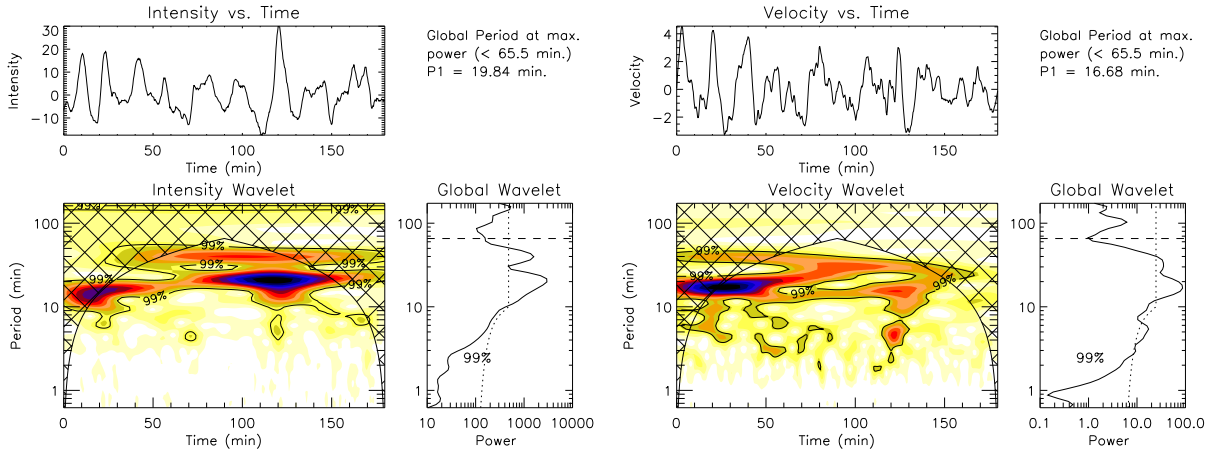


Figure 5.16: Wavelet result for the on-disk location at solar-$Y \approx 967''$ and solar-$X \approx -72''$ in Ne VIII 770 Å radiance (left side) and velocity (right side). In each set, the top panels show the relative (background trend removed) radiance/velocity smoothed over 3 min. Bottom left panels show the colour inverted wavelet power spectrum with 99 % confidence level contours, while bottom right panels show the global (averaged over time) wavelet power spectrum with 99 % global confidence level drawn. The period P1 at the location of the maximum in the global wavelet spectrum is printed above the global wavelet spectrum.

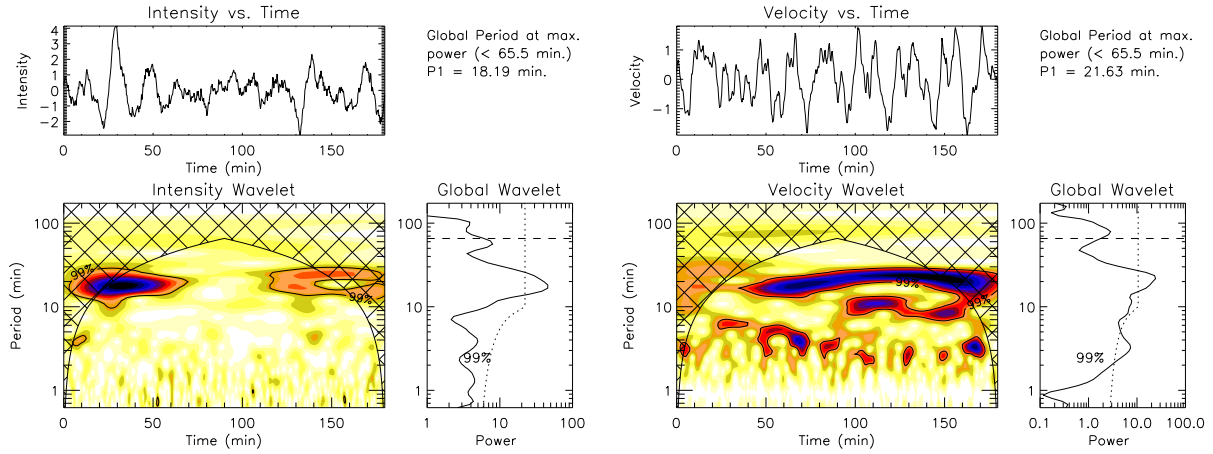


Figure 5.17: Wavelet analysis results corresponding to solar-$Y \approx 1020''$ in the Ne VIII radiance (left side) and in velocity (right side) at solar-$X \approx -72''$ (inter-plume region). See the caption of Figure 5.16 for a description of the different panels.

over $9''$ in the $Y$ direction (to increase the signal to noise ratio). Also from the wavelet power spectra (Figure 5.17), a clear presence of $\approx 15-20$ min periodicity in both radiance and Doppler shift was found. Wavelet power spectra of the Doppler width time series were also obtained at

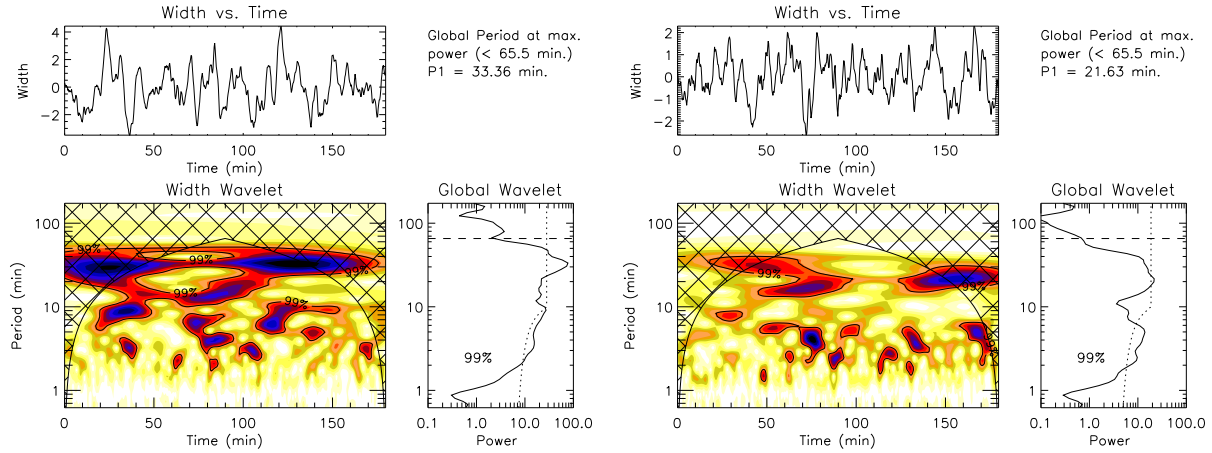


Figure 5.18: Wavelet analysis results for the oscillations in Doppler width of the Ne VIII line at solar-$Y\approx$ 967″ (left side) and at solar-$Y\approx$ 1020″ (right side) obtained at solar-$X\approx -72''$ (inter-plume region). See the caption of Figure 5.16 for a description of the different panels.

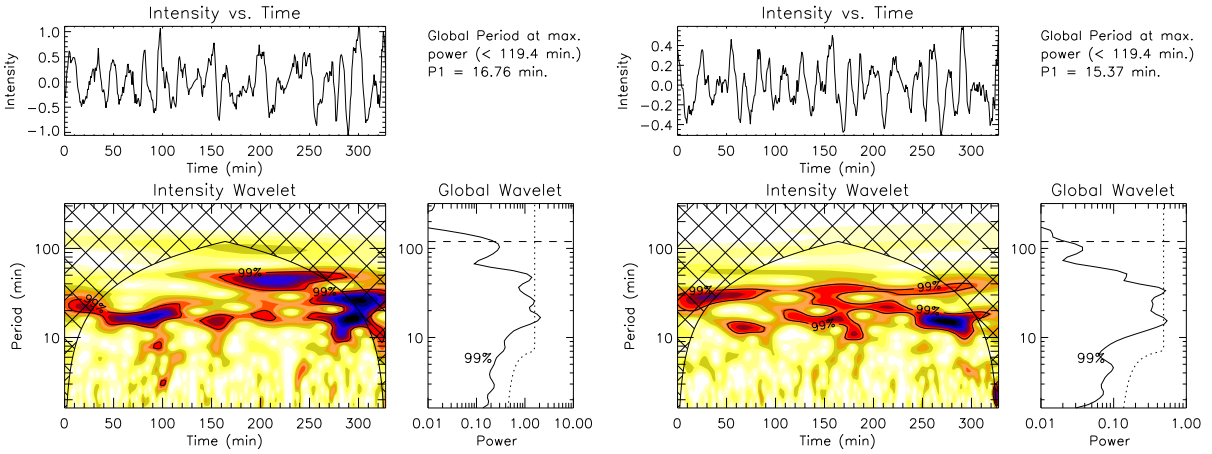


Figure 5.19: Wavelet analysis results corresponding to the Fe XII radiance at solar-$Y\approx$ 1020″ (left side) and at solar-$Y\approx$ 1120″ (right side) at solar-$X\approx -72''$ (inter-plume region). See the caption of Figure 5.16 for a description of the different panels.

the two locations and are shown in Figure 5.18. The analysis reveals a periodicity similar to that observed in radiance and in Doppler shift.

EIS Fe XII time series have been produced by averaging over 5″ and 9″ in the $X$ and $Y$ directions, respectively. Then a wavelet analysis was performed at two inter-plume locations; one near the limb (solar-$Y\approx$ 1020″) and the other further off-limb (solar-$Y\approx$ 1120″). The wavelet

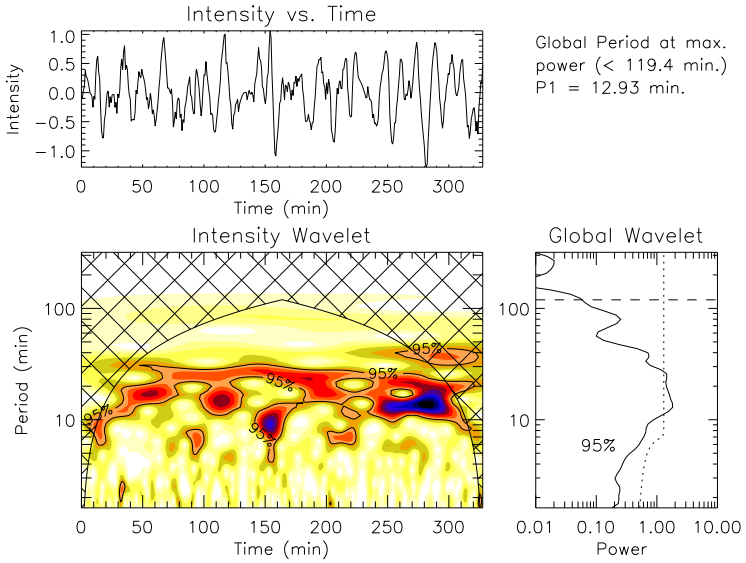


Figure 5.20: Wavelet analysis results corresponding to the Fe XII radiance at solar-$Y \approx 1030''$ and solar-$X \approx -39''$ (plume region). See the caption of Figure 5.16 for a description of the different panels. In this case, confidence contours are drawn at 95 % level.

power spectra are shown in Figure 5.19. Both heights show periodicity between 15 min and 20 min, consistent with the results from the $x$–$t$ map (see Figure 5.14). Furthermore, these periods are consistent with the periods obtained from Ne VIII. In summary, again it can be concluded that the propagating disturbance, which originates from the on-disk bright region, propagates off-limb and in the far off-limb inter-plume region.

In order to check the periods of propagating disturbances in the plume region, the wavelet analysis has been carried out also at location solar-$Y \approx 1030''$ and solar-$X \approx -39''$ by averaging over $9''$ in solar-$Y$ and $5''$ in solar-$X$, (see Figure 5.20). Also in this case, the period of propagation, ≈12–20 min, is consistent with the $x$–$t$ map in Figure 5.15. However, as seen from the $x$–$t$ map, these disturbances are not visible at greater heights above the limb.

### 5.4.3 Correlation Analysis

In the earlier subsections, we presented results from the Ne VIII and Fe XII lines only. Propagation properties of waves can also be studied by correlation analysis. First, we focus our attention on the on-disk bright region, where we expect the waves seen at the inter-plume location to originate. At this location ($Y \approx 967''$), we find clear presence of oscillations in different lines as recorded by SUMER and EIS (as tabulated in Table 5.1). For the on-disk study, we will concentrate on the correlation between different lines as recorded by SUMER and EIS, while for the off-limb study we will calculate correlation coefficients between different heights as recorded by the same Fe XII line. The correlations between the time series from two different lines have been obtained using the IDL routine *c_correlate* at different time delays between the two series. Correlation coefficients have been calculated for six line pairs and are plotted in the left panel of Figure 5.21. The time resolution is about 18 s for SUMER and 47 s for EIS (governed by the respective cadences). The time delay at the peak of correlation can be considered as the time delay between the oscillations in the two lines forming the pair. It can be seen that the level of correlation and the time delay are in inverse proportion, which means that the correlation is higher for the lines having smaller temperature separation and, because in coronal hole the temperature changes mainly as a function of height, smaller time delay. The correlation between He II and Fe XII is smaller and shows the largest time delay, whereas the correlation between He II and Fe X is comparatively high and has less time delay. If there would be height information available, then it would be possible to estimate the propagation speed of oscillations from one height to another. The radiance variation of several lines with respect to solar-$Y$ has been plotted in Figure 5.6 at solar-$X \approx -72''$. As described in O'Shea et al. (2006), the difference in the peak positions provides an estimate of the differences in the formation heights between different lines at that particular time and condition. Hence, using the correlation technique, the time delay between two lines can be obtained and using the limb brightening technique, the formation height difference can be estimated for a line pair. The results obtained have been summarized in Table 5.2. Due to the relatively poor temporal resolution, uncertainties in time delay measurements are large. Hence, for the on-disk

bright region, results obtained here can only be used to infer that waves are propagating from lower to higher heights in the solar atmosphere.

Table 5.2: Linear correlation coefficients between oscillations in different line pairs corresponding to the on-disk bright region.

| Line-Pair | log $T_{max}$ (K) | Correlation Coefficient | Time Delay[a] (s) | Height Diff.[b] (km) |
|---|---|---|---|---|
| He II/Fe XII | 4.9/6.1 | 0.242954 | 188 | 4509 |
| He II/Fe XI | 4.9/6.1 | 0.250901 | 94 | – |
| He II/Fe X | 4.9/6.0 | 0.322859 | 47 | 5628 |
| He II/Fe VIII | 4.9/5.6 | 0.307703 | 47 | 3180 |
| He II/Si VII | 4.9/5.8 | 0.564139 | 47 | 5363 |
| He II/Mg VII | 4.9/5.8 | 0.640592 | 47 | 4104 |
| He II/Mg VI | 4.9/5.6 | 0.496354 | 47 | 3654 |
| S V/Ne VIII | 5.2/5.8 | 0.504659 | 36 | 3647 |
| O IV/Ne VIII | 5.2/5.8 | 0.477825 | 54 | 2917 |

[a]Limited by time resolution defined by effective cadence of respective instruments.
[b]Limited by spatial resolution of respective instruments, ≈ 715 km.

A similar correlation analysis is applied to the off-limb inter-plume region at solar-$X \approx -72''$ using data from the same line, Fe XII, but at different heights with respect to solar-$Y \approx 1000''$. The results are plotted in the right panel of Figure 5.21. The time resolution is about ≈ 47 s, the EIS cadence. Also in this case, the level of correlations and time delays are in inverse proportion as expected. The measured time delays are plotted against solar-$Y$ in the left panel of Figure 5.22. The continuous line corresponds to a second-order polynomial fit applied to the data points (as marked by asterisks). The error bar on these time delays is obtained from the Half Width Half Maximum (HWHM) of the particular correlation plot. The dotted line corresponds to the fit to the slanted radiance ridges in the $x$–$t$ maps (white lines in Figure 5.14). The figure indicates that the travel time is decreasing with height indicating an acceleration, as was seen from the $x$–$t$ map of Fe XII in Figure 5.14. This figure provides an independent estimate of the acceleration.

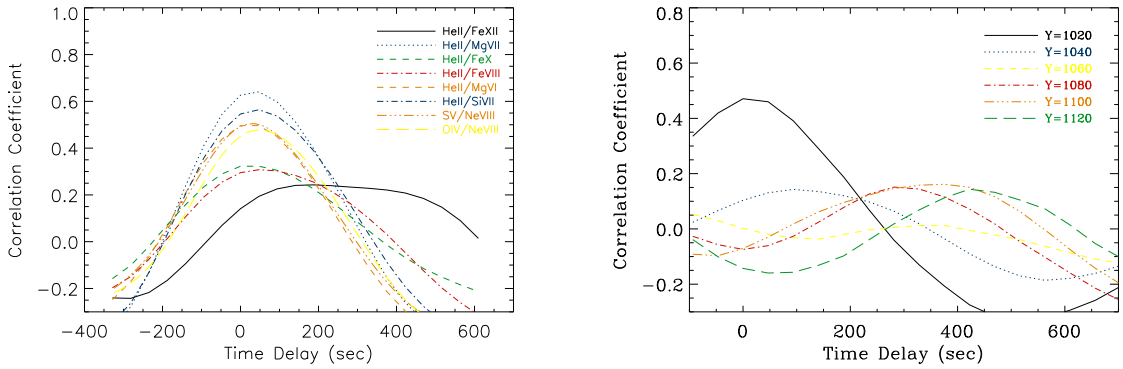


Figure 5.21: Left: correlation coefficients vs. time delay between the line pairs at the on-disk bright location ($X \approx -72''$, $Y \approx 967''$). The maximum correlation coefficient for a fixed line pair provides a measure of the travel time. Right: correlation coefficients vs. time delay in the inter-plume region for time series in the EIS Fe XII line. The correlation coefficients are calculated at different heights with respect to $Y \approx 1000''$.

The Alfvén wave speed through the quasi-static corona can be calculated from the expression $V_A = B/\sqrt{4\pi\rho}$. We use the density profile given by Teriaca et al. (2003) and take into account the super-radial fall of the magnetic field with height according to Kopp and Holzer (1976), with a base magnetic field of $\approx 0.65$ G. For comparison purpose, the Alfvén wave speed is also calculated by assuming a constant magnetic field of $\approx 0.65$ G with height. The measured time delays at different Solar-$Y$ in the inter-plume region are then compared with the travel time for a theoretical Alfvén mode. The Alfvénic time delays obtained assuming a magnetic field constant with height and expanding according to Kopp and Holzer (1976) are plotted, respectively, as a dashed and a dot-dashed line in the left panel of Figure 5.22. To estimate the propagation speed, we plot the right panel of Figure 5.22 which shows the variation of the propagation speed with respect to the height in the solar atmosphere. The speed is calculated by the time derivative of the fit to the measured time delays shown in the left panel of Figure 5.22 and is plotted as a continuous line. This speed is compared with the theoretically calculated propagation speed of Alfvén modes, plotted as dot-dashed and dashed lines, respectively, for the expanding and constant field case. It can be seen that the measured propagation speed is roughly consistent with being Alfvénic if we assume a field of 0.65 G at the base. From the figure, it can be seen that near the limb and off-limb the speed of propagation is about 130 km s$^{-1}$, increasing to more than

220 km $s^{-1}$ far off-limb, close to the speeds obtained from the *x–t* map in Figure 5.14. It also appears that above a certain height ($Y \approx 1080''$) the speed increases more rapidly. These results might indicate that physics of the propagation might also change at these heights.

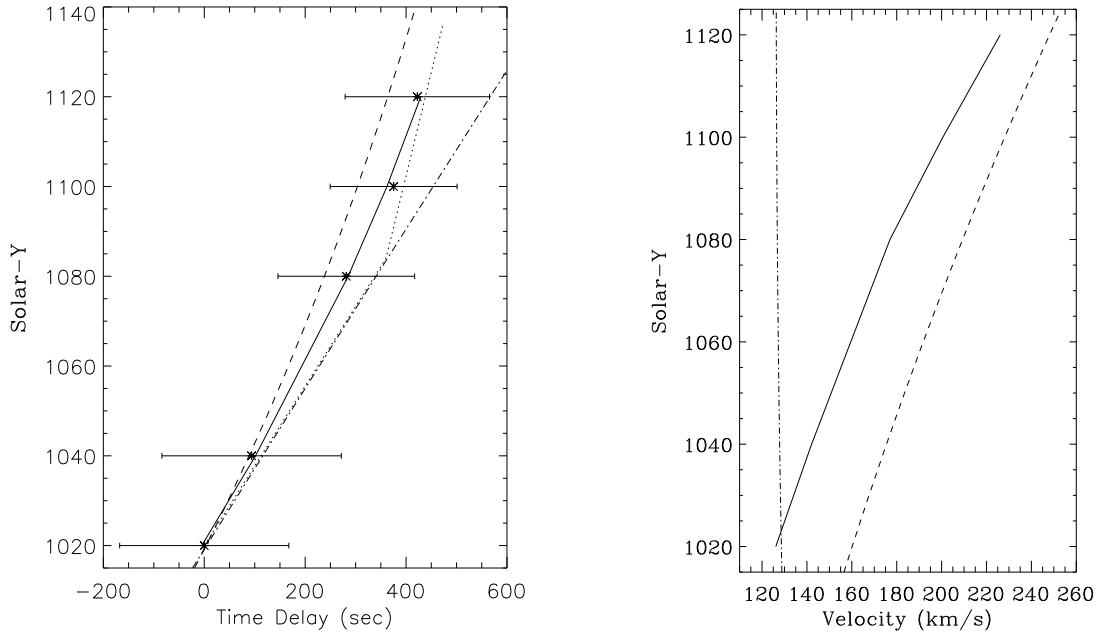


Figure 5.22: Left: variation of travel time with height in the inter-plume region. The asterisks represent the measured time delays from the right panel of Figure 5.21 while the continuous line corresponds to a second-order polynomial fit applied to the data points. The error bars on these time delays are obtained from the HWHM of the respective correlation peaks. The dotted line corresponds to the fit to the slanted radiance ridges in the *x–t* maps (white lines in Figure 5.14). The dashed and dot-dashed lines are the theoretically predicted Alfvénic time delays obtained assuming a magnetic field constant with height and expanding according to Kopp and Holzer (1976), respectively. The change in the slope indicates acceleration. Right: propagation speed with height in the inter-plume region. The continuous line is obtained after taking the time derivative of the fit to the data points in the left panel. The dashed and dot-dashed lines are the theoretically predicted Alfvén speeds obtained assuming a magnetic field constant with height and expanding according to Kopp and Holzer (1976), respectively.

## 5.5 Discussion

Our results show the propagation of disturbances from an on-disk region to the off-limb corona within the inter-plume region. These disturbances appear to originate from an on-disk bright location, presumably the foot-point of a coronal funnel, around solar-$Y \approx 967''$ (see Figure 5.13). No signature of propagation is visible below solar-$Y \approx 967''$. The propagation speed, as measured from the *x–t* map (distance–time map) of Ne VIII and Fe XII line radiance, increases with height. Outward propagating disturbances are also recorded in a plume structure within the EIS field of view, but the acceleration is almost zero. Furthermore, the disturbances become diffuse far off-limb as seen from the EIS Fe XII *x–t* map. From wavelet analysis, these disturbances have a periodicity in the range of 15–20 min in both regions and the periodicity is seen almost over the whole duration of observation, although the power is increasing and decreasing with time. A correlation analysis of the light curves of different spectral line pairs in the on-disk bright region reveals larger time-delays for line pairs with the larger difference in formation height (inferred from the limb brightening curves), indicating upward propagation. This upward propagation indicates that these waves are generated somewhere lower in the atmosphere, probably in the chromosphere, since these are also seen in He II and then propagate upward toward the off-limb region. In the off-limb region, cross-correlation between light curves from the same spectral line (Fe XII) but obtained at different heights above the limb shows time delays indicating outward propagation, in agreement with the results from the analysis of the *x–t* maps.

The propagating disturbances, clearly visible in the inter-plume region in the Ne VIII radiance *x–t* map, are not visible in the Ne VIII Doppler shift and width *x–t* maps. However, the wavelet analysis shows that both Doppler shift and width oscillations are present in the on-disk bright region and near off-limb with approximately the same periodicity as seen in radiance (see Figures 5.16–5.18), and they are also mostly in phase. The presence of oscillations in radiance and both resolved (Doppler shift) and unresolved (Doppler width) velocities with approximately the same period, is evidence of propagating waves with at least a compressional component in

the inter-plume lanes. The measured speeds of propagation of these waves from the Ne VIII line are 25 ± 1.3 km $s^{-1}$, 38 ± 4.5 km $s^{-1}$, and 130 ± 51 km $s^{-1}$ in the on-disk region, near the limb, and off-limb respectively. Fe XII data show that the propagation speed further increases to 330 ± 140 km $s^{-1}$ in the far off-limb region of inter-plume. In the plume region, instead, the observed off-limb propagation speed increases from 135 ± 18 km $s^{-1}$ to only 165 ± 43 km $s^{-1}$ far off-limb. Beyond this point, the radiance disturbances become diffuse. The increase in propagation speed is small and the acceleration is negligible within the given uncertainties.

The propagation speed becomes supersonic ($> C_S \approx 170$ km $s^{-1}$, for Fe XII line formation temperature) far off-limb in the inter-plume region. Moreover, near the limb region, the Ne VIII and Fe XII lines, which are in phase, show nearly equal propagation speeds for some overlapping region despite having quite different formation temperatures, suggesting that these propagating disturbances are temperature independent. This, together with the presence of oscillations in Doppler width and shift, may suggest that these waves are Alfvénic in nature. Pure Alfvén waves do not cause any density perturbation and thus would not cause any radiance fluctuation. However, in the real case of waves propagating in a density stratified atmosphere, non-linear effect may also cause small density fluctuations leading to radiance changes of a few percent (Tu and Marsch, 1995; Kaghashvili et al., 2009). Moreover, oscillations in the observed line widths can be caused by torsional Alfvén waves (Zaqarashvili, 2003; Van Doorsselaere et al., 2008). Hence, interpretation of these propagating disturbances in terms of Alfvén waves appears quite reasonable.

Furthermore, observed radiance oscillations can also be explained as an LOS effect of entirely incompressible MHD waves as described in Cooper et al. (2003a). In this model, when observed at an angle $\theta$ to the direction of propagation, the wave-induced deformation in a coronal loop causes brightness variations. This is because the amount of optically thin emitting plasma along the LOS changes as a function of time. Thus, the radiance variations can be produced even by entirely incompressible MHD waves.

Conversely, the measured propagation speeds are also consistent with the fast magneto-acoustic mode of propagation within the error bars of the propagation speeds in Ne VIII and Fe XII lines and explain the observed radiance oscillations due to their compressible nature. Hence, interpretation of these propagating disturbances in terms of fast magneto-acoustic waves also appears reasonable.

It should be noted that it is always the apparent propagation speed in the plane of the sky that is measured. The structures carrying the waves most likely form an angle with the plane of the sky and, thus, these propagation speeds are always a lower limit. However, in the case of the inter-plume region, we trace the origin of the wave to an on-disk bright region located at X$\approx -72''$ and Y$\approx 967''$. Assuming roughly radial propagation, this would imply an angle of $\approx 9^{\circ}$ with the plane of sky, leading to a difference between the apparent and real propagation speeds of less than 2 %, a negligible quantity. In the case of the plume, a careful inspection of Figure 5.4 shows that the plume is rooted very close to the visible limb and is lying close to the plane of the sky. This suggests that in this case the difference between the apparent and real propagation speeds is likely very small.

The kind of oscillations which are presented here are very similar to other already reported in the literature (e.g. DeForest and Gurman, 1998; Ofman et al., 2000; Banerjee et al., 2000a, 2001b; Morgan et al., 2004; O'Shea et al., 2006, 2007; Gupta et al., 2009; Banerjee et al., 2009b) in the on-disk and off-limb regions of coronal holes observed with different instruments. Banerjee et al. (2001b) have reported oscillations in on-disk network regions and in inter-plume regions similar to those reported here. Gupta et al. (2009) have calculated the speed of propagation in the on-disk bright region using the statistical technique and the measured speed was of the same order as reported here. All these observations indicate the presence of propagating MHD waves. Recently, McIntosh et al. (2010) detected propagating features in polar plumes using STEREO observations. These authors have interpreted these features in terms of high-speed jets of plasma travelling along the structures which repeat quasi-periodically, with repeat times ranging from 5 min to 25 min. This would be contrary to the widely held interpretation that this observational

phenomenon is due to compressive waves. One should also consider Doppler dimming results from UVCS and SUMER on-board SOHO, which show that velocities above 100 km $s^{-1}$ are reached only above 1.5 $R/R_{\odot}$ in either plumes or inter-plumes (Teriaca et al., 2003; Gabriel et al., 2003, 2005).

To our knowledge, this is the first time that a signature of accelerating Alfvénic waves or fast magneto-acoustic waves originating in an on-disk bright region has been observed in the near and far off-limb regions within 1.2 $R/R_{\odot}$. In the inter-plume region the disturbance is seen propagating up along the whole EIS slot length, whereas in the plume region it becomes diffuse far off-limb. In the inter-plume region the wave propagates farther in the corona with high acceleration, whereas in the plume region it may have been dissipated in the off-limb region. However, the lack of signature at greater heights in the plume may be simply due to merging with the background signal. This suggests that inter-plume regions may be the preferred channel for the acceleration of the fast solar wind. This conclusion is in agreement with earlier reports (Wang et al., 1997; Patsourakos and Vial, 2000; Giordano et al., 2000; Banerjee et al., 2001b; Teriaca et al., 2003).

## 5.6 Conclusions

### 5.6.1 April 2007 Dataset

The first observational detection of longitudinal waves came from analysing polarised brightness (density) fluctuations in white light data. Fluctuations with periods of about 9 min were detected in coronal holes at a height of about 1.9 $R_{\odot}$ by Ofman et al. (1997) using the white light channel of UVCS/SOHO. In a follow-up study, Ofman et al. (2000) determined the fluctuation periods to be in the range of 7 to 10 min. The propagation speeds of the fluctuations indicated values in the range of 160 to 260 km $s^{-1}$ at 2 $R_{\odot}$, which is slightly slower than the acoustic speed at

those heights. DeForest and Gurman (1998), using EIT 171 Å reported detection of outwardly propagating radiance perturbations at distances of 1.01 to 1.2 $R_{\odot}$, gathered in quasi-periodic groups of 3 to 10 periods, with periods of about 10 to 15 min. The projected speeds are about 75 to 150 km $s^{-1}$ and the relative amplitude (in density) was about 2 to 4 %. Usually these waves are observed propagating along the assumed coronal magnetic structures and, thus, along the magnetic field. Their speeds are usually much slower than the expected coronal Alfvén speed, which leads to their interpretation as longitudinally propagating slow magneto-acoustic waves. Slow magneto-acoustic waves follow magnetic field lines and propagate at the local sound speed. We detect the presence of long period oscillations with periods of 10 to 30 min in polar coronal holes within the range of 1 to 1.2 $R_{\odot}$, with a clear signature of propagation with velocities from 75 to 125 km $s^{-1}$, depending on the temperature of line formation. The measured propagation speeds are subsonic, indicating that they are slow magneto-acoustic in nature, which is consistent with earlier reports. Note that this detection has been confirmed through the analysis of data from two separate spectrometers on-board two different satellites. Thus we feel that this simultaneous detection makes the result very robust. We also find that the propagation speed in Fe XII ($\approx$125 km $s^{-1}$) is higher than that in Ne VIII ($\approx$75 km $s^{-1}$), as shown in the bottom panel of Figure 5.8. This may be a temperature effect, as the ratio of the Fe XII to Ne VIII propagation speeds, about 1.7, is close to the ratio of the sound speeds. Different propagating speeds observed in different lines may also be interpreted as an indication of the presence of structures with different temperatures along the LOS (e.g., weak plumes). The observed region can be either a bundle of magnetic threads of different temperatures, or have a transverse temperature profile. However, with the available data this statement remains a conjecture only. Finally, we note that the observed waves have no detectable signature in the LOS velocity, enforcing the idea of compressive longitudinal magneto-acoustic waves.

### 5.6.2 November 2007 Dataset

The analysis of Ne VIII and Fe XII radiance $x$–$t$ maps reveals the presence of outward propagating radiance disturbances in the off-limb and near off-limb regions of inter-plume with periodicities

of about 15–20 min. From the SUMER Ne VIII line radiance $x$–$t$ map, one can infer that the waves originate from a bright location (presumably the foot-point of a coronal funnel) and propagate toward the limb with a speed 25 ± 1.3 km $s^{-1}$. Around the limb the speed has increased to 38 ± 4.5 km $s^{-1}$, reaching 130 ± 51 km $s^{-1}$ off-limb. Further far off-limb, the speed of the propagation becomes 330 ± 140 km $s^{-1}$ as seen in the EIS Fe XII line. Similar propagating disturbances are also seen in the plume region but with negligible acceleration, if any. The waves are not visible far off-limb, suggesting that they may be dissipated or, more simply, merge into the background. The waves as recorded in the inter-plume regions are either Alfvénic or fast magneto-acoustic in nature (Gupta et al., 2010a) whereas the one seen in plumes are more likely slow magneto-acoustic type (Banerjee et al., 2009b). Tu et al. (2005) have conjectured that the solar wind outflow is launched by reconnection at network boundaries between open flux lines and intra-network closed loops. The intra-network closed loops are pushed by supergranular convection toward the network triggering reconnection. This scenario is consistent with our identification of the origin of the propagating disturbances in the inter-plume region with an on-disk bright region. These results support the view that the inter-plume regions are the preferred channel for the acceleration of the fast solar wind.

# Chapter 6

# Nature of Waves in Quiet Sun Region

## 6.1 Context

Though oscillations in the solar chromosphere were first detected in the 1960s, they are not yet well understood as in the photosphere. When the solar atmosphere is observed at chromospheric heights, a bright web-like cellular pattern now known as the 'chromospheric network' pattern is distinguishable in the Ca II H and K lines (Hale and Ellerman, 1904, see Figure 4.1). This Ca II network pattern overlies the photospheric magnetic field concentrations clustered in the supergranular down-flow lanes (Simon and Leighton, 1964; Skumanich et al., 1975). Regions inside the network pattern are called the internetwork. The distinct properties of these network and internetwork regions is subject to intense study (Hasan, 2008).

At chromospheric level, 5 min oscillations were detected in the network while 3 min oscillations were associated with the internetwork regions (Dame et al., 1984). Lites et al. (1993) found the 3 min internetwork oscillations to be well correlated with the oscillations in the underlying photosphere, while the long-period 5–20 min network oscillations were not correlated with underlying photospheric disturbances. Carlsson et al. (1997) observed phase differences between the continuum and chromospheric line intensities and interpreted them as a manifestation of upward propagating waves. Wikstøl et al. (2000) also showed from a phase difference

analysis a preponderance of upward-propagating waves in the upper chromosphere which drove oscillations in the transition region plasma, thus extending the evidence for upward-propagating waves from the photosphere up to the base of the corona. Judge et al. (2001) suggested that the chromosphere oscillates primarily in response to forcing by p-modes, and that they are often strongly influenced by magnetic effects before the oscillations can reach the transition region. Areas termed as 'magnetic shadows' surrounding the quiet Sun network elements which lack oscillatory power in the 2–3 min range were highlighted by Krijger et al. (2001).

Recently, Vecchio et al. (2007) showed that a large fraction of the quiet chromosphere was occupied by magnetic shadows which surrounded the network regions and originated from fibril-like structures observed in the core intensity of the Ca II line. Whereas Kontogiannis et al. (2010) found 3 and 5 min power enhancements around the network, forming power halos at photospheric heights which were replaced by magnetic shadows at chromospheric height which indicated the existence of both upward and downward propagating waves. While studying the magnetic network at the boundary of an equatorial coronal hole, Tian and Xia (2008) found a lack of power at high frequencies (5.0–8.3 mHz), while noting a significant power at low (1.3–2.0 mHz) and intermediate frequencies (2.6–4.0 mHz) above the magnetic network in the chromosphere and lower corona obtained from TRACE 1600 Å and 171 Å passbands, respectively.

In this chapter, we study the wave properties from a statistical point of view using data with a wide temperature coverage. We combine the capabilities of SOT/Hinode, MDI/SOHO, and TRACE and focusing our attention on the distribution of Fourier power over the quiet Sun. We also investigate the influence of small scale network magnetic fields on wave properties. For this, we analyse the power and phase difference between oscillations observed simultaneously in the chromosphere and the low transition region in bright magnetic regions (network), bright non-magnetic and dark non-magnetic (internetwork) regions of the quiet Sun. These observations are further supplemented by SUMER/SOHO data taken in transition region and low coronal spectral lines above these regions[1].

[1]Results discussed in this chapter are submitted for publication.

## 6.2 Observations

Table 6.1: Description of the observations.

| | SOT | TRACE | SUMER |
|---|---|---|---|
| Time (UT) | 11:50 – 16:59 | 11:50:18 – 16:59:46 | 14:06:19 – 16:41:05 |
| Passband/Wavelength | Ca II 3968 Å | 1550 Å | N IV 765 Å, Ne VIII 770 Å |
| Slit/Slot | $(112'' \times 56'')$ | $(384'' \times 384'')$ | $(1'' \times 120'')$ |
| Cadence (s) | 30 | 35 | 65 |

Simultaneous observations obtained near disk centre on $9^{th}$ April 2007 with the Solar Optical Telescope (SOT; Tsuneta et al., 2008b) on-board Hinode, Michelson Doppler Imager (MDI; Scherrer et al., 1995) on-board SOHO, Transition Region and Coronal Explorer (TRACE; Handy et al., 1999) and Solar Ultraviolet Measurements of Emitted Radiation (SUMER; Wilhelm et al., 1995) are used in this work.

TRACE images were obtained in the 1550 Å channel with a field of view (FOV) of $\approx 384'' \times 384''$, a pixel size of $0.5'' \times 0.5''$ and a cadence of 35 s. The Ca II data from SOT were taken with a FOV of $\approx 112'' \times 56''$, a cadence of 30 s and a pixel size of $0.11'' \times 0.11''$. The data were reduced using the standard solar software packages for the correction of missing pixels, cosmic ray hits, CCD bias effects and flat-field effects. All images from Hinode and TRACE were converted to SOHO view (L1). High resolution photospheric line-of-sight (LOS) magnetograms were obtained with MDI at a cadence of 1 min with a pixel size of $0.6'' \times 0.6''$ and a FOV of $\approx 620'' \times 300''$. All the images were co-aligned with respect to TRACE. We used an available procedure for co-aligning TRACE with SOT and MDI data. When images from different instruments are compared, it is important to consider the difference in their spatial resolution. First we created an IDL map for all the instruments which is a structure that contains two-dimensional image data with accompanying pixel coordinate and spatial scale information. We used the routine *coreg_map.pro* available in the SolarSoft library for resizing a map with respect to the other, by binning pixels, along with the routine *derot_map.pro* to de-rotate one map with respect to the time of the other map for solar rotation compensation taking into account the roll angle of

the satellite. These images were cross correlated and offset coordinates were obtained using the *get_corel_offset.pro* routine. These were then applied to SOT and MDI images. A SUMER raster was obtained before the start of the time series observations which was used to visually align with the TRACE images. The accuracy of the alignment was estimated to be within 2″. The SUMER time series were obtained with an exposure time of 16 s with rotational compensation on. In order to improve the signal strength of SUMER, 4 time frames were summed which resulted in an effective cadence of ≈ 65.3 s.

After the alignment, Figure 6.1 shows the location of the SUMER slit and the SOT slot FOV on the TRACE 1550 Å image. Contours on the image give the two polarities of the LOS magnetic field obtained from MDI.

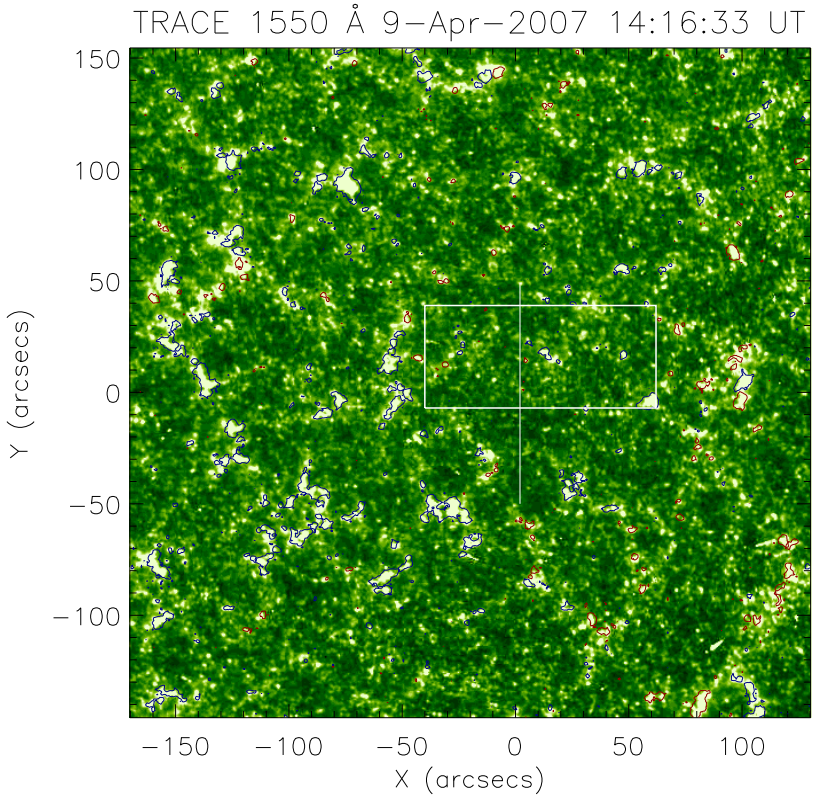


Figure 6.1: Quiet Sun region observed with TRACE 1550 Å passband on $9^{th}$ April 2007. Contour levels show the LOS magnetic field strength ≥ |30| G obtained from the corresponding MDI image. SOT FOV is over-plotted as a rectangular box, while the vertical line gives the location of SUMER slit.

## 6.3 Data Analysis

For our Fourier analysis, we choose the longest overlap data between TRACE, SOT and SUMER from the full time series. The selected TRACE and SOT observations started at 13:05:10 UT and ended at 15:29:41 UT. We had a few minutes data-gap before and after the selected SOT observations. Before this time interval, there was no data available for 12 min 29 s and after this time interval, there was no data available for 30 min 50 s in SOT time series. Data-gaps of a few seconds were still present in the data, these were linearly interpolated during the analysis. During the main time interval, 246 images were obtained in the TRACE 1550 Å passband with a cadence of 35 s, whereas 286 images were obtained with the Ca II broadband filter in SOT with a cadence of 30 s. SUMER time series began at 14:17:19 UT and ended at 16:29:51 UT, in which 488 time frames were obtained with an exposure time of 16 s in the N IV 765 Å and Ne VIII 770 Å spectral lines. For the analysis of the SUMER data, four time frames were binned together to improve the signal. We should note that the selected time series duration for the present quiet Sun oscillation study is longer than any previous study and is suitable to detect longer periodicities.

We extracted two sequences of sub-images from the TRACE data set, one having coverage of the MDI FOV and another one having coverage of the SOT FOV. The FOVs can be seen in Figure 6.1 with the over-plotted magnetic field contours being from MDI data. Similarly, Figure 6.2 shows TRACE and SOT images with the SOT FOV over-plotted with magnetic field contours. This figure also illustrates the accuracy of the co-alignment between the TRACE and SOT data. Figures 6.1 and 6.2 clearly show many bright magnetic (network) and dark non-magnetic (internetwork) regions. These distinguishable regions, gave us an opportunity to compare simultaneously the nature of the Fourier power and phase differences in both regions in a statistical manner. We applied Fourier analysis technique to the TRACE 1550 Å and SOT Ca II images and to the SUMER time series data obtained in the N IV and Ne VIII spectral lines. A variation of the Fourier power with frequency were obtained for each spatial pixel. The powers were then added together in four different frequency ranges from the full frequency range. The chosen frequency

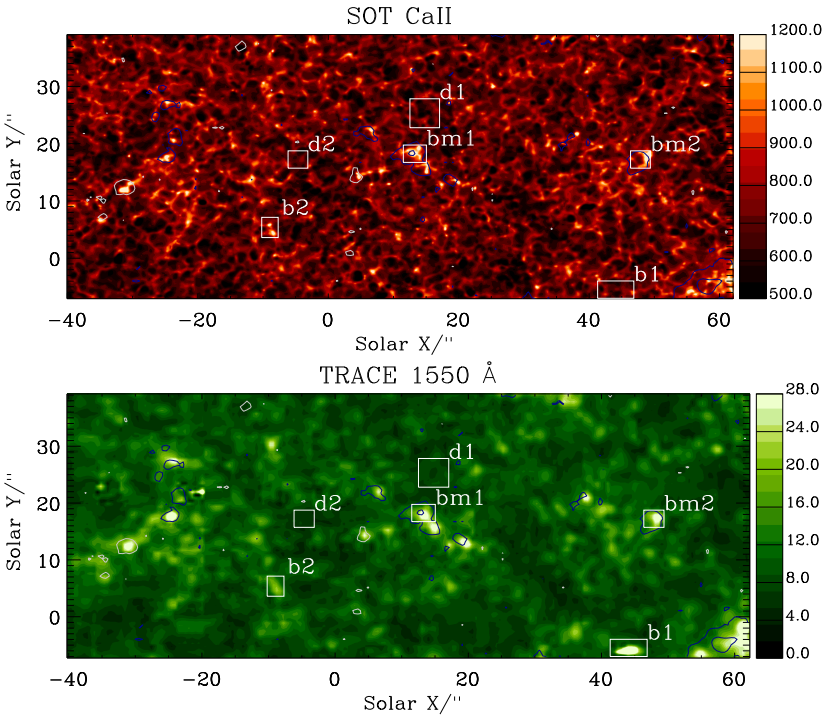


Figure 6.2: Ca II (top) and TRACE 1550 Å (bottom) images over-plotted with the corresponding MDI image. Contour levels give the LOS magnetic field strength of ≥ |25| G. The square boxes (bm1 and bm2), (b1 and b2) and (d1 and d2) correspond to bright magnetic, bright non-magnetic and dark non-magnetic regions, respectively.

ranges are: 4.14–8.27 mHz (2–4 min, to see the 3 min period), 2.76–4.02 mHz (4–6 min, to see the 5 min period), 1.15–2.64 mHz (6–15 min, to see the intermediate periods) and up to 1.15 mHz (above 15 min, to see the longer periods). These power maps can be found in Figures 6.3 and 6.4. In order to study the influence of he magnetic field on the oscillations, we classify three different regions namely, bright magnetic (bm), bright non-magnetic (b) and dark non-magnetic (d) regions. Bright magnetic regions are those where we see enhanced intensity along with co-spatial magnetic field concentrations as recorded by MDI. Bright non-magnetic regions correspond to enhanced intensity locations without detectable magnetic field. Other locations are classified as dark non-magnetic regions. Some specific examples of these regions are marked in Figure 6.2. Figure 6.5 shows the distribution of power with frequency corresponding to all three regions.

A wavelet analysis was also performed on the representative bright (network) and dark (in-

ternetwork) regions as identified in the TRACE 1550 Å *x–t* map (see Figure 6.6). The SUMER *x–t* map is shown in Figure 6.7. Wavelet results corresponding to SOT Ca II, TRACE 1550 Å, SUMER N IV 765 Å and Ne VIII 770 Å spectral lines are shown in Figures 6.8 and 6.9. A phase difference analysis was also performed between SOT Ca II and TRACE 1550 Å passbands. These phases were then added together in all the four frequency ranges mentioned earlier. These phase maps can be found in Figure 6.10. The statistical analysis technique used to calculate the time delay between the propagating waves from the layers of Ca II to the layers of TRACE 1550 Å intensity and corresponding phase delays are plotted in Figure 6.11 for the different regions.

## 6.4 Results and Discussion

Now we will discuss the distribution of power at different layers and phase differences as calculated for different layers of the quiet Sun.

### 6.4.1 Fourier Power Distribution in The SOT Ca II and TRACE 1550 Å Passband

In Figure 6.2, we show intensity images in the SOT Ca II and TRACE 1550 Å passbands for the same FOV. To obtain the oscillatory power distribution in SOT Ca II and TRACE 1550 Å datasets, a standard Fourier power analysis technique was applied to each pixel. While applying this, the standard spatial resolution of each instrument was retained and the original signal was used without any trend subtractions to avoid any kind of bias in the analysis. The resultant Fourier power maps in the frequency ranges 4.14–8.27 mHz, 2.76–4.02 mHz, 1.15–2.64 mHz and up to 1.15 mHz are shown in Figure 6.3 for both SOT Ca II and TRACE 1550 Å passbands and with SOT FOV. While the power maps with full TRACE 1550 Å FOV are shown in Figure 6.4.

*High frequency range:* the frequency range 4.14–8.27 mHz which is centred at 3 min shows a lack of power in bright magnetic (network) regions as compared to neighbouring dark non-

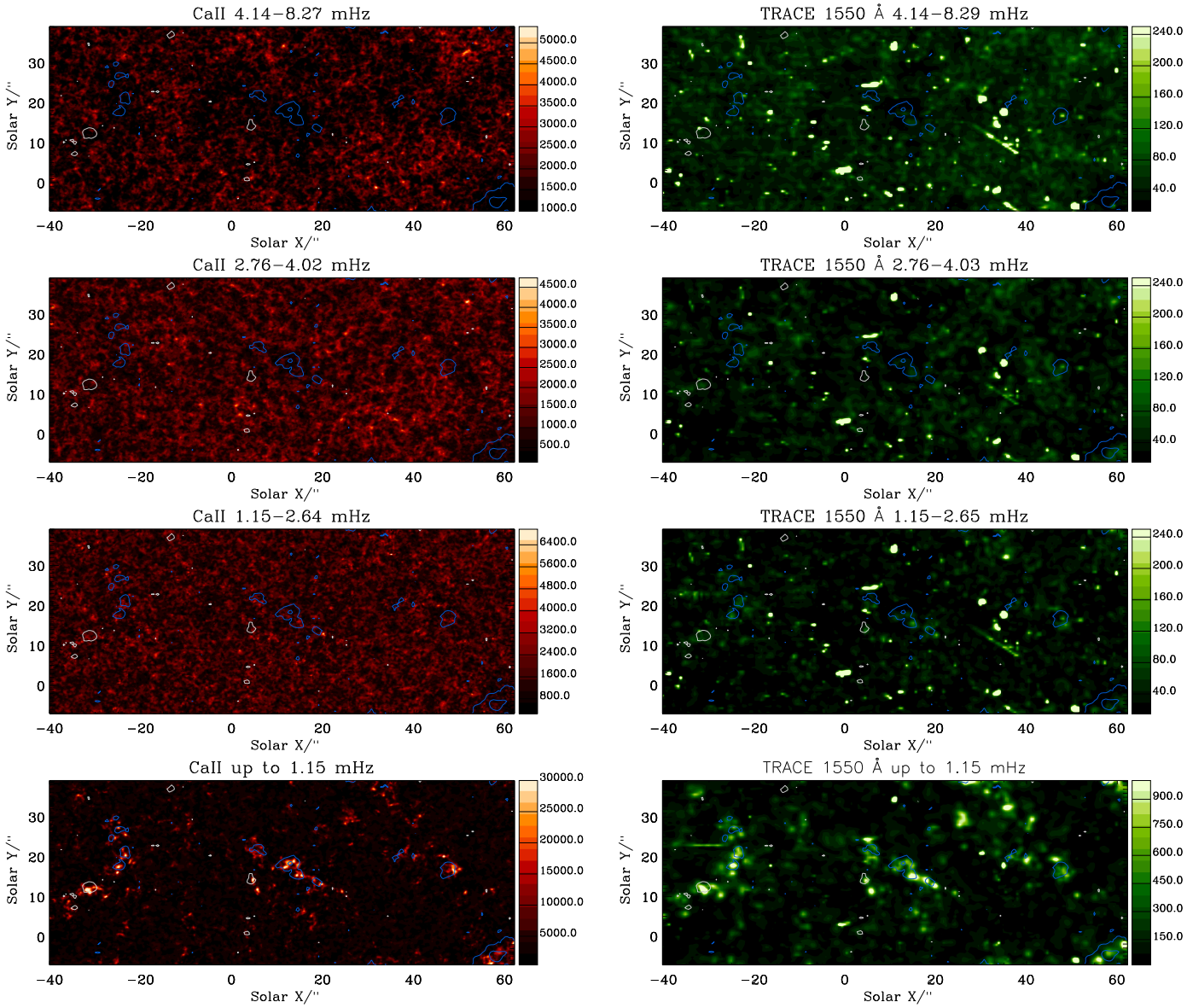


Figure 6.3: Oscillatory power map of Ca II (left panels) and TRACE 1550 Å (right panels) on $9^{th}$ April 2007 in different period ranges as labelled. Contour levels give the LOS magnetic field strength ≥ |25| G measured from MDI.

magnetic (internetwork) regions. This could be due to the presence of magnetic flux in the network regions. As the network photospheric flux tubes expand with height (Gabriel, 1976), chromospheric oscillations that appear to be dominant in the internetwork can be suppressed above the photospheric network elements as reported by Judge et al. (2001); Krijger et al. (2001) and recently by Vecchio et al. (2007); Kontogiannis et al. (2010) for the quiet Sun regions and

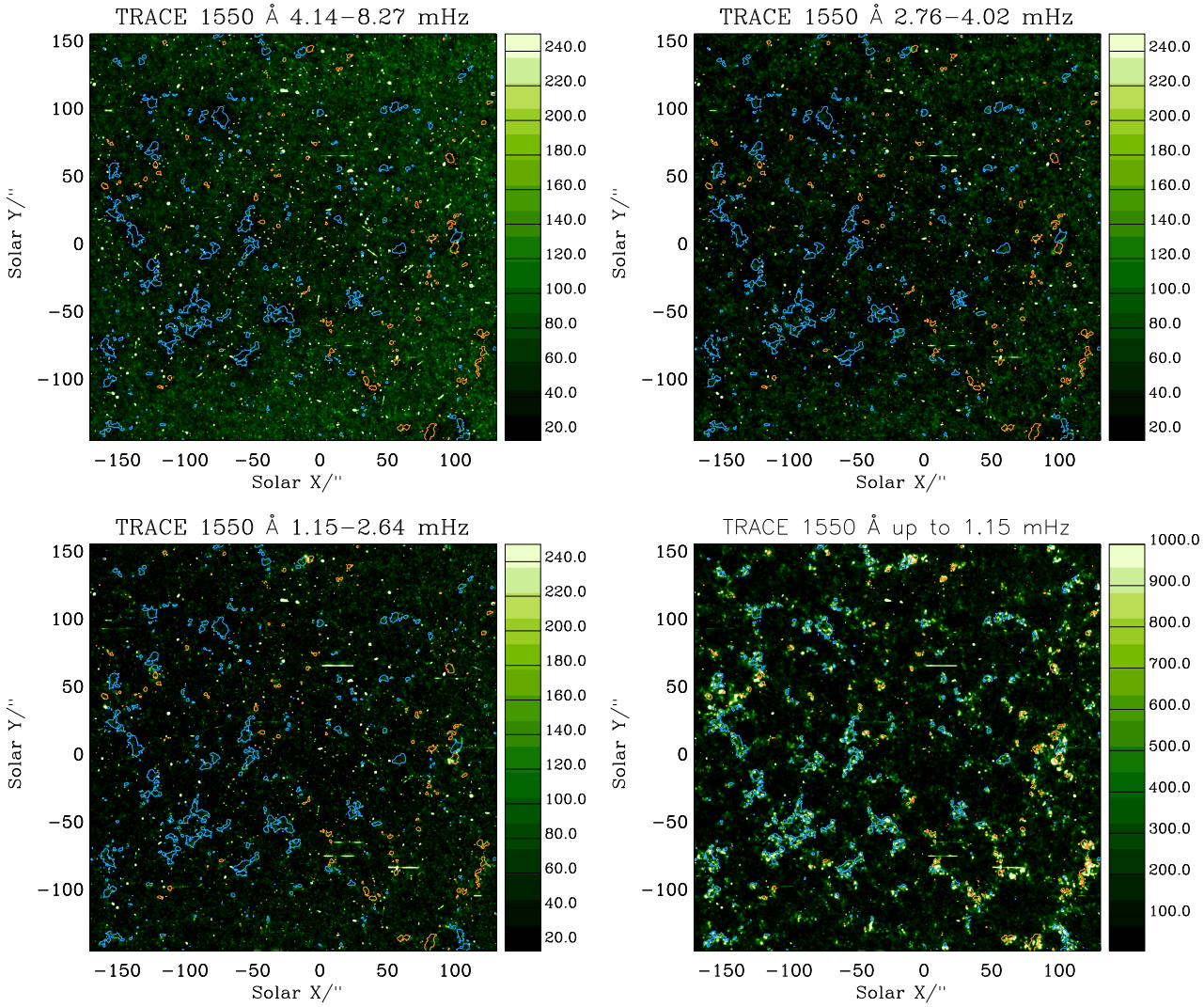


Figure 6.4: Oscillatory power map of TRACE 1550 Å in full FOV on $9^{th}$ April 2007 in different period ranges as labelled. Contour levels give the LOS magnetic field strength ≥ |30| G measured from MDI.

by Tian and Xia (2008) at the boundary of equatorial coronal hole region.

*Intermediate frequency range:* the frequency range 2.76–4.02 mHz which is centred at 5 min shows improved power at bright magnetic (network) regions as seen in the TRACE 1550 Å passband whereas there is still a lack of power in SOT Ca II at some places. There is a reduction in power in internetwork regions in both passbands as compared to the higher frequency range.

The observed power in both these range can be considered as a mixture of photospheric 5 min and chromospheric 3 min oscillations (Fossum and Carlsson, 2005).

The frequency range 1.15–2.64 mHz in TRACE 1550 Å also shows almost the same behaviour but here SOT Ca II shows an enhancement in power in bright magnetic (network) regions.

*Low frequency range:* the frequency range up to 1.15 mHz which covers periods above 15 min, shows a map which is completely dominated by significant power at bright magnetic (network) regions in both SOT Ca II and the TRACE 1550 Å passband.

The significant power at these low and intermediate frequencies can be explained with the inclined magnetic field lines at the boundaries of network structure which provide 'magneto-acoustic portals' through which low-frequency (< 5 mHz) magneto-acoustic waves can propagate into the solar chromosphere (Jefferies et al., 2006). These waves might provide a significant source of energy for balancing the radiative losses of the ambient solar chromosphere.

Figure 6.5 shows the typical Fourier power curves corresponding to each spatial pixel within the specific regions (bm1,bm2,b1,b2,d1 and d2) marked as boxes in Figure 6.2, in both the SOT Ca II (left panels) and TRACE 1550 Å (right panels) passbands. From this figure, it is clear that low frequency oscillations are completely dominating the power distribution in bright magnetic regions (top panels of Figure 6.5). Powers at other frequencies mainly between 3–5 mHz begin to appear in the bright non-magnetic regions (middle panels of Figure 6.5). Whereas power in both frequency ranges become comparable to each other only in the dark non-magnetic regions. These indicate that although the low frequency power is present in all the regions, power at frequencies between 3–5 mHz become comparable to them only in dark non-magnetic regions (internetwork). This is different from the findings of Lites et al. (1993) where they found a low frequency power only in network regions and a high frequency $\approx$ 5 mHz power in internetwork regions.

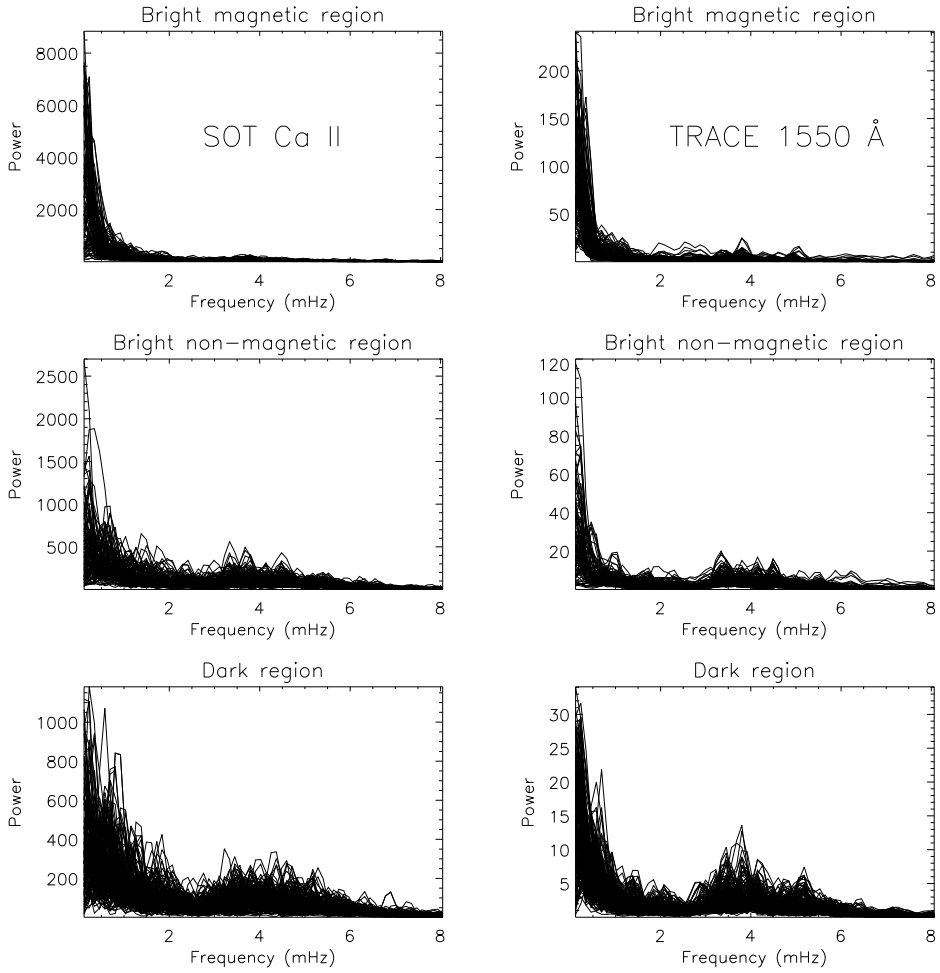


Figure 6.5: Power distribution of Ca II (left) and TRACE 1550 Å (right) for the few selected bright magnetic (bm1 and bm2), bright non-magnetic (b1 and b2) and dark non-magnetic (d1 and d2) regions as indicated in Figure 6.2.

### 6.4.2 Fourier Power Distribution in The SUMER Overlap Region

The Fourier power distribution was obtained across the SUMER slit in the N IV 765 Å and Ne VIII 770 Å spectral lines. From these SUMER lines, time–distance (*x*–*t*) maps were created to distinguish between bright and dark regions. The power distributions were obtained for the radiance distribution. Figure 6.7 shows both the *x*–*t* maps and power distributions. As the signal level in dark regions was very low, it yielded larger errors in the measured LOS velocity. Hence, we used only radiance oscillations for any analysis. In this case, again the bright regions are dominated by

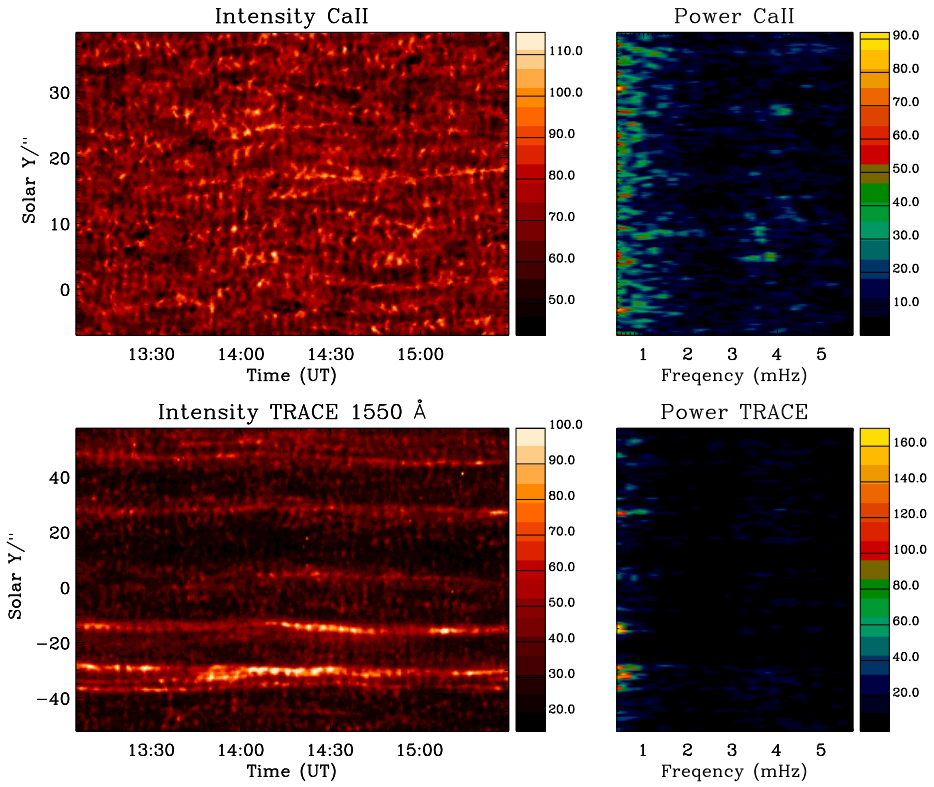


Figure 6.6: Panels show the *x*–*t* intensity map and respective power map of Ca II (top) obtained from SOT BFG images and TRACE 1550 Å (bottom) images at the overlap position with SUMER slit at solar-$X \approx 2''$.

low frequency oscillations in both spectral lines whereas high frequency oscillations are present in both, the bright and dark regions. For the same region, TRACE 1550 Å time–distance and power distribution maps were also created (see Figure 6.6). The power map is relatively cleaner and shows powers at low and high frequencies, distinctly.

### 6.4.3 Wavelet Analysis in Network and Internetwork Regions

In the SUMER overlap region, we identified the network and the internetwork regions from the TRACE 1550 Å *x*–*t* map (see left panel of Figure 6.6). Details on the wavelet analysis which provides information on the temporal variation of the signal, are described in Torrence and Compo (1998). For the convolution with the time series in the wavelet transform, the Morlet

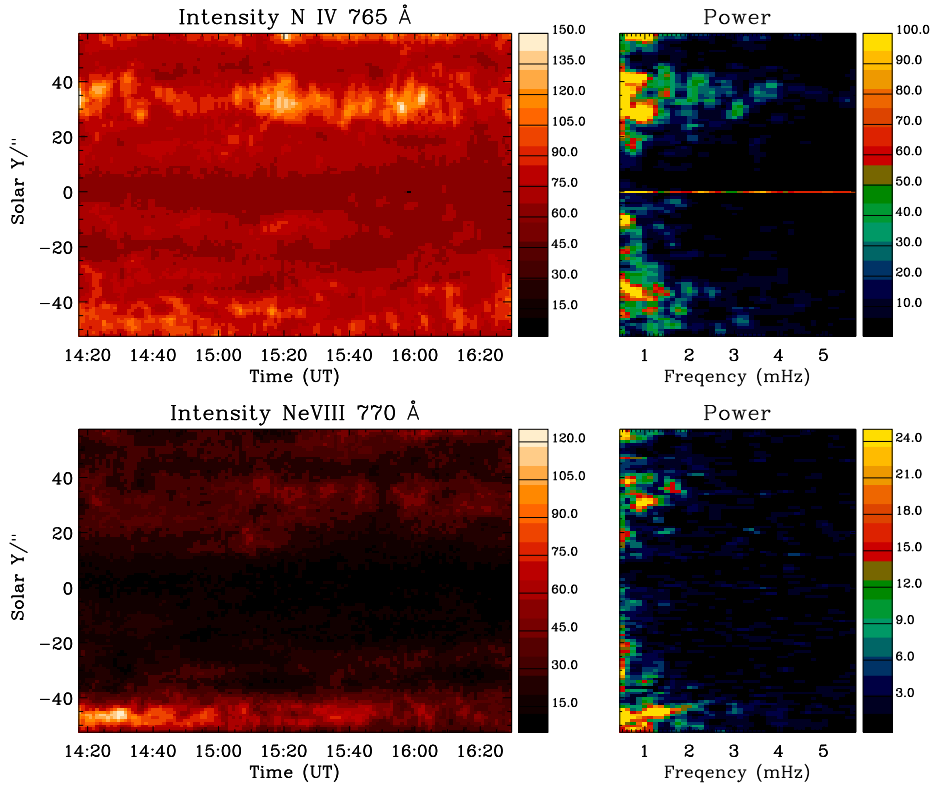


Figure 6.7: Panels show the $x$–$t$ radiance map and respective power map of N IV 765 Å (left) and Ne VIII 770 Å (right) across SUMER slit at solar-$X \approx 2''$.

function is chosen. SOT and TRACE data were rebinned to attain the same spatial resolution of $1''$ as SUMER. As the SUMER slit was positioned at solar-$X \approx 2''$, the identified network and internetwork regions are at solar-$Y \approx 28''$ and $\approx 39''$, respectively. Wavelet analysis was applied on the light curves obtained from SOT Ca II, TRACE 1550 Å and N IV 765 Å and Ne VIII 770 Å data for network and internetwork locations and are shown in Figures 6.8 and 6.9 where the top panels show the variation of the intensity with time.

In the wavelet spectrum, the cross-hatched regions are locations where estimates of the oscillation period becomes unreliable and it is called as the cone-of-influence (COI). As a result of the COI, the maximum measurable period is shown by a horizontal dashed line in the global wavelet plots. The global wavelet plots are obtained by taking the mean over the wavelet time domain which is very similar to the Fourier transform as both are giving the distribution of power

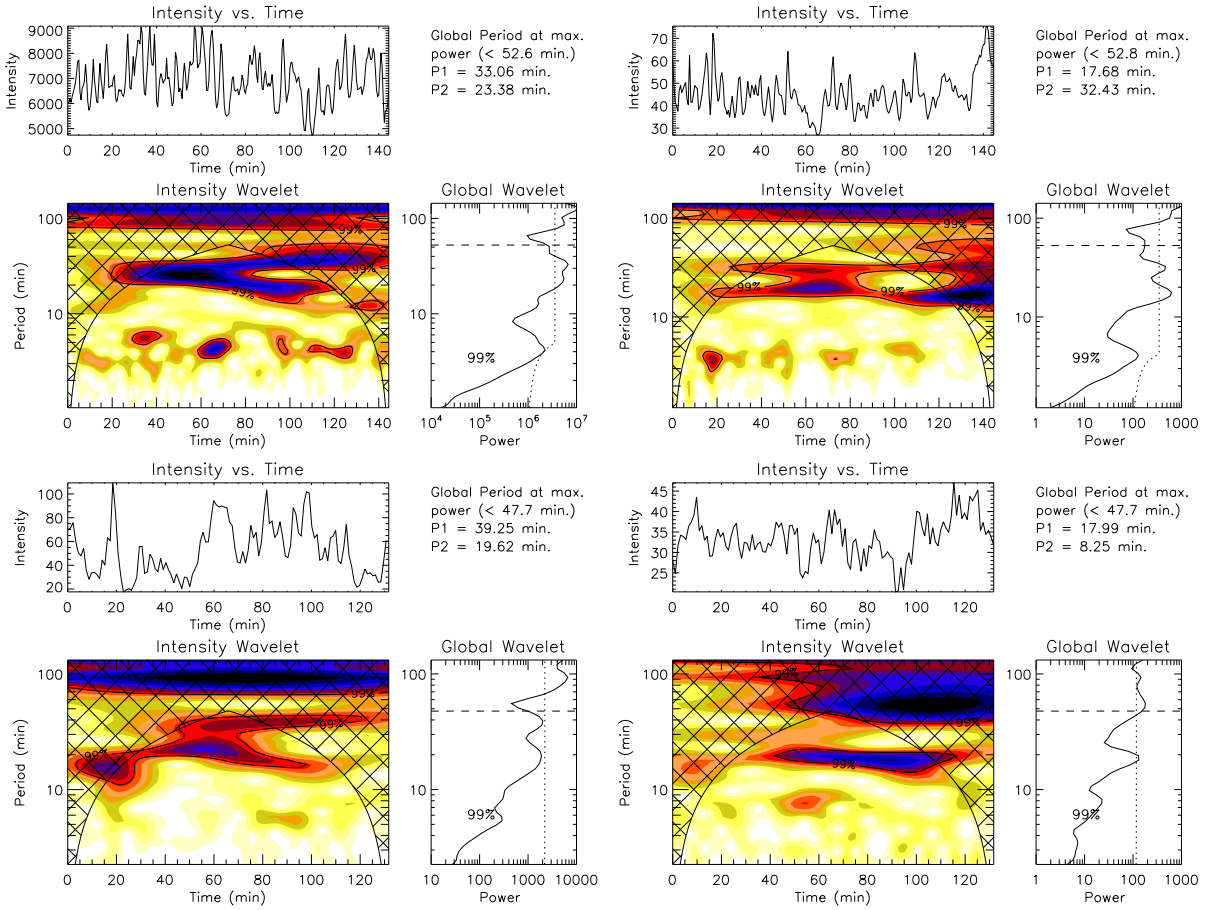


Figure 6.8: Wavelet results for the network location as identified from TRACE 1550 Å $x$–$t$ map at solar-$Y \approx 28''$ and solar-$X \approx 2''$ obtained from light curves of Ca II (top left), TRACE 1550 Å (top right), N IV (bottom left) and Ne VIII (bottom right). In each set, the top panels show The original light curve. Bottom left panels show the colour inverted wavelet power spectrum with 99 % confidence level contours while bottom right panels show the global (averaged over time) wavelet power spectrum with 99 % global confidence level drawn. The periods P1 and P2 at the locations of the first two maxima in the global wavelet spectrum are printed above the global wavelet spectrum.

with respect to period or frequency. The periods at the locations of the first two maximum in the global wavelet spectrum are printed above the global wavelet spectrum.

Here also the original signal was chosen without any trend subtraction to perform the wavelet transform. As a result of this, for few passbands or spectral lines, the peak period falls within the COI and the confidence level of other periods outside the COI appears less. However, in all

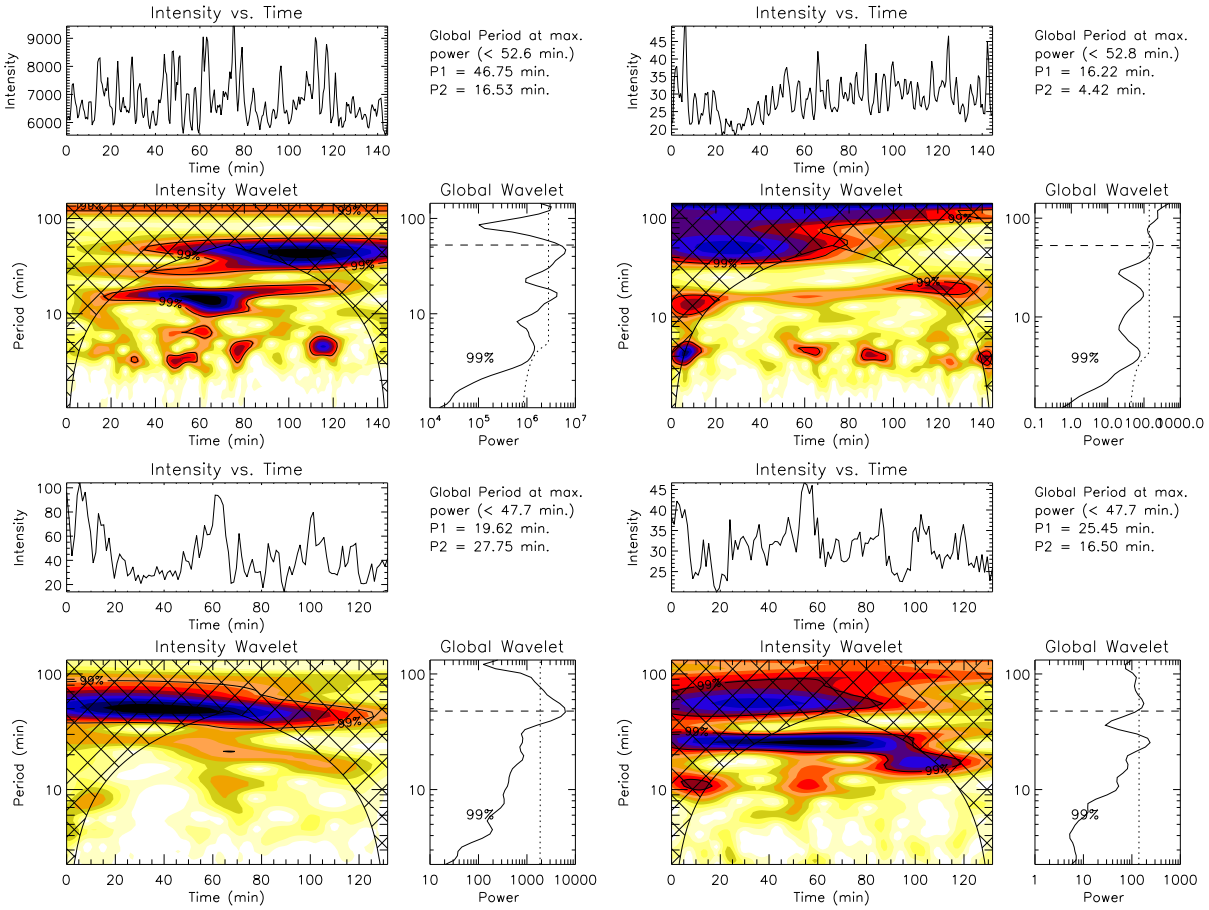


Figure 6.9: Wavelet results for the internetwork location as identified from TRACE 1550 Å $x$–$t$ map at solar-$Y \approx 39''$ and solar-$X \approx 2''$ obtained from the light curves of Ca II (top left), TRACE 1550 Å (top right), N IV (bottom left) and Ne VIII (bottom right). Descriptions about the different panels are same as in Figure 6.8.

Table 6.2: Periods of oscillations as obtained from the wavelet analysis in different lines in network and in neighbouring internetwork regions as identified from TRACE 1550 Å $x$–$t$ map.

| FG/line | Network region | | Internetwork region | |
|---|---|---|---|---|
| (Å) | P1 (min) | P2 (min) | P1 (min) | P2 (min) |
| Ca II 3968 | 33 | 23 | 17 | 4 |
| TRACE 1550 | 18 | 32 | 16 | 4 |
| N IV 765 | 39 | 20 | 20 | 28 |
| Ne VIII 770 | 18 | 8 | 25 | 16 |

the cases, clear peaks of different periodicities are visible in all the wavelet plots and these may become significant upon removal of periodicities lying within the COI. Based on the wavelet analysis plots in Figures 6.8 and 6.9, the detected periodicities outside the COI in network and internetwork regions are summarized in Table 6.2. As mentioned above, we have divided the period ranges as a low period (2–6 min), an intermediate period (6–15 min) and a higher period (above 15 min). From the table, we see that most of the observed periods (P1 and P2) in the network region are in the higher period range from about 20 min to 40 min. These are the periods which are dominating the power maps in the network regions in Figures 6.3 and 6.4. Whereas, the neighbouring internetwork region scenario is slightly different. The lower temperature lines viz., Ca II and TRACE 1550 Å show the dominant peak periods of about 4 min and 16 min which are similar to the powers seen in dark regions of Figures 6.3 and 6.4. The longer period present near 45 min in Ca II can be due to the Hinode orbital effect. While the higher temperature lines viz., N IV and Ne VIII show the dominant peak periods in the range 15–30 min which are more network rather than internetwork oscillation type. This can be explained as the expansion of the network region with height which are clearly seen in the *x*–*t* maps (see Figures 6.7 and 6.6). The network region identified from TRACE 1550 Å *x*–*t* map at solar-$Y \approx 28''$, when seen in N IV and Ne VIII *x*–*t* maps appears relatively broader. Due to this effect, internetwork region at solar-$Y \approx 39''$ as identified from TRACE 1550 Å could have been overshadowed by the expansion of a network region when seen at higher heights in the atmosphere through N IV and Ne VIII spectral lines. The smaller periods of internetwork nature begins to appear only after moving away $5'' - 6''$ in N IV and $9''$ in Ne VIII spectral lines.

Lites et al. (1993) found that the long period network oscillations in the chromosphere are not directly correlated with velocity fluctuations in the photosphere immediately underneath. Thus, they concluded that these disturbances are either confined to the chromosphere or are excited by photospheric events that take place at some horizontal distance from the point of observation. Spicules and their activities are closely related to the chromospheric network which extend upwards across the chromosphere reaching up to the height of the lower corona having typical life time of 5–15 min and longer (Beckers, 1972; Zaqarashvili and Erdélyi, 2009). Hence,

these spicules could be responsible for driving these long period network oscillations.

### 6.4.4 Phase Differences between SOT Ca II and TRACE 1550 Å Passband

As we see from the power maps in Figure 6.3 and oscillation periods from Table 6.2, the Ca II (chromosphere) and TRACE 1550 Å (low transition region) passbands show similar kind of oscillations. Hence, it is most likely that the waves producing these oscillations propagate between the different temperature regions as covered by both passbands. To investigate whether this is actually the case, we measured the phase delays in intensity between the two passbands as a function of frequency for each of the measurable pixels in the image. The SOT Ca II image array was rebinned to the spatial resolution of the TRACE instrument and the time series was linearly interpolated to obtain the same effective cadence as in the TRACE 1550 Å passband.

The phases were calculated from cross power spectral estimates, following the techniques outlined in Doyle et al. (1999), and is also described in Appendix B. In the similar way as we averaged the Fourier power in four bands, here we averaged the phases in four period bands and assigned an average phase difference to each pixel in each band. The resultant phase difference maps in the four frequency bands are shown in Figure 6.10. In the maps, brighter pixels correspond to positive phases (i.e. upward propagating waves), whereas darker pixels correspond to negative phases (i.e. downward propagating waves). Figure 6.10 clearly shows that the phase map for the high frequency band is globally darker in nature when compared to the phase maps of or the lower frequency bands. The phase map of the lowest frequency band (up to 1.15 mHz with periods 15 min and above) appears to be the brightest as compared to the other frequency ranges globally. This indicates the frequency dependent nature of the phase distributions.

For high frequency bands, the phases are more negative in nature whereas for low frequency bands, the phases are more positive. In sec. 6.4.1, we pointed out that low frequency power is mainly concentrated in network regions, whereas internetwork regions have both low and high

frequency powers. Hence, we interpret the positive phases at low frequency bands to be mainly due to upward propagating waves present in both network and internetwork regions, whereas the negative phases at high frequency bands are due to downward propagating waves in the internetwork regions. Also when each map is seen closely, a small mesh like structures is seen all over which indicates that the upward and downward propagation are in the neighbourhood. It is therefore difficult to identify the preferred locations of these meshes either in the network or in the internetwork regions.

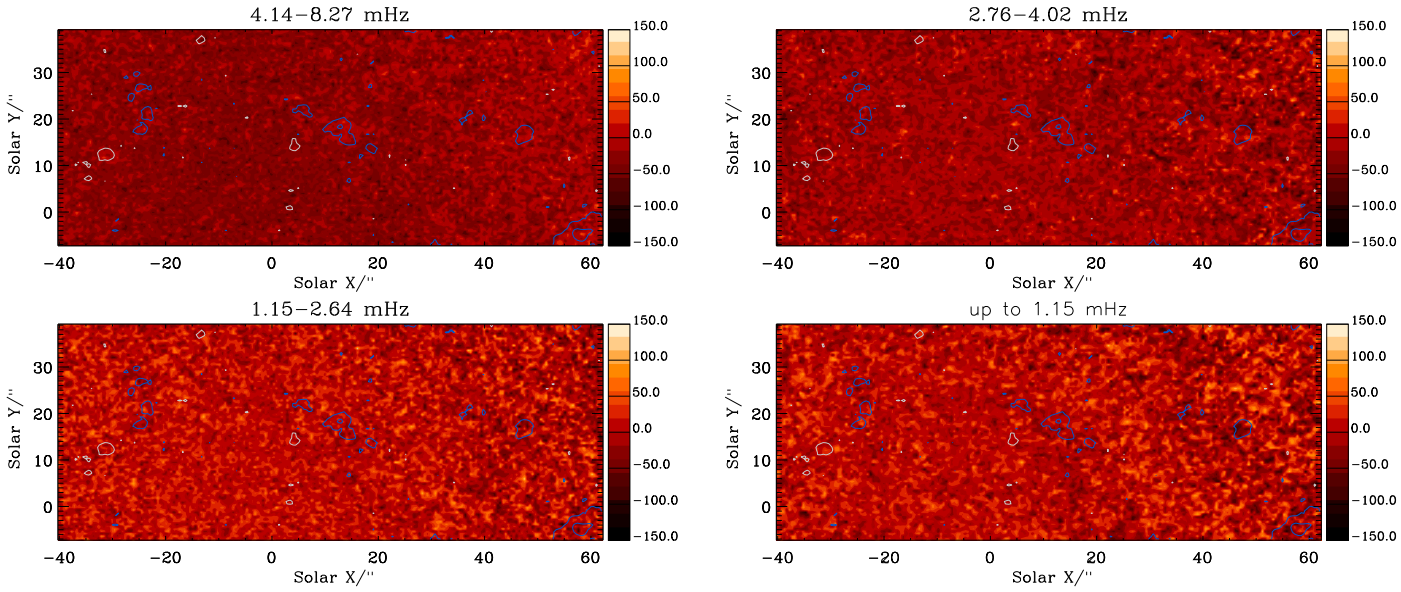


Figure 6.10: Phase difference maps obtained between Ca II and TRACE 1550 Å on $9^{th}$ April 2007 in different frequency bands as mentioned on the plot. Contour levels give the LOS magnetic field strength ≥ |25| G measured from MDI. Colour scales are in degrees.

Now for a specific location if one looks at the phase difference as a function of frequency it is governed by the equation (Athay and White, 1979):

$$\Delta\phi = 2\pi f T \tag{6.1}$$

where $f$ is the frequency and $T$ the time delay in seconds, the phase difference will vary linearly with $f$, and will change by 360° over frequency intervals of $\Delta f = 1/T$. This will give rise to parallel lines in $\Delta\phi$ versus $f$ plots at fixed frequency intervals ($\Delta f = 1/T$), corresponding to a

fixed time delay $T$. Hence it is possible to measure the time delay of wave propagation between two heights in the atmosphere for a specific location. To obtain the time delay corresponding to different regions viz., bright magnetic, bright non-magnetic and dark non-magnetic as marked in Figure 6.2, a phase distribution plots in Ca II and TRACE 1550 Å passbands were produced for these regions. Only phases (corresponding to each spatial pixel) where the squared coherencies are greater than a significance of 95.4 % ($2\sigma$) were used in the analysis (see O'Shea et al., 2006, 2007; Gupta et al., 2009). The errors in the phase was calculated based on the equation (A23) of Doyle et al. (1999). The calculated phase delays were plotted over the full $-180°$ to $+180°$ ($360°$) range and as a function of the measured oscillation frequency for all the three regions (see Figure 6.11). As expected, the phases were lined up along an inclined line as predicted by the phase equation (Equation 6.1) for all three regions. A straight line was fitted by taking into account all the phase point. From the slope of this straight line, the measured time delays are 10.3 ± 3.8 s, 23.1 ± 2.9 s, 28.7 ± 3.0 s for bright magnetic, bright non-magnetic and dark non-magnetic regions respectively. In this case, measured time delays are very small, therefore the fixed frequency intervals ($\Delta f = 1/T$) for the parallel lines is very large, and hence only one line

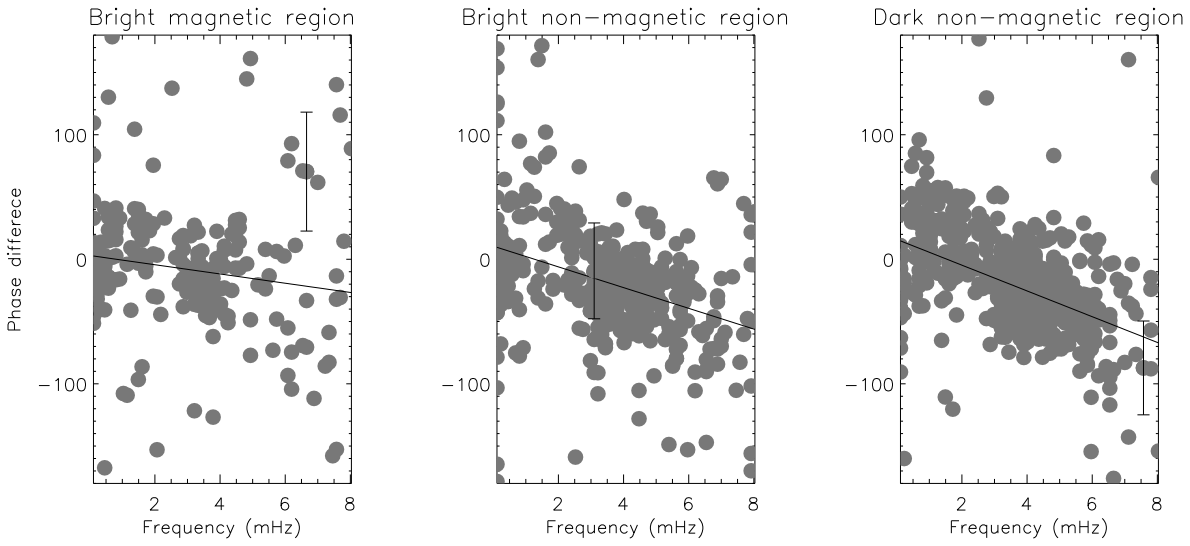


Figure 6.11: Different panels show the phase distribution of Ca II and TRACE 1550 Å for the selected bright magnetic, bright non-magnetic and dark non-magnetic regions and obtained time delays are 10.3 ± 3.8 s, 23.1 ± 2.9 s and 28.7 ± 3.0 s, respectively.

is visible in the plot as compared to the many parallel lines in previous studies. The measured small delays between two passbands indicates that these two covered regions are either formed very close in the solar atmosphere or wave propagation speed from one layer to another is very high or both. This analysis also indicates that the wave speed is smaller in non-magnetic regions as compared to magnetic regions.

## 6.5 Summary and Conclusion

Quiet Sun oscillations have been studied using the Fourier power and phase difference analysis from the intensity time series observed simultaneously in the SOT Ca II and TRACE 1550 Å. Oscillations were further mapped to transition region and low coronal heights using the SUMER N IV and Ne VIII spectral lines, above the bright network and its neighbouring internetwork regions. Fourier power maps reveal that, 3 min and 5 min power is suppressed around the bright magnetic network regions at chromospheric heights and suggest the existence of 'magnetic shadows' as seen recently by Vecchio et al. (2007); Tian and Xia (2008) and Kontogiannis et al. (2010), whereas above the 15 min period range we see very high power above the magnetic network, which forms the power halo like structure. Low period oscillations are only dominant in dark non-magnetic regions. Wavelet analysis reveals the presence of 15–30 min periodicities at chromospheric, transition region and low coronal heights corresponding to network regions. Intensity $x$–$t$ map at these heights indicates that the size of the magnetic network region is increasing with height which suppresses the internetwork oscillations. Phase difference analysis performed on SOT Ca II and TRACE 1550 Å passbands indicates that phases are frequency dependent. Time delay analysis between these passbands indicates different time delays corresponding to magnetic and non-magnetic regions.

As explained in Jefferies et al. (2006), the low frequency photospheric oscillations can propagate into the solar chromosphere through 'magneto-acoustic portals'. In a similar way these long period waves (> 5 min) can propagate up to coronal heights through inclined magnetic field lines

which could reduce the cut-off frequency (De Pontieu et al., 2004). Whereas if we look in open field regions, longer periods of 10–15 min have been detected along a polar plume (DeForest and Gurman, 1998; Banerjee et al., 2000a), and were explained as compressive waves by Ofman et al. (1999), 15–20 min period waves along inter-plume regions were observed by Gupta et al. (2010a) and explained as Alfvénic or fast mode waves (see Chapter 5). Banerjee et al. (2001c) has observed 2–4 mHz network oscillations in low chromospheric and transition region lines in both intensity and velocity, which were interpreted in terms of kink and sausage waves propagating upwards along thin magnetic flux tubes. Here intensity oscillations may result from the propagation of magneto-acoustic waves which could provide significant energy to heat the solar atmosphere. To extend this work we need spectral imaging data to identify the wave mode. This requires acquisition of long duration spectral and imaging data which may be obtained from the future observations from EIS and SOT on-board Hinode and AIA and HMI on-board SDO. In order to establish whether these waves are transverse or longitudinal to the magnetic field, observations of magnetic oscillations at varying limb distances are needed to measure the significant horizontal components of these motions.

# Chapter 7

# Oscillations in Corona Observed During Total Solar Eclipses

## 7.1 Context

It has been recognized that magnetic fields play an important role in heating of the solar corona. The identification of the process or processes responsible for coronal heating still remains an unsolved problem. The existence of fast or slow mode magneto-hydrodynamic waves in the solar corona is expected to cause intensity and velocity oscillations in the solar corona in the range of 1 Hz and lower frequencies (Ionson, 1978). The model by Hollweg (1981) indicates that the coronal plasma is heated by the damping of magneto-hydrodynamic (MHD) waves propagating from the lower solar atmosphere and dissipating through ion viscosity and electrical resistivity. Models by Porter et al. (1994) shows that waves with short periods could play a significant role in heating of the corona. The fast-mode MHD waves on the level of 1 % of the total radiative power could carry enough energy to heat the corona to millions of Kelvin. The typical cadence time of space based EUV imagers is 10 s or higher, which gives the minimal period of detected waves to be about 1–5 min as described in the previous chapters. Thus for the detection of propagating fast waves guided by coronal loops, the space based EUV imagers can not normally be used. On the other hand, time resolution of a second or better which can be achieved with ground

based coronographs, radioheliographs or during eclipses can be used to detect the propagating fast waves like Alfvén or fast MHD waves.

Koutchmy et al. (1983) made the spectroscopic observations in the green emission lines using a coronagraph and found evidence of fluctuations in the velocity measurements but did not detect intensity oscillations; however, Pasachoff and Landman (1984) did detect excess power in this emission line in the frequency range of 0.5–2.0 Hz using intensity measurements made during the total solar eclipse. During the total solar eclipse of 24 October 1995, Singh et al. (1997) made photometric measurements at a location on the solar corona in continuum with a photometer operated at 50 Hz. These intensity oscillations in the range of 0.2–0.02 Hz were interpreted in terms of fast magneto-acoustic waves. Again Cowsik et al. (1999) found the existence of intensity oscillations with similar periods but at some of the locations in the solar corona. The association of these locations with the coronal features could not be established due to limitations of observations. Williams et al. (2001, 2002); Katsiyannis et al. (2003) reported the observational discovery of rapidly propagating compressible wave trains in coronal loops with the SECIS instrument during a total solar eclipse of 11 August 1999. As the observed speed was estimated at about 2100 km $s^{-1}$, these waves were interpreted as fast magneto-acoustic modes. The waves were observed to have a quasi-periodic pattern with a mean period of about 6 s. They made the observations with frequency around 50 Hz at 12-bit resolution. While Pasachoff et al. (2002) made observations during the same eclipse at a slower rate of 10 Hz resolution but higher photometric accuracy and dynamic range of 16-bit. A Monte Carlo model of the data obtained by Pasachoff et al. (2002) suggests the presence of enhanced power, particularly in the range of 0.75–1.0 Hz and they concluded that MHD waves remain as a viable candidate for coronal heating.

During the total solar eclipse of March 29, 2006 we obtained images of the solar corona in the green and red emission lines with high cadence. Whereas during the total solar eclipse of July 22, 2009 we performed high resolution slit spectroscopy around the green and red emission lines simultaneously at a high cadence. In this chapter, we present the observation of intensity oscil-

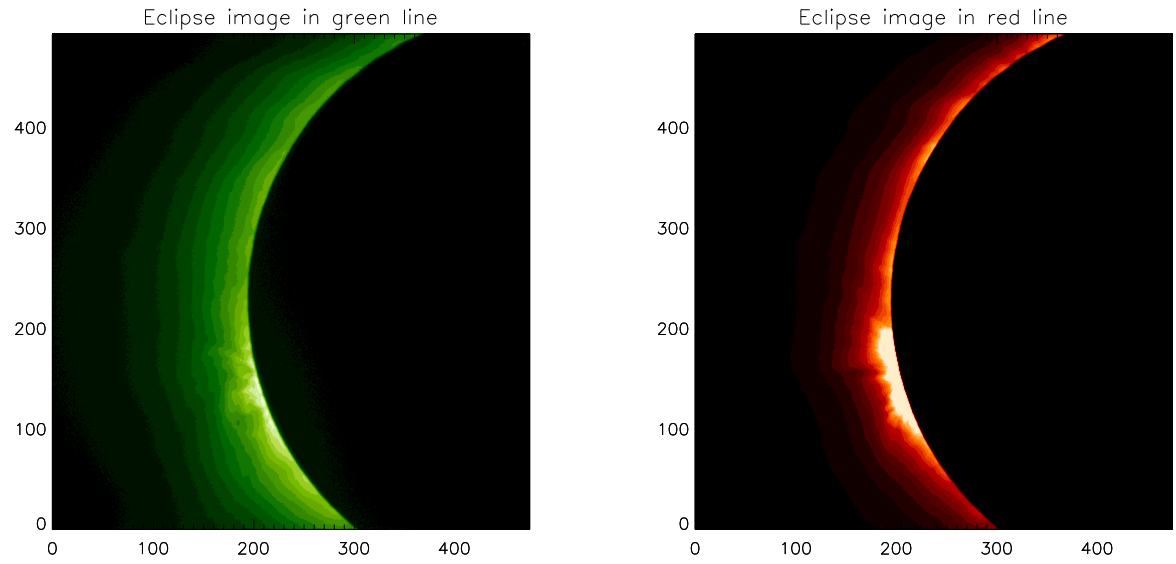


Figure 7.1: Intensity image of the green line (left panel) and red line (right panel) at the end of March 29, 2006 solar eclipse sequence.

lations and its associated location with the coronal features from the imaging data and present new results of the solar corona in terms of wave detection and diagnostics from the spectroscopic data.

## 7.2 Observations and Data Processing

### 7.2.1 Eclipse Observation on March 29, 2006

A camp was set up near a swimming pool of Sural Hotel at Manavgat (latitude 36° 49′ 8.6″ ; longitude 31° 18′ 29.2″ and elevation 20 m), Antalia, Turkey. Two 35 cm Meade telescopes were used to image the Sun and solar corona directly on the two CCD cameras. A focal length of 355.6 cm of the telescope yielded a solar image of 32.3 mm diameter. The 0.3 nm passband filters centred at 6374 Å and 5303 Å were kept near the focal plane separately in the two telescopes to enable us to record the solar corona in these emission lines simultaneously. The Peltier-cooled

CCD cameras with pixel size of $13.5 \times 13.5$ $\mu m^2$ provided an image scale of $0.8''$ pixel$^{-1}$. To make high cadence observations we decided to bin the output from the CCD cameras by $2 \times 2$, but after the image test during the eclipse we binned the output from the red line camera by $4 \times 4$ to enhance the signal and save the read out time. The green line images were taken by binning the camera output by $2 \times 2$ only. The data were read at 1 MHz with 16-bit. The coronal image was off centred at the camera since the $27.6 \times 27.6$ mm$^2$ size of the CCD chip was smaller than that of the size of the solar image. We made the observation of the solar corona on the east limb to enable us to monitor the image on the screen during the partial phases of the eclipse. The green line images could be recorded for 162.25 s with a cadence of 2.95 s with exposure time of 100 ms where as red line images could only be recorded for 80 s with a cadence of 2.0 s with exposure time of 300 ms due to last minute problem in the computer system. Time sequence observation for both the lines began at different times but ended at the same time just before the totality. It is very important to align the images using cross correlation technique. The last image taken just before the end of totality in both the lines has been used to cross correlate the images which results in the aligned images. After alignment the same pixel location corresponding to the two images can be chosen for comparing the oscillation patterns as observed by two different temperature lines. Figure 7.1 shows the images of the part of the solar corona recorded in the green and red lines respectively. The sky transparency and stability during the total solar eclipse was very good.

### 7.2.2 Eclipse Observation on July 22, 2009

We have made relatively high resolution spectroscopic observations during the total solar eclipse of July 22, 2009. The experiment was conducted at a location by the side of a big reservoir at Anji (latitude 30°28.1' N; Longitude 119°35.4' E; Elevation 890 m), China. A two mirror coelostat with first mirror of 30 cm and second mirror of 20 cm was installed at the location about 15 days before the eclipse date. The alignment of the coelostat was done using a 12.2 m focal length lens to form a sufficiently large image of the Sun to monitor the drift of the solar

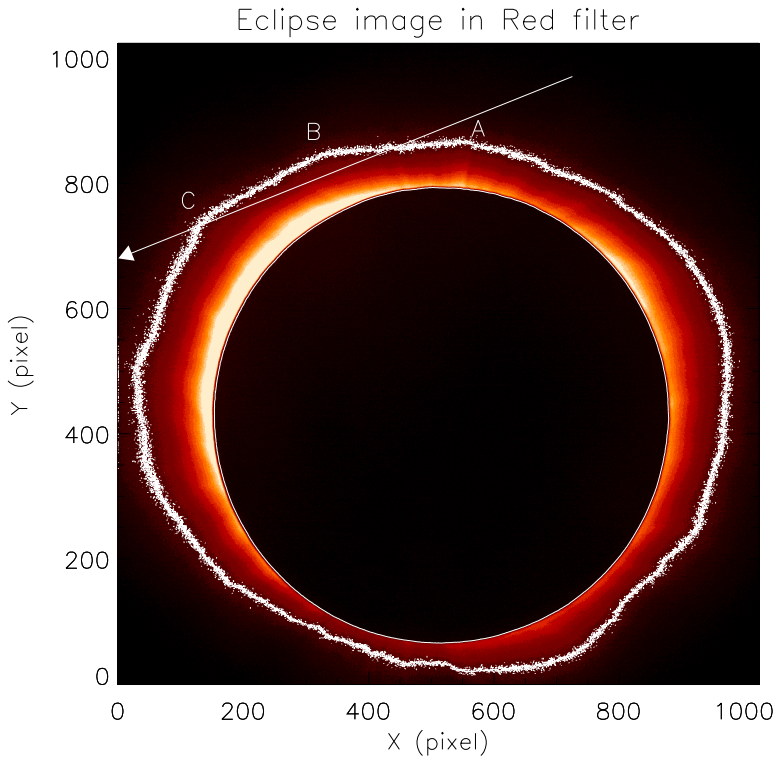


Figure 7.2: Position of the slit over-plotted on the context image on July 22, 2009 solar eclipse as recorded by the red filter. Arrow indicates direction of ascending order of slit pixel numbers. Letters A, B, and C indicate different magnetic structures along the slit.

image. The axes of the first mirror were adjusted before the eclipse day so that there was no noticeable drift of the image at the epoch of eclipse for about 15 min. A 10 cm objective lens with f-ratio of 10 formed 9.2 mm size image of the Sun on the slit of the spectrograph. The 130 micron slit of the spectrograph provided a spatial resolution of $26.7''$. A broad pass band interference filter with transmission from 5000–6600 Å was kept in front of the slit to separate out the various diffraction orders. We used a grating with 600 lines $mm^{-1}$ blazed at 2 micron at an angle such that we could obtain spectrum around the $3^{rd}$ order red and $4^{th}$ order green lines simultaneously using two CCD cameras, one for the red line and other for the green line. The spectrograph was operated in Littrow mode using 1.4 m focal lens with f-ratio of 10. The slit width of 130 micron limited the spectral resolution of 0.43 Å and 0.30 Å around the red and green emission lines respectively. Whereas the 13 micron pixel of the CCD camera was capable of providing a resolution is 0.043 Å and 0.030 Å respectively, in the red and green wavelengths.

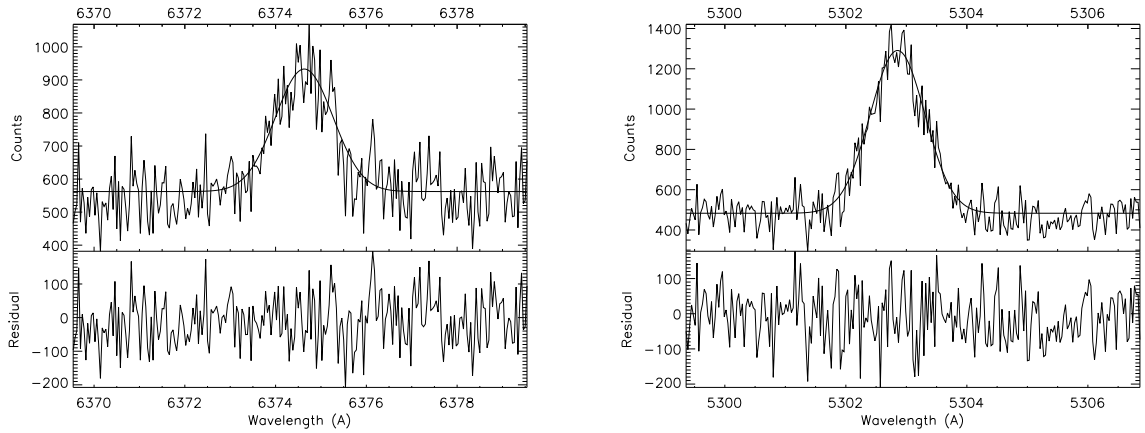


Figure 7.3: The left (right) panel shows the typical red (green) emission line profile obtained during July 22, 2009 solar eclipse at a location and over-plotted continuous line is the Gaussian function with a constant background fitted to the profile. The bottom panels give the residual while fitting the function.

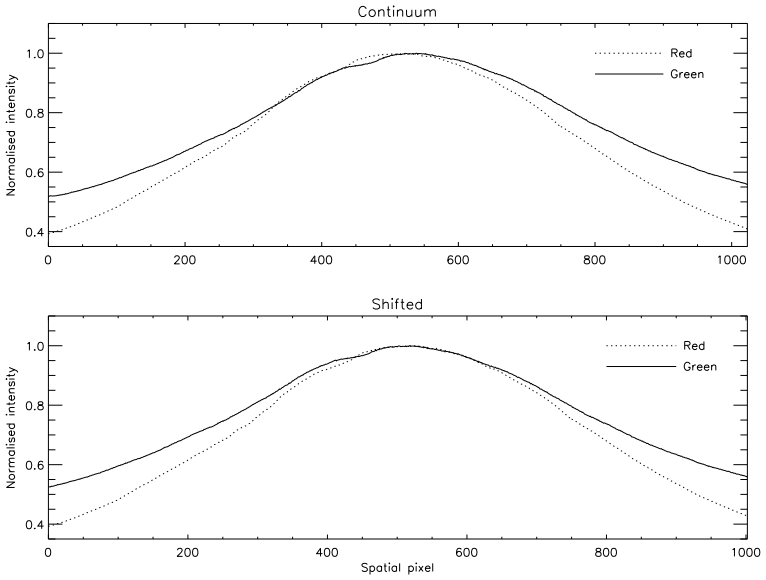


Figure 7.4: The top panel shows continuum intensity variation along the slit around the red and green wavelength range window on July 21, 2009 (a day before solar eclipse). Difference in peak position gives the offset between two windows which is about 21 pixels. The bottom panel shows the intensity variations after shifting the green window slit by 21 pixels.

We used $1k \times 1k$ Peltier cooled CCD camera of ANDOR make with frame transfer mode to record the spectra. The CCD cameras with 14-bit read out at 10 MHz were capable of providing spectra at the rate of 8 frames per second. The gains of the CCD camera were set at 200 to enhance the

signal to a reasonable level. Our tests with the Sun and moon indicated that an exposure time of 200 ms may be sufficient to take the spectrum of the solar corona but an exposure during the totality indicated that we need to give an exposure of 5 s to get good signal. This was probably due to the reason that the corona was week and the nearest point of the spectrograph slit was at 1.15 $R/R_{\odot}$ from the centre of the solar disk. We could get time sequence spectra in the green and red emission line for 270 s with an exposure time of 5 s after a trial exposure during the totality. In all we got 54 spectra in each line with good signal to noise ratio even though spectra appear little noisy due to high gain of the cameras. The position of the slit used for our analysis has been plotted over the eclipse image taken in red filter during the same time interval in Figure 7.2. Here the arrow indicates towards the increasing number of spatial pixels. Figure 7.3 shows the typical spectra obtained in the green and red emission lines. The spectroscopic data was recorded on $1k \times 1k$ CCD as 1k spatial pixels and 1k wavelength pixels. Many spatial pixels, corresponding to away from the limb and in the polar region did not record sufficient signal and hence have not been used to study the oscillations. To align spatial locations in the red and green lines spectra, we have used the simultaneously obtained green and red line spectra of the solar disk taken on 21st July, 2009 (a day before solar eclipse). We have taken the average of 50 frames, and located the pixel at which the intensity becomes maximum, the point of closest approach between the slit and the solar limb. Comparison between the two intensity distribution curves yields an offset of 21 pixels between the red and green line (see Figure 7.4). From the wavelength pixels, 250 pixels centred on green and red lines were chosen to derive the observed line profiles. To increase the signal to noise ratio, a four pixel binning have been applied on the spatial pixels. The resultant line profiles obtained from this are then fitted with the single Gaussian function and a constant background. Representative red and green line profiles corresponding to a typical location are shown in Figure 7.3. Further analysis has been done to study the variations of the line parameters in the spatial domain and temporal domain separately to have flexible approach in averaging the data in time and space. The continuum background has been used to normalize the respective red and green intensity because of passing clouds during the observations and used for further analysis. Figure 7.5 shows the variation of normalized intensity of red and green line with spatial pixels. It clearly shows different intensity distribution in green and red line (the

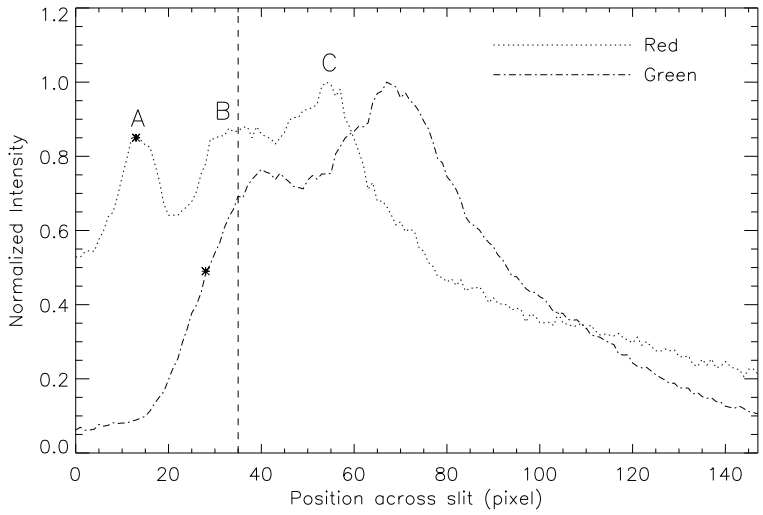


Figure 7.5: Variation of intensity along the slit in red and green line during July 22, 2009 solar eclipse. Variation is plotted after taking into account the offset obtained on previous day. The asterisk on two lines indicate location where oscillations are shown using the wavelet technique. The vertical dashed line indicates the position of closest approach between limb and slit. Letters A, B, and C indicate different magnetic structures along the slit.

intensity variations do not match) which could be attributed to the multi-loop and multi-thermal structures present in the corona. We will focus on two locations in the corona marked as asterisk symbols in Figure 7.5 for detailed discussion and comparison. The vertical dashed line indicates the position of closest approach (nearest point to the Sun).

## 7.3 Results from 2006 Eclipse

### 7.3.1 Analysis of Oscillations

In the top panel of Figure 7.6 we show the variation of intensity with time (in raw counts) for the green line. To study the oscillation properties we have subtracted the trend that may be due to variation in sky brightness as the totality progresses or long period variation and we plot the relative intensity variation in the lower panel of Figure 7.6. Because the coronal oscillations

often vary over time, the wavelet transform, which allows analysis on localized variations, is more suitable than the traditional Fourier analysis for our study. Details on the wavelet analysis, which provides information on the temporal variation of a signal, are described in Torrence and Compo (1998). For the convolution with the time series in the wavelet transform, we chose the Morlet function, as defined in Torrence and Compo (1998).

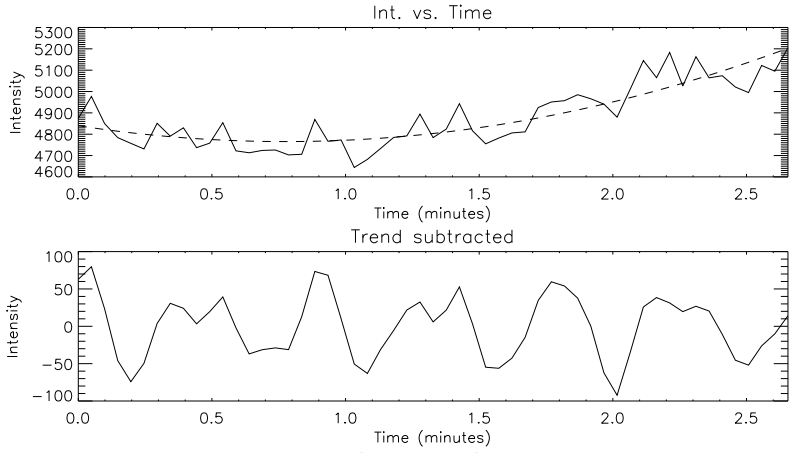


Figure 7.6: Intensity variation for a single pixel with co-ordinates (180,129) as recorded by the green line during March 29, 2006 solar eclipse.

In Figures 7.7–7.10 we show some representative examples of the type of the oscillations we measured in the off-limb region at the pixel location (180,129) and (197,93) in both the green and red lines respectively. Let us first focus on pixel location (180,129), which corresponds to a location at the top of the loop system (see Figure 7.1). The top panel of Figure 7.7 shows the variation of the intensity (hereafter we will use the term intensity for trend subtracted intensity), as a function of time. The oscillations shown in the upper panel had their background trend removed by subtracting from the original time series using a quadratic polynomial which fits the time series well. In the wavelet spectrum (the middle left panel), the cross-hatched regions are locations where estimates of oscillation period become unreliable. This is the so-called cone-of-influence (COI), see Torrence and Compo (1998). As a result of the COI, the maximum measurable period is shown by a dotted line in the global spectrum plots (middle right panel). The period shown in the global wavelet spectrum of Figure 7.7, measured at the location of the maximum in the global wavelet spectrum, together with an estimate of the probability indicates that this oscilla-

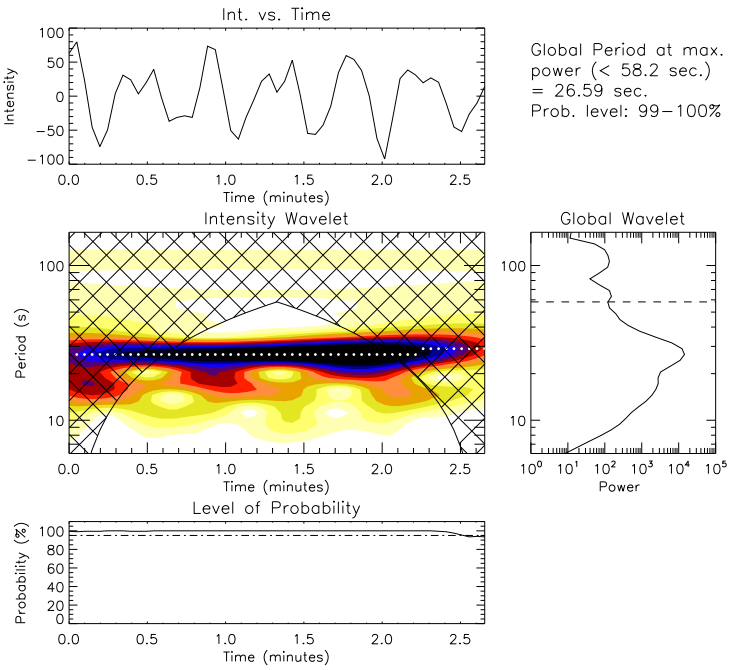


Figure 7.7: Wavelet analysis for the green line corresponding to pixel (180,129). The top panel shows the relative (background trend removed) intensity, the central panel shows the colour inverted wavelet power spectrum, the bottom panel shows the variation of the probability estimate associated with the maximum power in the wavelet power spectrum (marked with white lines), and the right middle panel shows the global (averaged over time) wavelet power spectrum. Above the global wavelet the period, measured from the maximum power from the global wavelet, together with probability estimate, is printed.

tion is not due to noise. The probability estimate was calculated using the randomisation method with 200 permutations as outlined in detail in O'Shea et al. (2001). Only those oscillations with a probability >95 % are considered to be significant. Below the wavelet power spectrum, in the lower panels, we show the variation of the probability estimate, calculated using the randomisation technique, associated with the maximum power at each time in the wavelet power spectrum. The location of the maximum power is indicated by the over-plotted white lines. We should also point out here that if we are interested in examining the weaker oscillations, sometime the stronger ones need to be filtered out first. In this analysis, since the duration of the red line time sequence is shorter and we cannot detect oscillations whose period is less than 4 s (cadence was 2 s) and above 27 s (because of COI), we filtered out periods outside this range. So for the red line after the trend subtraction we have applied the filtration also.

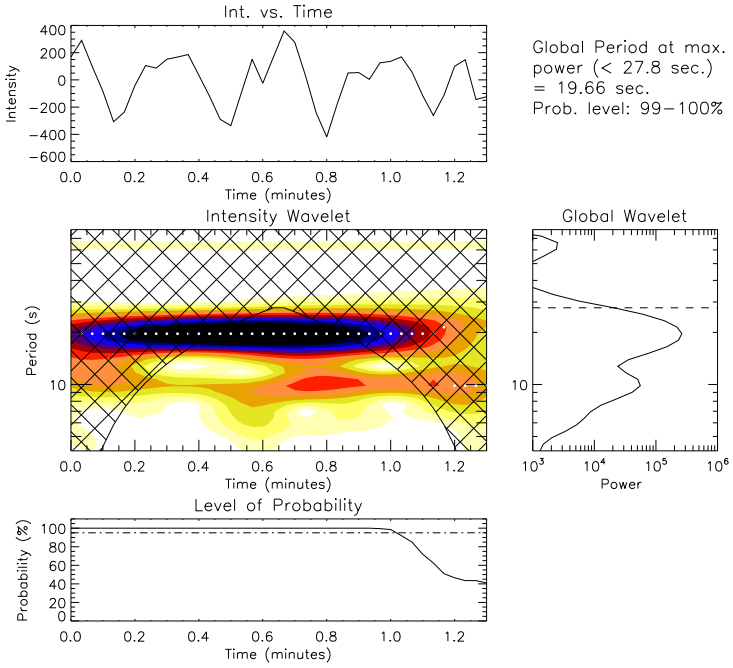


Figure 7.8: Wavelet analysis for the red line corresponding to pixel (180,129). Descriptions about the different panels are the same as in Figure 7.7.

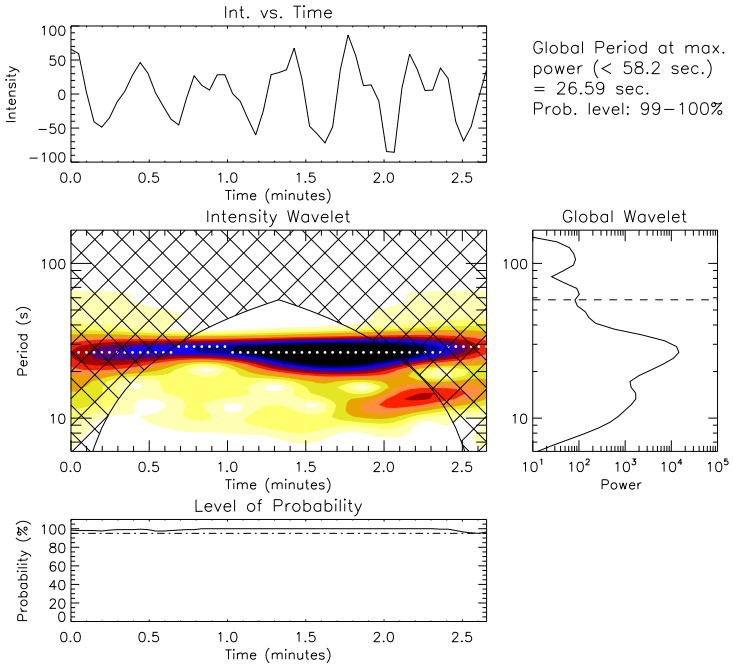


Figure 7.9: Wavelet analysis for another location away from the active region for pixel (197,93) for the green line. Descriptions about the different panels are the same as in Figure 7.7.

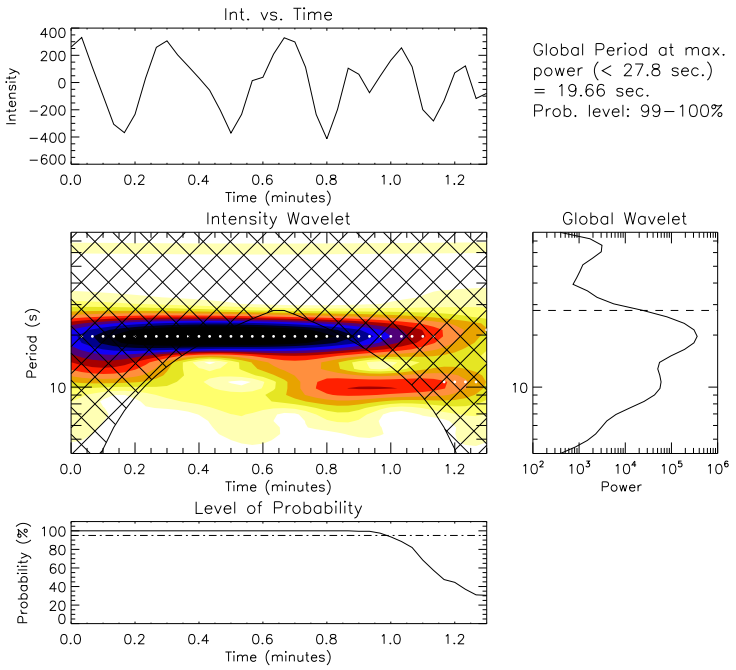


Figure 7.10: Wavelet analysis for another location away from the active region for pixel (197,93) for the red line. Descriptions about the different panels are the same as in Figure 7.7.

### 7.3.2 Statistical Analysis of Oscillations

Now to find out if the significant oscillations are always coming from coronal structures alone we did a statistical study of searching for oscillations for all pixels within our frame. The results are shown in Figure 7.11, corresponding to the green line. We have searched for significant oscillation periods below 35 s and with the probability estimates above 95 % (left panel) and 99 % (right panel). One can find that at several locations (marked with white dots) significant oscillation are present with high probability estimates. More importantly they do not correspond to the brightest locations of the active region loop system. Rather, the oscillations seem to be originating from the edges of the loops. We are not able to identify these locations in the red line as most of these pixels correspond to the very bright region and due to overexposure, CCD pixels have saturated.

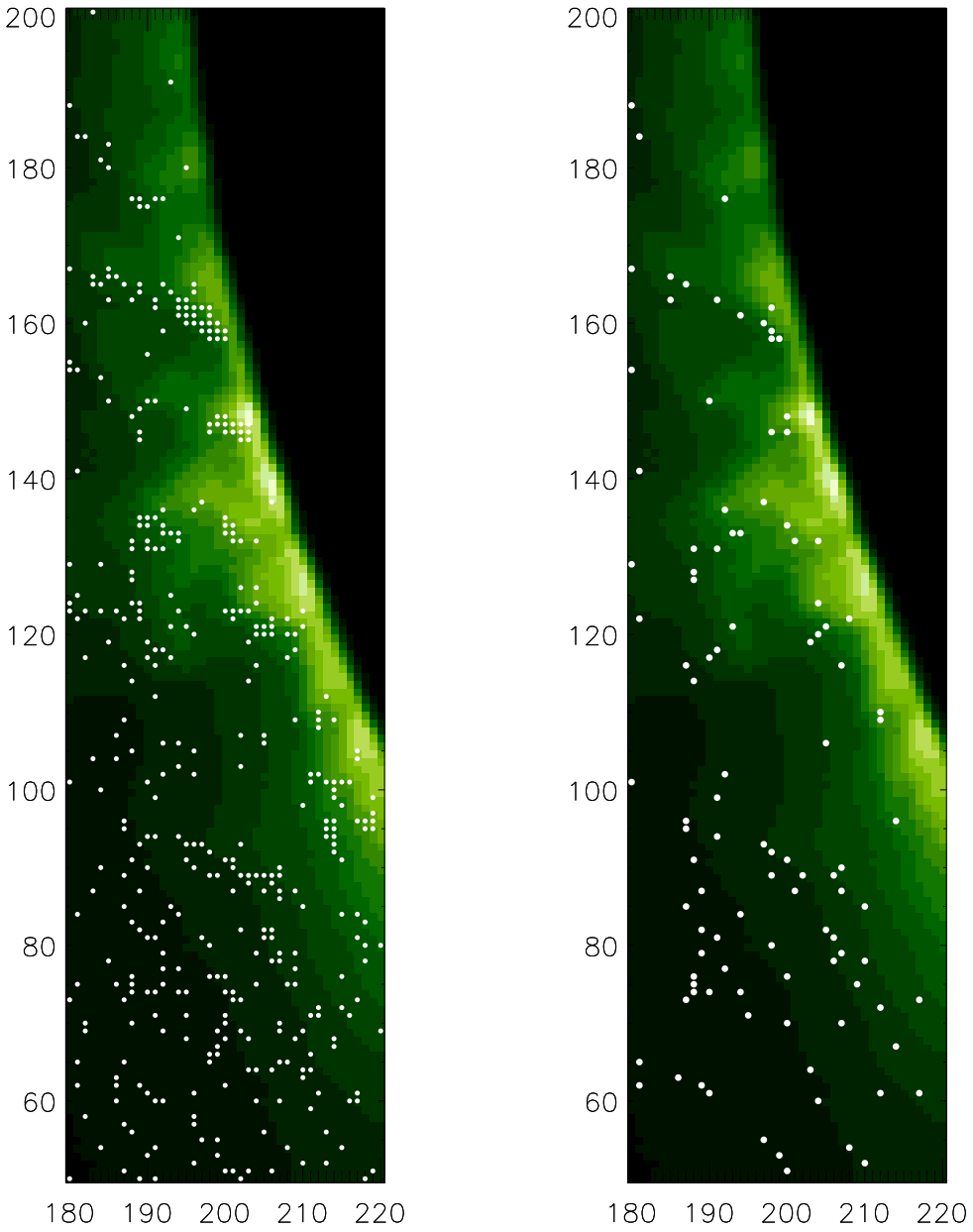


Figure 7.11: Part of the solar image in the green line where the marked locations have periodicity below 35 s and probability level above 95 % (left panel) and 99 % (right panel).

## 7.4 Results from 2009 Eclipse

### 7.4.1 Analysis of Oscillations

To study the oscillation property in the observed coronal structures during the total solar eclipse of 2009, we have again used the wavelet technique to find out the periodicity in the signal, if any.

In Figures 7.12–7.17, we show some representative examples of the type of the oscillations we measured in identified locations as shown in Figure 7.5. The top panel of Figure 7.12 shows the variation of the intensity, as a function of time. The oscillations shown in the upper panel had their background trend removed by subtracting a 10 point running average from the original time series.

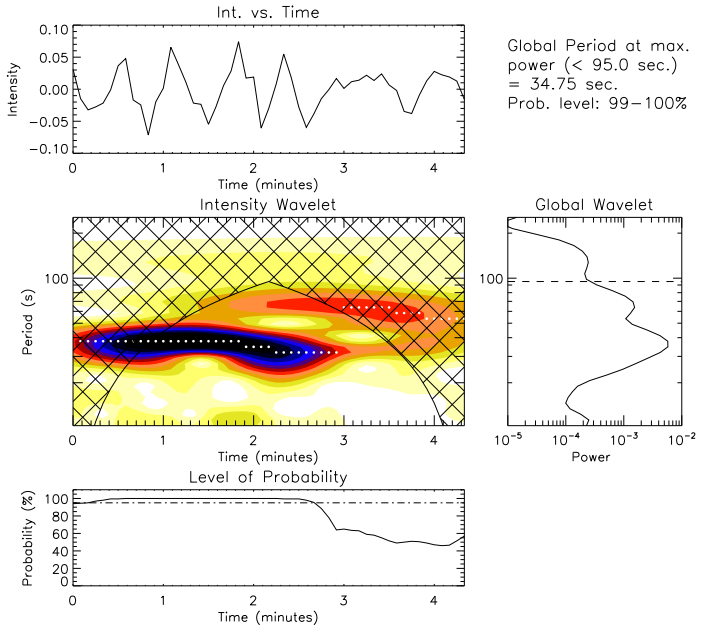


Figure 7.12: Wavelet analysis for the intensity measurements using the red emission line for the location marked in Figure 7.5. Descriptions about the different panels are the same as in Figure 7.7.

Figures 7.12–7.14 show the oscillation in line parameters of the red line at spatial pixel 13 as marked in Figure 7.5. The three parameters intensity, Doppler velocity and line width show the periodicity of 35 s, 32 s and 38 s respectively. These three oscillations can be considered as same which may have been triggered by the same driver. Whereas Figures 7.15–7.17 show the oscillations of period 54 s, 35 s and 35 s respectively in intensity, Doppler velocity and line width of green line at the edge of bright region as marked in Figure 7.5. The oscillations in velocity and width are of same period and for the same duration indicates that both are coupled together whereas intensity oscillation may have some different origin. To see the oscillations in different locations both in red and green lines, we checked the different locations with wavelet technique

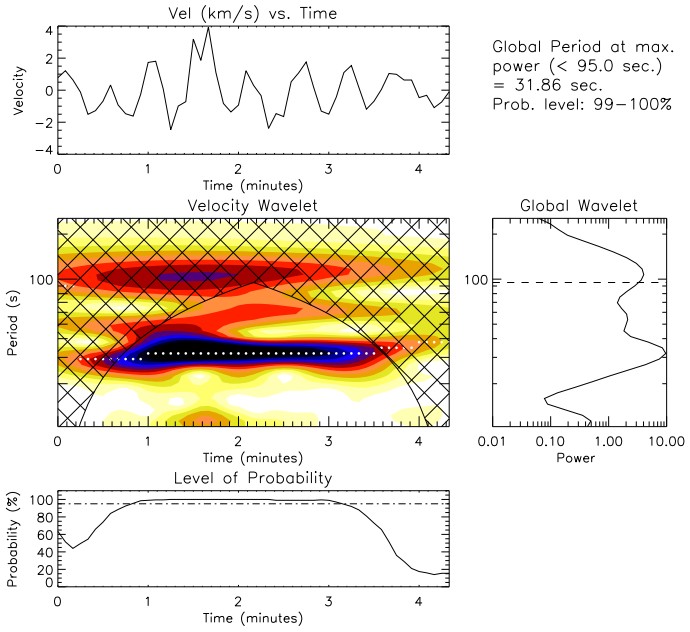


Figure 7.13: Wavelet analysis for the velocity measurements using the red emission line on the same location that in Figure 7.12. Descriptions about the different panels are the same as in Figure 7.7.

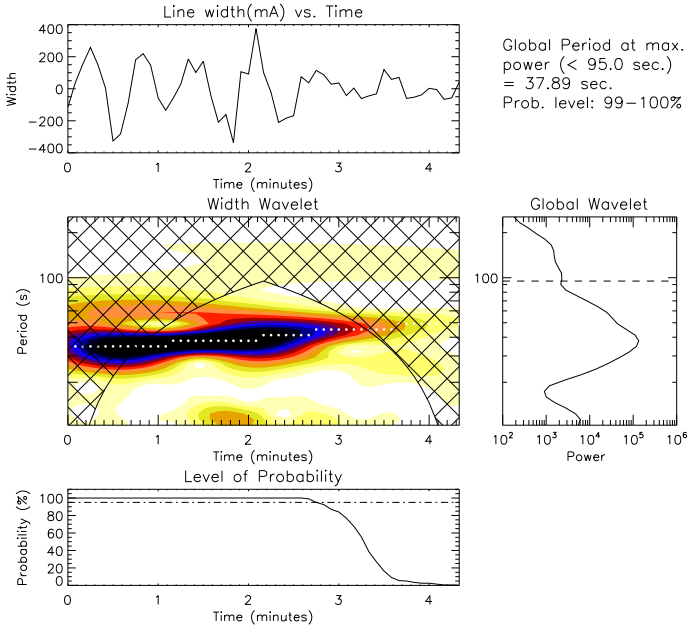


Figure 7.14: Wavelet analysis for the line width measurements using the red emission line on the same location that in Figure 7.12. Descriptions about the different panels are the same as in Figure 7.7.

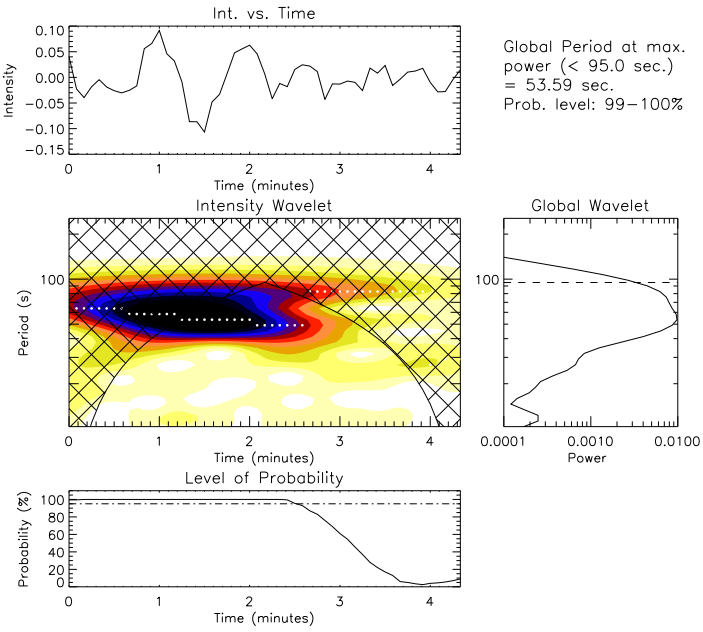


Figure 7.15: Wavelet analysis for the intensity measurements using the green emission line for the location marked in Figure 7.5. Descriptions about the different panels are the same as in Figure 7.7.

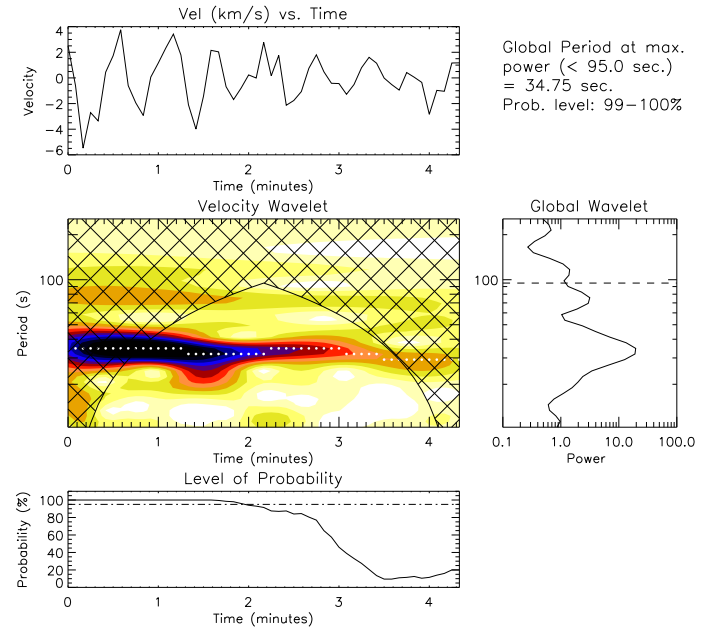


Figure 7.16: Wavelet analysis for the velocity measurements using the green emission line on the same location that in Figure 7.15. Descriptions about the different panels are the same as in Figure 7.7.

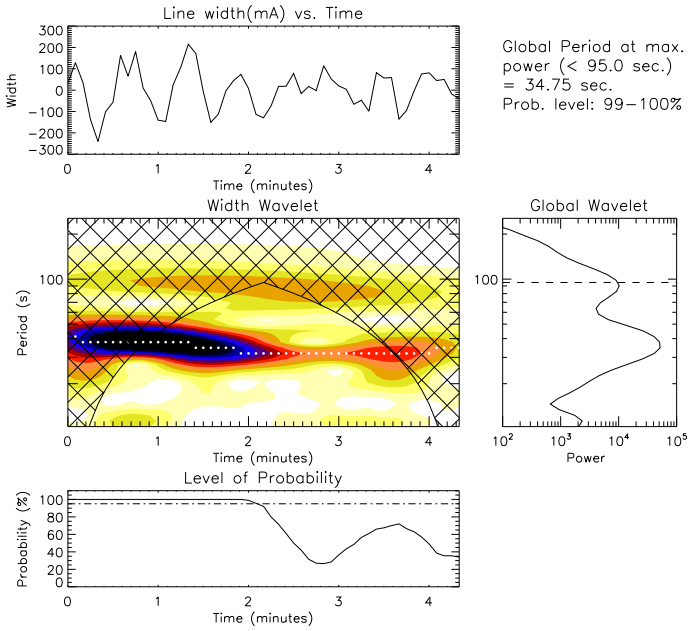


Figure 7.17: Wavelet analysis for the line width measurements using the green emission line on the same location that in Figure 7.15. Descriptions about the different panels are the same as in Figure 7.7.

and identified some locations where the oscillations can be seen in intensity, Doppler velocity and line width. The obtained results are summarised in Table 7.1 and 7.2 for the red and green line respectively. In the tables, the numbers within first brackets indicate the second prominent oscillation present whereas (?) indicates the low confidence level of primary oscillation. The results indicate that the oscillations are equally distributed over the coronal structure in both the lines except near the brightest region where we did not find any signature of oscillations. From both the tables it can be seen that the detected oscillations have period between the range of 30 to 60 s and out of three spectroscopic parameters at a location, at least two are showing nearly the same period of oscillations. The oscillations in intensity and Doppler velocity can be attributed to the compressional waves and that in line width may be due to the presence of torsional Alfvén waves. These oscillations may be due to the coupling between different modes of oscillations because of different physical circumstances and processes.

Table 7.1: Periods of oscillations observed in Red line at different locations:

| Position | Period (s) | | |
|---|---|---|---|
| | Intensity | Velocity | Width |
| 5 | 58 | 32 (45) | 45 |
| 10 | 37 | 54 (?) | 41 |
| 14 | 41 (29) | 29 | 29 |
| 19 | 41 | 58 (37) | 58 (35) |
| 25 | 58 (29) | 32 | 35 |
| 35 | 32 | 41 | 49 |
| 41 | 29 | 38 | 54 (29) |
| 45 | 49 (?) | 54 | 54 (32) |
| 50 | 45 (?) | 29 (45) | 49 (29) |
| 51 | 32 | 38 | 45 |
| 53 | 45 | 49 (29) | 45 |
| 60 | 38 | 38 | 38 |
| 64 | 45 | 41 | 45 |

Table 7.2: Periods of oscillations observed in Green line at different locations:

| Position | Period (s) | | |
|---|---|---|---|
| | Intensity | Velocity | Width |
| 25 | 29 | 49 (25) | 45 |
| 29 | 35 (51) | 69 (38) | 54 (32) |
| 39 | 49 (31) | 35 | 45 |
| 45 | 49 | 41 | 54 |
| 50 | 29 | 58 | 58 |
| 56 | 41 | 49 | 41 |
| 59 | 29 | 54 (32) | 35 |
| 60 | 54 (29) | 58 (25) | 38 |
| 66 | 32 (54) | 49 (29) | 54 |
| 83 | 35 | 41 | 45 |
| 85 | 49 (29) | 54 (35) | 54 |
| 94 | 64 (38) | 45 | 38 |
| 99 | 35 | 41 | 29 |

### 7.4.2 Wavelength–Time Maps

In the solar atmosphere, magnetic field lines clump into tight bundles and form flux tubes. Alfvén waves in flux tubes could manifest as torsional oscillations that create simultaneous blue and

red shifts, leading to the non-thermal broadening of any isolated line profile (Erdélyi and Fedun, 2007; Van Doorsselaere et al., 2008), and thus should be observed as full-width at half-maximum (FWHM) oscillations as seen in Jess et al. (2009). This oscillations of FWHM of red and green lines have been found from the wavelet analysis with significance levels exceeding 99 % as shown in Figures 7.14 and 7.17. For better visualisation of this FWHM and Doppler velocity oscillations, we have made a wavelength-versus-time plot using the red and green line profiles. Here we have first subtracted the background from original profile and then normalized the profile with the amplitude and plotted it with time as shown in Figure 7.18. The Doppler shift (velocity) and broadening (FWHM) oscillations are seen from these plots in both the red and green lines. The Doppler shifts are then removed by shifting all the line profiles at the first profile position, we have again plotted these wavelength-versus-time plot in Figure 7.19. Now the periodic variation of the line broadening (FWHM) in both the spectral lines are clearly visible as seen in the wavelet Figures 7.14 and 7.17. Hence from the analysis of time series of spectra in the green and red emission lines using wavelet technique and wavelength-time plot, it can be concluded that FWHM oscillates with periods between 30 to 60 s caused by the existence of waves in these coronal structures.

### 7.4.3 Intensity Ratio and Correlation Analysis

As here we have simultaneous temporal and spatial spectroscopic data in two coronal lines, it gives an opportunity to compare the different parameters of the two lines. In Figure 7.20, we are plotting the variation of line width along the slit for both the lines and also the intensity ratio of green and red line along the slit. In the figure, vertical dashed line gives the position of closest approach between slit and solar limb. From the figure, it can seen that the ratio of green to red line intensity is in between ≈0.5 to 2.2. Guhathakurta et al. (1993) have calculated the temperature of coronal structures using the intensity ratio of red to green line. Using there calculation, the temperature of these coronal structure can be estimated to ≈ 1.4 MK from the measured intensity ratio. The higher temperature of these coronal structure is expected as we find very strong signal

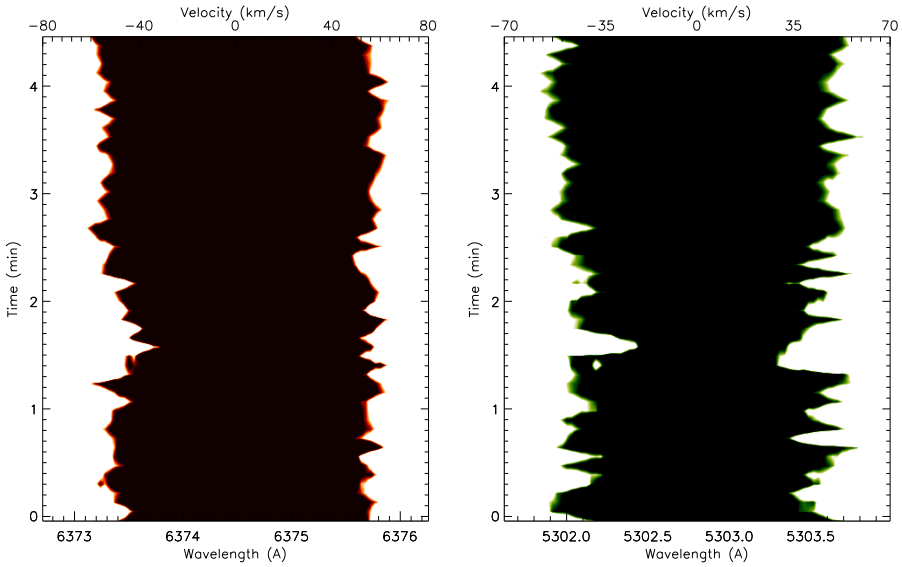


Figure 7.18: A wavelength-versus-time plot of the red (left panel) and green (right panel) profile showing the variation of line width at FWHM as a function of time at locations marked with asterisks in Figure 7.5. These figures clearly show the variation of red and blue shift and line broadening (FWHM) with time.

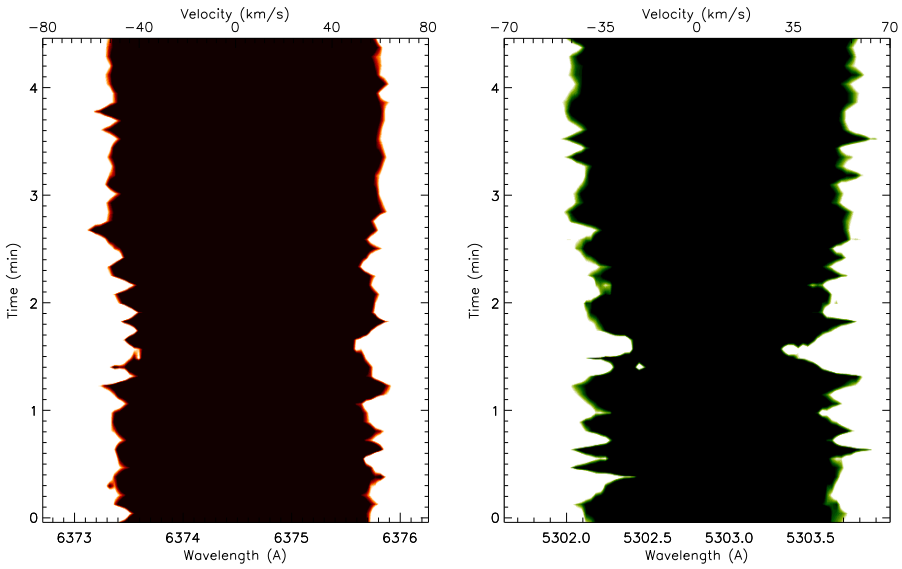


Figure 7.19: A wavelength-versus-time plot of the red (left panel) and green (right panel) profile showing the variation of line width at FWHM after removing the Doppler shift as a function of time at locations marked with asterisks in Figure 7.5. These figures clearly show the periodic variation of line broadening (FHWM) with time.

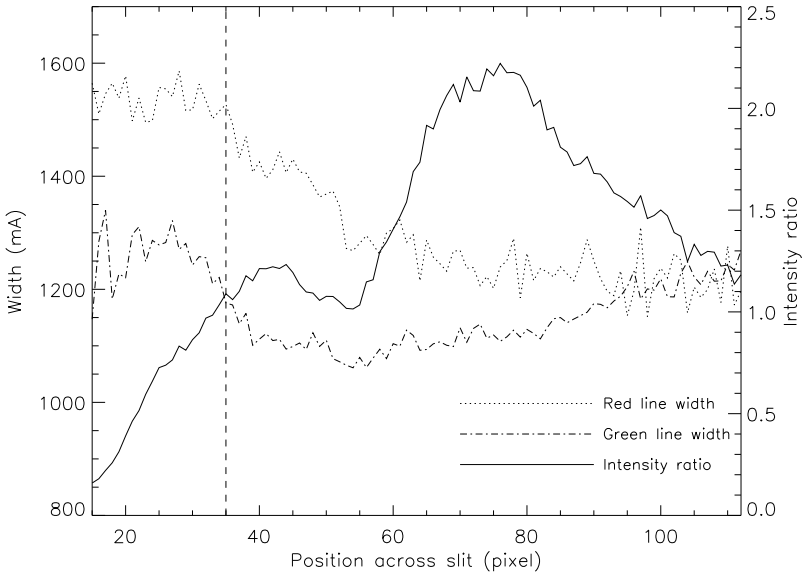


Figure 7.20: Variation of intensity ratio of green to red line and variation of green and red line width along the slit during July 22, 2009 solar eclipse. The vertical dashed line indicates the position of closest approach between limb and slit.

in the green line from the brightest region as compared to the red line.

Also, as we have simultaneous temporal and spatial spectroscopic data in two coronal lines, we have obtained the correlation co-efficients between the intensity oscillations of these two spectroscopic lines. The IDL routine *c_correlate* has been used to calculate the correlation co-efficient of red line intensity with respect to green line intensity at different time delays for all the locations across the slit. The obtained correlation map is plotted in Figure 7.21. The level of correlation between the two lines is in between -0.45 to 0.45 indicating that both lines are poorly correlated. It is noted that when we see this correlation plot closely, it indicates that both the lines are correlated when the time delays are large whereas are anti-correlated for the small time delays.

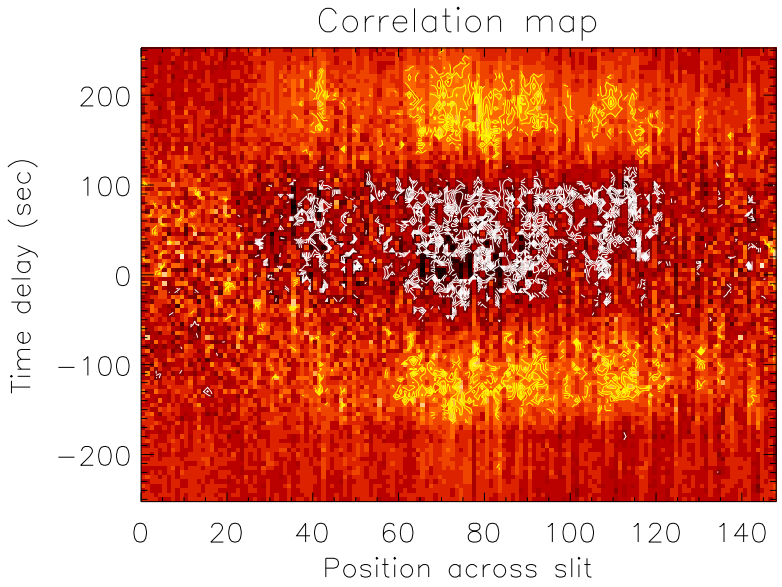


Figure 7.21: Nature of correlation between red and green line intensity oscillation at different time delays for all the locations across the slit. Yellow line contour gives the correlation coefficient between 0.1 to 0.45 whereas white line contours gives that in between -0.45 to -0.1 range.

## 7.5 Discussion and Conclusions

### 7.5.1 2006 Eclipse

Coronal structures can act as wave guides and propagating waves should have wavelengths shorter than the sizes of these structures. Now shorter wavelengths correspond to shorter periods of the waves, requiring high cadence observational tools. The typical cadence time of space-based EUV imagers is 10 s or higher, which gives the minimal period of detected waves to be about 1–5 min. Thus, the EUV imagers can not normally be used for the detection of propagating fast waves guided by coronal loops. On the other hand, time resolution of a second or better can be achieved with ground based coronographs, radioheliographs or during eclipses. Thus our experimental set up provides ideal opportunity for the detection of fast waves, which

are important for the heating of the corona.

From the Figures 7.7–7.9, we can see that the green line, which is a higher temperature line shows a oscillation of strongest power at period $\approx$ 27 s whereas the red line which is a comparatively lower temperature line shows that of $\approx$ 20 s oscillation at the same location. Note that the duration of the red line time series is smaller compared to the green one, this may be responsible for non detection of periods above 20 s in the red line. The second strongest peak can be seen in the wavelet plots at the $\approx$ 14 s and 10 s for the green and the red lines respectively. Recently, Jess et al. (2008) detected velocity oscillations in the He II 304 Å emission line formed at $T \approx 5\times10^4$ K obtained with the Extreme Ultraviolet Normal Incidence Spectrograph (EUNIS) sounding rocket instrument on 12 April 2006. They reported very similar period at the transition region, 26 ± 4 s, coupled with a velocity amplitude of ±10 km s$^{-1}$, detected over four complete cycles. They detect the presence of the oscillations at the edge of the active region. Though they have also reported detection of similar periodicity at higher temperature line, they conclude that there does not seem to have been any coupling between these two layers. They interpret these oscillations as signatures of the fast MHD wave, in particular, that of the fast body global sausage wave mode. We should point out here that we report similar periodicity with intensity, as we do not have any velocity information we can not comment on the velocity signature here. One should also note that Doppler shifts of emission lines may also cause a variation of observed 'intensity' when the emission lines are observed through a band-pass filter with a slope of its transmissibility. However, it is to be noted that in this observation we have used the narrow band filter in the converging beam. Therefore, the effective passband of the filter at FWHM is 4.5 Å. The spectra of the Sun and Moon taken through the filter using the converging beam with the same $f$-ratio indicate that the intensity of the filter reduces to 99 % of the peak value at 0.4 Å away from the central wavelength. Now, 0.4 Å shift in the wavelength implies a velocity of 23 km s$^{-1}$. This is the line-of-sight velocity and actual velocity need to be much more than this value to cause such shifts. Such large velocities in quiescent active region loop system and in their neighbourhood were not reported. We have observed intensity oscillations with an amplitude of more that 2 %. Hence the observed variations in the signal are more likely to be due to intensity

variations, though some component due to velocity variations cannot be ruled out.

Katsiyannis et al. (2003) reported the existence of high frequency MHD waves in coronal loops observed during the August 1999 total solar eclipse. They also used wavelet analysis to identify twenty $4'' \times 4''$ areas showing intensity oscillations. Their detections were in the frequency range 0.15–0.25 Hz (7–4 s), lasting for at least three periods at a confidence level of more than 99 % and arose just outside known coronal loops. They further suggested that these oscillations occur in low emission-measure or different loops associated with the active region. In the present study the nature of the oscillations near the active region which corresponds to pixel (180,129) is similar to the oscillations seen far from the active region at pixel (197,93). So, we can say that the oscillation seen is independent of the loop. The other possibility is that in this image we are not able to see the weaker part of the loop system which is extending very far out. To search for these oscillations in the various regions, we studied all the pixels from (180,50) to (220,200) in the green line. From the Figure 7.11, one should note that the spatial distribution of detected oscillations is not random and they seem to be prevalent on the edge of the bright loop and also present in the adjacent less intense regions. So, one can conjecture that these oscillations are travelling along the coronal loop edges. Since these oscillations are detected either at the fainter part of the active region and the tenuous part of the solar corona we may need a different mechanism to explain these oscillations. Cooper et al. (2003a,b) proposed a possible mechanism which attributes the detected intensity oscillations as a line-of-sight effect of entirely incompressible MHD waves. In this model, when observed at an angle $\theta$ to the direction of propagation, the wave-induced deformation in a coronal loop causes intensity variations. This is because the amount of optically thin emitting plasma along the line-of-sight changes as a function of time. Using the Cooper et al. (2003a) and Zaqarashvili and Roberts (2002) results, Katsiyannis et al. (2003) were able to provide a satisfactory explanation of how the detected incompressible MHD waves were created in the vicinity of an active region in the photosphere, transmitted through low emission-measure loops to the lower corona and then detected as intensity oscillations by their imaging system. The nature and location of our detection confirms this scenario quite satisfactorily. For many locations the relative intensity amplitude, as

recorded by the green line is about 1 %. Singh et al. (1997) have reported intensity amplitudes to lie in the range of 0.2–1.3 % of the coronal brightness. If these oscillations can be attributed to the presence of fast magneto-acoustic waves the energy flux will be sufficient to heat the active regions. We must point out that the present experimental set up does not allow us to study the velocity signatures these waves will carry. However, the velocity observation is important for a full diagnostics and this we have achieved during the next total solar eclipse in 2009.

### 7.5.2 2009 Eclipse

Coronal structures can act as wave guides and propagating waves should have wavelengths shorter than the sizes of these structures. Alfvén waves e.g., as torsional modes of coronal untwisted loops are incompressible and, therefore, do not perturb the density and, hence, do not modify the loop emission. But if the loop is twisted, torsional modes are compressible. The velocity perturbations of Alfvén waves, though, can be observed through variations of the Doppler shift. Whilst long period waves may show resolved Doppler shifts, short period waves, with periods less than a few minutes, can be observed only indirectly by measuring the additional broadening of coronal emission lines, i.e., non-thermal broadening. The measured variation in line width with density and height supports undamped wave propagation in coronal structures. This was strong evidence of outwardly propagating undamped Alfvén waves in the corona, which may contribute to coronal heating and high-speed solar wind in the case of coronal holes. Banerjee et al. (1998), and Banerjee et al. (2009a) measured the evolution of non-thermal broadening of the emission lines and found that the amplitude of unresolved thermal broadening (possibly, the Alfvén wave amplitude) is growing up to 1.2 $R/R_{\odot}$, then has a plateau to 1.5 $R/R_{\odot}$. The authors suggested that this phenomenon could be associated with non-linear overturning of the waves, but a rigorous theoretical modelling is still required. Fast spectroscopic observation will be ideal for detecting all the three modes of MHD wave propagation. Thus our experimental set up provides an ideal opportunity for the detection of these fast MHD waves, which are important for the heating of the corona.

Here we have reported 30 to 60 s periodicity in intensity, Doppler velocity and in FWHM in both green and red spectral lines. The oscillations in intensity and velocity can be attributed due to the compressional waves whereas that in FWHM can be due to torsional Alfvén waves in the coronal structures. Furthermore, the same period of oscillations in intensity as well as in FWHM can result due to the propagation of fast sausage mode, hence these oscillations can be due to the propagation of these fast sausage mode as well. Recently, it has been shown by Kaghashvili et al. (2009) that in an inhomogeneous plasma flows the Alfvén wave drives compressional fluctuations and all the propagation modes are coupled together. This suggests that in our observations these compressional signatures are due to the Alfvénic mode which is seen in line broadening oscillation. Also Cooper et al. (2003a,b) have suggested that the intensity fluctuation may arise due to the line-of-sight effect of propagation of transverse waves. Hence, these oscillations can be attributed due to the fast magneto-acoustic waves or due to the Alfvénic mode of propagation. The periodicity of this range in intensity have been already observed during 2006 eclipse as described in Section 7.3 (Singh et al., 2009) and by Jess et al. (2008) in the velocity at the edge of active region coronal loops, which they have interpreted as signatures of the fast MHD wave. This time we have detected these oscillation in FWHM (due to broadening in line-width) along with oscillation in intensity and velocity in the active region. Although here it is difficult to identify whether these oscillations are detected at the edge of coronal structures or not but can be interpreted as signature of fast MHD and torsional Alfvén waves. We have estimated the total energy flux due to Alfvén waves in these coronal structure which is given by Moran (2001) as,

$$F = \frac{1}{2}\rho\,\xi^2\,V_A \tag{7.1}$$

In this case, we have assumed average non-thermal velocity $\xi \approx 45$ km s$^{-1}$ and calculating $\rho$ and $V_A$ from Aschwanden et al. (1999) for an electron temperature of 1.5 MK and height of 100 Mm (beyond 1.15 $R/R_\odot$). The obtained electron density is then $4.69 \times 10^8$ cm$^{-3}$ for the base density of $2 \times 10^9$ cm$^{-3}$. Hence, $\rho = 1.2\,m_p\,N_e \approx 9.4 \times 10^{-16}$ g cm$^{-3}$ where $m_p$ the mass of proton, and a constant of 1.2 due to coronal He abundance. Whereas the Alfvén speed is about

1000 km $s^{-1}$ at 100 Mm (beyond 1.15 $R/R_{\odot}$) i.e. in the middle corona. Hence the obtained total energy flux is $F \approx 9.5 \times 10^5$ erg $cm^{-2}$ $s^{-1}$, which is one order less than the requirements of active region corona ($10^7$ erg $cm^{-2}$ $s^{-1}$) whereas is sufficient to heat the quiet corona ($3 \times 10^5$ erg $cm^{-2}$ $s^{-1}$) (Withbroe and Noyes, 1977).

In addition to the detailed study of the time variation of different line parameters at specific locations we have also tried to study the variation of line widths at different parts of the corona. We have also estimated the temperature using the line ratio technique. Recently, Voulgaris et al. (2010) have reported the relative intensity ratios of red and green line to be 0.577 and 2.161 during the Solar eclipses in 2006 and 2008 respectively. Whereas during this observation we have measured this ratio to be in between 0.45 to 1, this indicates that the relative intensity of red line has been decreased at least in this observed coronal structure. Here we have estimated the temperature of this coronal structure to be about 1.65 MK which may indicate that during the 2008 eclipse observation, the observed corona was hotter. It may be noted that solar corona has multi-temperature coronal structure as intensity ratios varies in different structures and with solar radii. The conclusion drawn by Voulgaris et al. (2010) depends on limited data on few coronal structures. One need to have observations for longer periods and over large portion of the solar corona to conclude the temperature varies with activity on shorter time scales. Observations in radio wavelength have shown that the corona to be cooler at the minimum phase of solar activity.

# Chapter 8

# Summary and Future Prospects

This thesis work deals with the detection and nature of propagating MHD waves in the different regions of solar atmosphere which plays an important role in heating of the solar corona and acceleration of the fast solar wind. For this purpose, several datasets obtained with the SUMER/SOHO and EIS/Hinode spectrometer, SOT/Hinode, TRACE imagers and spectral and imaging data during the total solar eclipses of 2006 and 2009, have been analysed. The brief description of all these instruments are given in Chapter 2.

Most of the observations were taken in EUV emission lines originating from transition region and coronal temperatures. Whereas observations taken during eclipses were in optical emission lines originating from coronal temperatures. Our results provide informations about the propagating MHD waves in different regions of the solar atmosphere, such as quiet and active regions and coronal holes. Particular attention was devoted to the coronal holes, both on-disk (network and internetwork regions) as well as off-limb (plume and inter-plume regions), with the goal of finding out which of these structures are source region and preferred channel of acceleration for the fast solar wind. The results have been used to identify the different modes and nature of these propagating MHD waves in these different regions.

Here we summarize the results obtained from this thesis work along with the conclusions

drawn, followed by the future prospects in the field.

## 8.1 Summary

In Chapter 4, we presented the nature of propagating waves in network and internetwork regions of on-disk part of coronal hole. Long time series (sit-and-stare) data obtained with the SUMER/SOHO spectrometer in N IV 765 Å and Ne VIII 770 Å spectral lines were used to search for the presence of waves in these two different regions from a statistical approach. A dominant period of $\approx$ 25 min have been observed from wavelet analysis (described in Appendix A) in both the spectral lines of network bright region which were interpreted due to the presence of propagating compressional waves. The statistical approach was applied on the calculated phase differences between the two spectral lines (described in Appendix B) to measure the time delay between them. We found that there is a difference in the nature of wave propagation where bright (network) regions show only upward propagation, as opposed to the dark (internetwork) regions which show evidence of both upward and downward propagating waves (see Figure 4.8). The resultant time delays were 778 ± 133 s (downwardly propagating) and −216 ± 37.8 s (upwardly propagating) in the internetwork regions whereas −717 ± 114 s in the network regions (only upwardly propagating). The corresponding wave speeds were measured to be $3.7 \pm 0.5$ and $-13.2 \pm 2.3$ km s$^{-1}$ in internetwork region and $-4 \pm 0.6$ km s$^{-1}$ in network regions respectively. All these measured speeds were subsonic, consistent with slow magneto-acoustic waves. We also pointed out that in this statistical study, more velocity oscillations were found than intensity oscillations which implies the presence of transverse-type waves, like Alfvénic.

We also looked for the evidence of propagating waves in off-limb coronal holes with the simultaneous data obtained with the SUMER/SOHO and EIS/Hinode spectrometer in Ne VIII 770 Å and Fe XII 195 Å spectral lines respectively. We identified the polar plume and inter-plume regions (see Figure 5.3). The presence of accelerating waves in a polar inter-plume region with a period of 15 min to 20 min were detected in both the spectral lines and a propagation speed

was increasing from 130 ± 14 km $s^{-1}$ just above the limb, to 330 ± 140 km $s^{-1}$ around 160″ above the limb. These waves were traced to originate from a bright region of the on-disk part of the coronal hole which can be visualized as the base of the coronal funnels. The adjacent plume region also showed the presence of propagating disturbance with the same range of periodicity but with propagation speeds in the range of (135 ± 18) km $s^{-1}$ to (165 ± 43) km $s^{-1}$ only. A comparison between the distancetime radiance map of the two regions indicated that the waves within the plumes are not observable (may be getting dissipated) far off-limb, whereas this is not the case in the inter-plume region (see Figures 5.14 and 5.15). We also performed a correlation analysis to find out the time delay between the oscillations at several heights in the off-limb region, these results were consistent with those from the analysis of the distancetime maps. To our knowledge, these results provided the first spectroscopic evidence of the acceleration of propagating disturbances in the polar region close to the Sun (within 1.2 $R/R_{\odot}$). We suggested that these waves are likely either Alfvénic or fast magneto-acoustic in the inter-plume region and slow magneto-acoustic in the plume region. We further concluded that inter-plumes are a preferred channel for the acceleration of the fast solar wind. These findings are described in detail in Chapter 5.

In the Chapter 6, we described the evidence of waves in the quiet Sun regions which were further divided into bright magnetic (network), bright non-magnetic and dark non-magnetic (internetwork) regions. The simultaneous observations were performed in Ca II filtergram from SOT/Hinode, TRACE 1550 Å passband and with SUMER/SOHO spectrometer in N IV 765 Å and Ne VIII 770 Å spectral lines to study the oscillations in these different regions. We detected the presence of long period oscillations with periods between 15 min to 30 min in bright magnetic regions. Oscillations were detected from chromospheric height to low coronal heights. Power maps showed that low period powers are mainly concentrated in dark regions whereas long period powers are concentrated in bright magnetic regions. We proposed that these 15 min and above periods can propagate up to the coronal heights through 'magneto-acoustic portals'. The phase difference between the oscillation in Ca II and TRACE 1550 Å passband were studied and found that the phases are more in negative side in high frequency bands, whereas in low

frequency bands the phases are more in positive side. This indicated the frequency dependent nature of phase distributions. However in this case only with the spectral imaging data, it was not possible to identify the mode of wave propagation. Moreover, we have already observed these kind of long period waves in polar inter-plume regions which were interpreted in terms of Alfvénic or fast mode. Interpretation of nature of these long period waves in these regions and search for their drivers will be one of our future objectives.

In Chapter 7, we described the total solar eclipse observations taken during 2006 and 2009. We searched for high frequency oscillations in active regions with spectral imaging and spectroscopic data. We found the oscillations of periods 27 s and 20 s in imaging data obtained in green (Fe XIV 5303 Å) and red (Fe x 6374 Å) coronal emission lines respectively. We searched for oscillations in all the pixels and found that significant oscillations with high probability estimates were present at boundary of active region and in the neighbourhood, rather than within the loops itself (see Figure 7.11). We also reported the detection of oscillations in intensity, velocity and line width having periods in the range of 25 s to 50 s with spectroscopic data again obtained in green and red coronal emission lines. Wavelength–time maps were created to get the clear signature of oscillations in full-width half maximum (FWHM) of line profile which were due to the torsional Alfvén waves (see Figures 7.18 and 7.19). These high frequency oscillations were interpreted in terms of presence of fast magneto-acoustic and torsional Alfvén waves.

Hence, the direct evidence of presence of propagating magneto-acoustic waves in the solar atmosphere were inferred with the EUV imagers and spectrometers (using distance–time radiance maps and wavelet analysis). The relative amplitudes of the detected waves were several percent and periodicities were in the range of several minutes. Evidence for Alfvén and fast magneto-acoustic waves were also found in both the imaging and spectral data. The source of these waves and the physical mechanism responsible for the observed periodicities have not yet been fully understood. Theoretical progress in this field is very much needed to explain the observed signatures. The results presented here in many chapters are reviewed by Banerjee et al. (2010).

## 8.2 Future Prospects

The detection of MHD waves in the solar corona is important for determining the presence and relevance of wave heating mechanisms since they are an obvious mode of transport to carry energy from the solar surface to the solar atmosphere. Such observations may also be use to improve the existing estimates of coronal properties, both from direct measurements and indirect methods such as coronal seismology.

*Coronal seismology*, a new field of solar physics that emerged over the last decade, provides unique information on basic physical properties of the solar corona. Measurement of the properties of MHD waves and oscillations (periods, wavelengths, amplitudes, temporal and spatial signatures, characteristic scenarios of the wave evolution), combined with a theoretical modelling of the wave phenomena (dispersion relations, evolutionary equations, etc.), leads to a determination of the mean parameters of the corona, such as magnetic field strength and transport coefficients. This approach is illustrated in Figure 8.1. This method of MHD coronal seismology was first suggested by Uchida (1970) for global seismology and by Roberts et al. (1984) for local seismology. This method has been recently applied to estimate the magnetic field strength (Nakariakov and Ofman, 2001) and the coronal dissipative coefficients such as the resistivity and viscosity (Nakariakov et al., 1999). These implementations are discussed in Nakariakov and Verwichte (2005). This technique can also provide unique information on electron density and filling factors.

Furthermore, the combination of observationally gained knowledge with MHD wave theory and direct numerical simulations of the phenomena, will be useful in the investigation of coronal plasmas. This makes the investigation of coronal MHD waves and oscillations to be an interesting, rapidly developing, and promising branch of solar physics.

Many of the observations of propagating MHD waves reported here have raised a number

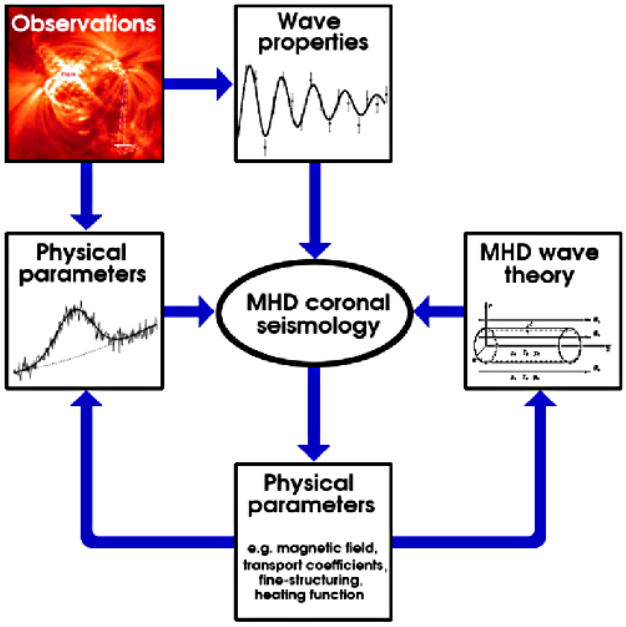


Figure 8.1: A scheme of the method of MHD coronal seismology. From Nakariakov and Verwichte (2005).

of questions, such as the excitation mechanisms, the damping mechanisms, detection of these waves in the environment of magnetic reconnection regions etc. We still lack in the physical understanding of these mechanisms.

Recently launched Atmospheric Imaging Assembly (AIA) on-board Solar Dynamics Observatory (SDO) has coronal seismology as one of its science goals and will allow us to develop the necessary improved understanding of the properties and other unresolved issues of the observed waves. The high cadence of AIA will extend the parameter space to higher frequencies as compared to the previous ones. The broad simultaneous temperature coverage will allow to study waves in parts of active regions and small-scale magnetic loops that have not yet been seen. With the guidance of significant advances in the theory of these waves (from 3-D MHD simulations), and complemented with spectroscopic measurements of densities and line-of-sight velocities (for example by EIS/Hinode), and reliable magnetic field extrapolations (e.g., from HMI/SDO), AIA will thus be the first instrument to fully exploit the potential of coronal seismology.

Recent MHD simulations indicate that all the wave modes propagate together within a magnetic structure in the solar corona. It may become possible to identify these different MHD modes by comparing the observed spectra from the Sun (may be from EIS/Hinode) to the synthesized spectra obtained from the simulations, which will be supplemented with the high cadence observations with the AIA/SDO.

On a longer time scale, more opportunities will open with the launch of the ESA *Solar Orbiter*[1] in the time-frame 2017-2018. For the first time ever, a spacecraft would adopt an almost solar-stationary orbit, taking the spacecraft down to about 0.23 AU from the Sun. This will view and diagnose the solar atmosphere with high spatial resolution and combine this with measurements of particles and fields made in-situ. Solar Orbiter will be the first satellite to provide close-up views of the Sun's polar regions, which are very difficult to see from Earth. It will also deliver data of the side of the Sun not visible from Earth.

The following instruments are selected for the assessment study phase of the mission.
Energetic Particle Detector (EPD), Extreme Ultraviolet Imager (EUI), Magnetometer (MAG), Coronagraph (METIS/COR), Visible Imager & Magnetograph (PHI), Radio and Plasma Waves (RPW), Heliospheric Imager (SoloHI), EUV Spectrometer (SPICE), X-ray Imager (STIX), Solar Wind Plasma Analyser (SWA), Suprathermal Ion Spectrograph (part of EPD).

The future of propagating MHD wave detection to get an estimate of its contribution in the solar coronal heating and acceleration of the fast solar wind looks very promising. With the present Hinode satellite, containing the Solar Optical Telescope (SOT) and the EUV Imaging Spectrometer (EIS), the just launched Solar Dynamics Observatory (SDO), containing the Atmospheric Imaging Assembly (AIA) and the upcoming *Interface Region Imaging Spectrograph* (IRIS[2]), means that it will soon be possible to obtain slit and image data at a much increased spectral and time resolution. For example, the AIA, offering a replacement for the TRACE in-

[1] `http://sci.esa.int/science-e/www/area/index.cfm?fareaid=45`
[2] `http://iris.lmsal.com/`

strument, allows the Sun to be imaged at ten different wavelengths, eight of them simultaneously, with a time resolution of $\approx$ 10 s. Whereas IRIS will obtain UV spectra and images with high resolution in space ($0.33''$) and time (1 s) focusing on the chromosphere and transition region of the Sun. The good spectral resolution of EIS will, in addition, allow the accurate measurement of non-thermal velocities and allow other studies that are based on the detailed measurement of line widths, together with a simultaneous measurement of electron density in different magnetic structures. Thus the future looks very promising.

# Appendix A: Wavelet Analysis[1]

Many times a time series exhibits non-stationarity in their statistics. While the series may contain dominant periodic signals, these signals can vary in both amplitude and frequency over long periods of time.

Ideally, one would like to separate the shorter period oscillations from the longer. The word 'oscillation' is used here to indicate any repeating fluctuation in the time series, regardless of whether the fluctuation repeats on a regular basis or not. The simplest method for analysing non-stationarity of a time series would be to compute statistics such as the mean and variance for different time periods and see if they are significantly different. While the running variance tells us what the overall strength of the signal was at certain times, it suffers from two major defects:

1. **Time Localization:** The shape of the curve is highly dependent on the length of the window used.
2. **Frequency Localization:** The running variance contains no information on the frequency of a periodic signal, only its amplitude.

One possibility would be to do a windowed (or running) Fourier transform (WFT), using a certain window size and sliding it along in time, computing the FFT at each time using only the data within the window. This would solve the second problem (frequency localization),

[1] `http://paos.colorado.edu/research/wavelets/wavelet1.html`

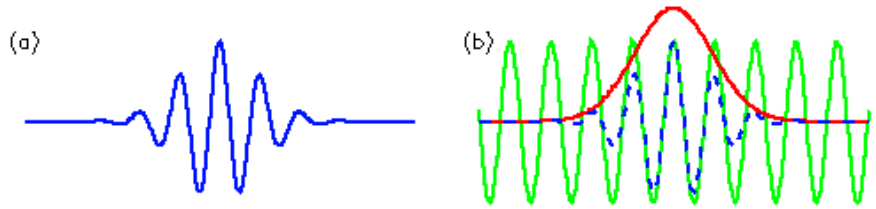


Figure A.1: (a) Morlet wavelet of arbitrary width and amplitude, with time along the x-axis. (b) Construction of the Morlet wavelet (blue dashed) as a Sine curve (green) modulated by a Gaussian (red).

but would still be dependent on the window size used. The main problem with the WFT is the inconsistent treatment of different frequencies: at low frequencies there so few oscillations within the window that the frequency localization is lost, while at high frequencies there are so many oscillations that the time localization is lost. Finally, the WFT relies on the assumption that the signal can be decomposed into sinusoidal components.

Wavelet analysis attempts to solve these problems by decomposing a time series into time/frequency space simultaneously. One gets information on both the amplitude of any 'periodic' signals within the series, and how this amplitude varies with time.

In Figure A.1, an example of a wave 'packet' is shown, of finite duration and with a specific frequency. This 'wavelet'has the advantage of incorporating a wave of a certain period, as well as being finite in extent. The wavelet shown in Figure A.1 (called the Morlet wavelet) is a Sine wave (green curve in Figure A.1) multiplied by a Gaussian envelope (red curve).

The Morlet wavelet shown in Figure A.1 is defined as the product of a complex exponential wave and a Gaussian envelope:

$$\psi_o(\eta) = \pi^{-1/4} e^{i\omega_o \eta} e^{-\eta^2/2} \tag{A.1}$$

where $\psi_o(\eta)$ is a *wavelet function*, that depends on a non-dimensional 'time' parameter $\eta$, and $\omega_o$ is the non-dimensional frequency.

Whereas the 'scaled Wavelets' are defined as,

$$\psi\left[\frac{(n'-n)\delta t}{s}\right] = \left(\frac{\delta t}{s}\right)^{1/2} \psi_o\left[\frac{(n'-n)\delta t}{s}\right] \tag{A.2}$$

where $s$ is the 'dilation' parameter used to change the scale, and $n$ is the translation parameter used to slide in time. The factor of $s^{-1/2}$ is a normalization to keep the total energy of the scaled wavelet constant.

The continuous wavelet transform of a discrete sequences $x_n$ with a scaled and translated version of $\psi_o(\eta)$:

$$W_n(s) = \sum_{n'=0}^{N-1} x_{n'} \psi^*\left[\frac{(n'-n)\delta t}{s}\right] \tag{A.3}$$

Where the (*) indicates the complex conjugate and $N$ is the number of points in the time series. By varying the *wavelet scale s* and translating along the *localized time index n*, one can construct a picture showing both the amplitude of any features versus the scale and how this amplitude varies with time. Although it is possible to calculate the wavelet transform using equation (A.3), it is considerably faster to do the calculation in Fourier space.

The discrete Fourier transform (DFT) of $x_n$ is

$$\hat{x}_k = \frac{1}{N} \sum_{n=0}^{N-1} x_n e^{-2\pi i k n/N} \tag{A.4}$$

Where $k = 0...N-1$ is the frequency index. In the continuous limit, the Fourier transform of a function $\psi(t/s)$ is given by $\hat{\psi}(s\omega)$. By the convolution theorem, the wavelet transform is the inverse Fourier transform of the product:

$$W_n(s) = \sum_{k=0}^{N-1} \hat{x}_k \hat{\psi}^*(s\omega_k) e^{i\omega_k n \delta t} \tag{A.5}$$

where the angular frequency is defined as

$$\omega_k = \begin{cases} \frac{2\pi k}{N\delta t} & : \quad k \leq \frac{N}{2} \\ -\frac{2\pi k}{N\delta t} & : \quad k > \frac{N}{2} \end{cases} \tag{A.6}$$

Using equation (A.5) and a standard Fourier transform routine, the continuous wavelet transform (for a given $s$) can be calculated at all $n$ simultaneously and efficiently.

# Appendix B: Phase Analysis

In this section, the uni- and bivariate analysis of observed time series is discussed. In general, the noise component in the signals has a relatively large variance which affects the significance of features in the power spectra. A controlled smoothing of the time series leads to a reduction of the variance and makes it possible to derive the required information from a signal. Smoothing is achieved by windowing in the time domain which corresponds to a convolution in the frequency domain. The treatment is closely followed from Jenkins and Watts (1968) and Doyle et al. (1999).

Consider two time series $x_p$ and $y_p$, with $p = 0, ..., N-1$, sampled at intervals of $\Delta$ seconds. These time series are considered as realization of two processes $X(t)$ and $Y(t)$. A statistical description requires knowledge of the following quantities:

- the mean values of the series

$$\bar{x} = \frac{1}{N}\sum_{p=0}^{N-1} x_p \ , \ \bar{y} = \frac{1}{N}\sum_{p=0}^{N-1} y_p \tag{B.1}$$

- the auto-covariance function (acvf) estimates

$$c_{xx}(\ell) = \frac{1}{N}\sum_{p=0}^{N-1-\ell} (x_p - \bar{x})(x_{p+\ell} - \bar{x}) \ , \tag{B.2}$$

$$c_{yy}(\ell) = \frac{1}{N} \sum_{p=0}^{N-1-\ell} (y_p - \bar{y})(y_{p+\ell} - \bar{y}) \tag{B.3}$$

Note that $c_{xx}(0) = \sigma_x^2$ and $c_{yy}(0) = \sigma_y^2$ are the variances of the time series. The functions $c_{xx}(\ell)$ and $c_{yy}(\ell)$ are even functions of lag $\ell$.

- the cross-covariance function (ccvf) estimates

$$c_{xy}(\ell) = \frac{1}{N} \sum_{p=0}^{N-1-\ell} (x_p - \bar{x})(y_{p+\ell} - \bar{y}) \ , \tag{B.4}$$

$$c_{yx}(\ell) = \frac{1}{N} \sum_{p=0}^{N-1-\ell} (x_{p+\ell} - \bar{x})(y_p - \bar{y}) \tag{B.5}$$

In this case, $c_{yx}(\ell) = c_{xy}(-\ell)$

- the even and odd ccvf estimates

$$l_{xy}(\ell) = (c_{xy}(\ell) + c_{xy}(-\ell))/2 \tag{B.6}$$

$$q_{xy}(\ell) = (c_{xy}(\ell) - c_{xy}(-\ell))/2 \tag{B.7}$$

The function $l_{xy}(\ell) = l_{xy}(-\ell)$ is even and the function $q_{xy}(\ell) = -q_{xy}(-\ell)$ is odd. Related quantities are the auto-correlation functions $r_{xx}(\ell) = c_{xx}(\ell)/c_{xx}(0)$ and $r_{yy}(\ell) = c_{yy}(\ell)/c_{yy}(0)$, and the cross-correlation function $r_{xy}(\ell) = c_{xy}(\ell)/\sqrt{c_{xx}(0)c_{yy}(0)}$. Here $\ell$ is a finite number of lags in the range $\ell = -L, ...L-1$ with $L$ approximately half times $N$.

Now, taking the discrete Fourier transform (DFT) of these functions. As $c_{xx}$, $c_{yy}$ and $l_{xy}$ are even and $q_{xy}$ is odd functions, the resulting DFT can be written in terms of cosine and sine transforms. The index $\jmath$ corresponds to frequency $\nu_\jmath = \jmath/(2L\Delta)$ with $\jmath = 0, ..., L$. The following transform result

- the smoothed spectral estimates

$$\overline{C}_{xx}(J) = c_{xx}(0) + 2\sum_{k=1}^{L-1} c_{xx}(k)\omega(k)cos\frac{\pi Jk}{L} \tag{B.8}$$

$$\overline{C}_{yy}(J) = c_{yy}(0) + 2\sum_{k=1}^{L-1} c_{yy}(k)\omega(k)cos\frac{\pi Jk}{L} \tag{B.9}$$

- the smoothed co- and quadrature spectral estimates

$$\overline{L}_{xy}(J) = l_{xx}(0) + 2\sum_{k=1}^{L-1} l_{xx}(k)\omega(k)cos\frac{\pi Jk}{L} \tag{B.10}$$

$$\overline{Q}_{xy}(J) = 2\sum_{k=1}^{L-1} q_{yy}(k)\omega(k)sin\frac{\pi Jk}{L} \tag{B.11}$$

with $\overline{Q}_{xy}(0) = \overline{Q}_{xy}(L) = 0$. Where $\omega(\ell)$ is a window function satisfying $\omega(-L) = \omega(L) = 0$. For the analysis in this work, the chosen window is Turkey function which is defined as:

$$\omega(k) = \frac{1}{2}\left(1 + cos\frac{\pi k}{L}\right) \tag{B.12}$$

From these smoothed estimates, the cross amplitude spectral estimate $\overline{A}_{xy}$, the gain $\overline{G}_{xy}$, the phase spectral estimate $\overline{F}_{xy}$ and the squared coherency spectral estimate $\overline{K}^2_{xy}$ can be defined as,

$$\overline{A}_{xy}(J) = \sqrt{\overline{L}^2_{xy}(J) + \overline{Q}^2_{xy}(J)} \tag{B.13}$$

$$\overline{G}_{xy} = \overline{A}_{xy}/\overline{C}_{xx}(J) \tag{B.14}$$

$$\overline{F}_{xy}(J) = arctan\left(-\frac{\overline{Q}_{xy}(J)}{\overline{L}_{xy}(J)}\right) \tag{B.15}$$

$$\overline{K}^2_{xy}(J) = \frac{\overline{A}^2_{xy}(J)}{\overline{C}_{xx}(J)\overline{C}_{yy}(J)} \tag{B.16}$$

the phase difference between $x_p$ and $y_p$ at frequency $\nu_J$ is given by $\overline{F}_{xy}(J)$. A positive phase

implies that $x_p$ lags behind $y_p$ by $\overline{F}_{xy}(j)/(2\pi\nu_j)$ seconds.

As described in Doyle et al. (1999), the confidence value for the squared coherency spectral estimate $\overline{K}^2_{xy}$ is given by

$$\overline{K}^2_{xy} = 1 - \alpha^{2/(\nu-2)} \tag{B.17}$$

So all $\overline{K}^2_{xy}(j) \geq \overline{K}^2_{xy}$ satisfy the confidence criterion. Where $\alpha$ is significance level and $\nu$ is $(8/3)(N/L)$ for the Turkey window function. Whereas the phase at frequency $j$ are given by

$$\overline{F}_{xy}(j) \pm arscsin\sqrt{f_{2,\nu-2}(\alpha)/Z(j)} \tag{B.18}$$

Where

$$Z(j) \equiv \frac{(\nu-2)\overline{K}^2_{xy}(j)}{2(1-\overline{K}^2_{xy}(j))} \quad and \tag{B.19}$$

$$f_{2,\nu-2}(\alpha) = \frac{\nu-2}{2}\left(\frac{1}{\alpha^{2/(\nu-2)}} - 1\right) \tag{B.20}$$

# Bibliography


Ahmad, I. A. and Withbroe, G. L. (1977). EUV analysis of polar plumes. *Solar Phys.*, 53:397–408.

Alazraki, G. and Couturier, P. (1971). Solar Wind Acceleration Caused by the Gradient of Alfven Wave Pressure. *Astron. & Astrophys.*, 13:380–+.

Alfvén, H. (1942). Existence of Electromagnetic-Hydrodynamic Waves. *Nature*, 150:405–406.

Antonucci, E., Dodero, M. A., and Giordano, S. (2000). Fast Solar Wind Velocity in a Polar Coronal Hole during Solar Minimum. *Solar Phys.*, 197:115–134.

Antonucci, E., Dodero, M. A., Giordano, S., Krishnakumar, V., and Noci, G. (2004). Spectroscopic measurement of the plasma electron density and outflow velocity in a polar coronal hole. *Astron. & Astrophys.*, 416:749–758.

Antonucci, E., Gabriel, A. H., and Patchett, B. E. (1984). Oscillations in EUV emission lines during a loop brightening. *Solar Phys.*, 93:85–94.

Armstrong, J. W. and Woo, R. (1981). Solar wind motion within 30 R solar masses - Spacecraft radio scintillation observations. *Astron. & Astrophys.*, 103:415–421.

Aschwanden, M. J. (1987). Theory of radio pulsations in coronal loops. *Solar Phys.*, 111:113–136.

Aschwanden, M. J. (2005). *Physics of the Solar Corona. An Introduction with Problems and Solutions (2nd edition)*.

Aschwanden, M. J., Newmark, J. S., Delaboudinière, J., Neupert, W. M., Klimchuk, J. A., Gary, G. A., Portier-Fozzani, F., and Zucker, A. (1999). Three-dimensional Stereoscopic Analysis of Solar Active Region Loops. I. SOHO/EIT Observations at Temperatures of (1.0-1.5) X 10ˆ6 K. *Astrophys. J.*, 515:842–867.

Aschwanden, M. J., Poland, A. I., and Rabin, D. M. (2001). The New Solar Corona. *Ann. Rev. Astron. Astrophys.*, 39:175–210.

Athay, R. G. and White, O. R. (1979). Chromospheric oscillations observed with OSO 8. IV - Power and phase spectra for C IV. *Astrophys. J.*, 229:1147–1162.

Banerjee, D., Erdélyi, R., Oliver, R., and O'Shea, E. (2007). Present and Future Observing Trends in Atmospheric Magnetoseismology. *Solar Phys.*, 246:3–29.

Banerjee, D., Gupta, G. R., and Teriaca, L. (2010). Propagating MHD Waves in Coronal Holes. *Space Sci. Rev.*, pages 120–+.

Banerjee, D., O'Shea, E., and Doyle, J. G. (2000a). Long-Period Oscillations in Polar Plumes as Observed by cds on Soho. *Solar Phys.*, 196:63–78.

Banerjee, D., O'Shea, E., Doyle, J. G., and Goossens, M. (2001a). Long period oscillations in the inter-plume regions of the Sun. *Astron. & Astrophys.*, 377:691–700.

Banerjee, D., O'Shea, E., Doyle, J. G., and Goossens, M. (2001b). Signatures of very long period waves in the polar coronal holes. *Astron. & Astrophys.*, 380:L39–L42.

Banerjee, D., O'Shea, E., Doyle, J. G., and Goossens, M. (2001c). The nature of network oscillations. *Astron. & Astrophys.*, 371:1137–1149.

Banerjee, D., Pérez-Suárez, D., and Doyle, J. G. (2009a). Signatures of Alfvén waves in the polar coronal holes as seen by EIS/Hinode. *Astron. & Astrophys.*, 501:L15–L18.

Banerjee, D., Teriaca, L., Doyle, J. G., and Lemaire, P. (2000b). Polar Plumes and Inter-plume regions as observed by SUMER on SOHO. *Solar Phys.*, 194:43–58.

Banerjee, D., Teriaca, L., Doyle, J. G., and Wilhelm, K. (1998). Broadening of SI VIII lines observed in the solar polar coronal holes. *Astron. & Astrophys.*, 339:208–214.

Banerjee, D., Teriaca, L., Gupta, G. R., Imada, S., Stenborg, G., and Solanki, S. K. (2009b). Propagating waves in polar coronal holes as seen by SUMER and EIS. *Astron. & Astrophys.*, 499:L29–L32.

Beckers, J. M. (1972). Solar Spicules. *Ann. Rev. Astron. Astrophys.*, 10:73–+.

Belcher, J. W. (1971). ALFVÉNIC Wave Pressures and the Solar Wind. *Astrophys. J.*, 168:509–+.

Belcher, J. W. and Davis, Jr., L. (1971). Large-amplitude Alfvén waves in the interplanetary medium, 2. *J. Geophys. Res.*, 76:3534–3563.

Bemporad, A., Matthaeus, W. H., and Poletto, G. (2008). Low-Frequency Ly$\alpha$ Power Spectra Observed by UVCS in a Polar Coronal Hole. *Astrophys. J. Lett.*, 677:L137–L140.

Berghmans, D. and Clette, F. (1999). Active region EUV transient brightenings - First Results by EIT of SOHO JOP80. *Solar Phys.*, 186:207–229.

Bertaux, J. L., Kyrölä, E., Quémerais, E., Pellinen, R., Lallement, R., Schmidt, W., Berthé, M., Dimarellis, E., Goutail, J. P., Taulemesse, C., Bernard, C., Leppelmeier, G., Summanen, T., Hannula, H., Huomo, H., Kehlä, V., Korpela, S., Leppälä, K., Strömmer, E., Torsti, J., Viherkanto, K., Hochedez, J. F., Chretiennot, G., Peyroux, R., and Holzer, T. (1995). SWAN: A Study of Solar Wind Anisotropies on SOHO with Lyman Alpha Sky Mapping. *Solar Phys.*, 162:403–439.

Bohlin, J. D., Sheeley, N. R., and Tousey, R. (1975). Structure of the sun's polar cap at wavelengths 240 - 600 Å. In M. J. Rycroft, editor, *Space Research XV*, pages 651–656.

Bond, G., Kromer, B., Beer, J., Muscheler, R., Evans, M. N., Showers, W., Hoffmann, S., Lotti-Bond, R., Hajdas, I., and Bonani, G. (2001). Persistent Solar Influence on North Atlantic Climate During the Holocene. *Science*, 294:2130–2136.

Boynton, G. C. and Torkelsson, U. (1996). Dissipation of non-linear Alfven waves. *Astron. & Astrophys.*, 308:299–308.

Brueckner, G. E., Howard, R. A., Koomen, M. J., Korendyke, C. M., Michels, D. J., Moses, J. D., Socker, D. G., Dere, K. P., Lamy, P. L., Llebaria, A., Bout, M. V., Schwenn, R., Simnett, G. M., Bedford, D. K., and Eyles, C. J. (1995). The Large Angle Spectroscopic Coronagraph (LASCO). *Solar Phys.*, 162:357–402.

Carlsson, M., Judge, P. G., and Wilhelm, K. (1997). SUMER Observations Confirm the Dynamic Nature of the Quiet Solar Outer Atmosphere: The Internetwork Chromosphere. *Astrophys. J. Lett.*, 486:L63+.

Casalbuoni, S., Del Zanna, L., Habbal, S. R., and Velli, M. (1999). Coronal plumes and the expansion of pressure-balanced structures in the fast solar wind. *J. Geophys. Res.*, 104:9947–9962.

Chae, J., Yun, H. S., and Poland, A. I. (1998). Temperature Dependence of Ultraviolet Line Average Doppler Shifts in the Quiet Sun. *Astrophys. J. Suppl.*, 114:151–+.

Chapman, R. D., Jordan, S. D., Neupert, W. M., and Thomas, R. J. (1972). Evidence for the 300-SECOND Oscillation from OSO-7 Extreme-Ultraviolet Observations. *Astrophys. J. Lett.*, 174:L97+.

Cooper, F. C., Nakariakov, V. M., and Tsiklauri, D. (2003a). Line-of-sight effects on observability of kink and sausage modes in coronal structures with imaging telescopes. *Astron. & Astrophys.*, 397:765–770.

Cooper, F. C., Nakariakov, V. M., and Williams, D. R. (2003b). Short period fast waves in solar coronal loops. *Astron. & Astrophys.*, 409:325–330.

Cowsik, R., Singh, J., Saxena, A. K., Srinivasan, R., and Raveendran, A. V. (1999). Short-period intensity oscillations in the solar corona observed during the total solar eclipse of 26 February 1998. *Solar Phys.*, 188:89–98.

Cranmer, S. R. (2009). Coronal Holes. *Living Reviews in Solar Physics*, 6:3–+.

Cranmer, S. R. and van Ballegooijen, A. A. (2005). On the Generation, Propagation, and Reflection of Alfvén Waves from the Solar Photosphere to the Distant Heliosphere. *Astrophys. J. Suppl.*, 156:265–293.

Culhane, J. L., Harra, L. K., James, A. M., Al-Janabi, K., Bradley, L. J., Chaudry, R. A., Rees, K., Tandy, J. A., Thomas, P., Whillock, M. C. R., Winter, B., Doschek, G. A., Korendyke, C. M., Brown, C. M., Myers, S., Mariska, J., Seely, J., Lang, J., Kent, B. J., Shaughnessy, B. M., Young, P. R., Simnett, G. M., Castelli, C. M., Mahmoud, S., Mapson-Menard, H., Probyn, B. J., Thomas, R. J., Davila, J., Dere, K., Windt, D., Shea, J., Hagood, R., Moye, R., Hara, H., Watanabe, T., Matsuzaki, K., Kosugi, T., Hansteen, V., and Wikstol, Ø. (2007). The EUV Imaging Spectrometer for Hinode. *Solar Phys.*, 243:19–61.

Curdt, W., Brekke, P., Feldman, U., Wilhelm, K., Dwivedi, B. N., Schühle, U., and Lemaire, P. (2001). The SUMER spectral atlas of solar-disk features. *Astron. & Astrophys.*, 375:591–613.

Curdt, W., Kucera, A., Rybák, J., Schühle, U., and Wöhl, H. (1997). Dynamical Properties of the Chromosphere and Transition Region in the Supergranular Network: What Precision of the Spectral Line Characteristics Can be Reached? In A. Wilson, editor, *Fifth SOHO Workshop: The Corona and Solar Wind Near Minimum Activity*, volume 404 of *ESA Special Publication*, pages 307–+.

Curdt, W., Landi, E., and Feldman, U. (2004). The SUMER spectral atlas of solar coronal features. *Astron. & Astrophys.*, 427:1045–1054.

Dame, L., Gouttebroze, P., and Malherbe, J. (1984). Observation and analysis of intensity oscillations in the solar K-line. *Astron. & Astrophys.*, 130:331–340.

Dammasch, I. E., Wilhelm, K., Curdt, W., and Hassler, D. M. (1999). The NE BT VIII (lambda 770) resonance line: solar wavelengths determined by SUMER on SOHO. *Astron. & Astrophys.*, 346:285–294.

De Moortel, I., Ireland, J., and Walsh, R. W. (2000). Observation of oscillations in coronal loops. *Astron. & Astrophys.*, 355:L23–L26.

De Moortel, I., Ireland, J., Walsh, R. W., and Hood, A. W. (2002). Longitudinal intensity oscillations in coronal loops observed with TRACE I. Overview of Measured Parameters. *Solar Phys.*, 209:61–88.

De Pontieu, B. and Erdélyi, R. (2006). The nature of moss and lower atmospheric seismology. *Royal Society of London Philosophical Transactions Series A*, 364:383–394.

De Pontieu, B., Erdélyi, R., and James, S. P. (2004). Solar chromospheric spicules from the leakage of photospheric oscillations and flows. *Nature*, 430:536–539.

De Pontieu, B., McIntosh, S., Hansteen, V. H., Carlsson, M., Schrijver, C. J., Tarbell, T. D., Title, A. M., Shine, R. A., Suematsu, Y., Tsuneta, S., Katsukawa, Y., Ichimoto, K., Shimizu, T., and Nagata, S. (2007a). A Tale of Two Spicules: The Impact of Spicules on the Magnetic Chromosphere. *Pub. Astron. Soc. Japan*, 59:655–+.

De Pontieu, B., McIntosh, S. W., Carlsson, M., Hansteen, V. H., Tarbell, T. D., Schrijver, C. J., Title, A. M., Shine, R. A., Tsuneta, S., Katsukawa, Y., Ichimoto, K., Suematsu, Y., Shimizu, T., and Nagata, S. (2007b). Chromospheric Alfvénic Waves Strong Enough to Power the Solar Wind. *Science*, 318:1574–.

DeForest, C. E. and Gurman, J. B. (1998). Observation of Quasi-periodic Compressive Waves in Solar Polar Plumes. *Astrophys. J. Lett.*, 501:L217+.

DeForest, C. E., Hoeksema, J. T., Gurman, J. B., Thompson, B. J., Plunkett, S. P., Howard, R., Harrison, R. C., and Hassler, D. M. (1997). Polar Plume Anatomy: Results of a Coordinated Observation. *Solar Phys.*, 175:393–410.

Delaboudinière, J., Artzner, G. E., Brunaud, J., Gabriel, A. H., Hochedez, J. F., Millier, F., Song, X. Y., Au, B., Dere, K. P., Howard, R. A., Kreplin, R., Michels, D. J., Moses, J. D., Defise, J. M., Jamar, C., Rochus, P., Chauvineau, J. P., Marioge, J. P., Catura, R. C., Lemen, J. R., Shing, L., Stern, R. A., Gurman, J. B., Neupert, W. M., Maucherat, A., Clette, F., Cugnon, P., and van Dessel, E. L. (1995). EIT: Extreme-Ultraviolet Imaging Telescope for the SOHO Mission. *Solar Phys.*, 162:291–312.

Dolla, L. and Solomon, J. (2008). Solar off-limb line widths: Alfvén waves, ion-cyclotron waves, and preferential heating. *Astron. & Astrophys.*, 483:271–283.

Domingo, V., Fleck, B., and Poland, A. I. (1995). The SOHO Mission: an Overview. *Solar Phys.*, 162:1–37.

Doschek, G. A. and Feldman, U. (1977). The coronal temperature and nonthermal motions in a coronal hole compared with other solar regions. *Astrophys. J. Lett.*, 212:L143–L146.

Doyle, J. G., Banerjee, D., and Perez, M. E. (1998a). Coronal line-width variations. *Solar Phys.*, 181:91–101.

Doyle, J. G., van den Oord, G. H. J., O'Shea, E., and Banerjee, D. (1998b). Waves in the solar transition region. *Solar Phys.*, 181:51–71.

Doyle, J. G., van den Oord, G. H. J., O'Shea, E., and Banerjee, D. (1999). Exploring the dynamical nature of the lower solar chromosphere. *Astron. & Astrophys.*, 347:335–347.

Edlén, B. (1943). Die Deutung der Emissionslinien im Spektrum der Sonnenkorona. Mit 6 Abbildungen. *Zeitschrift fur Astrophysik*, 22:30–+.

Erdélyi, R. (2007). Magnetohydrodynamic Waves. In S. S. Hasan & D. Banerjee, editor, *Kodai School on Solar Physics*, volume 919 of *American Institute of Physics Conference Series*, pages 122–137.

Erdélyi, R. and Ballai, I. (2007). Heating of the solar and stellar coronae: a review. *Astronomische Nachrichten*, 328:726–733.

Erdélyi, R. and Fedun, V. (2007). Are There Alfvén Waves in the Solar Atmosphere? *Science*, 318:1572–1574.

Erdélyi, R., Malins, C., Tóth, G., and de Pontieu, B. (2007). Leakage of photospheric acoustic waves into non-magnetic solar atmosphere. *Astron. & Astrophys.*, 467:1299–1311.

Erdélyi, R. and Taroyan, Y. (2008). Hinode EUV spectroscopic observations of coronal oscillations. *Astron. & Astrophys.*, 489:L49–L52.

Evans, J. W. and Michard, R. (1962). Observational Study of Macroscopic Inhomogeneities in the Solar Atmosphere. III. Vertical Oscillatory Motions in the Solar Photosphere. *Astrophys. J.*, 136:493–+.

Fedun, V., Erdélyi, R., and Shelyag, S. (2009). Oscillatory Response of the 3D Solar Atmosphere to the Leakage of Photospheric Motion. *Solar Phys.*, 258:219–241.

Fedun, V., Shelyag, S., and Erdélyi, R. (2011). Numerical Modeling of Footpoint-driven Magneto-acoustic Wave Propagation in a Localized Solar Flux Tube. *Astrophys. J.*, 727:17–+.

Fontenla, J. M., Avrett, E. H., and Loeser, R. (1990). Energy balance in the solar transition region. I - Hydrostatic thermal models with ambipolar diffusion. *Astrophys. J.*, 355:700–718.

Fossum, A. and Carlsson, M. (2005). High-frequency acoustic waves are not sufficient to heat the solar chromosphere. *Nature*, 435:919–921.

Foukal, P., Fröhlich, C., Spruit, H., and Wigley, T. M. L. (2006). Variations in solar luminosity and their effect on the Earth's climate. *Nature*, 443:161–166.

Fröhlich, C., Romero, J., Roth, H., Wehrli, C., Andersen, B. N., Appourchaux, T., Domingo, V., Telljohann, U., Berthomieu, G., Delache, P., Provost, J., Toutain, T., Crommelynck, D. A., Chevalier, A., Fichot, A., Däppen, W., Gough, D., Hoeksema, T., Jiménez, A., Gómez, M. F., Herreros, J. M., Cortés, T. R., Jones, A. R., Pap, J. M., and Willson, R. C. (1995). VIRGO: Experiment for Helioseismology and Solar Irradiance Monitoring. *Solar Phys.*, 162:101–128.

Gabriel, A. H. (1976). A magnetic model of the solar transition region. *Royal Society of London Philosophical Transactions Series A*, 281:339–352.

Gabriel, A. H., Abbo, L., Bely-Dubau, F., Llebaria, A., and Antonucci, E. (2005). Solar Wind Outflow in Polar Plumes from 1.05 to 2.4 R. *Astrophys. J. Lett.*, 635:L185–L188.

Gabriel, A. H., Bely-Dubau, F., and Lemaire, P. (2003). The Contribution of Polar Plumes to the Fast Solar Wind. *Astrophys. J.*, 589:623–634.

Gabriel, A. H., Grec, G., Charra, J., Robillot, J., Roca Cortés, T., Turck-Chièze, S., Bocchia, R., Boumier, P., Cantin, M., Cespédes, E., Cougrand, B., Crétolle, J., Damé, L., Decaudin, M., Delache, P., Denis, N., Duc, R., Dzitko, H., Fossat, E., Fourmond, J., García, R. A., Gough, D., Grivel, C., Herreros, J. M., Lagardère, H., Moalic, J., Pallé, P. L., Pétrou, N., Sanchez, M., Ulrich, R., and van der Raay, H. B. (1995). Global Oscillations at Low Frequency from the SOHO Mission (GOLF). *Solar Phys.*, 162:61–99.

Gary, G. A. (2001). Plasma Beta above a Solar Active Region: Rethinking the Paradigm. *Solar Phys.*, 203:71–86.

Giordano, S., Antonucci, E., Noci, G., Romoli, M., and Kohl, J. L. (2000). Identification of the Coronal Sources of the Fast Solar Wind. *Astrophys. J. Lett.*, 531:L79–L82.

Goldstein, B. E., Smith, E. J., Balogh, A., Horbury, T. S., Goldstein, M. L., and Roberts, D. A. (1995a). Properties of magnetohydrodynamic turbulence in the solar wind as observed by Ulysses at high heliographic latitudes. *Geophys. Res. Lett.*, 22:3393–3396.

Goldstein, M. L., Roberts, D. A., and Matthaeus, W. H. (1995b). Magnetohydrodynamic Turbulence In The Solar Wind. *Ann. Rev. Astron. Astrophys.*, 33:283–326.

Golub, L., Deluca, E., Austin, G., Bookbinder, J., Caldwell, D., Cheimets, P., Cirtain, J., Cosmo, M., Reid, P., Sette, A., Weber, M., Sakao, T., Kano, R., Shibasaki, K., Hara, H., Tsuneta, S., Kumagai, K., Tamura, T., Shimojo, M., McCracken, J., Carpenter, J., Haight, H., Siler, R., Wright, E., Tucker, J., Rutledge, H., Barbera, M., Peres, G., and Varisco, S. (2007). The X-Ray Telescope (XRT) for the Hinode Mission. *Solar Phys.*, 243:63–86.

Gömöry, P., Rybák, J., Kučera, A., Curdt, W., and Wöhl, H. (2006). SOHO/CDS observations of waves above the network. *Astron. & Astrophys.*, 448:1169–1175.

Guhathakurta, M., Fisher, R. R., and Altrock, R. C. (1993). Large-scale coronal temperature and density distributions, 1984-1992. *Astrophys. J. Lett.*, 414:145–148.

Gupta, G. R., Banerjee, D., Teriaca, L., Imada, S., and Solanki, S. (2010a). Accelerating Waves in Polar Coronal Holes as Seen by EIS and SUMER. *Astrophys. J.*, 718:11–22.

Gupta, G. R., O'Shea, E., Banerjee, D., Popescu, M., and Doyle, J. G. (2009). On the statistical detection of propagating waves in polar coronal holes. *Astron. & Astrophys.*, 493:251–257.

Gupta, G. R., O'Shea, E., Banerjee, D., Popescu, M., and Doyle, J. G. (2010b). Statistical Detection of Propagating Waves in a Polar Coronal Hole. In S. S. Hasan & R. J. Rutten, editor, *Magnetic Coupling between the Interior and Atmosphere of the Sun*, pages 433–436.

Hale, G. E. and Ellerman, F. (1904). Calcium and Hydrogen Flocculi. *Astrophys. J.*, 19:41–+.

Handy, B. N., Acton, L. W., Kankelborg, C. C., Wolfson, C. J., Akin, D. J., Bruner, M. E., Caravalho, R., Catura, R. C., Chevalier, R., Duncan, D. W., Edwards, C. G., Feinstein, C. N., Freeland, S. L., Friedlaender, F. M., Hoffmann, C. H., Hurlburt, N. E., Jurcevich, B. K., Katz, N. L., Kelly, G. A., Lemen, J. R., Levay, M., Lindgren, R. W., Mathur, D. P., Meyer, S. B., Morrison, S. J., Morrison, M. D., Nightingale, R. W., Pope, T. P., Rehse, R. A., Schrijver, C. J., Shine, R. A., Shing, L., Strong, K. T., Tarbell, T. D., Title, A. M., Torgerson, D. D., Golub, L., Bookbinder, J. A., Caldwell, D., Cheimets, P. N., Davis, W. N., Deluca, E. E., McMullen, R. A., Warren, H. P., Amato, D., Fisher, R., Maldonado, H., and Parkinson, C. (1999). The transition region and coronal explorer. *Solar Phys.*, 187:229–260.

Harrison, R. A. (1987). Solar soft X-ray pulsations. *Astron. & Astrophys.*, 182:337–347.

Harrison, R. A., Sawyer, E. C., Carter, M. K., Cruise, A. M., Cutler, R. M., Fludra, A., Hayes, R. W., Kent, B. J., Lang, J., Parker, D. J., Payne, J., Pike, C. D., Peskett, S. C., Richards, A. G., Gulhane, J. L., Norman, K., Breeveld, A. A., Breeveld, E. R., Al Janabi, K. F., McCalden, A. J., Parkinson, J. H., Self, D. G., Thomas, P. D., Poland, A. I., Thomas, R. J., Thompson, W. T., Kjeldseth-Moe, O., Brekke, P., Karud, J., Maltby, P., Aschenbach, B., Bräuninger, H., Kühne, M., Hollandt, J., Siegmund, O. H. W., Huber, M. C. E., Gabriel, A. H., Mason, H. E., and Bromage, B. J. I. (1995). The Coronal Diagnostic Spectrometer for the Solar and Heliospheric Observatory. *Solar Phys.*, 162:233–290.

Hasan, S. S. (2008). Chromospheric dynamics. *Advances in Space Research*, 42:86–95.

Hollandt, J., Schühle, U., Paustian, W., Curdt, W., Kühne, M., Wende, B., and Wilhelm, K. (1996). Radiometric calibration of the telescope and ultraviolet spectrometer SUMER on SOHO. *Applied Optics*, 35:5125–5133.

Hollweg, J. V. (1981). Alfven waves in the solar atmosphere. II - Open and closed magnetic flux tubes. *Solar Phys.*, 70:25–66.

Hovestadt, D., Hilchenbach, M., Bürgi, A., Klecker, B., Laeverenz, P., Scholer, M., Grünwaldt, H., Axford, W. I., Livi, S., Marsch, E., Wilken, B., Winterhoff, H. P., Ipavich, F. M., Bedini, P., Coplan, M. A., Galvin, A. B., Gloeckler, G., Bochsler, P., Balsiger, H., Fischer, J., Geiss, J., Kallenbach, R., Wurz, P., Reiche, K., Gliem, F., Judge, D. L., Ogawa, H. S., Hsieh, K. C., Möbius, E., Lee, M. A., Managadze, G. G., Verigin, M. I., and Neugebauer, M. (1995). CELIAS - Charge, Element and Isotope Analysis System for SOHO. *Solar Phys.*, 162:441–481.

Howard, R. A., Moses, J. D., Vourlidas, A., Newmark, J. S., Socker, D. G., Plunkett, S. P., Korendyke, C. M., Cook, J. W., Hurley, A., Davila, J. M., Thompson, W. T., St Cyr, O. C., Mentzell, E., Mehalick, K., Lemen, J. R., Wuelser, J. P., Duncan, D. W., Tarbell, T. D., Wolfson, C. J., Moore, A., Harrison, R. A., Waltham, N. R., Lang, J., Davis, C. J., Eyles, C. J., Mapson-Menard, H., Simnett, G. M., Halain, J. P., Defise, J. M., Mazy, E., Rochus, P., Mercier, R., Ravet, M. F., Delmotte, F., Auchere, F., Delaboudiniere, J. P., Bothmer, V., Deutsch, W., Wang, D., Rich, N., Cooper, S., Stephens, V., Maahs, G., Baugh, R., McMullin,

D., and Carter, T. (2008). Sun Earth Connection Coronal and Heliospheric Investigation (SECCHI). *Space Science Reviews*, 136:67–115.

Ionson, J. A. (1978). Resonant absorption of Alfvenic surface waves and the heating of solar coronal loops. *Astrophys. J.*, 226:650–673.

Jefferies, S. M., McIntosh, S. W., Armstrong, J. D., Bogdan, T. J., Cacciani, A., and Fleck, B. (2006). Magnetoacoustic Portals and the Basal Heating of the Solar Chromosphere. *Astrophys. J. Lett.*, 648:L151–L155.

Jenkins, G. M. and Watts, D. G. (1968). *Spectral Analysis and its Applications.*

Jess, D. B., Mathioudakis, M., Erdélyi, R., Crockett, P. J., Keenan, F. P., and Christian, D. J. (2009). Alfvén Waves in the Lower Solar Atmosphere. *Science*, 323:1582–1585.

Jess, D. B., Rabin, D. M., Thomas, R. J., Brosius, J. W., Mathioudakis, M., and Keenan, F. P. (2008). Transition Region Velocity Oscillations Observed by EUNIS-06. *Astrophys. J.*, 682:1363–1369.

Judge, P. G., Tarbell, T. D., and Wilhelm, K. (2001). A Study of Chromospheric Oscillations Using the SOHO and TRACE Spacecraft. *Astrophys. J.*, 554:424–444.

Kaghashvili, E. K., Quinn, R. A., and Hollweg, J. V. (2009). Driven Waves as a Diagnostics Tool in the Solar Corona. *Astrophys. J.*, 703:1318–1322.

Katsiyannis, A. C., Williams, D. R., McAteer, R. T. J., Gallagher, P. T., Keenan, F. P., and Murtagh, F. (2003). Eclipse observations of high-frequency oscillations in active region coronal loops. *Astron. & Astrophys.*, 406:709–714.

King, D. B., Nakariakov, V. M., Deluca, E. E., Golub, L., and McClements, K. G. (2003). Propagating EUV disturbances in the Solar corona: Two-wavelength observations. *Astron. & Astrophys.*, 404:L1–L4.

Klimchuk, J. A. (2006). On Solving the Coronal Heating Problem. *Solar Phys.*, 234:41–77.

Kohl, J. L., Esser, R., Gardner, L. D., Habbal, S., Daigneau, P. S., Dennis, E. F., Nystrom, G. U., Panasyuk, A., Raymond, J. C., Smith, P. L., Strachan, L., van Ballegooijen, A. A., Noci, G., Fineschi, S., Romoli, M., Ciaravella, A., Modigliani, A., Huber, M. C. E., Antonucci, E., Benna, C., Giordano, S., Tondello, G., Nicolosi, P., Naletto, G., Pernechele, C., Spadaro, D., Poletto, G., Livi, S., von der Lühe, O., Geiss, J., Timothy, J. G., Gloeckler, G., Allegra, A., Basile, G., Brusa, R., Wood, B., Siegmund, O. H. W., Fowler, W., Fisher, R., and Jhabvala, M. (1995). The Ultraviolet Coronagraph Spectrometer for the Solar and Heliospheric Observatory. *Solar Phys.*, 162:313–356.

Kontogiannis, I., Tsiropoula, G., and Tziotziou, K. (2010). Power halo and magnetic shadow in a solar quiet region observed in the H$\alpha$ line. *Astron. & Astrophys.*, 510:A41+.

Kopp, R. A. and Holzer, T. E. (1976). Dynamics of coronal hole regions. I - Steady polytropic flows with multiple critical points. *Solar Phys.*, 49:43–56.

Kosugi, T., Matsuzaki, K., Sakao, T., Shimizu, T., Sone, Y., Tachikawa, S., Hashimoto, T., Minesugi, K., Ohnishi, A., Yamada, T., Tsuneta, S., Hara, H., Ichimoto, K., Suematsu, Y., Shimojo, M., Watanabe, T., Shimada, S., Davis, J. M., Hill, L. D., Owens, J. K., Title, A. M., Culhane, J. L., Harra, L. K., Doschek, G. A., and Golub, L. (2007). The Hinode (Solar-B) Mission: An Overview. *Solar Phys.*, 243:3–17.

Koutchmy, S., Zhugzhda, I. D., and Locans, V. (1983). Short period coronal oscillations - Observation and interpretation. *Astron. & Astrophys.*, 120:185–191.

Krieger, A. S., Timothy, A. F., and Roelof, E. C. (1973). A Coronal Hole and Its Identification as the Source of a High Velocity Solar Wind Stream. *Solar Phys.*, 29:505–525.

Krijger, J. M., Rutten, R. J., Lites, B. W., Straus, T., Shine, R. A., and Tarbell, T. D. (2001). Dynamics of the solar chromosphere. III. Ultraviolet brightness oscillations from TRACE. *Astron. & Astrophys.*, 379:1052–1082.

Landi, E. and Cranmer, S. R. (2009). Ion Temperatures in the Low Solar Corona: Polar Coronal Holes at Solar Minimum. *Astrophys. J.*, 691:794–805.

Lau, Y. and Siregar, E. (1996). Nonlinear Alfven Wave Propagation in the Solar Wind. *Astrophys. J.*, 465:451–+.

Leighton, R. B., Noyes, R. W., and Simon, G. W. (1962). Velocity Fields in the Solar Atmosphere. I. Preliminary Report. *Astrophys. J.*, 135:474–+.

Lemaire, P., Wilhelm, K., Curdt, W., Schule, U., Marsch, E., Poland, A. I., Jordan, S. D., Thomas, R. J., Hassler, D. M., Vial, J. C., Kuhne, M., Huber, M. C. E., Siegmund, O. H. W., Gabriel, A., Timothy, J. G., and Grewing, M. (1997). First Results of the SUMER Telescope and Spectrometer on SOHO - II. Imagery and Data Management. *Solar Phys.*, 170:105–122.

Lites, B. W., Kubo, M., Socas-Navarro, H., Berger, T., Frank, Z., Shine, R., Tarbell, T., Title, A., Ichimoto, K., Katsukawa, Y., Tsuneta, S., Suematsu, Y., Shimizu, T., and Nagata, S. (2008). The Horizontal Magnetic Flux of the Quiet-Sun Internetwork as Observed with the Hinode Spectro-Polarimeter. *Astrophys. J.*, 672:1237–1253.

Lites, B. W., Rutten, R. J., and Kalkofen, W. (1993). Dynamics of the solar chromosphere. I - Long-period network oscillations. *Astrophys. J.*, 414:345–356.

Lou, Y. (2002). Damping of Low-Frequency Alfvén Waves in Fast Polar Coronal Winds from the Rotating Sun. *Astrophys. J. Lett.*, 571:L187–L190.

Malins, C. and Erdélyi, R. (2007). Direct Propagation of Photospheric Acoustic p Modes into Nonmagnetic Solar Atmosphere. *Solar Phys.*, 246:41–52.

Mariska, J. T. (1992). *The solar transition region*.

Marsh, M. S., Walsh, R. W., De Moortel, I., and Ireland, J. (2003). Joint observations of propagating oscillations with SOHO/CDS and TRACE. *Astron. & Astrophys.*, 404:L37–L41.

McComas, D. J., Barraclough, B. L., Funsten, H. O., Gosling, J. T., Santiago-Muñoz, E., Skoug, R. M., Goldstein, B. E., Neugebauer, M., Riley, P., and Balogh, A. (2000). Solar wind observations over Ulysses' first full polar orbit. *J. Geophys. Res.*, 105:10419–10434.

McComas, D. J., Elliott, H. A., Schwadron, N. A., Gosling, J. T., Skoug, R. M., and Goldstein, B. E. (2003). The three-dimensional solar wind around solar maximum. *Geophys. Res. Lett.*, 30(10):100000–1.

McIntosh, S. W., Innes, D. E., de Pontieu, B., and Leamon, R. J. (2010). STEREO observations of quasi-periodically driven high velocity outflows in polar plumes. *Astron. & Astrophys.*, 510:L2+.

Moran, T. G. (2001). Interpretation of coronal off-limb spectral line width measurements. *Astron. & Astrophys.*, 374:L9–L11.

Moran, T. G. (2002). Solar and Heliospheric Observatory/Solar Ultraviolet Measurements of Estimated Radiation ultraviolet array detector distortion correction. *Review of Scientific Instruments*, 73:3982–3987.

Morgan, H., Habbal, S. R., and Li, X. (2004). Hydrogen Ly$\alpha$ Intensity Oscillations Observed by the Solar and Heliospheric Observatory Ultraviolet Coronagraph Spectrometer. *Astrophys. J.*, 605:521–527.

Müller-Mellin, R., Kunow, H., Fleißner, V., Pehlke, E., Rode, E., Röschmann, N., Scharmberg, C., Sierks, H., Rusznyak, P., McKenna-Lawlor, S., Elendt, I., Sequeiros, J., Meziat, D., Sanchez, S., Medina, J., Del Peral, L., Witte, M., Marsden, R., and Henrion, J. (1995). COSTEP - Comprehensive Suprathermal and Energetic Particle Analyser. *Solar Phys.*, 162:483–504.

Munro, R. H. and Withbroe, G. L. (1972). Properties of a Coronal "hole" Derived from Extreme-Ultraviolet Observations. *Astrophys. J.*, 176:511–+.

Nakariakov, V. M. and Ofman, L. (2001). Determination of the coronal magnetic field by coronal loop oscillations. *Astron. & Astrophys.*, 372:L53–L56.

Nakariakov, V. M., Ofman, L., and Arber, T. D. (2000). Nonlinear dissipative spherical Alfvén waves in solar coronal holes. *Astron. & Astrophys.*, 353:741–748.

Nakariakov, V. M., Ofman, L., Deluca, E. E., Roberts, B., and Davila, J. M. (1999). TRACE observation of damped coronal loop oscillations: Implications for coronal heating. *Science*, 285:862–864.

Nakariakov, V. M. and Verwichte, E. (2005). Coronal Waves and Oscillations. *Living Reviews in Solar Physics*, 2:3–+.

Neugebauer, M. and Snyder, C. W. (1962). Solar Plasma Experiment. *Science*, 138:1095–1097.

Noci, G., Kohl, J. L., Antonucci, E., Tondello, G., Huber, M. C. E., Fineschi, S., Gardner, L. D., Naletto, G., Nicolosi, P., Raymond, J. C., Romoli, M., Spadaro, D., Siegmund, O. H. W., Benna, C., Ciaravella, A., Giordano, S., Michels, J., Modigliani, A., Panasyuk, A., Pernechele, C., Poletto, G., Smith, P. L., and Strachan, L. (1997). First results from UVCS/SOHO. *Advances in Space Research*, 20:2219–2230.

Ofman, L. (2004). Three-fluid model of the heating and acceleration of the fast solar wind. *Journal of Geophysical Research (Space Physics)*, 109(A18):7102–+.

Ofman, L. (2005). MHD Waves and Heating in Coronal Holes. *Space Science Reviews*, 120:67–94.

Ofman, L. and Davila, J. M. (1995). Alfvén wave heating of coronal holes and the relation to the high-speed solar wind. *J. Geophys. Res.*, 100:23413–23426.

Ofman, L. and Davila, J. M. (1997). Do First Results from SOHO UVCS Indicate That the Solar Wind Is Accelerated by Solitary Waves? *Astrophys. J. Lett.*, 476:L51+.

Ofman, L. and Davila, J. M. (2001). Three-Fluid 2.5-dimensional Magnetohydrodynamic Model of the Effective Temperature in Coronal Holes. *Astrophys. J.*, 553:935–940.

Ofman, L., Nakariakov, V. M., and DeForest, C. E. (1999). Slow Magnetosonic Waves in Coronal Plumes. *Astrophys. J.*, 514:441–447.

Ofman, L., Romoli, M., Poletto, G., Noci, G., and Kohl, J. L. (1997). Ultraviolet Coronagraph Spectrometer Observations of Density Fluctuations in the Solar Wind. *Astrophys. J. Lett.*, 491:L111+.

Ofman, L., Romoli, M., Poletto, G., Noci, G., and Kohl, J. L. (2000). UVCS WLC Observations of Compressional Waves in the South Polar Coronal Hole. *Astrophys. J.*, 529:592–598.

Orozco Suárez, D., Bellot Rubio, L. R., del Toro Iniesta, J. C., Tsuneta, S., Lites, B. W., Ichimoto, K., Katsukawa, Y., Nagata, S., Shimizu, T., Shine, R. A., Suematsu, Y., Tarbell, T. D., and Title, A. M. (2007). Quiet-Sun Internetwork Magnetic Fields from the Inversion of Hinode Measurements. *Astrophys. J. Lett.*, 670:L61–L64.

O'Shea, E., Banerjee, D., and Doyle, J. G. (2006). Magnetoacoustic wave propagation in off-limb polar regions. *Astron. & Astrophys.*, 452:1059–1068.

O'Shea, E., Banerjee, D., and Doyle, J. G. (2007). A statistical study of wave propagation in coronal holes. *Astron. & Astrophys.*, 463:713–725.

O'Shea, E., Banerjee, D., Doyle, J. G., Fleck, B., and Murtagh, F. (2001). Active region oscillations. *Astron. & Astrophys.*, 368:1095–1107.

Parker, E. N. (1958). Dynamics of the Interplanetary Gas and Magnetic Fields. *Astrophys. J.*, 128:664–+.

Pasachoff, J. M., Babcock, B. A., Russell, K. D., and Seaton, D. B. (2002). Short-Period Waves That Heat the Corona Detected at the 1999 Eclipse. *Solar Phys.*, 207:241–257.

Pasachoff, J. M. and Landman, D. A. (1984). High-frequency coronal oscillations and coronal heating. *Solar Phys.*, 90:325–330.

Patsourakos, S. and Vial, J.-C. (2000). Outflow velocity of interplume regions at the base of Polar Coronal Holes. *Astron. & Astrophys.*, 359:L1–L4.

Phillips, K. J. H., Feldman, U., and Landi, E. (2008). *Ultraviolet and X-ray Spectroscopy of the Solar Atmosphere*. Cambridge University Press.

Popescu, M. D., Banerjee, D., O'Shea, E., Doyle, J. G., and Xia, L. D. (2005). Very long period activity at the base of solar wind streams. *Astron. & Astrophys.*, 442:1087–1090.

Popescu, M. D., Doyle, J. G., and Xia, L. D. (2004). Network boundary origins of fast solar wind seen in the low transition region? *Astron. & Astrophys.*, 421:339–348.

Porter, L. J., Klimchuk, J. A., and Sturrock, P. A. (1994). The possible role of MHD waves in heating the solar corona. *Astrophys. J.*, 435:482–501.

Priest, E. R. (1984). *Solar magneto-hydrodynamics*.

Raouafi, N., Harvey, J. W., and Solanki, S. K. (2007). Properties of Solar Polar Coronal Plumes Constrained by Ultraviolet Coronagraph Spectrometer Data. *Astrophys. J.*, 658:643–656.

Reeves, E. M. (1976). The EUV chromospheric network in the quiet sun. *Solar Phys.*, 46:53–72.

Roberts, B. (2004). MHD Waves in the Solar Atmosphere. In H. Lacoste, editor, *SOHO 13 Waves, Oscillations and Small-Scale Transients Events in the Solar Atmosphere: Joint View from SOHO and TRACE*, volume 547 of *ESA Special Publication*, pages 1–+.

Roberts, B., Edwin, P. M., and Benz, A. O. (1984). On coronal oscillations. *Astrophys. J.*, 279:857–865.

Saha, M. N. (1921). On a Physical Theory of Stellar Spectra. *Royal Society of London Proceedings Series A*, 99:135–153.

Saito, T., Kudoh, T., and Shibata, K. (2001). What Determines the Height of Spicules? I. Alfvén-Wave Model and Slow-Wave Model. *Astrophys. J.*, 554:1151–1158.

Sakurai, T., Ichimoto, K., Raju, K. P., and Singh, J. (2002). Spectroscopic Observation of Coronal Waves. *Solar Phys.*, 209:265–286.

Scherrer, P. H., Bogart, R. S., Bush, R. I., Hoeksema, J. T., Kosovichev, A. G., Schou, J., Rosenberg, W., Springer, L., Tarbell, T. D., Title, A., Wolfson, C. J., Zayer, I., and MDI Engineering Team (1995). The Solar Oscillations Investigation - Michelson Doppler Imager. *Solar Phys.*, 162:129–188.

Schrijver, C. J. (2001). The Coronae of the Sun and Solar-type Stars (CD-ROM Directory: contribs/schrijv). In R. J. Garcia Lopez, R. Rebolo, & M. R. Zapaterio Osorio, editor, *11th Cambridge Workshop on Cool Stars, Stellar Systems and the Sun*, volume 223 of *Astronomical Society of the Pacific Conference Series*, pages 131–+.

Schrijver, C. J., Title, A. M., Berger, T. E., Fletcher, L., Hurlburt, N. E., Nightingale, R. W., Shine, R. A., Tarbell, T. D., Wolfson, J., Golub, L., Bookbinder, J. A., Deluca, E. E., McMullen, R. A., Warren, H. P., Kankelborg, C. C., Handy, B. N., and de Pontieu, B. (1999). A new view of the solar outer atmosphere by the Transition Region and Coronal Explorer. *Solar Phys.*, 187:261–302.

Simon, G. W. and Leighton, R. B. (1964). Velocity Fields in the Solar Atmosphere. III. Large-Scale Motions, the Chromospheric Network, and Magnetic Fields. *Astrophys. J.*, 140:1120–+.

Singh, J., Cowsik, R., Raveendran, A. V., Bagare, S. P., Saxena, A. K., Sundararaman, K., Krishan, V., Naidu, N., Samson, J. P. A., and Gabriel, F. (1997). Detection of Short-Period Coronal Oscillations during the Total Solar Eclipse of 24 October, 1995. *Solar Phys.*, 170:235–252.

Singh, J., Hasan, S. S., Gupta, G. R., Banerjee, D., Muneer, S., Raju, K. P., Bagare, S. P., and Srinivasan, R. (2009). Intensity Oscillation in the Corona as Observed during the Total Solar Eclipse of 29 March 2006. *Solar Phys.*, 260:125–134.

Skumanich, A., Smythe, C., and Frazier, E. N. (1975). On the statistical description of inhomogeneities in the quiet solar atmosphere. I - Linear regression analysis and absolute calibration of multichannel observations of the Ca/+/ emission network. *Astrophys. J.*, 200:747–764.

Spangler, S. R. (2002). The Amplitude of Magnetohydrodynamic Turbulence in the Inner Solar Wind. *Astrophys. J.*, 576:997–1004.

Stark, B. A. (1996). Wave resonances and induced flow due to nonlinear Alfvén waves in a stratified atmosphere. *J. Geophys. Res.*, 101:15615–15628.

Suzuki, T. K. (2004). Coronal heating and acceleration of the high/low-speed solar wind by fast/slow MHD shock trains. *Mon. Not. Roy. Astron. Soc.*, 349:1227–1239.

Suzuki, T. K. and Inutsuka, S. (2005). Making the Corona and the Fast Solar Wind: A Self-consistent Simulation for the Low-Frequency Alfvén Waves from the Photosphere to 0.3 AU. *Astrophys. J. Lett.*, 632:L49–L52.

Taroyan, Y. and Erdélyi, R. (2009). Heating Diagnostics with MHD Waves. *Space Science Reviews*, 149:229–254.

Telloni, D., Antonucci, E., and Dodero, M. A. (2007). Outflow velocity of the $O^{+5}$ ions in polar coronal holes out to 5 R. *Astron. & Astrophys.*, 472:299–307.

Teriaca, L., Banerjee, D., and Doyle, J. G. (1999). SUMER observations of Doppler shift in the quiet Sun and in an active region. *Astron. & Astrophys.*, 349:636–648.

Teriaca, L., Poletto, G., Romoli, M., and Biesecker, D. A. (2003). The Nascent Solar Wind: Origin and Acceleration. *Astrophys. J.*, 588:566–577.

Tian, H., Marsch, E., Tu, C.-Y., Xia, L.-D., and He, J.-S. (2008). Sizes of transition-region structures in coronal holes and in the quiet Sun. *Astron. & Astrophys.*, 482:267–272.

Tian, H. and Xia, L. (2008). Network oscillations at the boundary of an equatorial coronal hole. *Astron. & Astrophys.*, 488:331–337.

Timothy, A. F., Krieger, A. S., and Vaiana, G. S. (1975). The structure and evolution of coronal holes. *Solar Phys.*, 42:135–156.

Tomczyk, S., McIntosh, S. W., Keil, S. L., Judge, P. G., Schad, T., Seeley, D. H., and Edmondson, J. (2007). Alfvén Waves in the Solar Corona. *Science*, 317:1192–.

Torrence, C. and Compo, G. P. (1998). A Practical Guide to Wavelet Analysis. *Bulletin of the American Meteorological Society*, 79:61–78.

Torsti, J., Valtonen, E., Lumme, M., Peltonen, P., Eronen, T., Louhola, M., Riihonen, E., Schultz, G., Teittinen, M., Ahola, K., Holmlund, C., Kelhä, V., Leppälä, K., Ruuska, P., and Strömmer, E. (1995). Energetic Particle Experiment ERNE. *Solar Phys.*, 162:505–531.

Tsuneta, S., Ichimoto, K., Katsukawa, Y., Lites, B. W., Matsuzaki, K., Nagata, S., Orozco Suárez, D., Shimizu, T., Shimojo, M., Shine, R. A., Suematsu, Y., Suzuki, T. K., Tarbell, T. D., and Title, A. M. (2008a). The Magnetic Landscape of the Sun's Polar Region. *Astrophys. J.*, 688:1374–1381.

Tsuneta, S., Ichimoto, K., Katsukawa, Y., Nagata, S., Otsubo, M., Shimizu, T., Suematsu, Y., Nakagiri, M., Noguchi, M., Tarbell, T., Title, A., Shine, R., Rosenberg, W., Hoffmann, C., Jurcevich, B., Kushner, G., Levay, M., Lites, B., Elmore, D., Matsushita, T., Kawaguchi, N., Saito, H., Mikami, I., Hill, L. D., and Owens, J. K. (2008b). The Solar Optical Telescope for the Hinode Mission: An Overview. *Solar Phys.*, 249:167–196.

Tsurutani, B. T., Ho, C. M., Arballo, J. K., Goldstein, B. E., and Balogh, A. (1995). Large amplitude IMF fluctuations in corotating interaction regions: Ulysses at midlatitudes. *Geophys. Res. Lett.*, 22:3397–3400.

Tu, C. and Marsch, E. (1994). On the nature of compressive fluctuations in the solar wind. *J. Geophys. Res.*, 99:21481–+.

Tu, C. and Marsch, E. (1995). MHD structures, waves and turbulence in the solar wind: Observations and theories. *Space Science Reviews*, 73:1–210.

Tu, C.-Y., Zhou, C., Marsch, E., Xia, L.-D., Zhao, L., Wang, J.-X., and Wilhelm, K. (2005). Solar Wind Origin in Coronal Funnels. *Science*, 308:519–523.

Uchida, Y. (1970). Diagnosis of Coronal Magnetic Structure by Flare-Associated Hydromagnetic Disturbances. *Pub. Astron. Soc. Japan*, 22:341–+.

Ulmschneider, P., Priest, E. R., and Rosner, R., editors (1991). *Mechanisms of Chromospheric and Coronal Heating*.

Vaiana, G. S. (1976). The X-ray corona from SKYLAB. *Royal Society of London Philosophical Transactions Series A*, 281:365–374.

Vaiana, G. S., Davis, J. M., Giacconi, R., Krieger, A. S., Silk, J. K., Timothy, A. F., and Zombeck, M. (1973). X-Ray Observations of Characteristic Structures and Time Variations from the Solar Corona: Preliminary Results from SKYLAB. *Astrophys. J. Lett.*, 185:L47+.

Van Doorsselaere, T., Nakariakov, V. M., and Verwichte, E. (2008). Detection of Waves in the Solar Corona: Kink or Alfvén? *Astrophys. J. Lett.*, 676:73–75.

Vecchio, A., Cauzzi, G., Reardon, K. P., Janssen, K., and Rimmele, T. (2007). Solar atmospheric oscillations and the chromospheric magnetic topology. *Astron. & Astrophys.*, 461:L1–L4.

Vernazza, J. E., Avrett, E. H., and Loeser, R. (1981). Structure of the solar chromosphere. III - Models of the EUV brightness components of the quiet-sun. *Astrophys. J. Suppl.*, 45:635–725.

Verwichte, E., Nakariakov, V. M., and Cooper, F. C. (2005). Transverse waves in a post-flare supra-arcade. *Astron. & Astrophys.*, 430:L65–L68.

Voulgaris, A., Athanasiadis, T., Seiradakis, J. H., and Pasachoff, J. M. (2010). A Comparison of the Red and Green Coronal Line Intensities at the 29 March 2006 and the 1 August 2008 Total Solar Eclipses: Considerations of the Temperature of the Solar Corona. *Solar Phys.*, 264:45–55.

Walsh, R. W. and Ireland, J. (2003). The heating of the solar corona. *Astron. Astrophys. Rev.*, 12:1–41.

Wang, T. J., Ofman, L., and Davila, J. M. (2009a). Propagating Slow Magnetoacoustic Waves in Coronal Loops Observed by Hinode/EIS. *Astrophys. J.*, 696:1448–1460.

Wang, T. J., Ofman, L., Davila, J. M., and Mariska, J. T. (2009b). Hinode/EIS observations of propagating low-frequency slow magnetoacoustic waves in fan-like coronal loops. *Astron. & Astrophys.*, 503:L25–L28.

Wang, Y.-M., Sheeley, Jr., N. R., Dere, K. P., Duffin, R. T., Howard, R. A., Michels, D. J., Moses, J. D., Harvey, J. W., Branston, D. D., Delaboudiniere, J.-P., Artzner, G. E., Hochedez, J. F., Defise, J. M., Catura, R. C., Lemen, J. R., Gurman, J. B., Neupert, W. M., Newmark, J., Thompson, B., and Maucherat, A. (1997). Association of Extreme-Ultraviolet Imaging Telescope (EIT) Polar Plumes with Mixed-Polarity Magnetic Network. *Astrophys. J. Lett.*, 484:L75+.

Wikstøl, Ø., Hansteen, V. H., Carlsson, M., and Judge, P. G. (2000). Chromospheric and Transition Region Internetwork Oscillations: A Signature of Upward-propagating Waves. *Astrophys. J.*, 531:1150–1160.

Wilhelm, K. (2006). Solar coronal-hole plasma densities and temperatures. *Astron. & Astrophys.*, 455:697–708.

Wilhelm, K., Curdt, W., Marsch, E., Schühle, U., Lemaire, P., Gabriel, A., Vial, J.-C., Grewing, M., Huber, M. C. E., Jordan, S. D., Poland, A. I., Thomas, R. J., Kühne, M., Timothy, J. G., Hassler, D. M., and Siegmund, O. H. W. (1995). SUMER - Solar Ultraviolet Measurements of Emitted Radiation. *Solar Phys.*, 162:189–231.

Wilhelm, K., Dammasch, I. E., Marsch, E., and Hassler, D. M. (2000). On the source regions of the fast solar wind in polar coronal holes. *Astron. & Astrophys.*, 353:749–756.

Wilhelm, K., Lemaire, P., Curdt, W., Schuhle, U., Marsch, E., Poland, A. I., Jordan, S. D., Thomas, R. J., Hassler, D. M., Huber, M. C. E., Vial, J., Kuhne, M., Siegmund, O. H. W., Gabriel, A., Timothy, J. G., Grewing, M., Feldman, U., Hollandt, J., and Brekke, P. (1997). First Results of the SUMER Telescope and Spectrometer on SOHO - I. Spectra and Spectroradiometry. *Solar Phys.*, 170:75–104.

Williams, D. R., Mathioudakis, M., Gallagher, P. T., Phillips, K. J. H., McAteer, R. T. J., Keenan, F. P., Rudawy, P., and Katsiyannis, A. C. (2002). An observational study of a magneto-acoustic wave in the solar corona. *Mon. Not. Roy. Astron. Soc.*, 336:747–752.

Williams, D. R., Phillips, K. J. H., Rudawy, P., Mathioudakis, M., Gallagher, P. T., O'Shea, E., Keenan, F. P., Read, P., and Rompolt, B. (2001). High-frequency oscillations in a solar active region coronal loop. *Mon. Not. Roy. Astron. Soc.*, 326:428–436.

Withbroe, G. L. (1983). Evidence for temporal variations in polar plumes. *Solar Phys.*, 89:77–88.

Withbroe, G. L. and Noyes, R. W. (1977). Mass and energy flow in the solar chromosphere and corona. *Ann. Rev. Astron. Astrophys.*, 15:363–387.

Woch, J., Axford, W. I., Mall, U., Wilken, B., Livi, S., Geiss, J., Gloeckler, G., and Forsyth, R. J. (1997). SWICS/Ulysses observations: The three-dimensional structure of the heliosphere in the declining/minimum phase of the solar cycle. *Geophys. Res. Lett.*, 24:2885–2888.

Xia, L. D., Marsch, E., and Curdt, W. (2003). On the outflow in an equatorial coronal hole. *Astron. & Astrophys.*, 399:L5–L9.

Xia, L. D., Marsch, E., and Wilhelm, K. (2004). On the network structures in solar equatorial coronal holes. Observations of SUMER and MDI on SOHO. *Astron. & Astrophys.*, 424:1025–1037.

Zaqarashvili, T. V. (2003). Observation of coronal loop torsional oscillation. *Astron. & Astrophys.*, 399:L15–L18.

Zaqarashvili, T. V. and Erdélyi, R. (2009). Oscillations and Waves in Solar Spicules. *Space Sci. Rev.*, 149:355–388.

Zaqarashvili, T. V. and Roberts, B. (2002). Swing wave-wave interaction: Coupling between fast magnetosonic and Alfvén waves. *Phys. Rev. E*, 66(2):026401–+.

Zhang, J., Woch, J., Solanki, S. K., von Steiger, R., and Forsyth, R. (2003). Interplanetary and solar surface properties of coronal holes observed during solar maximum. *Journal of Geophysical Research (Space Physics)*, 108:1144–+.

Zirker, J. B. (1993). Coronal heating. *Solar Phys.*, 148:43–60.